UNIVERSITE LIBRE DE BRUXELLES

Faculté des Sciences Appliquées

Laboratoire de Chimie quantique et Photophysique

Inversion des spectres infrarouges enregistrés par l'instrument SOIR à bord de la sonde Venus Express

Inversion of the infrared spectra recorded by the SOIR instrument on board Venus Express

Arnaud Mahieux

sous la direction de M. Herman et A.C. Vandaele

2006 - 2011

Remerciements

Il est de coutume de remercier au début d'un tel travail tous ceux qui, de près ou de loin, ont contribué à le rendre possible, et surtout de le voir se terminer. A l'aulne d'en écrire les dernières pages, je voudrais profiter de cette ultime page blanche qui m'est offerte pour remercier chaleureusement tous ceux, sans qui, ce travail n'aurait pu aboutir. Je suis heureux de pouvoir le faire aujourd'hui avec mon enthousiasme le plus intense et le plus sincère, et de leur rendre le mérite qui leur appartient.

Je désire tout d'abord remercier Michel Herman pour avoir accepté de m'encadrer dans ce travail, ainsi que tous les membres du comité d'accompagnement de la thèse, Ann Carine Vandaele, Michel Godefroid, Jean Vander Auwera et Jean-Claude Gérard.

Je remercie également chalereusement les membres du jury, qui ont acceptés de prendre le temps de lire et d'évaluer ce (long) travail, Gérard Degrez (ULB) - Président, Michel Herman (ULB), Jean Vander Auwera (ULB) - Secrétaire, Ann Carine Vandaele (IASB), Emile Biémont (UMons - ULg), Jean-Claude Gérard (ULg), Jean-Loup Bertaux (LATMOS) et Michel Godefroid (ULB).

La réalisation de ce travail n'aurait pu être possible sans l'aide sans failles d'Ann Carine Vandaele, qui m'a soutenu, conseillé, aiguillé, fait confiance durant ces quatre années. Je tiens à la remercier tout particulièrement pour toute l'énergie, toute la bonne volonté et toute la patience qu'elle y a mise à mes côtés. Je pense aussi tout spécialement à Valérie Wilquet, avec qui j'ai eu la chance de travailler, d'échanger, parler - aussi bien de nos recherches scientifiques que de ce qui aère et libère l'esprit - qui m'a énormément écouté, conseillé et encouragé. Je lui dois un tout grand merci. Je veux remercier aussi chaleureusement Rachel Drummond et Séverine Robert, pour leur écoute, leurs nombreux commentaires, et les nombreuses relectures du travail. Je tiens à exprimer à toutes ma profonde gratitude pour leurs compréhensions et encouragements continus, et ce jusqu'à la rédaction de ces dernières lignes. Du fond du coeur, merci à vous 4 !

J'aimerais également grandement remercier l'équipe française du LATMOS (CNRS) pour les nombreuses interactions fructueuses qui ont jalonnées la réalisation de ce travail : Jean-Loup Bertaux, PI de l'instrument, Franck Montmessin, Aurélie Reberac, Emilie Royer, Vincent Sarago, Eric Villard et Anni Määttänen, ainsi que l'équipe russe (IKI) : Oleg Korablev, Anna Fedorova et Denis Belyaev.

A Bruxelles, je tiens à remercier au sein de l'IASB l'équipe d'ingénieurs de SOIR et plus particulièrement : Eddy Neefs, Bojan Ristic, Denis Nevejans, Sophie Berkenbosh et Roland Clairquin pour toutes nos collaborations quotidiennes. Je remercie également l'équipe IT pour les nombreux redémarrages des serveurs, la gestion des si nombreux processus lancés sur les machines, les problèmes d'accès, les questions récurrentes et l'ensemble des soucis informatiques rencontrés au cours de ce travail de recherche. Je pense à Johan Bulke, Fabienne Leclere, Frédéric Counerotte, Vincent Letocart et Arnaud Lefebvre. Un mot également pour Yannick Willame de l'équipe Mars, qui m'aura fait tant rire depuis trois ans. Ensuite, j'aimerais remercier mes collègues de l'IASB pour nos échanges au quotidien, toujours avec le sourire, et pour certains pour nos discussions scientifiques ou autres, Fabien Darrouzet, Alexis Merlaud, Romain Maggiolo, Filip Vanhellemont, Caroline Fayt, Corinne Vigouroux, Gaia Pinardi, Christine Bingen, David Bolsée, Didier Fussen, Nina Mateshvili, Christian Hermans, Jeroen Maes, Nuno Pereira, Jeroen Van Gent, Sébastien Vis-

cardy et tous les autres collègues de l'Institut. Un mot tout particulier à Christophe Lerot pour le $\sqrt{\pi}$, il comprendra... Un grand merci aussi à l'équipe administrative et au secrétariat de l'IASB.

Dans l'équipe de Venus Express, je tiens à remercier chaleureusement Håkan Svedhem, Dmitri Titov et Olivier Witasse, ainsi que Sanjay Limaye, Thomas Widemann, Guido Sonnabend, Manuela Sornig, Miguel López Valverde et Manuel López Puertas pour leurs conseils avisés, leur temps et leur gentillesse.

Je remercie également le CNES, le CNRS, Roskomos et l'Académie russe des Sciences. Le programme de recherche a été financé par la Politique Scientifique Fédérale (Belgian Federal Science Policy Office) et l'Agence Spatiale Européenne (ESA, programme PRODEX, contrats C 90268, 90113 et 17645).

Enfin, je tiens à remercier mes parents, mes frères et soeur et l'ensemble de mes proches pour leur gentillesse et leur compréhension durant ces derniers mois. Je réserve un mot tout particulier pour Maykel, tout d'abord pour le simple fait d'être à mes côtés, ensuite pour m'avoir soutenu, supporté, encouragé et nourri durant tout ce temps. Je lui garde toute ma gratitude et mon estime. Merci aussi à Camille et à Céline pour cette écoute et cette amitié que vous m'avez offerte. Merci à Jean, pour ses encouragements, et sans qui ma route n'aurait jamais croisé le chemin passionnant de ce travail de recherche.

Merci à tous ceux, amis et connaissances, qui de près ou de loin, ont permis à ce travail d'aboutir.

Résumé

Vénus, deuxième planète du système solaire, souvent appelée soeur de la Terre, car présentant des caractéristiques de taille et de masse similaires, est fort différente de notre planète. En effet, son atmosphere est beaucoup plus dense et dynamiquement active que celle de la Terre. Dans ce travail, nous nous concentrerons sur la région s'étendant de 70 km à 180 km d'altitude : la mésosphère et la basse thermosphère.

SOIR, acronyme de *Solar Occultation in the InfraRed*, est un instrument russo-franco-belge embarqué à bord de la mission Venus Express de l'Agence Spatiale Européenne. Il utilise un réseau à échelle comme élément diffractant. La plage de nombre d'onde mesurable par SOIR s'étend de 2200 cm^{-1} à 4400 cm^{-1}, ou 4.3 μm à 2.2 μm en longueur d'onde. Les ordres de diffraction utiles varient de 101 à 194. Un filtre acousto-optique - AOTF - est utilisé comme passe-bande pour sélectionner les ordres de diffraction. La résolution de l'instrument varie de 0.13 à 0.24 cm^{-1}.

Du fait d'un temps de développement raccourci, presque toutes les calibrations de l'instrument ont dû être réalisées en vol. Elles comprennent les calibrations relatives au réseau à échelle (angle exact de Blaze et fonction de Blaze), au détecteur (non-uniformité pixel à pixel, courbe de sensibilité spectrale, relation entre les pixels et les nombres d'onde, résolution de l'instrument, intervalle d'échantillonnage spectral, rapport signal sur bruit, background thermique) et à l'AOTF (relation entre la radio-fréquence d'excitation de l'AOTF et les nombres d'onde, fonction de transfert de l'AOTF). L'approche et la réalisation de ces différentes calibrations sont présentées dans le présent travail. Les caractéristiques de l'instrument y sont également décrites.

Un algorithme d'inversion spectrale a été développé pour le cas spécifique de SOIR. Tenant compte du mode de mesure, l'occultation solaire, la méthode de la pelure d'oignons a été implémentée dans un algorithme dit de l'Estimation Optimale. Cette méthode permet d'inverser l'ensemble des mesures spectrales en une fois, et également d'en tirer d'autres informations, comme l'amélioration de certaines caractéristiques instrumentales. Les paramètres qui sont ajustés au sein de l'algorithme sont la densité de la ou des espèces absorbant dans la région spectrale concernée, la température, les paramètres de la ligne de base, qui permettent de déterminer les caractéristiques des aérosols, le déplacement Doppler des raies qui trouve principalement son origine dans la vitesse de déplacement du satellite, et l'amélioration de certaines calibrations. Une étude de sensibilité des différents paramètres de l'algorithme est également présentée, ainsi qu'une évaluation des erreurs instrumentales systématiques.

Dans l'ensemble des spectres enregistrés durant les 4 premières années de la mission, des profils verticaux de CO_2, CO, H_2O, HDO, SO_2, H_2SO_4, HCl et HF ont été obtenus. Des valeurs limites de densité de OCS, H_2CO, O_3 et CH_4 ont également été calculées.

Les résultats concernant le dioxyde de carbone sont développés dans le texte. Des profils verticaux de CO_2 s'étendant de 70 km à 180 km d'altitude sont analysés en profondeur. Ils sont comparés aux profils dits hydrostatiques, et des hypothèses quant à la dynamique agissant au niveau des deux terminateurs de Vénus sont formulées.

Samenvatting

Venus, de tweede planeet van het zonnestelsel, wordt vaak gezien als de zusterplaneet van de Aarde. Er is immers een grote gelijkenis tussen de afmetingen en de massa van de twee planeten. Venus verschilt echter zeer sterk van onze planeet. Haar atmosfeer is wat dichter en er heerst een veel dynamischer activiteit. Dit werk zal zich toespitsten op het gebied tussen 70 en 180 km hoogte: de mesosfeer en de thermosfeer.

SOIR, acroniem van *Solar Occultation in the Infrared*, is een Russisch-Frans-Belgisch instrument aan boord van de Venus Express missie van de Europese Ruimtevaartorganisatie. Het instrument is opgebouwd rond een echelle rooster die gebruikt wordt als diffractief element. Het golfnummergebied van SOIR trekt zich uit van 2200 cm^{-1} tot 4400 cm^{-1}, of 4.3 μm tot 2.2 μm in golflengte. De bruikbare diffractieordes gaan van 101 tot 194. Er wordt gebruik gemaakt van een acousto-optisch banddoorlaatfilter - AOTF - om afzonderlijke diffractieordes te selecteren. De spectrale resolutie van het instrument ligt tussen 0.13 en 0.24 cm^{-1}.

Ten gevolge van een gebrek aan tijd tijdens de ontwikkelingsfase van het instrument, moesten bijna alle kalibraties tijdens de vlucht gebeuren. Die kalibraties betreffen het echelle rooster (berekenen van de blaze angle en de blaze-functie), de detector (pixel-tot-pixel niet-uniformiteit, spectrale gevoeligheidscurve, pixel-golflengte relatie, resolutie, spectraal bemonsteringsinterval, signaal-ruisverhouding en thermische achtergrond) en de AOTF (radiofrequentie-golfnummer relatie en transfertfunctie). De methodologie en de berekeningswijze van deze verschillende kalibraties zullen in dit werk worden voorgesteld. Ook de voornaamste eigenschappen van het instrument zullen beschreven worden.

Speciaal voor SOIR werd een spectraal inversiealgoritme ontwikkeld. Dit *Optimal Estimation* algoritme maakt gebruik van de uienschilmethode en houdt rekening met de specifieke meetmethode van het instrument, namelijk de zonsverduisteringtechniek. Het algoritme laat toe alle spectrale metingen tegelijk te inverteren, maar resulteert ook in een verbeterde kennis van de instrumentparameters. De parameters die worden berekend zijn: de dichtheid van de gezochte bestanddelen, de temperatuur, de *base line* parameters die informatie bevatten over de aerosolinhoud, de verschuiving van de spectrale lijnen ten gevolge van de snelheid van de satelliet, en enkele verbeterde instrumentparameters. Een gevoeligheidsstudie van de algoritmeparameters werd uitgevoerd en onder meer de systematische instrumentfouten worden geëvalueerd.

Uit de ganse set spectra die gedurende de eerste vier jaar van de missie werden gemeten, werden verticale profielen voor CO_2, CO, H_2O, HDO, SO_2, H_2SO_4, HCl en HF afgeleid. Grenswaarden voor de dichtheid van OCS, H_2CO, O_3 en CH_4 werden berekend.

De resultaten voor CO_2 worden uitvoerig in de tekst beschreven, aan de hand van een grondige analyse van de verticale profielen die tussen 70 en 180 km werden opgemeten. Er wordt een vergelijking gemaakt met de hydrostatische profielen, en hypothesen over het dynamische gedrag van de atmosfeer aan beide terminatoren worden geformuleerd.

Abstract

Venus, second planet of the solar system, is often seen as the sister planet of the Earth. In terms of size and mass, they are indeed very similar, but the Venus atmosphere is much thicker and active. The altitude region extending from 70 km to 180 km is studied in this thesis, namely the mesosphere and the lower thermosphere.

SOIR, which stands for Solar Occultation in the InfraRed, is a Russian / French / Belgian instrument flying on board of the Venus Express (VEX) spacecraft of the European Space Agency. The diffracting device of SOIR is an echelle grating. The wavenumber region studied ranges from 2200 cm^{-1} to 4400 cm^{-1}, or 4.3 μm to 2.2 μm in wavelength. The diffraction orders used with SOIR vary from 101 to 194. To select the required echelle grating diffraction order, an Acousto-Optical Tunable Filter - AOTF - is located after the entrance slit of the instrument. The instrument resolution varies from 0.13 to 0.24 cm^{-1}.

SOIR was developed in a very short time. Thus, virtually all the calibrations had to be made in-flight. These concern the echelle grating (exact Blaze angle computation, Blaze function), the detector (pixel-to-pixel non-uniformity, spectral sensitivity curve, pixel-to-wavenumber relationship, instrument resolution, spectral sampling interval, signal-to-noise ratio, thermal background) and the AOTF (wavenumber to AOTF frequency relation, AOTF transfer function). The procedure for and the computation of these calibrations are described in this work, as well as the instrument characteristics.

A spectral inversion algorithm was developed specifically for the SOIR measurement technique: the solar occultation. The onion peeling method is implemented using the Optimal Estimation Method. It allows the inversion of the spectral data in one go, and also the enhancement of some instrumental characteristics. The algorithm variables are the densities of the species absorbing in the diffraction order, the temperature of the atmosphere under study, the spectral background parameters, that allow the determination of the Venus aerosols characteristics, the Doppler shift (mainly linked to the shift induced by the satellite displacement), and the improvement of some instrumental calibrations. A sensitivity study on the algorithm parameters is also presented, and the instrumental systematic errors are investigated.

Vertical profiles of CO_2, CO, H_2O, HDO, SO_2, H_2SO_4, HCl and HF are derived from the spectra measured during the first 4 mission years. Upper limits on OCS, H_2CO, O_3 and CH_4 have also been calculated.

We focus on the carbon dioxide results in the present study. A selection of vertical profiles extending from 70 km to 180 km are analyzed in details. They are compared to the hydrostatic profiles, and propositions concerning the terminators' dynamics are formulated.

Contents

List of Figures

List of Tables

Chapter 1

Introduction

Venus is the second brightest object in the night sky after the Moon and it has always awakened the curiosity of mankind.

Systematic Earth based observations of Venus have been conducted for a few centuries but a complete comprehension has only been achieved thanks to the Soviet and American missions to Venus that started in the 1960s. Probes and spacecrafts were sent to the morning star during three decades. The last one, the US Magellan mission, ended in the early 1990s. These missions and observations enabled the understanding of the main Venus atmospheric mechanisms.

For a very long time, Venus has been thought to host a very similar environment to the one we live in, but it now appears to be a very different world. On Earth, the greenhouse effect warms the atmosphere at the surface level by about 30 K, while on Venus the greenhouse effect increases the temperature by almost 350 K. This is mainly due to the fact that the principal atmospheric compound is carbon dioxide, and that Venus is surrounded by a thick cloud layer composed of sulfuric acid droplets, which both play a role in the greenhouse effect. This cloud layer extends from 40 km to 65 km and rotates quickly around the planet, with winds reaching 300 km/h at the cloud top.

These previous missions and observations raised many questions concerning the chemistry taking place in the atmosphere and the global circulation, such as the working principle of the two polar dipoles associated to the mid-atmosphere superrotation, the species involved in the greenhouse effects, the upper atmospheric mechanisms, etc.

The European Space Agency mission Venus Express was launched at the end of 2005 and reached its target in May 2006, so more than 10 years after the last American mission. It is the first European mission to Venus. Its payload is composed of 7 instruments, wherein the SOIR instrument. Venus Express is the sister mission of the Mars Express mission, and a large part of its design and instruments have been inherited from it. The aims of the mission are various: to study the atmosphere chemistry and dynamics, the cloud layer, the magnetic fields, the plasma, etc.

SOIR is an infrared spectrometer, that has been designed and built by an international team including the Belgian Institute for Space Aeronomy (IASB-BIRA), the French Service d'Aéronomie (now LATMOS) of the CNRS and the Space Research Institute of the Russian Academy of Sciences (IKI).

The instrument performs solar occultations of the highest regions of the Venus atmosphere, above the cloud layer, between 70 and 180 km of altitude. Due to this particular measurement technique, all the measurements take place at the terminator, i.e. at 6.00 AM or 6.00 PM. Vertical profiles of various species are derived from measurements. Important dynamics are thought to take place at different altitudes of the Venus terminator, that the SOIR instrument aims to discern.

SOIR was successfully built in a very short time but few calibrations could be performed before launch. Moreover, the spare instrument is now flying on the spacecraft, as the initial spectrometer

was seriously damaged during vibration tests.

In the present manuscript, the complete calibration of the different main instrument elements is presented: the echelle grating that is used as diffracting device, the acousto-optic tunable filter working as an order selection apparatus and the detector of the instrument. These use the Sun as a light source.

Thanks to the calibration, the spectra recorded during each solar occultation can be studied. An algorithm, called Asimat, using the optimal estimation method combined with the onion peeling approach has been written to invert the spectra. The algorithm has been thorough studied, with an emphasis on the sensitivity to its different parameters. It derives the vertical profiles of the density of the targeted species, of the baseline, also used to derive the aerosols properties, and of the rotational temperature. Many Venus atmospheric compounds and their isotopologues have been investigated, such as carbon dioxide (CO_2), carbon monoxide (CO), water (H_2O), hydrochloric acid (HCl), hydrofluoric acid (HF) and sulfur dioxide (SO_2). For other compounds, such as methane (CH_4), carbonyl sulfide (OCS), sulfur monoxide (SO), formaldehyde (H_2CO), ozone (O_3), etc. detection limits have been calculated.

Carbon dioxide results are presented to illustrate the capabilities of the SOIR instrument coupled with the Asimat algorithm. Density and rotational temperature profiles extending between 90 km and 180 km are presented. They are analyzed and compared to the profiles obtained from the hydrostatic equation. The possible non-local thermodynamical effects are investigated, as well as the stability of the atmosphere.

Finally, future and parallel studies that could be conducted are proposed.

The publications in scientific journals of the author are listed in Appendix A. A list of all the abbreviations is available in Appendix B, and a list of the main variables used in the equations presented in the text is given in Appendix C.

Chapter 2

The planet Venus

2.1 Introduction

Venus, also known as the morning or evening star, takes its name from the Roman goddess of love and beauty.

It is the second planet in the Solar system, orbiting around the Sun between Mercury and the Earth. It does not have any natural satellite and is the second brightest object in the night sky, after the Moon. Its apparent magnitude [1] varies from -3.8 to -4.6. It is observable from Earth in the early evening or morning, as it is located closer to the Sun than the Earth.

Venus orbits around the Sun in 224.65 Earth days. The Venusian sidereal day lasts for 243 Earth days. This means that a Venusian day is longer than a Venusian year. The planet spins in the retrograde direction, i.e. in the opposite direction to most of the other planets of the solar system. On Venus, the Sun rises in the West and sets in the East. The solar day, or the elapsed time between two sunrises for a non-moving observer on the surface of the planet, lasts for 116.75 Earth days.

The mean distance between Venus and the Sun is 108,208,930 km, or 0.723 AU. The eccentricity of the orbit is very low (< 0.01). Venus reaches its inferior conjunction every 584 days, lying at about 41 million km from Earth.

The rotation axis is quasi perpendicular to the ecliptic, with an inclination angle of 177.3°. No seasons are observed on the planet.

Venus is often seen as the sister planet of the Earth because of their similarities in size and mass. Its main characteristics are summarized in Table 2.1.

Characteristics	Venus	Earth
Radius	6,051.8 km	6,371.0 km
Earth Radius	0.9499	1
Mass	4.87 $\times 10^{24}$ kg	5.97 $\times 10^{24}$ kg
Earth mass	0.815	1
Sidereal rotation period	-243 Earth days	1 Earth day
Sidereal year	224.65 Earth days	365.15 Earth days
Axial tilt	177.3°	23.44°
Distance to the Sun	0.723 AU	1 AU

Table 2.1: Main characteristics of Venus

Despite these similarities, Venus and the Earth are very different from each other. Firstly, Venus does not seem to have any constant magnetic field, which protects a planet from the solar

1. The lower the magnitude, the brighter in the sky the object is.

wind and space radiations. Secondly, the atmosphere is much thicker, with very high temperature and pressure at the surface: about 730 K and a pressure of 92 atm. Thirdly, it seems that no plate tectonics have taken place on Venus for millenia. Fourthly, the atmosphere and the crust of Venus are very dry, with less than 0.002 % of water in the atmopshere [Grinspoon (1993)]. And finally, Venus does not possess any natural satellite. Images taken by VIRTIS in the infrared and VMC in the ultraviolet on-board Venus Express are given in Figure 2.1. They show the upper cloud structure on the day (in the UV) and night sides (in the IR). The South polar vortex is clearly seen.

The Venus surface appears to have been shaped by very active volcanism, though it does not appear that Venus is currently active. 167 giant volcanoes, over 100 km across, have been counted [Bougher *et al.* (1997b)]. About a thousand crater impacts have been found on the surface, with diameters ranging from 3 to 280 km. No craters smaller than 3 km in diameter are observed. Indeed, the smaller meteorites are destroyed before they reach the surface due to the dense atmosphere. Figure 2.2 presents the Venus map as it was recorded by the US Magellan mission (1990-1994).

The history of the exploration of Venus is summarized in the next Section, and a summary of the knowledge of the Venus atmosphere is given in Section 2.3.

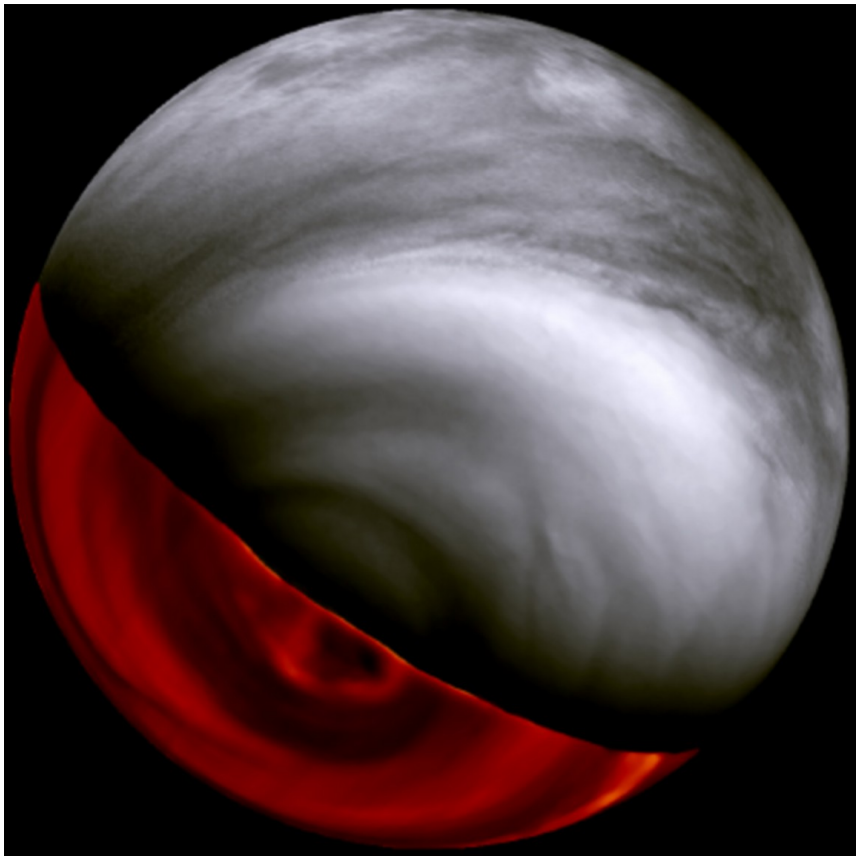

Figure 2.1: Image of Venus combining measurements from VMC and VIRTIS on board Venus Express. Credit: ESA.

2.2 Venus exploration

Venus was discovered a long time ago. Several cultures historically held its appearances as a morning and evening star to be those of two separate bodies. During the 6^{th} century BC, it was probably Pythagoras who recognized that the morning and evening stars were a single body [Fegley Jr. (2004)]. In the early 17^{th} century, Galileo found out that it showed phases like the Moon.

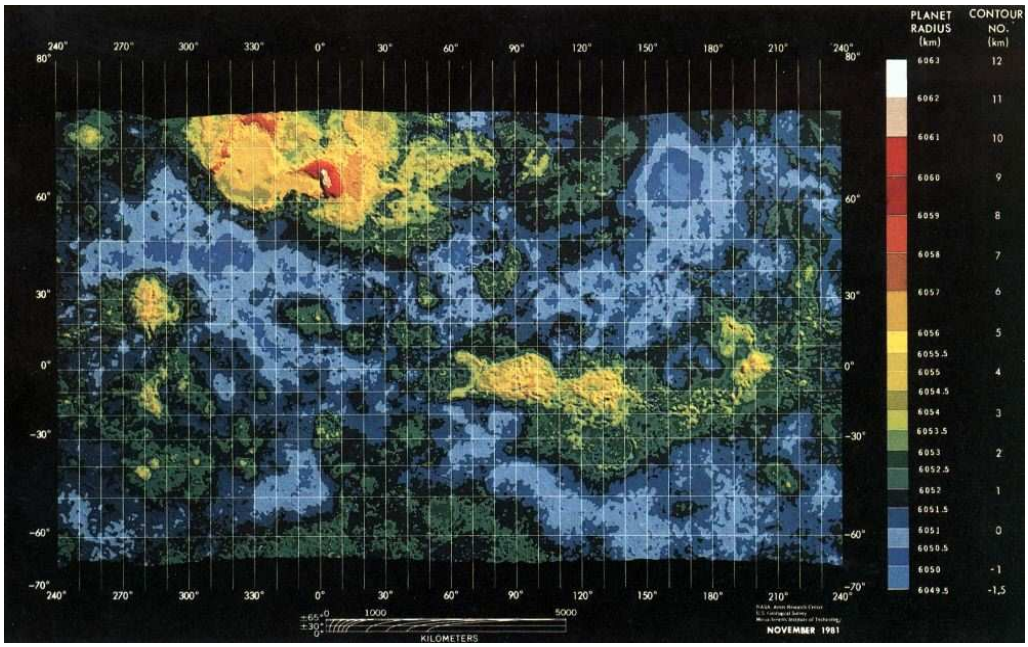

Figure 2.2: Map of Venus, as probed by the US Magellan mission radar, showing the elevated areas in yellow: Ishtar Terra in the Northern hemisphere and Aphrodite Terra just below the Equator to the East. The lowest parts are in blue. Credit: NASA.

Its atmosphere was discovered in 1761 by Mikhail Lomonosov, and observed by Johann Schröter in 1790 from the fact that the planet seemed a bit crescent. He correctly assumed that it was due to the scattering of the sunlight in the dense atmosphere. Finally, during the 18^{th} century, Cassini tried to evaluate the rotation period of the planet from the atmospheric features movement, but incorrectly found a value of 24 hours.

During the 20^{th} century, extensive ground-based campaigns started with the use of spectroscopic and radar observations, followed in the 1960s by an intensive campaign of spacecraft missions. A list summarizes all the missions sent to Venus in Appendix D.

The in-situ and space observations of Venus started in 1961 with the launch of the Russian spacecraft Venera 1 on February 12. The spacecraft never reached its target as contact was lost 7 days after launch. The first spacecraft to reach Venus was the United States Mariner 1. The Soviet Venera program ran 16 spaceships to Venus between 1962 and 1983; they returned images of the ground using landing probes (see Figure 2.3) vertical temperature and density profiles, atmospheric composition studies and surface radar maps. Venera 11 returned evidence of electrical storms in the atmosphere. The Vega 1 and 2 program completed the Russian Venus space program, by sending two probes to Venus on their way to the Halley comet. It returned atmospheric composition data.

On the US side, the Mariner program sent four probes to Venus between 1962 and 1969. The first one exploded during the launch phase. The other ones reached Venus and studied its atmosphere, returning density and temperature profiles and focused on the clouds. Later, in 1978, Pioneer Venus was put in orbit around Venus, with the aim of sending landing probes to the surface. Five probes were launched from the orbiter, but only one returned data from the surface for a relevant time. The orbiter studied the atmosphere for 13 years. In 1989, the US Magellan probe was launched to perform a quasi-complete mapping of the surface (98%) from its orbit using a radar.

Between 1989 and 2005, no spacecraft were launched to directly study Venus. However, Venus was observed by Galileo (in 1990) and Cassini (in 1998 and 1999) during flybys on their respective

missions to the outer planets. In 2005, the European Space Agency (ESA) launched the Venus Express mission, or VEX. The mission will be described in Section 2.4. In May 2010, the Japan Aerospace Exploration Agency (JAXA) launched the Akatsuki spacecraft (*Dawn* in Japanese), previously named Planet-C, for studying the atmosphere of the planet [Nakamura *et al.* (2007)]. It should have been inserted in orbit in December 2010, but the spacecraft could not be captured by the Venus gravity field. The Japanese will try another gravitational insertion in 6 years.

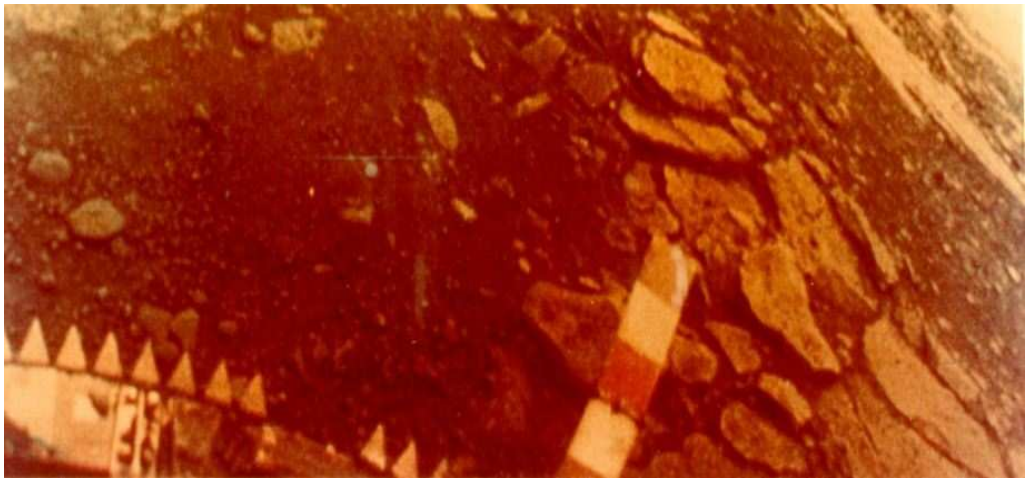

Figure 2.3: Image taken from the surface of Venus by the Russian Venera 13 lander. Credit: Russian Space Agency.

2.3 The atmosphere of Venus

2.3.1 Introduction

The Venus atmosphere is mostly composed of CO_2 (96.5%) and N_2 (3.5%) up to 120 km. Trace gases are also present, such as H_2O, CO, HCl, HF, SO_2, SO, OCS, H_2CO, etc. The reviews in Esposito *et al.* (1997) and de Bergh *et al.* (2006) summarize the vertical profiles and the composition as measured during previous missions to Venus. The trace gases are involved in complex chemical processes in the atmosphere: for example photochemical reactions between CO_2, SO_2, H_2O and HCl lead to the formation of sulfuric acid aerosols between 60 and 70 km.

The ground temperature is almost the same on both night and day sides of the planet.

The atmosphere can be divided in three different regions, based on the temperature gradient. Thus, the composition and the local operating chemistry will be different from region to region. They are called the troposphere, the mesosphere and the thermosphere.

Figure 2.4 summarizes the temperature and pressure vertical profiles of the Venus atmosphere at noon as a function of altitude.

The troposphere is located below 60 km, where the thermochemistry is dominant, because very little solar ultraviolet radiations can reach that region. The cloud layer is located across the upper

troposphere and the lower mesosphere. It covers the 30 to 70 km region, across the troposphere and the mesosphere, with the main cloud deck located between 45 and 65 km. The cloud layer is in superrotation around the planet, in the zonal [2] direction. The wind speed reaches values close to 100 m/s. Figure 2.5 depicts the zonal wind that can be found in the cloud layer.

The mesosphere, extending from 60 to ≈ 100 km, receives enough solar ultraviolet radiation so that photochemistry is dominant (photon-driven reactions).

The thermosphere, above ≈ 100 km, has a low density and overlaps with the ionosphere so that the photodissociation, ion-neutral, ion-ion reactions are increasingly dominant as we go up in the atmosphere.

As SOIR takes measurements in the upper mesosphere and the thermosphere, a dynamical, thermodynamical and chemical description of these regions of the atmosphere is given hereafter.

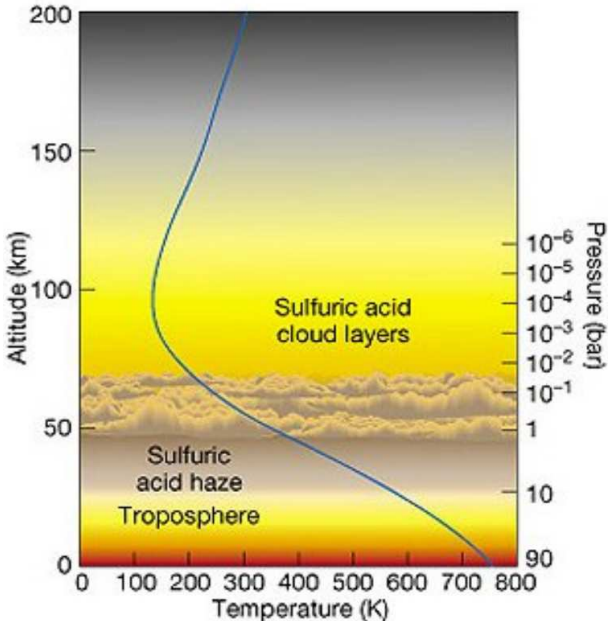

Figure 2.4: The Venus atmosphere during day conditions. The Figure shows the cloud layer in the atmosphere, the mean temperature profile on the day side, the altitude and the pressure. Credit: 2005 Pearson Prentice Hall, Inc.

2.3.2 The mesosphere

The temperature reaches a minimum value of 170 K at 100 km. Temperature profiles were measured by Pioneer Venus, as well as by the various Venera probes that entered the atmosphere [Zasova *et al.* (2007)]. These observations show relatively low day-side temperatures above 140 km, less than 300 K, even if the distance to the Sun is small. A sharp collapse to very cold night-side temperatures around 120 K across the terminator was observed. Large temperature variations were measured by the Pioneer Venus probes: 10 K at an altitude of 70 - 80 km, and 35 K at 130 km.

The temperature profiles show some interesting features in the mesosphere, and are interlinked with the wind distribution. Much of the latitudinal, zonal and vertical motions in the Venus atmosphere are driven by the variations in the solar energy absorption by sulfuric acid droplets present in the cloud layers [Jenkins *et al.* (2002)].

Between 65 and 90 km, the poles are up to 20 K warmer than the tropics. It induces a reversed meridional temperature gradient, which was observed by the Pioneer Venus Orbiter. This

2. A zonal flow concerns the west - east wind component.

anomalous thermal structure was confirmed by the Venera 15 measurements. Also, an inverse equatorial to pole temperature gradient was observed between 70 to 100 km by Pioneer Venus [Lellouch *et al.* (1997)], associated by the decay of the cloud top super-rotation.

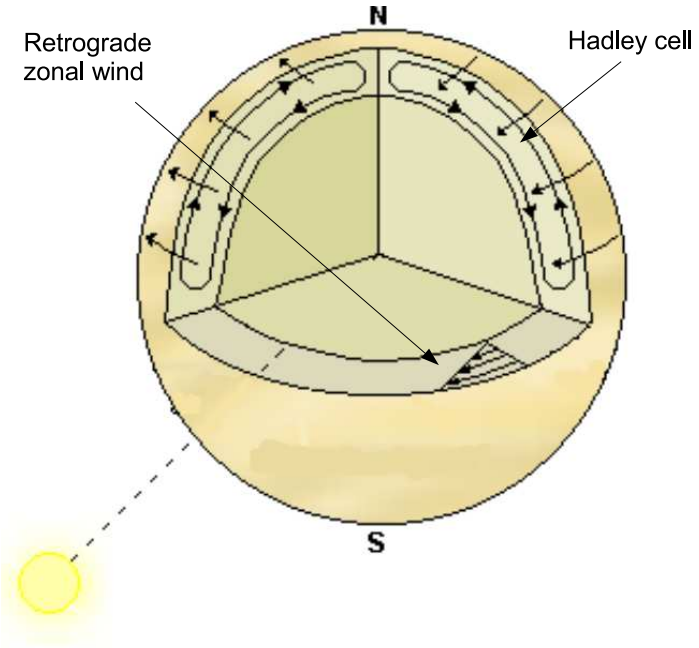

Figure 2.5: Zonal winds in the cloud layer of Venus.

A cold collar is observed between 60° and 75° of latitude around 70 km. The temperature is 30 K colder than at the Equator and a large vertical temperature inversion develops at these latitudes. This particularity creates jet winds which take place at around 53° and 65 km of altitude, with speeds reaching 140 m/s in the morning and 120 m/s in the evening. These jet winds vary in position as well as in speed.

Above 75°, the temperature profile is quasi isothermal between 65 to 75 km. Above 75 km and below 100 km, the temperature increases with latitude. The super-rotation must thus decrease between 70 and 90 km, to satisfy the thermal wind equation [3]. It is observed that the cyclostrophic [4] balance breaks down at these latitudes. Indeed, opposite to the Earth where Coriolis forces are predominant, the low rotation rate on Venus turns the atmospheric flows in the mesosphere to follow the cyclostrophic equation. The zonal wind at cloud top are retrograde with speeds of 90 - 100 m/s at the Equator, with a polarward meridional component [5], increasing with latitude to 10 m/s at 45°. They are in cyclostrophic balance, at least below 75 km, as described by Schubert (1983).

The temperature and the wind measurements show that the mesosphere is dynamically an intermediate region characterized by significant time variability.

The mesosphere is also characterized by wave propagation generated in the cloud layer right

3. The thermal wind equation is the relation between the horizontal temperature gradient and the vertical wind shear [Petty (2008)].

4. A cyclostrophic flow describes a steady-state flow taking place in a spatially-varying pressure field. In this approximation, the frictional and Coriolis actions are neglected or non-existent, and the centripetal acceleration due to the planet curvature is entirely sustained by the pressure gradient [Ackerman & Knox (2007)].

5. A meridional flow describes the north - south wind component.

below it: many types of waves are superimposed on the mean thermal and dynamical state, such as small scale gravity waves, diurnal and semi-diurnal thermal tides. These waves have a significant impact on the overall circulation. The typical horizontal size of the gravity waves is around 100 km. They start to dissipate at around 120 to 140 km due to saturation [Bougher *et al.* (1997a)].

2.3.3 The thermosphere

2.3.3.1 Chemical composition

The thermosphere is mostly composed of the following gases: O, He, N, O, CO_2, NO, CO, C and H. CO_2 becomes the main component while decreasing in altitude, reaching 96.5 % below 120 km. O becomes the more abundant constituent of the thermosphere above 155 km on the dayside, and 140 km on the nightside. Small changes between the dayside and nightside are observed in the thermosphere density and temperature profiles with solar activity [Kasprzak *et al.* (1997)]. The CO_2 chemistry will be further described later in this section.

2.3.3.2 Wind circulation

Two main flow patterns are observed in the thermosphere: a stable subsolar to anti-solar circulation driven by solar heating and a retrograde super-rotating zonal flow, with high variability, and presenting symmetric cells above 120 km. These patterns are presented in Figure 2.6.

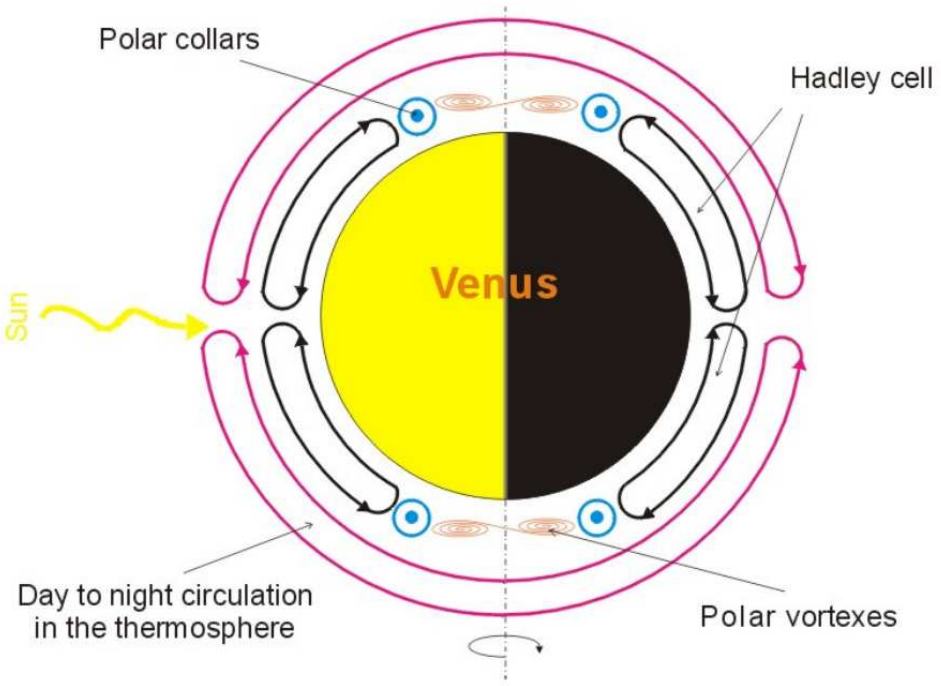

Figure 2.6: Representation of the upper mesosphere and thermosphere wind distribution on Venus in a meridian plane. On this picture, the Hadley cells and the subsolar to antisolar circulations are shown. The polar vortex driving the rotation of the cloud decks and the cold collar described in Section 2.3.2 are also represented.

The strong subsolar to antisolar circulation results from the large temperature gradient between day and night in the thermosphere [Bougher *et al.* (1997a)]. The horizontal velocity of the

subsolar to antisolar flow is believed to increase with angular separation from the subsolar point, reaching a maximum at the terminator [Sornig *et al.* (2008)]. The vertical structure is unlike the terrestrial thermosphere: on Venus, the nightside thermosphere is called cryosphere, because of the very low temperatures that are encountered in that region, due to fast radiative cooling of CO_2. Also, the temperature changes over the terminator are very abrupt. This temperature difference between day and night turns into a horizontal pressure gradient. The dayside solar heating results in an expansion of the dayside thermosphere: the height of a given pressure surface rises/falls with increasing/decreasing temperature. The large diurnal density variation suggests a significant contraction of the nightside thermosphere [Bougher *et al.* (1997a)].

It was suggested [Limaye *et al.* (1982); Rossow *et al.* (1980)] that the upper atmospheric super-rotation could be maintained in part by a mean meridional flow such as a Hadley cell [6], which transports both heat and westward zonal angular momentum to the poles at the cloud tops. There is a certain evidence for a cloud-level Hadley cell, and the specific characteristics such as the number of cells, the degree of its polar extension and the altitude level of its equatorward return branches is not well known.

2.3.4 Carbon chemistry

Carbon dioxide is the major constituent of the Venus atmosphere, and represents 96.5% up to an altitude of $\approx$ 110 km.

A carbon chemical cycle exists on Venus. It includes the photodissociation of CO_2 on the dayside by the solar UV at high altitude into CO and excited O. A significant fraction of these compounds is then transported from the day to the night side by the subsolar to antisolar circulation active in the thermosphere. On the nightside, O_2 is produced from the active excited O, and the emission of a highly variable oxygen airglow is observed on both day and nightside [Gérard *et al.* (2008)]. The lifetime of molecular oxygen in the atmosphere is supposed to be very short, as few direct measurements of this compound could be obtained up to now. Finally, O_2 and CO are converted in CO_2 via catalytic processes, using for example ClO_x and HCl compounds [Mills & Allen (2007)]. A strong vertical transport is supposed to take O and CO down in the atmosphere [Bougher *et al.* (1997a)].

Measurements of CO, product of the photodissociation of CO_2, are available at various altitudes from previous measurements. Below the cloud top, values around 28 ppm $\pm$ 8 ppm [7] have been reported at the cloud bottom (around 40 km) [Pollack *et al.* (1993); Taylor *et al.* (1997); Marcq *et al.* (2006)], decreasing with altitude to 17 ppm $\pm$ 1 ppm at 12 km [Gel'man *et al.* (1980)]. Many measurements of CO in the mesosphere and thermosphere have also been performed; summaries and results can be for example found in von Zahn *et al.* (1980),Clancy *et al.* (2008) and Gilli *et al.* (2009).

A clear latitudinal dependence of CO has been observed, with a enhancement at high latitude: an increase of $\approx$ 35% beyond 47° N has been measured by Collard & al. (1993), and later decreased to $\approx$10 - 15% beyond 40° North and South [Marcq *et al.* (2005, 2006)].

CO increases with altitude, and the vertical gradient has been measured and varies between 1.2 $\pm$ 0.5 ppm/km [Pollack *et al.* (1993)] and 0.6 $\pm$ 0.4 ppm/km [Taylor *et al.* (1997); Marcq *et al.* (2006)].

The isotopic ratio of the various carbon compounds isotopologues has been measured to be the same as on Earth [Bézard *et al.* (1987); Clancy & Muhleman (1991)].

2.3.5 Water

From measurements, water is present in low quantities below the clouds: the planet is very dry. A value of 30 $\pm$ 10 ppm on the nightside have been measured at 1.18 μm [Crisp *et al.* (1991);

6. The Hadley cell describe a flow motion that rises at the Equator and a descending motion at higher latitude. On Earth, three Hadley cells are observed, between the Equator and the subtropics, between the tropics and $\approx 60°$ and between that latitude and the poles.

7. Ppm stands for parts per million.

Pollack *et al.* (1993); de Bergh (1995)]. From Venera 11, 13 and 14, values of 20 to 40 ppm in the 5 to 60 km region have been measured, while the retrieved water quantity at the surface was found to turn between 50 and 70 ppm at the surface [Ignatiev *et al.* (1997)]. Groundbased measurements on the nightside returned values of 30 ± 10 ppm [Taylor *et al.* (1997)].

The horizontal variation has also been studied from the Galileo mission data, and values lower by 20% between altitudes of 0 and 15 km [Drossart *et al.* (1993)] and between 30 and 45 km have been observed [Marcq *et al.* (2006)]. Some local variations known as "hot spots" have been observed, where about 200 ppm of water has been reported. They have never been observed afterwards, and no explanation could be given for these phenomena [Taylor *et al.* (1997)]. The question of vertical variations has not yet been solved.

The ratio of deuterium to hydrogen is much greater than on Earth: HDO/H_2O on Venus is 120 times higher than on our planet. No other compounds than H_2O containing hydrogen are present with mixing ratios higher than 5 ppm. The planet is loosing water because H escapes to space after H_2O dissociation in the upper atmosphere. Note that large abundance of Argon have been reported on Venus [Donahue *et al.* (1997)].

From the HDO/H2O ratio, one can conclude that the planet was probably once wet. A theory [McElroy *et al.* (1982)] using present atomic hydrogen escape concludes that the lower limit of H_2O on Venus was about 0.3% of a terrestrial ocean 4.5 Gyears ago, resulting in an ocean with a depth of several meters to tens of meters.

In the upper atmosphere, water has been measured by the SOIR instrument [Bertaux *et al.* (2007); Fedorova *et al.* (2008)]: values of 1 ppm between 80 and 110 km have been derived for H_2O, and 0.09 ppm for HDO. The measured HDO/H_2O ratio turns around 0.12.

2.3.6 Wave propagation

Direct evidence of mesospheric wave propagation in the thermosphere was observed, out of horizontal periodic density fluctuations, with wavelengths between 100 and 600 km [Kasprzak *et al.* (1993)]. The measured amplitudes and relative phases of the fluctuations of He, O, N_2 and CO_2 were found to vary with the molecular weight of the species [Bougher *et al.* (1997a)].

2.4 The Venus Express mission

Venus Express (VEX) is the sister mission of the Mars Express mission (MEX). It was proposed in 2001. It reused the design of the MEX mission, and was developed in a very short time. The VEX Mission was launched from the Baikonour cosmodrome in Kazakhstan, on November 9, 2005 by a Soyuz-FG/Fregat rocket. After maneuvers in space to correct the trajectory, the spacecraft arrived at Venus on April 11, 2006 after a 150 days journey. The satellite was placed in a 24 hours polar orbit.

The nominal mission started on June 4, 2006 for two Venus sidereal years (486 Earth days), so until October 2007. It was extended two times for four other sidereal years in total, making that the mission would end in December 2012.

The periapsis of the orbit is located above the North pole, at an altitude varying between 180 and 250 km. The apoapsis is located above the south pole, at an altitude of 65,000 km. An elliptic orbit was chosen for several reasons, the main one being that it offers the possibility to have close views of the Northern hemisphere, and wider views of the Southern hemisphere.

The satellite is a cube of 1.65 m by 1.7 m by 1.4 m, weighting 1,270 kg. On two sides of the spacecraft solar panels are placed to supply electricity to its equipment. The inside temperature is maintained at 25° C. Each side of the spacecraft is named after the axes to which it is associated: +X, -X, +Y, -Y, +Z and -Z. The axes are depicted in Figure 2.7. When deployed, the solar panels are rotating along the Y axis to maximize solar input.

The aim of the mission is to study the seven following topics [Svedhem *et al.* (2007)]:
– atmospheric structure;

- atmospheric dynamics;
- atmospheric composition and chemistry;
- cloud layers and haze [8];
- energy balance and greenhouse effect;
- plasma environment and escape processes;
- surface properties and geology.

A summary concerning the mission can be found on the ESA website:
`http://sci.esa.int/science-e/www/object/index.cfm?fobjectid=33010`.

The payload of the spacecraft consists of seven instruments [Svedhem *et al.* (2007)]. The role of each one is described in Appendix E. The position of all the instruments on the spacecraft is shown in Figure 2.8. The SOIR instrument, the focus of this work, is further described in the next Chapter.

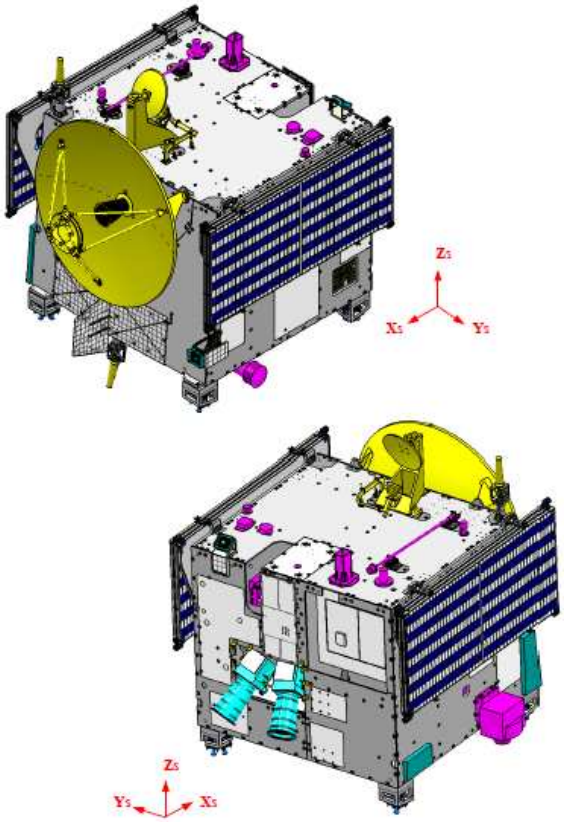

Figure 2.7: Representation of VEX with the axis definition. The solar panels are located on the +Y and -Y sides. They are retracted on the Figure. Credit ESA.

8. Haze is an atmospheric phenomenon describing the fact that dust and large particles obscure the atmosphere.

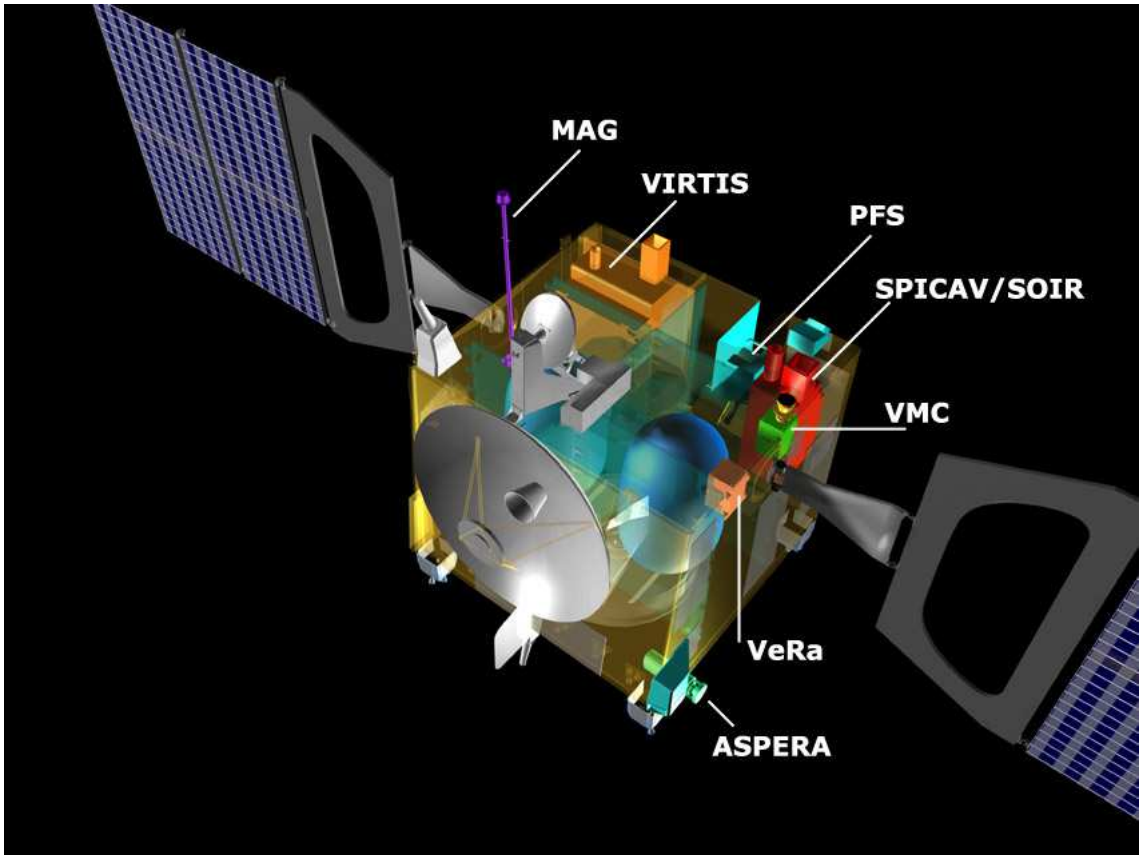

Figure 2.8: VEX spacecraft with instruments positions. Credit ESA.

Chapter 3

The SOIR instrument

3.1 Introduction

The acronym SOIR stands for *Solar Occultation in the Infrared*.

SOIR is an innovative, compact and high resolution infrared spectrometer. It is built to probe the atmosphere of Venus using the solar occultation method, therefore to record solar spectra. It measures from 2.2 μm to 4.3 μm, or 4400 cm^{-1} to 2200 cm^{-1}. It was designed at the Belgian Institute for Space Aeronomy in Brussels, Belgium, in collaboration with LATMOS, CNRS, France, and the Russian Academy of Science, IKI, Russia. It is one of the three channels of the French instrument SPICAV/SOIR flying on the mission VEX. The SPICAV instrument is composed of two channels, SPICAV-IR (0.7 - 1.7 μm), measuring in the infrared, and SPICAV-UV (0.11 - 0.31 μm), in the ultraviolet. SPICAV is a sister version of the SPICAM instrument [Bertaux *et al.* (2000, 2006)] flying on the Mars Express spacecraft of the European Space Agency. A complete description of SPICAV can be found in Bertaux *et al.* (2007).

SOIR is a low mass instrument, weighting 6.5 kg, confined in a small volume: 414 mm by 254 mm by 210 mm. The volume and the mass were restricted, because SOIR had to be superimposed to the preexisting instrument SPICAV, and to fit inside the spacecraft. The power required by the instrument to operate is less than 17 W [Nevejans *et al.* (2006)].

3.2 The SOIR optics

3.2.1 General description

The instrument is located on the $+Y$ side of the spacecraft for critical thermal reasons [Nevejans *et al.* (2006)]. The solar viewing angle is located at 60° to the $+Y$ side of the spacecraft with respect to the optical axis.

A solid and mechanical view of the SOIR instrument is given in Figure 3.1, and Figure 3.2 shows a three dimensional view, with a ray tracing projection inside the instrument.

The entrance optics of SOIR, (1) on Figure 3.2, are equipped with a fixed periscope-like device to allow the instrument to look at the Sun, when the spacecraft is oriented adequately. The entrance slit has a diameter of 20 mm. After the entrance optics, the light is sent to the Acousto-Optical Tunable Filter, or AOTF (2) (Section 3.2.4). At the exit of the AOTF, the light enters the spectrometer entrance optics (3): the light is focused using a lens in the spectrometer slit. A second lens is used to project the light through an off-axis parabolic mirror (4) on the echelle grating (5) (Section 3.2.2). The refracted light is then reflected on the same parabolic mirror (4). It is finally recorded by the detector (6) (Section 3.2.3). The parabolic mirror is used twice in the

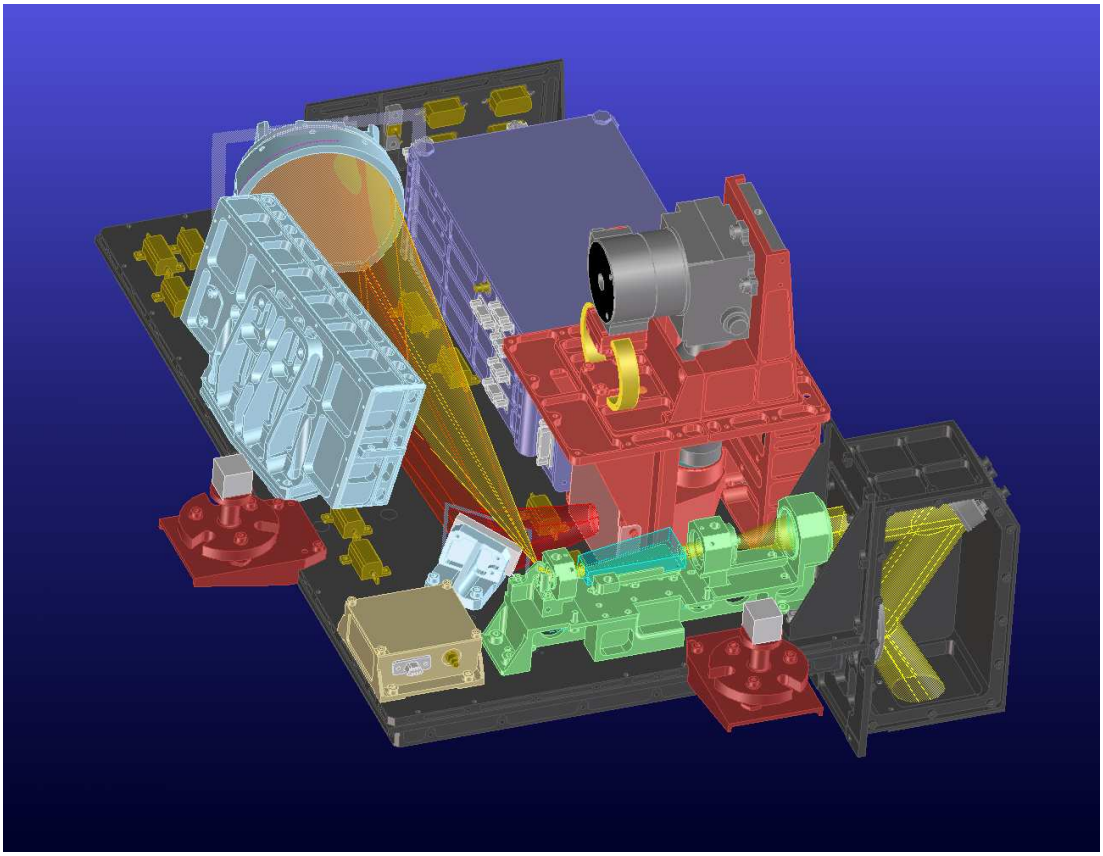

Figure 3.1: Solid and mechanical view of the main parts of SOIR, from Nevejans *et al.* (2006).

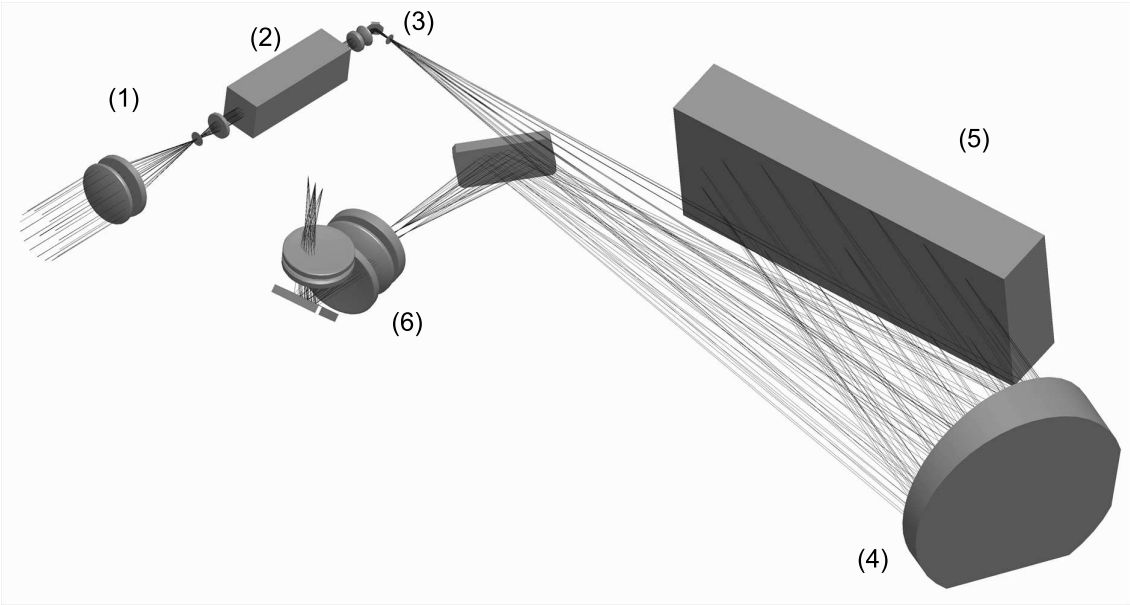

Figure 3.2: Three-dimensional representation of the main SOIR optic elements and ray tracing. (1) is the entrance optics, and is followed by the acousto-optical tunable filter (2) and its exit optics (3) that focus the light on the parabolic mirror (4). The light is diffracted by the echelle grating (5) and the parabolic mirror (4) focuses it on the detector (6), from Nevejans *et al.* (2006).

optical path in order to reduce the weight of the instrument. It also reduces the overall size of SOIR.

The field of view (FOV) of the instrument is imposed by the apparent size of the Sun as seen from Venus: 44 arcmin. For that reason, the FOV in the spectral direction is limited to 30 arcmin, to prevent solar limb darkening effects [1] [Nevejans *et al.* (2006)]. A FOV of 2 arcmin in the spatial direction is considered, to obtain a good vertical resolution of the instrument.

In the next paragraphs, we give a theoretical description of the three main elements of the SOIR instrument: the echelle grating, the acousto-optical tunable filter and the detector.

3.2.2 The echelle grating

The diffracting device of SOIR is an echelle grating. This is a diffracting device built on a plate, on which parallel and equidistant grooves are ruled. These grooves can have different profiles; for SOIR the saw-tooth profile has been chosen. They all have the same width. Each groove is a narrow plane mirror. The groove spacing σ is the distance between two successive grooves. The groove density N is the reciprocal of the groove spacing.

The SOIR echelle grating has a groove density of 4 grooves/mm, a groove spacing of 250 μm and an effective surface of 60 mm by 134 mm. The total number of grooves is equal to 560. It was manufactured by Bach Research Corporation, Boulder, Colorado, USA. It is made of aluminum, and the coating material is gold.

The diffraction relation can be written as [Palmer (2002)]

$$\sigma \cdot (\sin\beta + \sin\alpha) = n \cdot \lambda \tag{3.1}$$

$$\sin\beta + \sin\alpha = n \cdot N \cdot \lambda \tag{3.2}$$

with σ the groove spacing, n the diffraction order, α the incident angle and β the refracted angle, calculated to the normal of the plate of the grating device.

From the above relations, one can see that order overlapping occurs, as the same refracting angle is reproduced for different light wavelength in different orders of diffraction. To avoid this inconvenient characteristic, a wavelength filter is placed before the echelle grating: the Acousto-Optical Tunable Filter, that is described in Section 3.2.4.

The Blaze angle θ_B is defined as the inclination angle of the grooves to the baseplate, and is also equal to the mean of the incident and refracted angles

$$\theta_B = \frac{\alpha + \beta}{2} \tag{3.3}$$

All the angles are shown in Figure 3.3.

The wavelength corresponding to that refracted angle is the Blaze wavelength λ_B

$$\lambda_B = \frac{2}{N \cdot n} \cdot \sin\theta_B \cdot \cos(\alpha - \theta_B) \tag{3.4}$$

Working at an incident angle close to the Blaze angle in order n concentrates most of the energy in that order, as the n^{th}-order diffracted light describes a mirror reflection with respect to the facet surface of the grooves. This configuration is called the Littrow configuration. A quasi-Littrow configuration is used for SOIR.

Thanks to the fact that the echelle grating is working in this quasi-Littrow configuration, the parabolic mirror - element (4) in Figure 3.1 - can be used twice.

The useful diffraction orders range from 101 to 194. Table 3.1 summarizes the characteristics of the SOIR echelle grating, while Appendix F lists the diffraction orders with their bounds and central wavenumber.

1. Limb darkening refers to the diminishing of intensity in the image of the Sun as one moves from the center of the image to the limb of the image [Neckel & Labs (1994)].

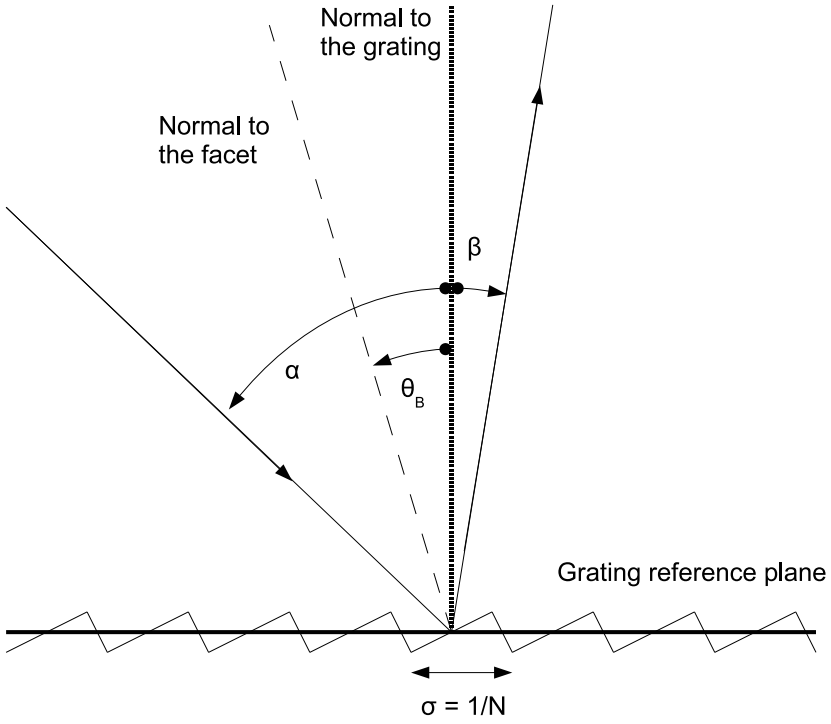

Figure 3.3: Definition of the angles used to calculate the echelle grating relations.

Variable name	Symbol	Value
Blaze angle	θ_B	63.2°
Groove spacing	σ	250 μm
Angle between the incident ray and the plane perpendicular to the grooves; it contains also the grating normal	γ	2.60098°
Angle between the incident ray and the facet normal in the plane perpendicular to the grooves; it contains also the grating normal	α_B	-0.019707°
Incident angle	$\alpha = \theta_B + \alpha_B$	

Table 3.1: List and values of the angles and characteristics of the SOIR echelle grating for the calculation of the Blaze angle.

The angular dispersion is the separation of any two wavelengths, and is defined as the rate of change of angle with the change of wavelength. It is expressed as

$$\frac{\Delta\beta}{\Delta\lambda} = \frac{n}{\sigma \cdot \cos\beta} \tag{3.5}$$

This relation shows that for small wavelength variations, angular separation is proportional to the order of diffraction. Moreover, the smallest is the groove spacing, the highest gets the dispersion. And finally, that the dispersion gets higher when the refracted angle has higher values.

The free spectral range (FSR) is the spectral width of a diffraction order: it is the range of wavelengths in a given spectral order for which superposition of light from adjacent orders does not occur. It comes from the fact that for a given incidence and refraction angle, the grating equation is satisfied for a different wavelength for each integral diffraction order n. For SOIR, the FSR equals ≈ 20 cm^{-1}.

For the case of SOIR, the grating is not placed exactly in the plane normal to the incident light beams. It is tilted by an angle γ (see Table 3.1 for the value). The grating equation gets slightly modified:

$$\sigma \cdot (\sin\beta + \sin\alpha) = \frac{n \cdot \lambda}{\cos\gamma} \tag{3.6}$$

The consequences are that the Blaze angle is also slightly modified, and thus moves the Blaze wavelength. It was used during the conception phase to obtain the best wavenumber configuration with respect to the studied spectra without changing the whole echelle grating.

3.2.3 The detector

The detector system is a modified Sofradir integrated detector Dewar cooler assembly. It is sensitive to radiation in the 1.7 to 4.3 μm spectral region. It consists of a two-dimensional array of photovoltaic HgCdTe pixels. It is cooled by a Stirling-type cooler [2] (Ricor) to about 88 K, and is cooled down before every measurement. The nominal time to cool is 600 s in order to reach the working temperature.

The detector has 256 pixels in the spatial direction and 320 pixels in the spectral direction. But only 32 lines in the spatial direction of the detector are illuminated: lines 188 to 220. Figure 3.4 shows this characteristics. Each pixel has a size of 30 by 30 μm.

The detector width for orders 101 to 122 is smaller than the FSR, and, hence, the detector looses part of the spectrum. For orders 123 to 194, the inverse happens; the detector width is equal or greater than the FSR and the detector is not completely covered by the selected order.

3.2.4 The acousto-optical tunable filter

The acousto-optical tunable filter, or AOTF, is a wavelength sorting device. It is a solid-state optical filter made of a TeO_2 crystal. It was designed and manufactured by AFAR, NPO SPURT (Zelenograd, Moscow region).

It operates by the principle of acousto-optical diffraction in an anisotropic medium. It is commanded by an electrical signal, which is transformed into an acoustic wave at a given radio frequency by a transducer glued on the crystal. The acoustic wave modifies the index of refraction inside the crystal. The incident light beam is separated into three components: an unpolarized, a vertically and an horizontally polarized light beam. Each one exits the crystal with a different angle, thus at a different position on the exit side of the crystal. In the SOIR configuration, only the vertically polarized light beam is selected. The Figure 3.5 presents the ordinary and extraordinary beams at the entrance, inside and at the exit of the crystal. This system has the advantage of not using a polarizer, which reduces the weight of the instrument [Nevejans *et al.* (2006)].

2. The idealized Stirling cycle consists of four thermodynamic processes acting on the working fluid. (1) Isothermal Expansion. (2) Isochoric heat-removal. (3) Isothermal Compression. (4) Isochoric heat-addition.

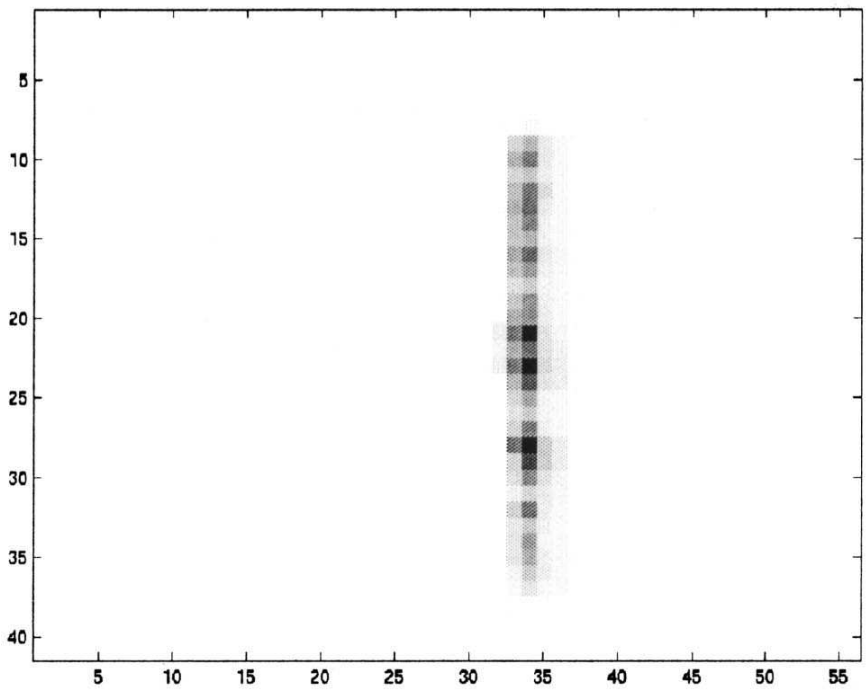

Figure 3.4: Image of spectrometer slit on detector with monochromatic 3.39 μm laser source. The horizontal axis is the relative pixel number along the detector row, i.e. the spectral axis, and the vertical axis is the relative pixel number along the detector column, i.e. the spatial axis. Credit: IASB-BIRA

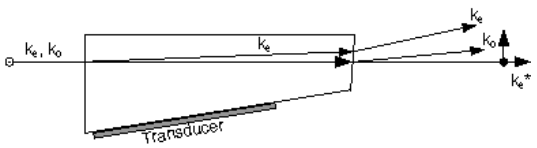

Figure 3.5: AOTF: Incoming ordinary (K_o) and extraordinary (K_e) beams and outgoing useful diffracted extraordinary beam (K_e^*), from Nevejans *et al.* (2006).

Figure 3.6 shows the configuration of SOIR's AOTF with the orientation, the size and the facet angles of the crystal axes, the position of the transducer, and the diameter of the light beam.

The choice of an AOTF as bandpass filter has multiple reasons. Firstly, it does not contain any moving parts. This is crucial for space missions, as moving parts contain motors which may fail during the launch or mission life of the spacecraft. Secondly, the access to any part of the spectrum is fast and precise, as it is electrically commanded and the acoustic wave stabilization time lasts for a few milliseconds. Thus, the diffraction order selection is performed by tuning the AOTF, and selecting the appropriate radio frequency excitation to obtain the desired diffraction order wavelength.

The characteristics of the AOTF are summarized in Table 3.2.

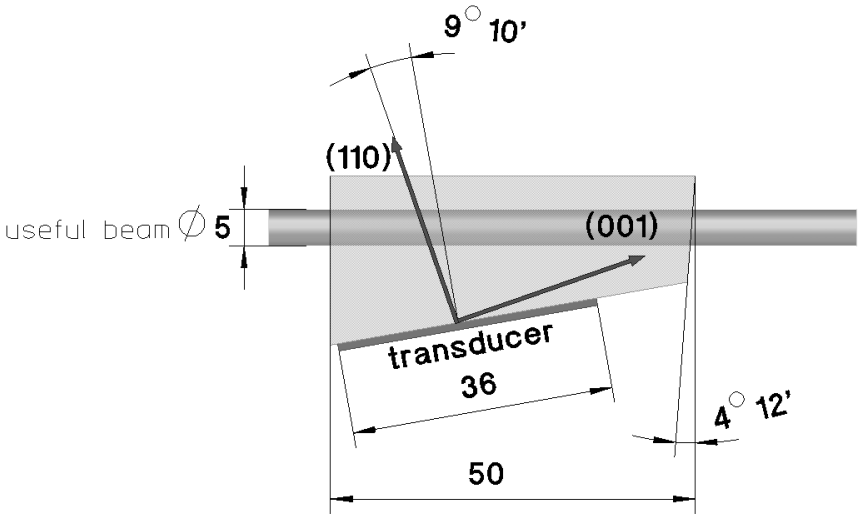

Figure 3.6: SOIR AOTF configuration with orientations of the crystal axes. Dimensions in millimeters, from Nevejans *et al.* (2006).

Characteristic	Value or range	Unit
Spectral bandwidth (FWHM)	≈ 24	cm^{-1}
Wavelength range	2.325 to 4.25	μm
Wavenumber range	2200 to 4400	cm^{-1}
Frequency range	13.5 to 25	MHz

Table 3.2: List and values of the characteristics of the acousto-optical tunable filter.

The tuning relation and the AOTF transfer function are two important characteristics of the bandpass filter. The first one links the AOTF frequency to a wavenumber, and thus allows to tune the filter, while the second one describes how the AOTF spectrally filters the light at a given radio-frequency.

At a fixed radio frequency f_{AOTF}, the AOTF selects only a narrow wavelength band. The central wavelength λ of a given band is determined by the momentum matching condition [Song

& Gweon (2008)]. The momentum condition occurs when the group velocity of the extraordinary wave is collinear to the ordinary wave. It can be estimated by the following expression [Chang *et al.* (1996)], also called the tuning relation of the AOTF:

$$f_{AOTF} = \frac{\nu_{speed} \cdot \Delta n}{\lambda} \cdot \sqrt{\sin^4 \theta_i + 2sin^2 2\theta_i} \tag{3.7}$$

where θ_i is the incident angle, ν_{speed} the acoustic velocity and Δn the birefringence of the crystal. The tuning function follows approximately a $\frac{1}{\lambda}$ law, but not exactly because of the wavelength dependence of the refractive index. The refractive index of TeO_2 were measured by Uchida (1971), and the dependence of the birefringence on wavelength was shown to follow the simple approximation formula [Yano & Watanabe (1976)]:

$$\Delta n = \frac{a}{\lambda - \lambda_c} + b \tag{3.8}$$

where a, b and λ_c are constants ($a = 7.156$ nm, $b = 0.1338$ and $\lambda_c = 262.9$ nm for TeO_2).

The intrinsic passband of an AOTF is determined by the effect of momentum mismatch. It is caused by the wavelength deviation from the exact wave vector momentum matching condition in the filter transmission [Chang *et al.* (1996)]. In first approximation, the transmission of an AOTF can be written as:

$$T_{AOTF} = T_0 \cdot \mathrm{sinc}^2 \left(\frac{\lambda - \lambda_0}{\Delta \lambda_{FWHM}} \right) \tag{3.9}$$

with λ_0 the peak wavelength, T_0 the peak transmission, $\mathrm{sinc}\,(\Delta x) = \frac{\sin(\pi \cdot \Delta x)}{\pi \cdot \Delta x}$, and $\Delta \lambda_{FWHM}$ is the bandpass FWHM [3]. The FWHM can also be approximated [Chang *et al.* (1996)] by

$$\Delta \lambda_{FWHM} = \frac{1.8 \cdot \pi \cdot \lambda_0^2}{b_\lambda \cdot L \cdot \sin^2 \theta_i} \tag{3.10}$$

where L is the acoustic length in the crystal:

$$L = \frac{W}{\cos(\theta_i - \alpha)} \tag{3.11}$$

with W as the transducer width (36 mm), α as the angle of incidence of the acoustic wave ($9°10'$), and b_λ the dispersive constant. Its expression in terms of the other parameters is

$$b_\lambda = 2\pi \cdot \left(\Delta n - \lambda \cdot \frac{\partial \Delta_n}{\partial \lambda} \right) = 2\pi \cdot \left(\Delta n - \frac{\lambda \cdot a}{(\lambda - \lambda_c)^2} \right) \tag{3.12}$$

with a and λ_c are the parameters defined in Equation (3.8).

Equation (3.10) can be rewritten in terms of wavenumber

$$\Delta \nu_{FWMH} = \frac{1.8 \cdot \pi}{b_\lambda \cdot L \cdot \sin^2 \theta_i} \tag{3.13}$$

which indicates that the FWHM bandpass is essentially constant when expressed in wavenumber, if the dependence of b_λ on wavelength is neglected.

3.3 Measurement strategy

To probe the Venus atmosphere, SOIR performs solar occultations. A solar occultations occurs when the satellite orbital plane around the planet crosses the penumbra cylinder of the planet. The solar occultation event is preceded by an ingress case, before entering the penumbra, and is followed by an egress case, after exiting the penumbra. It does not occur during every orbit, as

3. The FWHM is the full width at half maximum. This concept is used for Gaussian functions, but also for sinc and sinc^2 functions.

the orbital plane is rotating relative to the direction axis Sun - Venus. For the VEX mission, the occultation seasons occur approximately every three months, for a period of about two months. A complete description of the solar occultation principle is given later in the text (see Section 4.2.2.3).

During most of these two events, i.e. an ingress or an egress case, the SOIR instrument is turned on, and probes the Venus atmosphere. Here is a description of the procedure.

When a solar occultation is foreseen, the satellite rotates in order that the optical axis of SOIR points towards the Sun.

We consider in the following description that the tangent altitude decreases with time: it is the ingress case of the occultation. The situation when the tangent altitude increases with time, i.e. an egress, can be solved in the same way as described here, but the time has to be reversed.

A few minutes before the solar occultations starts, the instrument is turned on. After the precooling phase of the detector, which lasts for 600 s, the instrument starts to record spectra in the selected order(s). This occurs before the line of sight crosses the Venus atmosphere. In the present study, it is supposed that the Venus atmosphere extends up to 220 km. This operation starts early enough to ensure that at least 40 spectra are taken during this phase. These spectra are summed up, and the result is taken as the Sun spectrum. The spectra that were recorded at altitudes lower than 220 km are divided by the Sun spectrum, and result in transmittance spectra, that are analyzed further. The tangent altitudes of each spectrum, defined as the altitude to Venus at which the SOIR line of sight is nearest the center of Venus, i.e. is parallel to the limb, define the layers in the atmosphere [Mahieux *et al.* (2008)].

Unfortunately, SOIR can not perform such measurements during all occultations, as the other instruments may be working at the same time. Since all the instruments are located on the same side of the spacecraft, it requires a different orientation relative to Venus and the Sun. It is the case for nadir measurements or limb viewing for example. Moreover, when Venus is at superior conjunction relative to the Earth, the events may be canceled. A low telemetry download rate or simply no communication possible between the satellite and the Earth [Titov & al. (2006)] is the reason as the Sun may be located between Venus and our planet.

3.4 Data description

When the measured data are acquired by the SOIR detector and by the SPICAV/SOIR electronics, they have to be handled on-board to satisfy some telemetry constraints. SOIR has also the possibility to take measurement under different modes, that allow either to study the instrument characteristics, or to acquire scientific data concerning the atmosphere. Finally, all these spectra are processed on Earth to reach different data levels, in order to allow the SOIR team to study them.

The telemetry constraints and their implications, the SOIR modes of operation and the different data levels are described in the following sections.

3.4.1 SOIR telemetry constraints and detector lines combination

We explain here how the measurements taken by the detector pixels are combined before being sent to Earth. Indeed, from inner telemetric constraints imposed by the CPU of the SPICAV instrument, SOIR can send 8 measurements per second to the Earth.

From the instrument characteristics and the different operations that have to be performed on board (see Appendix G for a description on the detector dark current handling), the instrument can measure at most a spectrum every 250 ms, thus 4 per second [Nevejans *et al.* (2006)] because of limited instrument telemetry allocation. To avoid detector saturation, the integration times are limited to 20 or 30 ms. To improve the overall signal-to-noise ratio, a number of measurements can be accumulated as long as the total measuring time remains below 250 ms [Nevejans *et al.* (2006); Mahieux *et al.* (2008)].

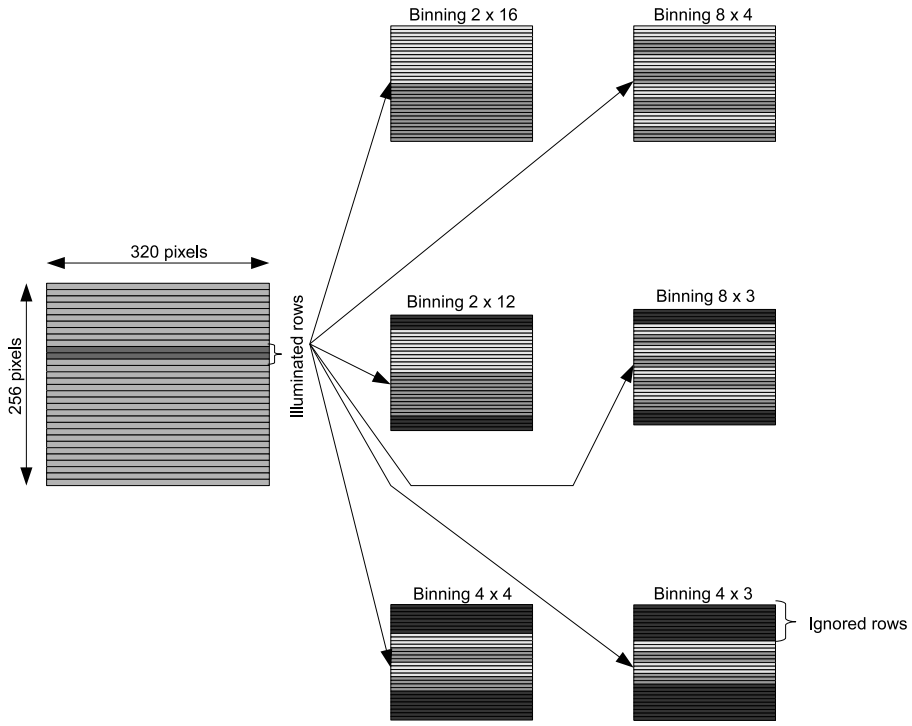

Figure 3.7: Detector is an array of 320 x 256 pixels. Because of the dimension of the slit, only 32 rows in the spatial direction are illuminated. Several binning configurations of rows are defined, and are depicted here. The different binning cases are listed in Table 3.3.

To satisfy the above described conditions, the information recorded on the 32 detector lines have to be summed up on-board, before sent being to Earth. Each group of summed lines is called a bin.

It has also been observed that the side pixel lines (188 to 191 and 217 to 220, 8 in total in the spatial direction) have a very bad signal-to-noise ratio. They are probably less illuminated, due to some optical misalignments in the instrument. From these considerations, the decision was taken to remove from data collection these pixel lines after orbit 332 (19/03/2007).

From these criteria, different possibilities may be chosen to group the scanned pixel lines. The options are either to have a better spatial resolution by reducing the number of scanned orders, or to increase the number of scanned orders to maximize the spectral coverage, but to have a poorer vertical resolution. Each combination is called a binning group or binning case. Note that every combination does not use all the lines. They are summarized in Table 3.3 and depicted in Figure 3.7.

For the sake of simplicity, the spectral pixel lines is called pixel from now on, and the binning case is called simply binning.

The most used configuration in the solar occultation mode is the 2 x 12 binning case, because it offers the possibility to measure 4 different diffraction orders during a single occultation. Because two bins are read on the detector, it also results in two simultaneous measurements of the same diffraction orders, but at slightly different altitudes [4].

The binning case 4 x 4 and 4 x 3 are actually the same as binning cases 8 x 4 and 8 x 3, but not considering bins 1, 2, 7 and 8 of binning cases 8 x 4 and 8 x 3, and matching bins 3, 4, 5 and

4. See Section 4.2.1 for the explanation.

6 to bins 1, 2, 3, 4 of binning cases 4 x 4 and 4 x 3, as it is depicted in Figure 3.7. The purpose of these other configurations is to enhance the vertical resolution of the instrument.

Denomination (Binning configuration)	Number of scanned orders	Number of lines in each bin	Number of binning groups
2 x 16	4	16	2
2 x 12	4	12	2
4 x 4	2	4	4
4 x 3	2	3	4
8 x 4	1	4	8
8 x 3	1	3	8

Table 3.3: List of the binning possibilities. The denomination of each case, the number of scanned orders allowed by the telemetry, the number of detector lines in each bin and the number of datasets for each scanned order are given.

3.4.2 The different modes of operation

3.4.2.1 Introduction

Four measurement modes were created. Two modes are dedicated to atmospheric measurements: the occultation and nadir modes, characterized by fixed and constant values of the AOTF frequency; the two other modes, used for calibrations, are the fullscan and miniscan modes. In these last modes, the AOTF frequency is regularly stepped. It is used to make calibrations and/or cover a wider wavenumber range. The fullscan mode can also be used during solar occultations.

3.4.2.2 Solar occultation mode

This mode is used to scan the atmosphere during the solar occultations.

SOIR is pointing towards the Sun as the latter sets or rises. One of the binning configurations described in Table 3.3 and Figure 3.7 is chosen.

If we consider the binning case that is the most used (2 x 12), four diffraction orders are scanned every second, alternating every 250 ms. Two data sets are created for each diffraction order, one for each bin, but at slightly different altitudes.

This mode is used to construct vertical profiles (Chapter 4), but with a poorer geographical coverage, as we are constrained to the Venus terminator (Chapter 5).

3.4.2.3 Nadir mode

This mode is equivalent to the occultation mode, except from the fact that SOIR is looking at nadir. The number of accumulations, and the integration time are increased, to reduce the signal-to-noise ratio. All the binning possibilities listed in Table 3.3 can be used. No solar spectra are taken before the measurement. Up to now, the few nadir observations were not extensively analyzed. They are not discussed further in the present work. It has to be noted that SOIR was not designed to perform such measurements.

This mode is used to derive column densities, with a better geographical coverage, as the measurements can be taken anywhere on the dayside of the planet.

3.4.2.4 Fullscan mode

In the fullscan mode, the AOTF frequency is stepped by the same radio frequency step every 250 ms in order to cover the whole spectral domain. The minimum and maximum frequencies

correspond to the center of SOIR's orders 101 (12,848 kHz corresponding to 2266 cm^{-1}) and 194 (26,287 kHz corresponding to 4353 cm^{-1}). The order to AOTF frequency correspondence is given in Appendix F.

Such measurements are performed while looking at the Sun outside the Venus atmosphere, but also during occultations, i.e. during ingress or egress cases.

This mode is used to study and derive the Blaze function (Section 3.5.2.1), the pixel-to-pixel non-uniformity (Section 3.5.3.1), the spectral sensitivity (Section 3.5.3.2), the pixel to wavenumber relation (Section 3.5.3.3) and the spectral resolution (Section 3.5.3.4).

3.4.2.5 Miniscan mode

In this mode, the AOTF frequency is stepped by the same radio frequency step in order to cover a small domain, and to precisely analyze a particular feature, e.g. a deep Fraunhofer solar absorption line. The miniscans are exclusively used for scanning the solar spectrum outside the atmosphere of Venus.

The AOTF characteristics, such as the AOTF frequency versus wavenumber relation (Section 3.5.4.2), and the AOTF bandpass transfer function (Section 3.5.4.4), are derived from miniscan measurements. In the first case, the frequency step is chosen in order to be small enough to capture the signal maximum corresponding to the maximum absorption of a solar line, while in the second case, the frequency step must be wide enough to completely cover a Fraunhofer solar absorption line.

3.4.3 Data archiving

The spectra measured by SOIR are received in compressed files from ESOC, the European Space Operations Center, in Darmstadt, Germany. Different levels of data are defined, depending of the treatment that they are going through. This is called the data pipeline, and a summary of the data pipeline is reported here. A complete description can be found in Neefs *et al.* (2006).

Each measurement receives a name, based on the date it was recorded and on its type. Because the orbital period of VEX is 24 hours, different measurements can be done during one day, for example an egress, an ingress and miniscans. The format is `YYYYMMDD_TCC` where `YYYY` is the year of the orbit, `MM` is the month, `DD` is the day, `T` is the type of measurement and `CC` is the measurement number done during that orbit, starting from 1. The types of measurement are summarized in Table 3.4.

Five internal levels are defined: 0.0, 0.1, 0.2, 0.3 and 1.0. Geometry files are generated, and information about the quality of the fit is given, contained in a quality byte (see next sections for these files description). Here is a description of the different data sets.

Measurement type	Acronym
Ingress	`I`
Egress	`E`
Sun fullscan	`F`
Atmospheric fullscan	`A`
Miniscan	`M`
Nadir	`N`
Other calibration	`C`

Table 3.4: List of the measurements types of SOIR and their acronyms.

3.4.3.1 Geometry files

These files contain all the information necessary for the computation of the pointing direction of the instrument. The filename is `YYYYMMDD_TCC.csv`. It is given as a csv file (csv stands for comma-separated-value). The data that it contains are:

- the UTC time;
- the SOIR pointing angle;
- the altitude of VEX to the Venus surface;
- the tangent altitude of the measurement;
- the velocity of VEX projected on the line of sight;
- the latitude of the measurement point;
- the longitude of the measurement point;
- a text column giving the PENS (penumbra starting time) and the PENE (penumbra ending time) times.

3.4.3.2 Quality byte

The quality byte defines the quality of the measurement using an 8 bit binary number.

The first 4 bits tell if errors were encountered while producing the data. Errors may come from safe modes [5] of the spacecraft, or if the telecommand has not been received by the instrument.

Table 3.5 summarizes all the quality byte combinations.

The 4 last bits concern the warnings. The quality of the Sun spectrum built to derive transmittances is here evaluated. The condition to have a good solar spectrum is the following: at least 40 recorded spectra before reaching a tangent altitude of 220 km need to be taken in consideration to build the Sun spectrum. If this is not the case, a warning is issued, and several options are considered in order to define the Sun spectrum, see Table 3.5. The detector possible saturation is also mentioned, if it is observed during treatment (it turns into negative values). Also, the very bad definition of the Sun spectrum are communicated, for example if the inertial mode of the satellite could not be held during the whole measurement (for example if the spacecraft inertial wheels have encountered a sudden problem).

Case	Description
0000 0000	No problem, no warning, occultation usable
0001 0000	Error: No telecommand received
0010 0000	Error: Detector temperature problem: too high
0011 0000	Error: Any other kind of error
0000 0001	Warning: Detector saturation
0000 0010	Warning: 40 points above 200 km
0000 0011	Warning: 30 points above 200 km
0000 0100	Warning: 20 points above 200 km
0000 0101	Warning: 20 points above 180 km
0000 0110	Warning: 20 points above 160 km
0000 0111	Warning: 20 points above 140 km
0000 1000	Warning: 20 points above 120 km
0000 1001	Warning: 20 points below 120 km
0000 1010	Warning: Very bad definition of the Sun regression

Table 3.5: Quality byte. List of all the error or warning issues while building the data set to level 0.3.

3.4.3.3 Internal level 0.0

The internal level 0.0 contains the compressed files as they are received from ESOC.

5. A safe mode of the spacecraft is generated when any incident that could put the satellite in danger occur, such as sudden loss of communication with the Earth, defects with the solar panels...

3.4.3.4 Internal level 0.1

The files are decompressed, each file is a csv file format, and has a name corresponding to the time it is recorded. The format is `tmYYYYMMDDHHMMSS.csv` where `HH` is the hour, `MM` are the minutes and `SS` are the seconds.

The file contains:

- the time information needed to compute the exact time of the measurement;
- a 9 column matrix. The first column is the pixel number, the 8 other columns are the detector readouts corresponding to the 8 data sets that are measured (see Section 3.4.1 for description);
- all the telecommand sent to SOIR. It allows to recover the integration time, the binning, the number of accumulations, the AOTF frequencies, the AOTF stepping parameters in the case of fullscan or miniscan;
- some temperature measurements taken inside the instrument (on the baseplate, on the AOTF, on the detector, and close to the echelle grating);
- the voltages of some electronic components.

The files start to be created when the instrument is turned on. For this reason, the 600 first files do not contain any spectral data, as the detector is cooled down to 88 K during that phase (see Section 3.2.3). No measurement is done during this phase. The files are used to check if the temperature of the detector correctly reached its nominal working value.

A typical example of measured spectra is given in Figure 3.8, presenting the pixels versus ADU [6] measured spectra.

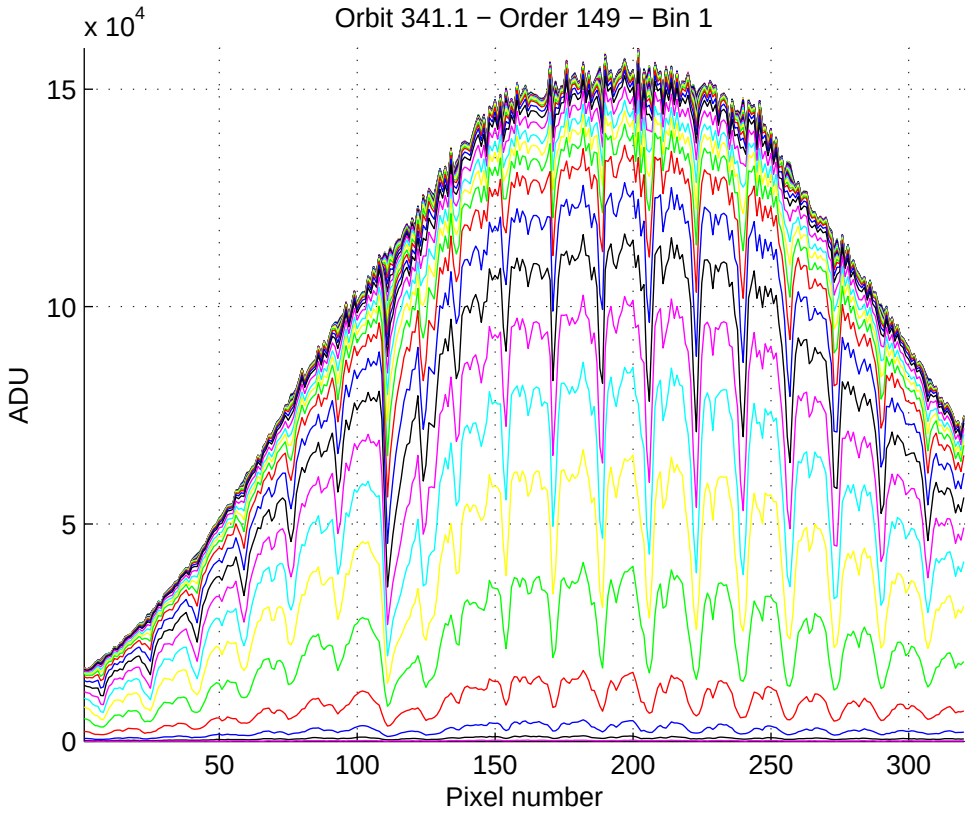

Figure 3.8: Data set of orbit 341.1 (28/03/2007) bin 1 in order 149 at level 0.1. The data are given in terms of pixels and ADU unit.

6. ADU stands for Analog to Digital Unit.

3.4.3.5 Internal level 0.2

The spectra are corrected for the detector non-linearity at low value. This treatment is realized by the engineering team of the instrument, but in order to be complete, the procedure is described in Appendix G. The filenames are the same as in level 0.1. All the files present at level 0.1 are available at level 0.2.

A typical example of recorded spectra is given in Figure 3.9, presenting the pixels versus corrected ADU measured spectra.

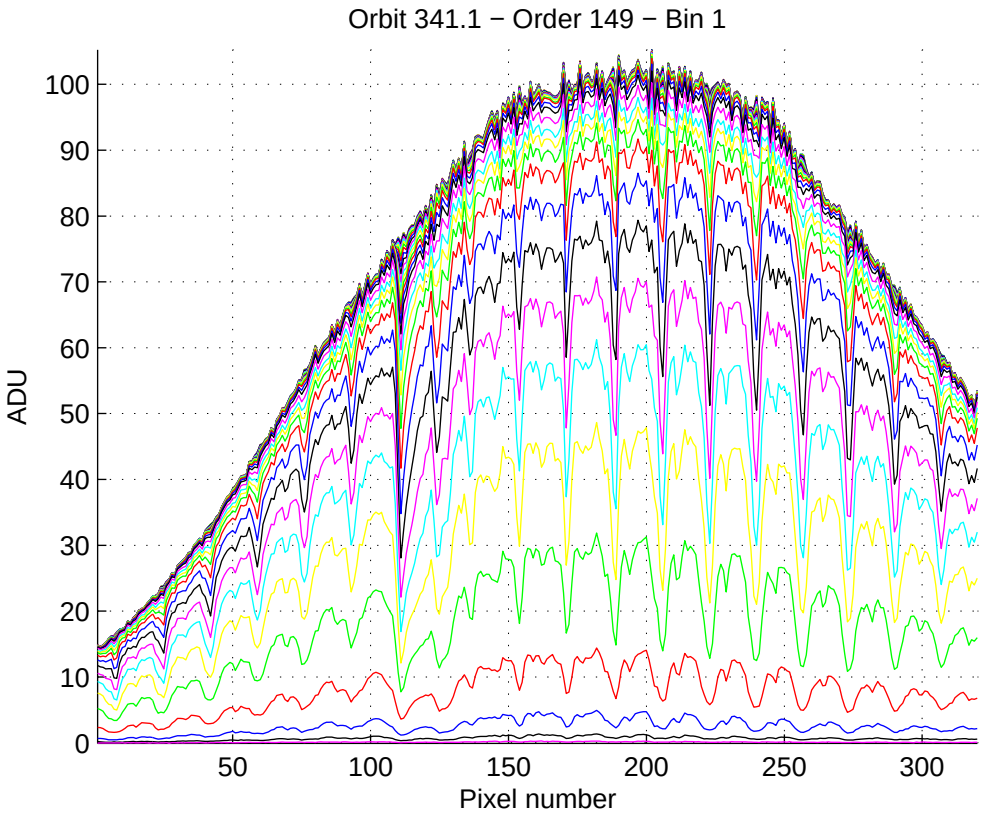

Figure 3.9: Data set of orbit 341.1 (28/03/2007) bin 1 in order 149 at level 0.2. The data are given in terms of pixels and ADU unit.

3.4.3.6 Internal level 0.3

The wavenumber scale of each measurement is calculated, corresponding to the AOTF frequency that is asked. The Sun spectrum outside the atmosphere is calculated for each of the 8 data sets that are measured, as explained in Section 3.3, and divide the data in order to obtain transmittances. Only the spectra that have tangent altitudes between 220 km and 60 km are present.

The filenames are slightly different from the lower levels: there is now one file for each scanned order. Thus, at most four files per second, in the case of binning 2 x 12 or 2 x 16. The filename format is `tmYYYYMMDDHHMMSS_orderOOO.csv` where `OOO` is the diffraction order, ranging from 101 to 194. The order is calculated from the AOTF frequency as explained in Section 3.5.4.3.

A characteristic example of measured spectra is given in Figure 3.10, presenting the wavenumber versus transmittance measured spectra.

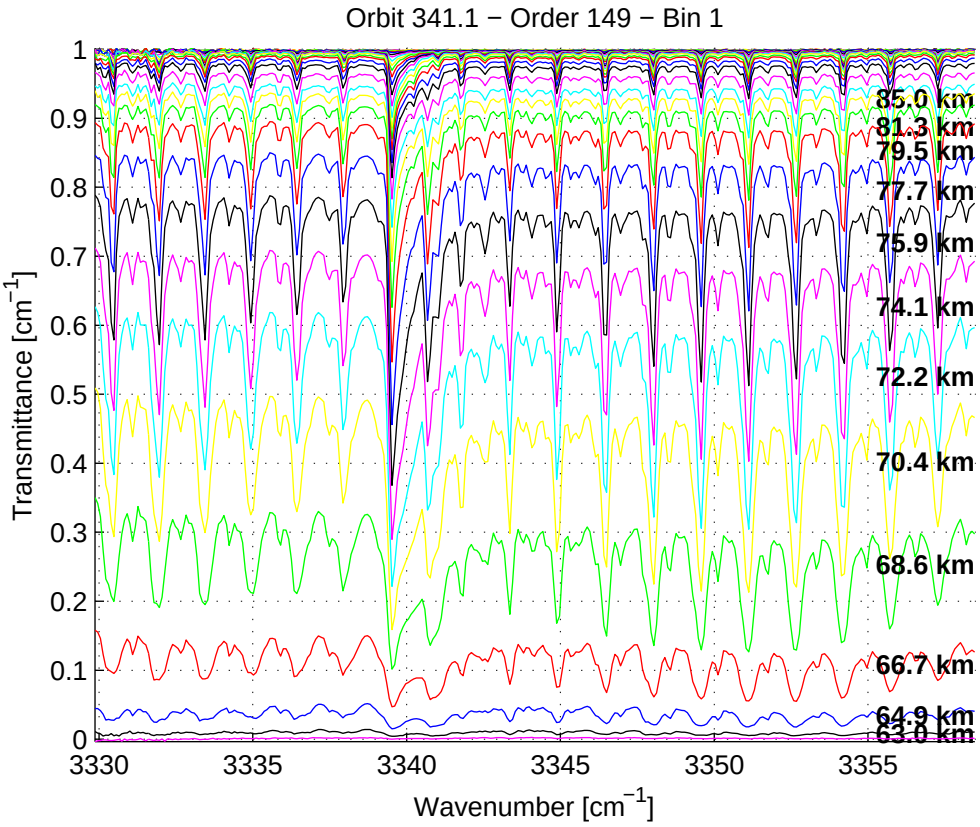

Figure 3.10: Data set of orbit 341.1 (28/03/2007) bin 1 in order 149 at level 0.3. The data are given in terms of wavenumber and transmittance. The corresponding tangent altitude is given.

3.4.3.7 Internal level 1.0

They contain exactly the same information as level 0.3, except for the file format that corresponds to the PSA format required by ESA for archiving [Neefs *et al.* (2006)].

3.5 Calibrations

3.5.1 Introduction

Most of the SOIR calibrations could not be performed before the launch of the satellite. For this reason, they are done in-flight, while looking at the Sun as a source. They concern calibrations of the echelle grating, the AOTF transfer function and the detector. These results were published in Mahieux *et al.* (2008, 2009).

In the following sections, we investigate the different elements relevant to the calibration needed for the optimal interpretation of the SOIR data.

3.5.2 Echelle grating

3.5.2.1 Blaze function

The blaze function represents the efficiency of the grating in terms of refracted angle [Engman & Lindblom (1982)]. The efficiency is maximum when the refracted angle is equal to the incident angle. When the deviation between the angles increases, it is thus not the case. The blaze function represents this effect. The angles are defined in Section 3.2.2.

The blaze function BF is obtained from the relations [Pyo (2003)]

$$BF = \begin{cases} \operatorname{sinc}\left(\frac{1}{\lambda}\cdot\frac{\sigma\cdot\cos\gamma\cdot\cos\alpha}{\cos\alpha_B}\cdot(\sin\alpha_B+\sin(\beta-\theta_B))\right)^2 & \text{if } \alpha\geq\beta \\ \left(\frac{\cos\beta}{\cos\alpha}\right)^2\cdot\operatorname{sinc}\left(\frac{1}{\lambda}\cdot\frac{\sigma\cdot\cos\gamma\cdot\cos\alpha}{\cos\alpha_B}\cdot(\sin\alpha_B+\sin(\beta-\theta_B))\right)^2 & \text{if } \alpha<\beta \end{cases} \tag{3.14}$$

$$\frac{n\cdot\lambda}{\sigma\cdot\cos\gamma} = \sin\alpha+\sin\beta \tag{3.15}$$

$$\alpha = \alpha_B+\theta_B \tag{3.16}$$

The values listed in Table 3.1 were measured on Earth before launch. The blaze function can be computed, and its values are presented as a function of the detector pixel number and the diffraction order in Figure 3.11. It is clearly seen that the blaze function takes lower values on the side pixels when going to high orders. The reason is the dispersion which becomes larger for higher diffraction orders.

3.5.3 Detector

3.5.3.1 Pixel-to-pixel non-uniformity

The pixel-to-pixel non-uniformity (PPNU) is an intrinsic characteristic of the detector. It comes from the difference in quantum efficiency of the detector pixels, and originates from the fact that the physical properties of each pixel of the detector differ slightly. It is also called flat-field [Mahieux *et al.* (2008)].

In a laboratory, pixel-to-pixel non-uniformity is measured by illuminating the detector directly, without passing through the spectrometer, with a homogeneous light source. By repeating this measurement several times, and with different exposure times, the influence of the latter is removed

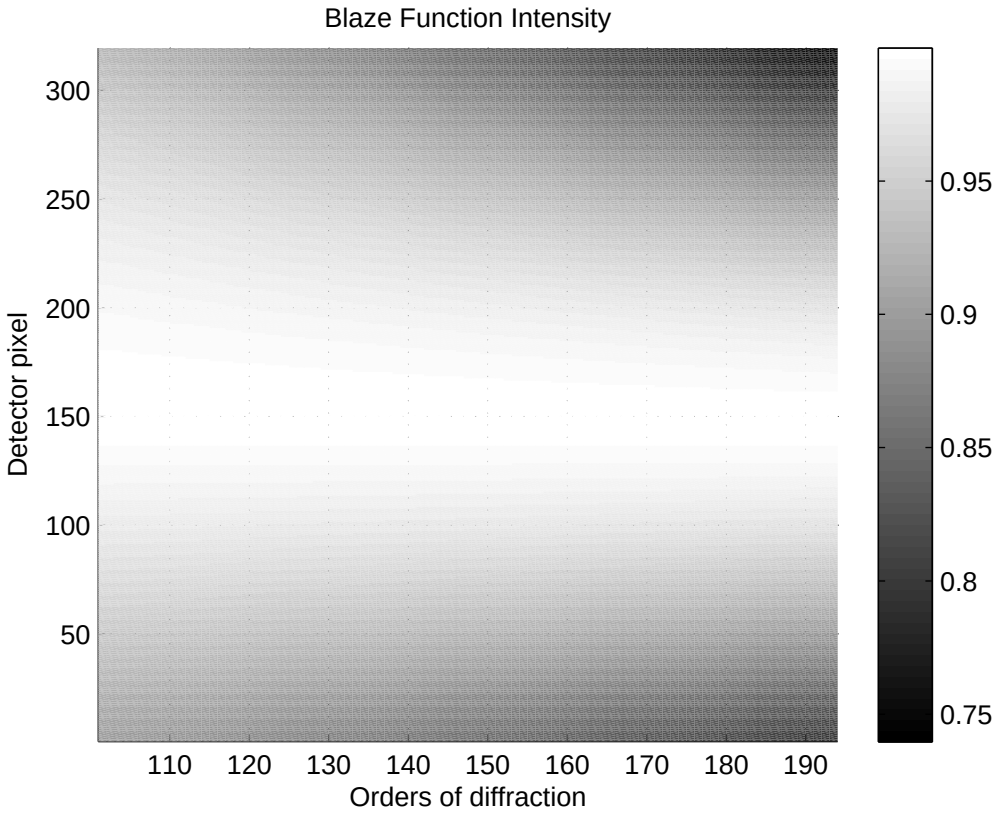

Figure 3.11: Blaze function intensity (gray scale), computed using Equations (3.16), as a function of the diffraction order and the pixel number.

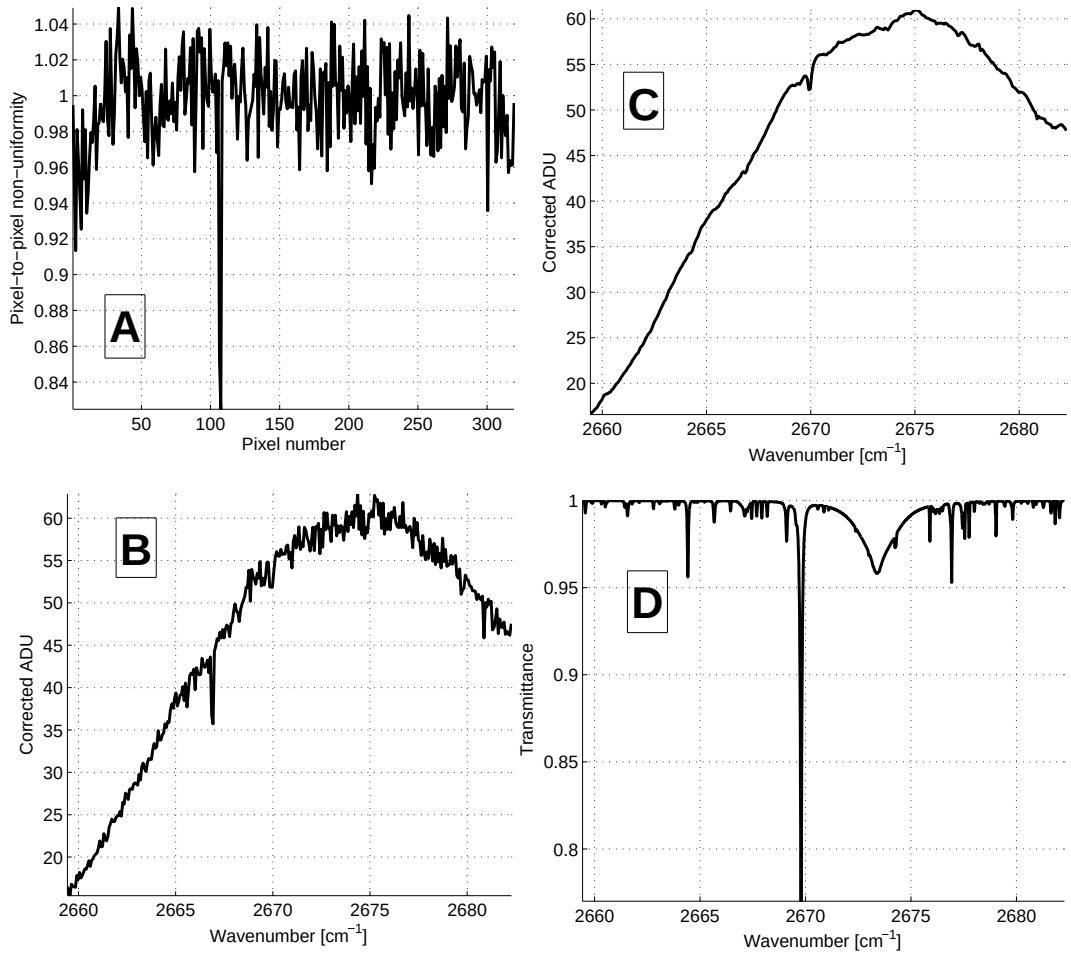

Figure 3.12: Pixel-to-pixel non-uniformity. Panel A shows the pixel-to-pixel non-uniformity measured during fullscan 140.1 (08/09/2006) on bin 1 in the binning case 2 x 12. Panel B shows the raw spectra taken at 04:11:13 UTC in diffraction order 119 at an AOTF frequency of 15,525 kHz. Panel C shows the same spectrum corrected for pixel-to-pixel non-uniformity, while Panel D depicts the solar spectrum [Hase *et al.* (2009)] at the same wavelength).

and random noise can be reduced. This correction has to be applied to the raw signal recorded during a real measurement, and compensates for the different response from pixel to pixel.

However in the case of SOIR, because of the lack of time for the instrument development and the test schedule, the measurements described above could not be done before launch. An estimation can be extracted from the SOIR raw spectra of fullscan measurements while looking at the Sun outside of the atmosphere. Several orders were selected (32 in total) that correspond to spectral regions where no or only weak solar lines are present ($< 0.06\%$ of transmittance). A high number of spectra coresponding to the same order were used to statistically reduce the random noise. High-pass filtering of those spectra removes the general response curve of the AOTF, of the optics and of the spectrometer, leaving only the pixel-to-pixel non-uniformity.

As by definition this uniformity depends on the physical pixel and thus on the chosen binning, one must construct the flat-field correction functions for every binning configuration described in Table 3.3. They differ from bin to bin, as the results of the sum of different spectral pixel lines. Also, as this characteristic may evolve with time, this calibration is routinely performed.

Fullscan number	Date	Binning 8 x 3	Binning 8 x 4	Binning 2 x 12	Binning 2 x 16
106.1	05/08/2006				X
140.1	08/09/2006		X	X	X
209.1	16/11/2006				X
264.1	10/01/2007		X	X	X
494.6	27/08/2007		X	X	X
496.6	29/08/2007		X	X	X
498.6	31/08/2007		X	X	X
500.6	02/09/2007		X	X	X
680.6	01/03/2008		X	X	X
682.6	03/03/2008		X	X	X
695.7	16/03/2008		X	X	X
703.7	24/03/2008		X	X	X
859.6	26/08/2008		X	X	X
897.12	04/10/2008	X		X	X
899.6	06/10/2008	X		X	X
962.5	08/12/2008		X	X	X
1210.2	12/08/2009	X		X	X
1210.3	12/08/2009	X		X	X
1210.4	12/08/2009	X		X	X
1210.5	12/08/2009	X		X	X
1210.6	12/08/2009	X		X	X

Table 3.6: List of fullscan measurements used for calculating the pixel-to-pixel non-uniformity (Paragraph 3.5.3.1), and the detector sensitivity (Paragraph 3.5.3.2)

The pixel-to-pixel non-uniformity is given in Figure 3.12 for bin 1 of binning case 2 x 12, measured during the orbit 140.1. The calculated values are depicted in Panel A. A raw spectrum taken during the same orbit (08/09/2006 04:11:13 UTC), but in an order presenting deep solar lines, is shown in Panel B. The same spectrum, but corrected for pixel-to-pixel non-uniformity is shown in Panel C. The solar spectrum taken from Hase *et al.* (2009) is presented in Panel D. The solar line at 2669.5 cm^{-1} is clearly seen in Panel C, whereas it was not clearly observed in Panel B. Indeed, one could wrongly think that a solar line was located at 2667 cm^{-1}, where the strongest absorption line was observed in Panel B.

The pixel-to-pixel non-uniformity measurements were calculated from all the fullscan that were performed during the whole campaign. A list of the available fullscan measurements is given in Table 3.6.

3.5.3.2 Spectral sensitivity curve

The spectral sensitivity curve represents the spectral dependence of the whole SOIR instrument as a function of the incoming light wavelength. Because the wavelength is selected through the AOTF, the spectral sensitivity may be expressed in terms of AOTF frequency, after the pixel-to-pixel non-uniformity is removed from the spectra. An important contribution to the irregular shape comes from the AOTF diffraction efficiency dependence on wavelength, as well as on the imperfect matching of the radio-frequency driver output impedance to the AOTF driver impedance.

The spectral sensitivity curve is obtained from direct Sun measurements, during fullscan measurements [Mahieux *et al.* (2008)]. As it may vary with time, it is repeatedly monitored. The solar line as well as the pixel-to-pixel non-uniformity are removed from the spectra using a low-pass filter, as exposed in the previous paragraph. Since the same order is scanned many times during a fullscan, spectra of the same order, i.e. with the same AOTF frequency, are summed up to improve the statistics.

Based on the spectral sensitivity curve, optimized integration times were determined for each diffraction order.

Figure 3.13 shows the sensitivity curve obtained during fullscan 962.5 (08/12/2008), presented with the AOTF frequency along the x-axis, the pixel number along the y-axis and the sensitivity along the z-axis (colors in the graph). As a function of AOTF frequency, the sensitivity is best around 18,500 kHz (3134 cm^{-1}, order 140), 22,000 kHz (3679 cm^{-1}, order 164) and 24,500 kHz (4071 cm^{-1}, order 181). In terms of pixel number, the sensitivity is good between 100 and 300, and very low values are observed for pixels ranging from 1 and 100. This characteristic may be induced by the Blaze function, as it reaches lower values away on these side pixels.

All the fullscan used for calculating the spectral sensitivity curves are listed in Table 3.6.

3.5.3.3 Wavenumber to pixel relation

The wavenumber to pixel relation gives, for a given diffraction order, the wavenumber value of a given pixel [Mahieux *et al.* (2008)].

The refracted angle is, to a first approximation, a polynomial function of the pixel number:

$$p = F \cdot \cos(\beta) \approx F \cdot \left(1 - \frac{(\beta - \theta_B)^2}{2}\right) \tag{3.17}$$

where p is the pixel number, F is the focal distance, θ_B is the blaze angle and β is the refracted angle, which has small variations around the blaze angle.

We model the relation linking the pixel to the wavenumber and diffraction order by a second order polynomial, as well as its reciprocal.

To obtain these relations [Mahieux *et al.* (2008)], Sun spectra from fullscan measurements can be used. From the raw spectra at level 0.2, the position of the solar lines can be found. The pixel-to-pixel non-uniformity and the spectral sensitivity are first removed. They are compared to an existing solar lines catalogue, in the present study we chose Hase *et al.* (2009). The strong solar lines are matched with the peaks seen in the measured spectra. The order addition (see Sections 3.2 and 4.5.3) is an important drawback during this operation, as strong lines coming from adjacent orders may interfere with solar lines from the studied diffraction order. For that reason, this calibration needs to be done manually, in order to obtain a reliable relation. It has only been done on one fullscan: 264.1 (10/01/2007), because of the large amount of work it represents.

We will see later in the text (see Section 4.6.5) that only a first approximation of this relation is necessary to correctly study the SOIR spectra, as this calibration can be obtained on atmospheric absorption lines during the solar occultations, see Section 4.6.5.

The strongest solar lines (≈ 100) are selected from the whole wavenumber range.

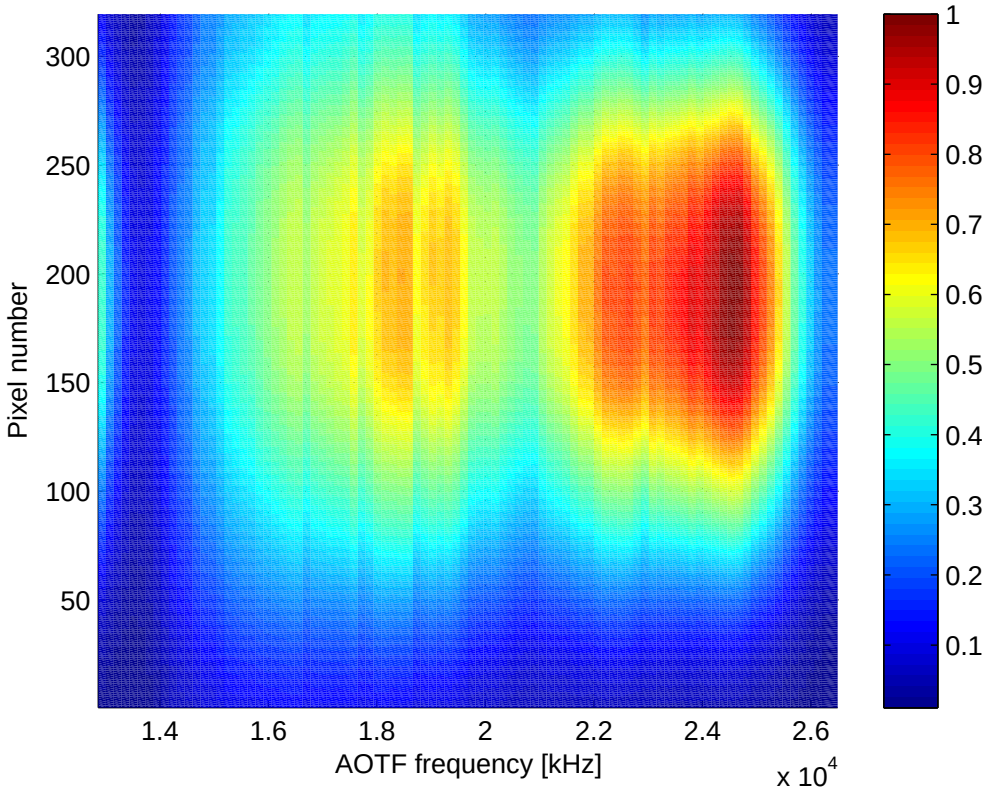

Figure 3.13: Spectral sensitivity surface (color scale) obtained from fullscan 962.5 (08/12/2008) for bin 1 in the binning case 8 x 4. The graph gives the relative sensitivity as a function of the AOTF frequency and of the pixel number. View from top.

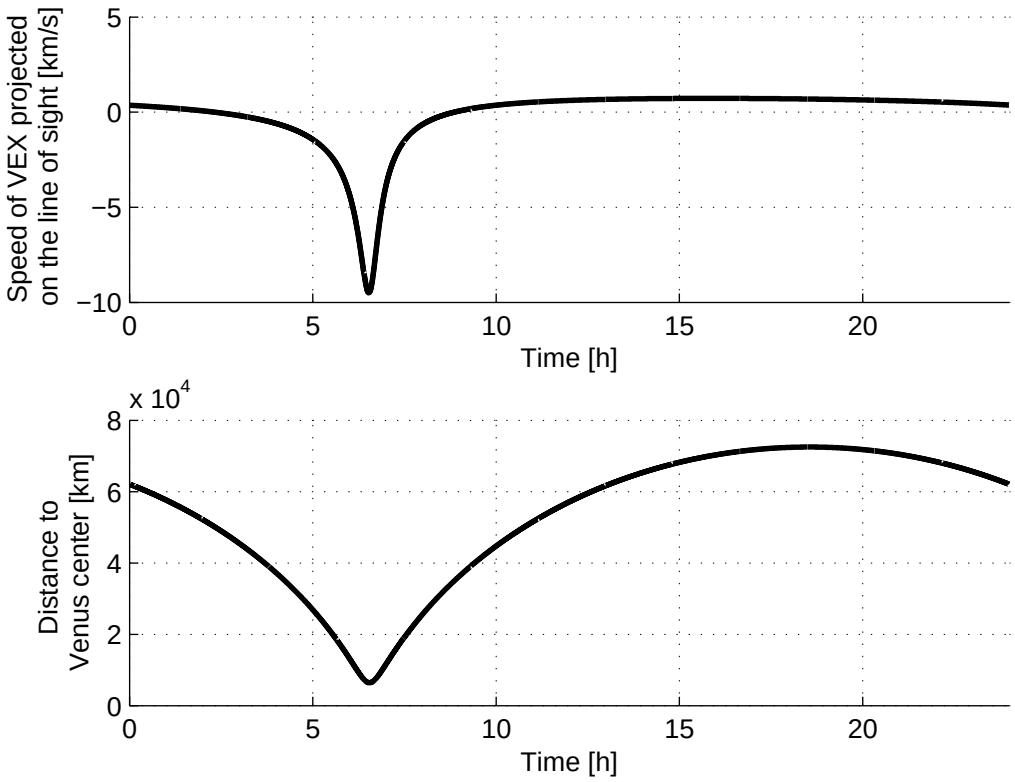

Figure 3.14: The top Panel shows the modulus of the velocity of the spacecraft during orbit 341 (28/03/2007) projected on the line of sight of SOIR. The bottom Panel shows the distance to Venus center. The velocity varies between -9 km/s to 2 km/s. Depending on the configuration spacecraft / Venus / Sun, the sign of the velocity can be opposite.

During this calibration, one has to consider the velocity of the satellite, which may attain large values. This relative movement between the spacecraft and the Sun induces a Doppler shift:

$$f_{rec} = \frac{1-\frac{v_{rec}}{c}}{1-\frac{v_{em}}{c}} \cdot f_{em} \tag{3.18}$$

$$\tilde{\nu}_{rec} = \frac{1-\frac{v_{em}}{c}}{1-\frac{v_{rec}}{c}} \cdot \tilde{\nu}_{em} \tag{3.19}$$

where f_{rec} and f_{em} are the recorded and emitted frequencies, $\tilde{\nu}_{rec}$ and $\tilde{\nu}_{em}$ are the recorded and emitted wavenumbers, and v_{rec} and v_{em} are the velocity of the recorder and the emitter. The velocity is calculated along the SOIR line of sight, and is positive for the receiver if the source is moving away from the receiver; for the emitter, it is positive if the receiver is moving towards the source. In the case of SOIR, we assume that the Sun is not moving, so $v_{em} = 0$. The relation (3.19) becomes:

$$\tilde{\nu}_{rec} = \frac{1}{1-\frac{v_{rec}}{c}} \cdot \tilde{\nu}_{em} \tag{3.20}$$

with v_{rec} projected on the line of sight of SOIR, positive if SOIR is moving away from the Sun, and negative in the other case. Figure 3.14 shows the evolution of the projected velocity on the line of sight of VEX during orbit 341 (28/03/2007) on the 24 hours period, as well as the distance to the center of Venus. Depending when the measurement is done, the velocity can have very different values. The fullscan and miniscan can be performed anytime during the orbit. However occultations only occur close to the periapsis, when the spacecraft has a very large velocity.

At a typical wavenumber of 3500 cm^{-1} with a typical velocity of 8 km/s, the shift is of the order of 0.093 cm^{-1}, larger than the spectral width of a pixel, see next Section.

After these corrections, two polynomials are obtained, for each bin of each binning case. The first one gives the pixel number for a given wavenumber and diffraction order, and the second gives the wavenumber for a given pixel and diffraction order.

$$p = \left(a \cdot \left(\frac{\tilde{\nu}}{n}\right)^2 + b \cdot \frac{\tilde{\nu}}{n} + c\right) \tag{3.21}$$

$$\frac{\tilde{\nu}}{n} = \left(a' \cdot p^2 + b' \cdot p + c'\right) \tag{3.22}$$

Figure 3.15 shows the pixel to wavenumber relation obtained from fullscan 264.1 for bin 1 of binning case 2 x 12.

The relations obtained from fullscans 264.1 and 264.2 (10/01/2007) for a 2 x 12 binning case are given in Table 3.7.

Bin	c	b	a
1	2.234784120e+001	5.821114581e-004	6.155002887e-008
2	2.234778198e+001	5.856544358e-004	4.862254410e-008

Table 3.7: Values of the coefficients of equations (3.22) and (3.21) of the pixel to wavenumber relation obtained for bin 1 and 2 in the binning case 2 x 12 during fullscans 264.1 and 264.2 (10/01/2007)

3.5.3.4 Instrument line profile and spectral sampling interval

Two fundamental parameters defining the performance of a spectrometer are its spectral sampling interval (SSI) [7] and its instrument line profile (ILP) [8]. Based on theoretical optical design, the SSI was predicted to have a value of 0.1 cm^{-1} and the FWHM of the ILP a value of 0.2 cm^{-1} [Nevejans *et al.* (2006)].

Before flight both characteristics were verified using a He-Ne laser line at 3.39 μm and in a rudimentary test with the Sun as a source. Although these tests confirmed the order of magnitude

7. The spectral sampling interval is the spacing between two sample points in the spectrum.
8. The instrument line profile is defined as the instrument response to a monochromatic spectral line.

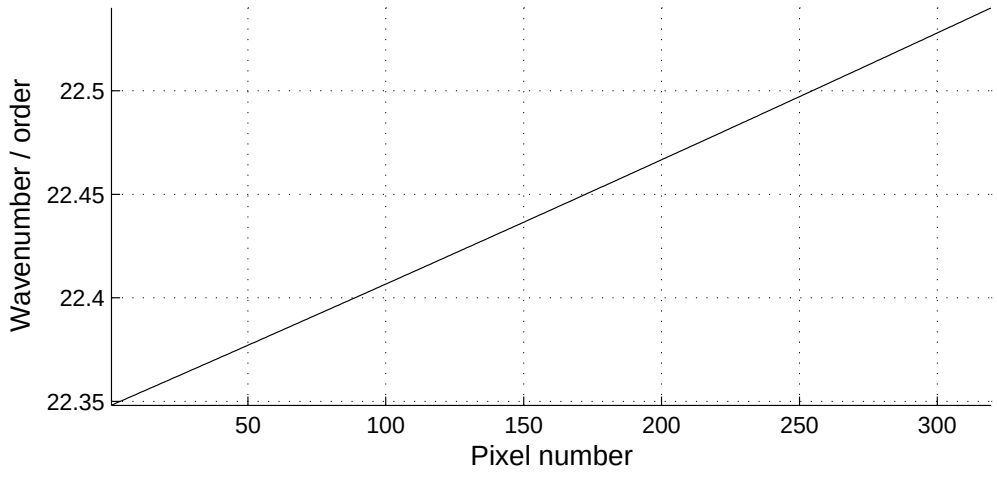

Figure 3.15: Relation between the pixel number and the wavenumber divided by the order $\frac{\tilde{\nu}}{n}$ for bin 1 of binning case 2 x 12 from fullscan 264.1 (10/01/2007).

of both SSI and ILP, they are valid only in a very limited part of the spectral domain. No systematic spectral resolution performance tests over the entire domain could be carried out before launch. Therefore, during flight more detailed resolution measurements were performed, making use of atmospheric absorption lines in spectral recordings.

Instrument line profile (ILP)

The ILP of SOIR was approximated by a Gaussian function whose width was determined by comparing observed atmospheric absorption lines to a model, and whose surface is equal to one.

It is known that the width of the spectral lines at infinite resolution is generally much smaller than the SOIR resolution, about 1/100. Thanks to this, we know that the width at half maximum of observed absorption isolated lines is a very good approximation of the instrument ILP. Indeed, mathematically, the atmospheric spectrum at infinite resolution is convolved by the ILP. If the profile of the atmospheric lines at infinite resolution is assumed to be close to a Gaussian, we know that the convolution result of these two Gaussian functions turns into a Gaussian profile:

$$\begin{aligned} G_{atmos}(S_{atmos}, \tilde{\nu}_{atmos}, FWHM_{atmos}) \quad &\otimes \\ G_{ILP}(S_{ILP} = 1, \tilde{\nu}_{ILP} = 0, FWHM_{ILP}) \quad &= \\ G'_{atmos}(S_{atmos}, \tilde{\nu}_{atmos}, FWHM_{ILP}) & \end{aligned} \tag{3.23}$$

with $\otimes$ denoting the convolution product, G_{atmos} the profile of the atmospheric absorption line, which has a surface of S_{atmos}, a wavenumber position $\tilde{\nu}_{atmos}$ and a full width at half maximum of $FWHM_{atmos}$, and the G_{ILP} the ILP profile, which has a unity surface S_{ILP}, is centered in 0 and a full width at half maximum of $FWHM_{ILP} >> FWHM_{atmos}$.

Indeed, the convolution of a Gaussian curve of width $FWMH_1$ by another Gaussian of width $FWMH_2$ results in a Gaussian of width $\sqrt{FWMH_1^2 + FWMH_2^2}$, which is approximately equal to $FWMH_1$ if $FWMH_2 << FWMH_1$.

The calculation procedure is the following. We consider the spectra taken in an orbit, for a given order and one bin. These spectra were all taken at different altitudes, and we assume that we are going down in altitude in the atmosphere. The spectra corresponding to the first appearance of an atmospheric absorption structure until its extinction are selected, which occurs when the transmission reaches values close to zero. This condition is simple, because the signal to noise ratio is known, and the calculation of the noise level is straightforward. The absorption lines are then localized.

The evaluation of the ILP on an absorption line is done as follows. First, the position of the minimum of the line is measured. Then, its depth is calculated as the difference of the minimum and the two first encountered maxima located on both sides of the minimum. However, it has been decided that these maxima need to fulfill the following conditions to be selected: the wavenumber difference should be less than 0.6 cm^{-1}, the transmittance difference less than $5{\cdot}10^{-4}$ and their absolute transmittance more than 0.95.

An example is shown in Figure 3.16, where a spectrum is selected from orbit 341.1, order 149, bin 1. The tangent altitude equals to 108 km. The line candidates are presented with a small dot at their minimum value, while the ones that are selected under the conditions described here above have a large dot at their minimum. The crosses depict all the local maxima observed in the spectrum. For each selected line (5 in this case) and considering the local maxima, the edges of the line are presented as circles. The ILP measurement corresponds to the small thick lines, and the measured values are reported on the graph. The ILP values are averaged on all measurements taken during one occultation in one order.

This procedure has been applied on all the spectra measured by SOIR between 01/05/2006 and 01/01/2011, covering more than 1200 occultations (300 orbits for which 4 orders were measured) for each bin. Note that reliable information could not be obtained for each occultations. The number of points to build the statistics is presented in Table 3.8.

The fits for bins 1 and 2 are presented in the top and bottom Panels of Figure 3.17 respectively. All the measurements are presented, and the standard deviation on each single measurement is given as the vertical bars. The error weighted fits are given as the solid lines. The FWHM of the ILP varies between 0.1 and 0.23 cm^{-1}. The standard deviation of each fit is given in Table 3.8.

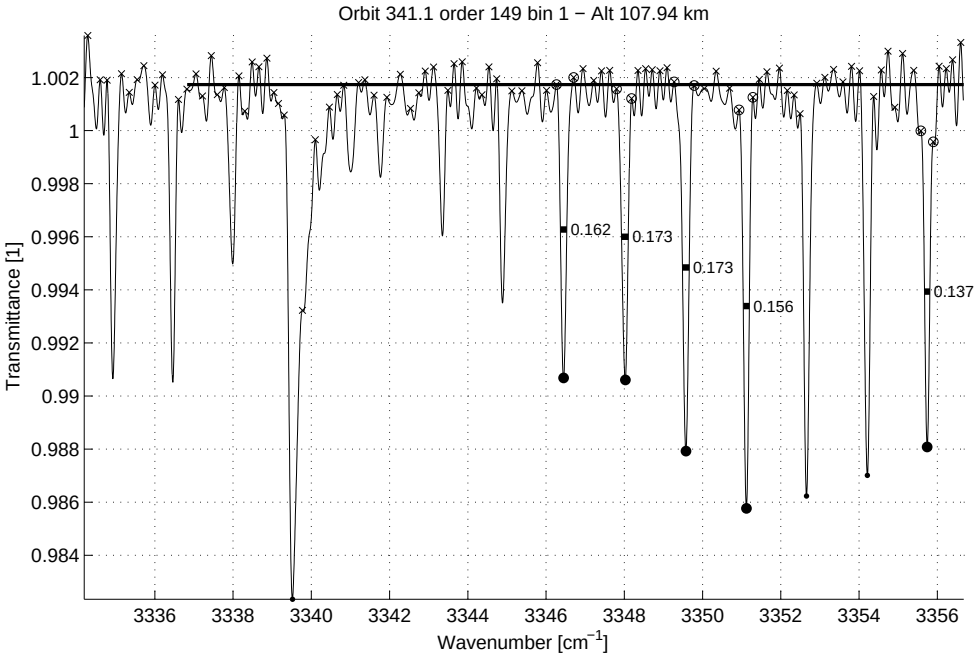

Figure 3.16: Example of the ILP fit for orbit 341 case 1 order 149 bin 1 at an altitude of 108 km. The thin curve is the measured transmittance, as a function of the wavenumber. The observed absorption lines correspond to rovibrational CO_2 transitions. The large thick line is an evaluation of the baseline. The crosses are the positions of all the maxima. The points are the minima. The thick points are the minima that are selected using the procedure explained in the text. The circles are their corresponding maxima. The small thick lines are the measurements of the ILPs on the absorption lines, the numbers are the measurements. The values are in cm^{-1}.

	Number of points	Standard deviation [cm^{-1}]
Bin 1	768	$2.49 \cdot 10^{-2}$
Bin 2	413	$2.03 \cdot 10^{-2}$

Table 3.8: Characteristics of the ILP fit. The Table gives for bins 1 and 2 of binning 2 x 12 the number of points used to calculate the regression, and the standard deviation of this regression.

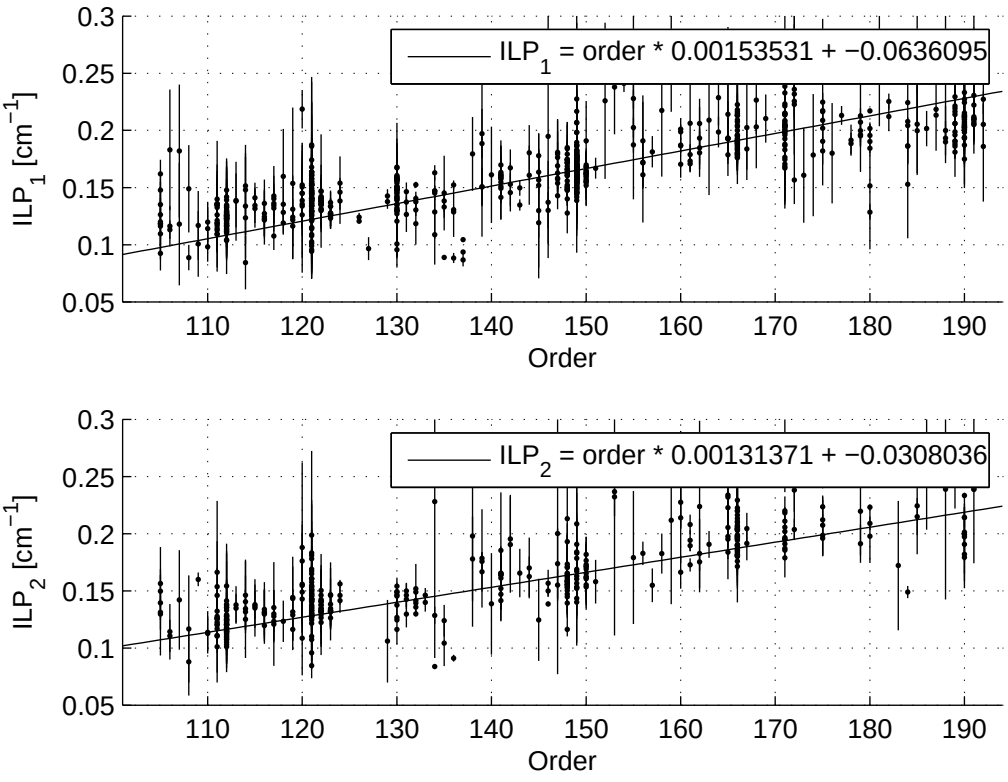

Figure 3.17: FWHM of the ILP calculation for bins 1 (top) and 2 (bottom) from all the atmospheric lines in all the measurements. The vertical lines are the standard deviations on all the ILP measurements obtained during one occultation measuring one order.

Spectral sampling interval (SSI)

The SSI is easily obtained from the pixel width calculation: it is the spectral width of a pixel.

The values of the SSI are plotted in Figure 3.18 for bin 1 of binning case 2 x 12. The spectral width is increasing with the pixel number as well as with the diffraction order, because of the angular dispersion (Equation (3.5)). It varies between 0.03 and 0.06 cm^{-1}.

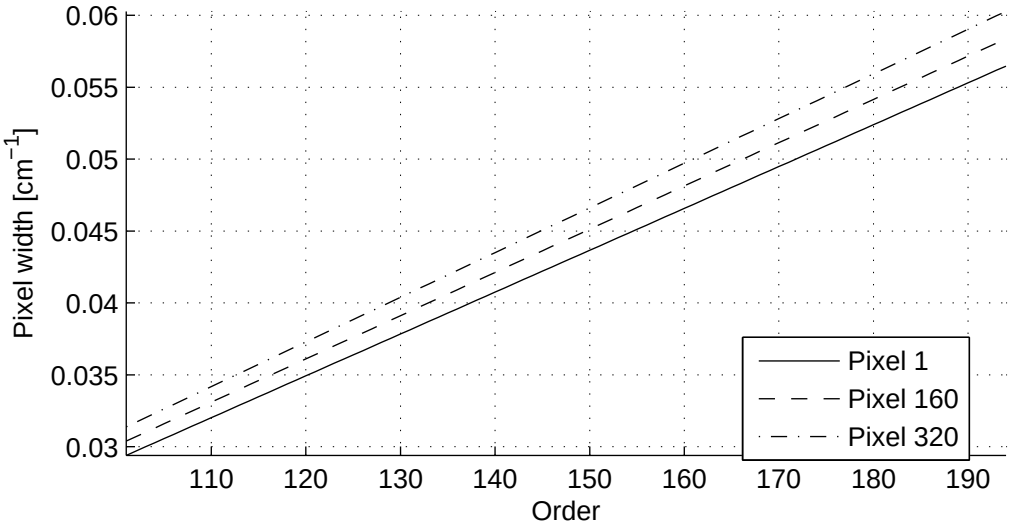

Figure 3.18: Spectral sampling interval: dependence of the pixel size, as a function of the pixel number and the diffraction order. Results for bin 1 of binning case 2 x 12.

3.5.3.5 Signal-to-noise ratio

The signal-to-noise ratio is calculated here from spectra at level 0.3 [Mahieux *et al.* (2008)].

For a given occultation, the spectra taken at altitudes between 220 km and 180 km are selected. The signal standard deviation on pixels p_i 100 to 300 is calculated, and turns into the signal-to-noise of the spectrum using the relation:

$$S2N = \frac{1}{\sqrt{\frac{1}{N}\sum_{180\text{km}<z<220\text{km}} \text{var}\left(T_z(p_i = 100:300)\right)}} \tag{3.24}$$

with $T_z(p_i = 100:300)$ the transmittance of the pixels p_i 100 to 300 of the spectra measured at an altitude between 180 and 220 km, N is the number of spectra satisfying the criterion, z is the altitude and $S2N$ is the signal-to-noise ratio.

Only the central pixels are considered, because the side pixels (from 1 to 99 and 301 to 320) have very low signal-to-noise ratio as they are less illuminated, as it is explained in the sensitivity Section (Section 3.5.3.2). For a given occultation in a given order and for a given bin, the standard deviations calculated on all the spectra which satisfy the altitude criterion specified here above are summed up and the average is taken.

Figure 3.19 is an example of signal-to-noise calculation for a particular orbit (341.1, 28/03/2007) in order 149 taken at level 0.3. One spectrum (measured at 06:26:50 UTC) is taken to illustrate the procedure. In this spectrum, the signal corresponding to pixels 100 to 300 is selected, and the standard deviation on this signal is calculated. The same procedure is applied on all the spectra measured at altitudes between 220 and 180 km, and the signal to noise ratio corresponding to this occultation in these given bin and order is obtained from Equation (3.24).

The values of the signal-to-noise ratio vary from 500 to 4,000. Figure 3.20 shows the variation of the signal to noise ratio from order to order.

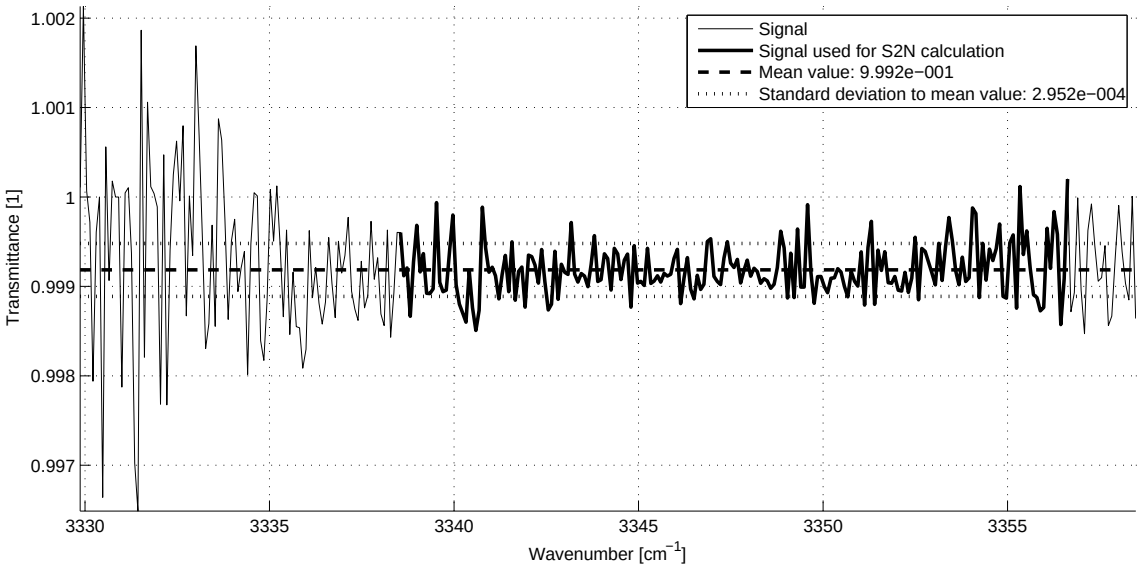

Figure 3.19: Calculation procedure of the signal-to-noise ratio on one spectrum of an occultation. Example on orbit 341.1 (28/03/2007), order 149 and bin 1 measured at 06:26:50 UTC at data level 0.3. The standard deviation is calculated on pixels 100 to 300. The Figure presents the spectrum in plain, the bold spectrum is the range used to calculate the signal-to-noise. The mean value on this range is plotted in dashed, and the standard deviation to the mean is in dotted. The same procedure is applied to all the spectra satisfying the altitude condition of Equation (3.24), and the signal to noise ratio is obtained from the same equation.

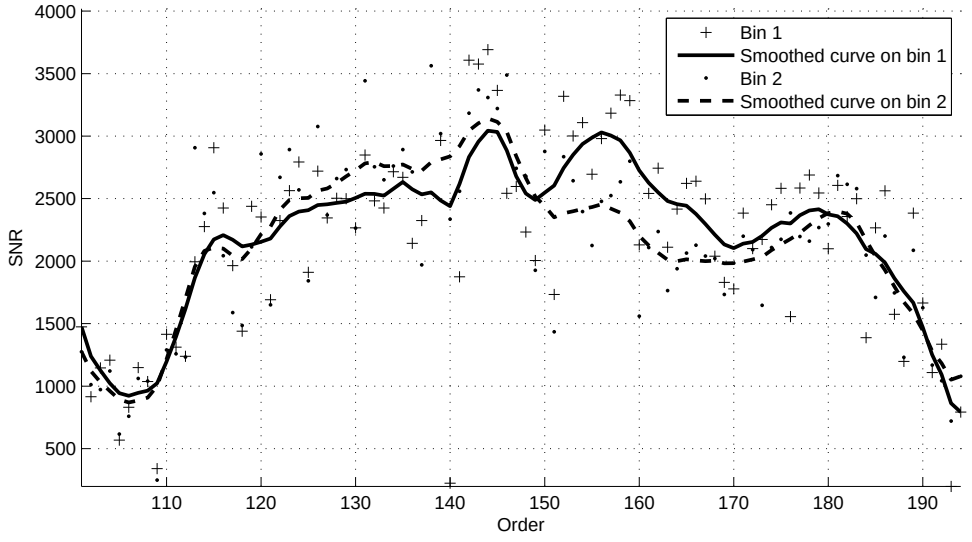

Figure 3.20: Evolution of the signal to noise ratio as a function of the order on bin 1 and 2. The crosses and dots are the values for bin 1 and 2, while the lines are smoothed curves passing through the points.

3.5.4 Acousto-optical tunable filter

3.5.4.1 Introduction

The choice of the AOTF bandwidth is important: it should be less than the FSR of the echelle grating. This requirement ensures that there is no interference nor superposition of light coming from different orders. As the FSR, the AOTF bandwidth is measured in term of FWHM. Because the FSR equals ≈ 22.38 cm^{-1}, the initial bandwidth of SOIR was designed to be 20 cm^{-1} [Nevejans *et al.* (2006)]. However in-flight measurements showed that the bandwidth is close to ≈ 24 cm^{-1} [Mahieux *et al.* (2008)], which increases the order leakage overlap on the detector. Indeed, when a given order n is selected, the spectral lines observed on the detector do not only come from order n, but may also come from the orders aside. Usually, when studying the SOIR spectra, the orders $n-3$, $n-2$, $n-1$, n, $n+1$, $n+2$, $n+3$ are considered.

Two calibrations are necessary to correctly derive the spectra from the SOIR observations: the AOTF frequency to wavenumber relation, also named the tuning relation, and the AOTF transfer function shape. The way to derive them is explained in this Section.

3.5.4.2 AOTF frequency to wavenumber relation

The AOTF passband function differs from what is described in Section 3.2.4. It is broadened by several effects:
- the divergence of the incident optical beam, which is not perfectly focused on the entrance facet of the crystal;
- the angular spread of the acoustic beam inside the crystal due to some misplacements of the acoustic emitter;
- the optical non-uniformity of the acousto-optical material.

In fact, here we see that the AOTF transmission in SOIR, in particular its width and peak position, is different for each of the two detector bins defined in Section 3.4.1.

Let us consider the binning case 2 x 16. In the normal mode of observation used for solar occultation measurements two spectra are recorded simultaneously, corresponding to two bins of 16 detector lines, further defined as bin 1 (detector lines 188 to 203) and bin 2 (detector lines 204 to 219) spectrum, see Section 3.2 and Figure 3.7. For both bin 1 and bin 2 spectra, a tuning function and AOTF bandpass functions have to be determined, as Equation (3.10) (page 23) shows that the width of the AOTF bandpass function depends on wavelength.

The miniscan observations are dedicated to the determination of the AOTF bandpass function [Mahieux *et al.* (2008)]. Each miniscan was centered on an AOTF frequency corresponding to a well-defined solar line. The solar lines are listed in a solar catalogue [Hase *et al.* (2009)]. Each of them is observed on a precise group of pixels. Other solar lines from the neighborhood of the targeted one are often also visible on other pixels, which allows the retrieval of many more AOTF bandpass functions at the same time. The study of the measured intensity variation as a function of the applied frequency allows the precise characterization of the bandpass function. The determination of the tuning relation is performed by determining the position of the function maximum.

Several frequency steps for the miniscan observation were defined and applied:
- 1 kHz
- 5 kHz
- 15 kHz
- 20 kHz

The spectra that are used are full Sun spectra, coming from data level 0.2.

A spectrum correction procedure is applied. It first handles the pixel-to-pixel non-uniformity (Section 3.5.3.1) and then the sensitivity of the instrument (Section 3.5.3.2). On top of that, spectra are flattened using a baseline level; since the observed solar line is recorded on a pixel group, the levels in the adjacent pixels can act as a reference level for the base level subtraction. The residual base level is fitted by a second order polynomial. The result of the procedure is shown in Figure 3.21.

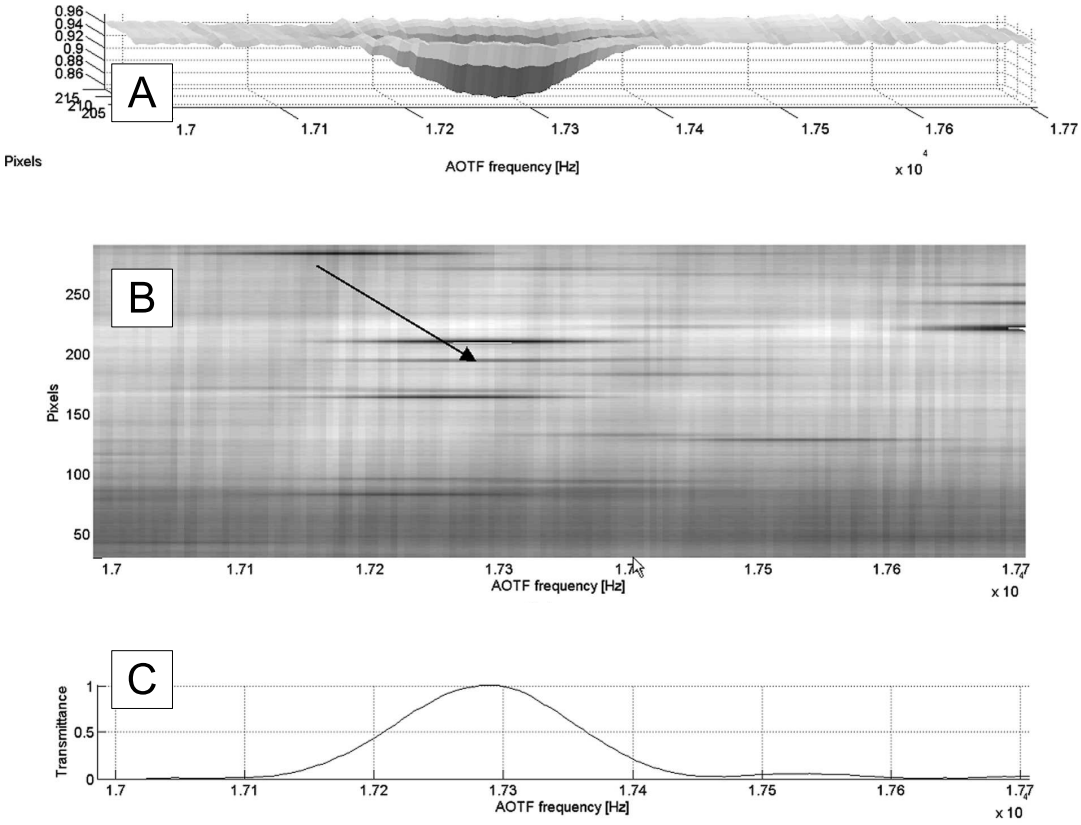

Figure 3.21: Depiction of a miniscan. Panel A shows a line in three dimensions as it may be observed during a miniscan, as a function of the pixel number and the AOTF frequency. Panel B shows the entire miniscan after the pixel-to-pixel non-uniformity as well as the spectrometer sensitivity are removed. The solar lines are seen as the black lines on the spectrum, at a given pixel value. Panel C shows the pixel line on which the solar line falls. The curve seen is the AOTF transfer function, from which the background still needs to be removed.

The same procedure is applied to all available miniscans. Because the relation between the AOTF frequency and the wavenumber may change with time, the miniscans are separated in time groups, to monitor the changes. They are listed in Table 3.9.

Beginning orbit	End orbit	Beginning date	End date	Number of miniscans
142	502	10/09/2006	04/09/2007	50
651	703	31/01/2008	24/03/2008	56
856	859	23/08/2008	26/08/2008	23
897	930	04/10/2008	06/11/2008	34
959	971	05/12/2008	17/12/2008	35
1013	1096	28/01/2009	20/04/2009	38
1174	1267	07/07/2009	09/10/2009	55

Table 3.9: List of the available AOTF calibrations from miniscans.

The AOTF transfer function is modeled by a sinc-square function

$$I(\tilde{\nu}) = I \cdot \left[\text{sinc}\left(0.886 \cdot \frac{\tilde{\nu} - \tilde{\nu}_0}{\Delta\tilde{\nu}_0}\right)\right]^2 \tag{3.25}$$

where I, $\tilde{\nu}_0$, and $\Delta\tilde{\nu}_0$, are parameters whose values are obtained by best fitting this expression to the observed AOTF bandpass functions, while fitting the baseline level by a second order polynomial function.

Using such an approximation, an AOTF bandpass function can be derived at any given wavenumber of the investigated spectral range.

The determination of the AOTF bandpass function maximum position gives the tuning relation. It is illustrated in Figure 3.22, where the tuning function is plotted for bins 1 and 2 of a 2 x 12 binning case configuration. The miniscans were measured between orbits 142 and 502.

The error on the maximum position (presented as the vertical bars in Figure 3.22) resulting from the AOTF function fit were used as weighting factors. The tuning function can be fitted by a second order polynomial linking the radio frequency f_{AOTF} (in [kHz]) to the wavenumber $\tilde{\nu}$ (in [cm^{-1}]) by

$$\tilde{\nu} = a_{AOTF} \cdot f_{AOTF}^2 + b_{AOTF} \cdot f_{AOTF} + c_{AOTF} \tag{3.26}$$

where a_{AOTF}, b_{AOTF}, and c_{AOTF} are the coefficients of the polynomial. This function describes the frequency position of the maximum of the AOTF bandpass function versus the wavenumber. It is important, because a small shift of the bandpass can introduce large deformations in the transmitted spectrum. The error on the function has also been calculated. For a binning equal to 12 and for bin 1, the mean value of the error is 0.83 cm^{-1}. The color of the points in Figure 3.22 represents the AOTF temperature at the time of measurement. It only covers a range of 3° C. From these Figures no detectable temperature dependency was observed either for the tuning function, the variation being within the error bars.

Figure 3.23 illustrates the fit applied to derive the AOTF bandpass function using the solar line at 2948.7 cm^{-1}.

Using Equation (3.25), a first guess of the FWHM of the AOTF transfer function can be obtained. Indeed, $\Delta\tilde{\nu}_0$ is the FWMH of the fitted sinc-square function. This value equals $\approx$ 24 cm^{-1}.

3.5.4.3 AOTF frequency to diffraction order relation

The question is, knowing the excitation frequency of the AOTF, to determine which diffraction order was scanned. Indeed, for high orders values, the same wavenumber region is recorded by different orders. To achieve this, a simple rule was decided. The AOTF frequency f_{AOTF} is

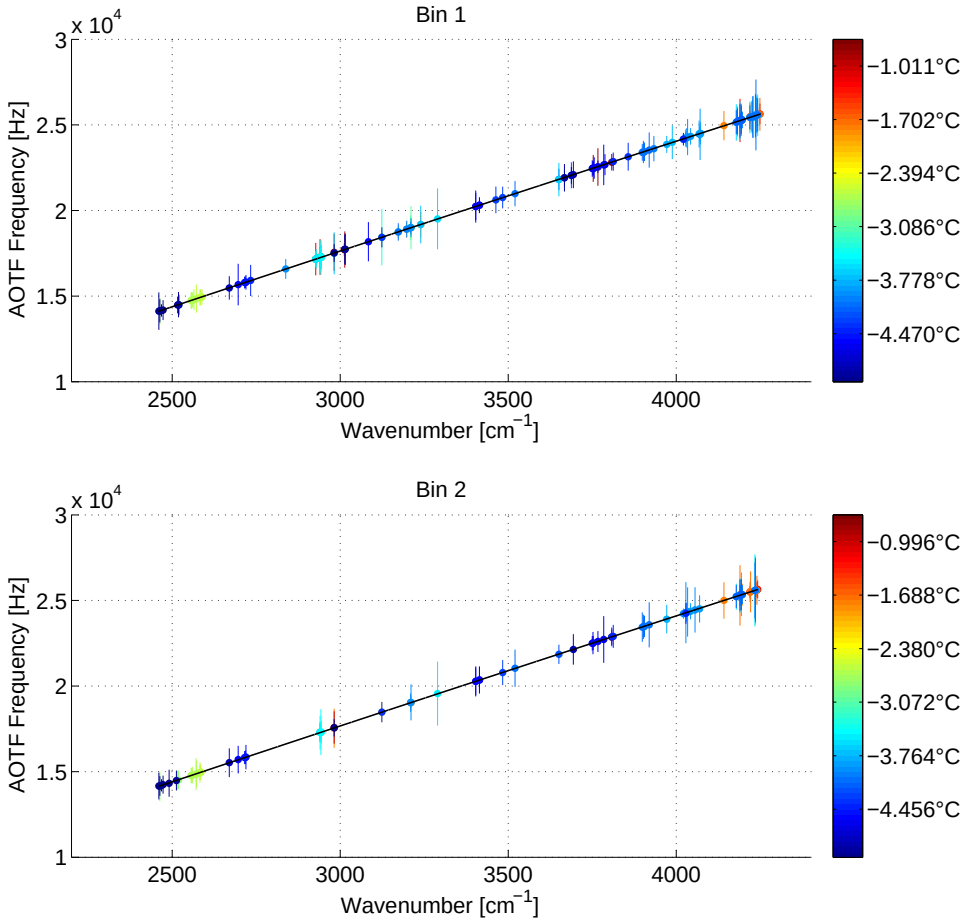

Figure 3.22: Tuning function resulting from the fit of the miniscans that occurred between orbit 142 and 502 (55 in total). The fit is done in the 2 x 12 binning case, and is given for bin 1 and bin 2. The error bars plotted are the maximum position ($\tilde{\nu}_0$) error resulting from the fit of each AOTF function. The color represents the mean temperature of the AOTF during each miniscan, i.e. a temperature probe measures the AOTF temperature (as mentioned in Section 3.4.3.4).

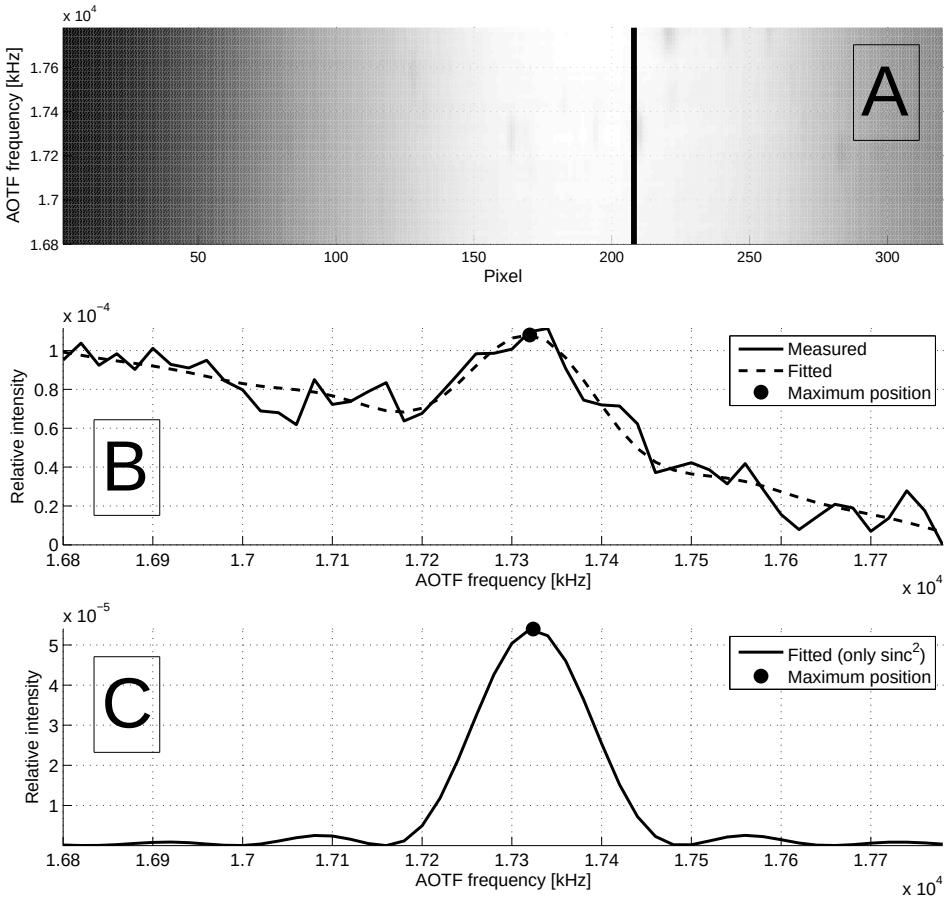

Figure 3.23: Example of AOTF fit for AOTF frequency to wavenumber fit. The fit done in bin 1 of binning case 2 x 12 of miniscan 361.2 (17/04/2007) on a solar line at 2948.7 cm^{-1}. Panel A shows the whole miniscan, as a function of pixel number and AOTF frequency. The base level is not constant, having lower values for pixels between 0 and 100, and pixels between 300 and 320. This results from the sensitivity of the spectrometer, which has not been removed in this case. The solar lines are seen as darker spots on the graph. The black line shows the pixel line studied in the current case. Panel B is a cut off following the black line of the surface presented in Panel A. The plain curve is a measured value. The dotted curve shows the fit, using a sinc-square and a second order polynomial background. Panel C shows the sinc-square only, without the background. The dots in Panels B and C is the position of the maximum, or the AOTF frequency of the maximum of the solar line studied.

transformed into its equivalent wavenumber $\tilde{\nu}_{AOTF}$, and the order is chosen such that the spectral distance between its central wavenumber and $\tilde{\nu}_{AOTF}$ is minimum:

$$n_{AOTF} = \min\left(\left\|\tilde{\nu}^{mean}_{AOTF,i} - \tilde{\nu}_{AOTF}\right\|\right), i = 101, ..., 194 \tag{3.27}$$

with n_{AOTF} the selected order, $\tilde{\nu}^{mean}_{AOTF,i}$ the central wavenumber of the SOIR order i.

3.5.4.4 AOTF transfer function

Introduction

As described in the previous Section, it was shown theoretically that the AOTF transfer function can be modeled using a sinc-square function [Glenar *et al.* (1994); Xu & Stroud (1992)]. However, data processing shows that this model does not seem to suit the SOIR AOTF.

A new method has been derived to determine the transfer function of the AOTF using only in-flight measurements, i.e. direct Sun observations [Mahieux *et al.* (2009)]. The miniscans are used for this purpose.

Propagation of the light through the SOIR crystal

If we consider that light travels as planar waves through the AOTF crystal, the transfer function can be modeled fairly well by a single sinc-square function [Gottlieb (1994)]. However, after the launch of the VEX spacecraft, we realized that the width of the AOTF transfer function had changed and that the side lobes of the function were different to what had been measured on Earth before launch [Mahieux *et al.* (2008)]. We interpret this change as the result of some damage suffered by the device during the take off phase or during the vibration tests before launch. Because of this probable slight damage of the AOTF crystal, one could consider that the medium is no longer perfectly homogeneous; the light would no longer travel as a planar wave. There are two consequences to this:

1. the light at the output is the result of several planar waves propagating through the crystal;
2. the transmission through the crystal depends on the physical portion of the medium which is passed through.

The bandpass function is then:

1. modeled as the sum of several sinc-square functions;
2. dependent on the position of the detector rows, therefore on the binning case.

Moreover, it should be noted that the AOTF function depends on the radio-frequency applied to the device, and therefore on the wavelength of the light transmitted through the crystal.

Measurement description

The solar lines [Hase *et al.* (2009)] measured during the miniscan are used to realize this calibration.

As explained in Section 3.5.4.1, the absorption lines from three orders with a higher diffraction number and three orders with a lower diffraction number compared to the central order can have a significant contribution to the measured spectrum. In here, the solar absorption lines used for the current study were carefully chosen in such a way that no line from any of the -2 to $+2$ adjacent orders falls on the same pixels nor on nearby pixels of the detector. This is easily performed knowing the relation between the diffraction order and the wavenumber, which allows the accurate determination of the pixel number on which each solar line falls. The solar absorption lines studied have also a minimum of 0.92 in transmittance. The solar lines have also been chosen such that they cover the entire spectral range probed by the instrument, as the AOTF bandpass function depends on its central wavelength. The pixel-to-pixel variation (Section 3.5.3.1) and the spectrometer sensitivity (Section 3.5.3.2) variation are first removed from the spectra.

Procedure

In the following we distinguish between a local and a global model. The local model allows the definition of the parameters needed to construct the AOTF bandpass function from a given solar line, i.e. corresponding to a given central wavenumber. This is repeated as many times as the number of selected solar lines. The global model is then used to draw trends in the fitted parameters as a function of wavenumber, so that the AOTF bandpass function can be built for any given wavenumber.

Local model

The model that is used to fit the AOTF transfer function is a sum of 5 sinc-square functions:

$$AOTF(\tilde{\nu}) = \sum_{i=-2}^{2} \max(0, I_i) \cdot \mathrm{sinc}^2 \left[0.886 \cdot \frac{\tilde{\nu} - \tilde{\nu}_{0_i}}{FWHM_i} \right] \tag{3.28}$$

where $\tilde{\nu}$ is the wavenumber, I_i are the intensity coefficients, $\tilde{\nu}_{0_i}$ the relative wavenumber position of the maximum of the sinc-square functions, and $FWHM_i$ the full width at half maximum of each sinc-square function. It results in 14 variables to fit, as the first relative wavenumber $\tilde{\nu}_{0_0}$ has to be equal to zero, i.e. centered on the maximum.

A decision had to be made on the number of sinc-square functions to use. This number had to be odd, as the number of sinc-square had to be the same on both sides of the central sinc-square. It turned out that 7 cannot be used, because no reliable information can be obtained so far away from the AOTF maximum, as the miniscans that we used for this work do not cover that region. Five sinc-square functions is the maximum number that could be used.

These parameters are fitted for each observed solar absorption line selected above using a Simplex algorithm. Constraints are also defined: all the I_i and $FWHM_i$ values have to be positive, even after convergence; the values of the $\tilde{\nu}_{0_i}$ must remain in well distinct intervals, defined as multiples of $FWHM_0$, as illustrated in Figure 3.24.

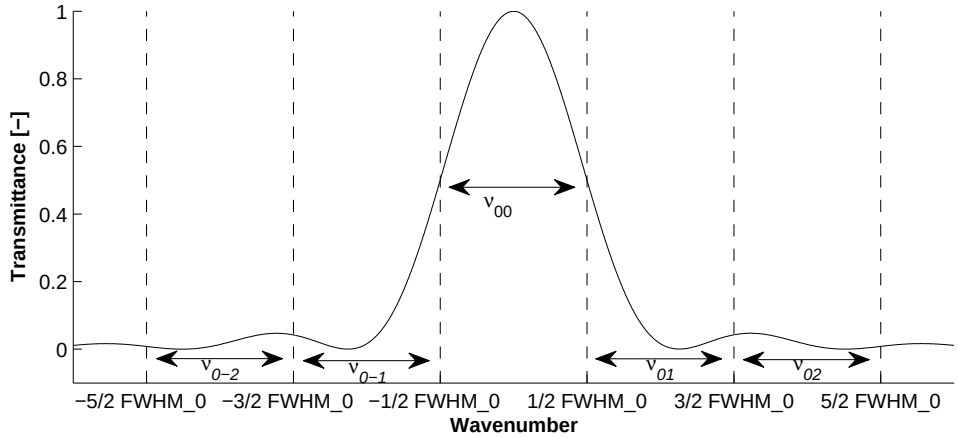

Figure 3.24: Definition of the interval variation of the $\tilde{\nu}_{0_i}$. This is a plot of one sinc-square function (the one noted "0") to show how the position of the $\tilde{\nu}_{0_i}$ is constrained using the value of $FWHM_0$. The width of the arrows equals to $FWHM_0$.

The average wavenumber width of the miniscans is 81 cm^{-1}. A good guess value for $FWHM_0$ turns around 24 cm^{-1} (Section 3.5.4.2). As the miniscans are not always centered on the solar line, up to three AOTF transfer function intervals may be measured using one solar line. Therefore, using several measurements of one line, one can reconstruct a maximum of 5 intervals. The inner three intervals are very well defined, and the outer two are less certain.

The fit is performed on a set of measurements of each solar line, and for each measurement the pixel-to-pixel variation as well as the spectrometer sensitivity variation is tentatively removed.

The residual background is modeled for each measurement by a linear function, which may differ from miniscan to miniscan. For each measurement j, the model becomes:

$$AOTF_j(\tilde{\nu}) = \underbrace{\sum_{i=-2}^{2} \max(0, I_i) \cdot \mathrm{sinc}^2 \left[0.886 \cdot \frac{\tilde{\nu} - \tilde{\nu}_{0_i}}{FWHM_i} \right]}_{AOTF(\tilde{\nu})} + \alpha_j \cdot \tilde{\nu} + \beta_j \tag{3.29}$$

where α_j and β_j are the coefficients of the background of the measurement j, and the I_i, $\tilde{\nu}_{0_i}$ and $FWHM_i$ are the coefficients common to each measurement of the same line.

Global model: Variation of the local AOTF transfer function model with wavenumber

The local model defined in the above Section can be performed for all the selected solar absorption lines throughout the whole SOIR spectral range. However, each separate local model is assumed to be related to the other ones, because the evolution of the bandpass function with wavenumber is smooth (see Figures 3.28 and 3.29). We have supposed that the 14 parameters were varying linearly across the SOIR spectral range.

$$X = a_X \cdot \tilde{\nu} + b_X \tag{3.30}$$

where X is one of the 14 parameters defining the AOTF function (I_i, $\tilde{\nu}_{0_{i(i\neq 0)}}$ or $FWHM_i$), a_X the linear coefficient and b_X the constant coefficient.

Finally, a set of 28 coefficients has to be fitted. This fit is also performed using a Simplex algorithm, but with no constraints.

Interaction between the global and local models

The local models are all driven by the global model. They each receive a set of 14 initial variables obtained from the linear regression of the global model at the wavenumber of the solar absorption line, i.e. the accurate wavenumber of the maximum of the central sinc-square function. Each local model returns a fitted set of the 14 variables, which are used by the global model for fitting its 28 variables a_X and b_X. The interaction between the global and the local model is presented in Figure 3.25.

The set of 28 parameters a_X and b_X, where X may be $FWMH$, I or $\tilde{\nu}_0$, is obtained when convergence is achieved. Figure 3.26 shows the convergence of parameters a_{FWHM_0} and b_{FWHM_0} as well as a_{I_1} and b_{I_1} of bin 1 in the 2 x 12 binning case, as well as the convergence of the fit residuals of the global model.

Results

The method described in this Section is applied to all the miniscans performed between September 10, 2006 (orbit 142) and October 10, 2009 (orbit 1267), and grouped as listed in Table 3.9. The retrievals are performed for all the binning cases defined in Table 3.3. Figure 3.27 shows the local fit for the 2943.70 cm^{-1} solar line. Similar fits are obtained for all the 30 solar lines scanned.

It has to be noted that the AOTF transfer function obtained using this technique is the mirror of the one that has to be used for spectra analyses. This finds its explanation in the miniscan measurement scheme. The solar line may be considered as a Dirac peak. It is scanned while slightly incrementing the AOTF frequency value, i.e. while moving the physical AOTF functions along the wavenumber axis to the right. As the source remains fixed, and the recorder shifts in terms of wavenumber, what we record is the symmetrical of the AOTF transfer function.

If one could displace the solar line, we would obtain directly the AOTF transfer function. The AOTF transfer functions obtained in different orders are shown in Figure 3.28. Figure 3.29 shows the AOTF transfer function along the whole SOIR wavenumber scale for bin 1 in the 2 x 12 binning case.

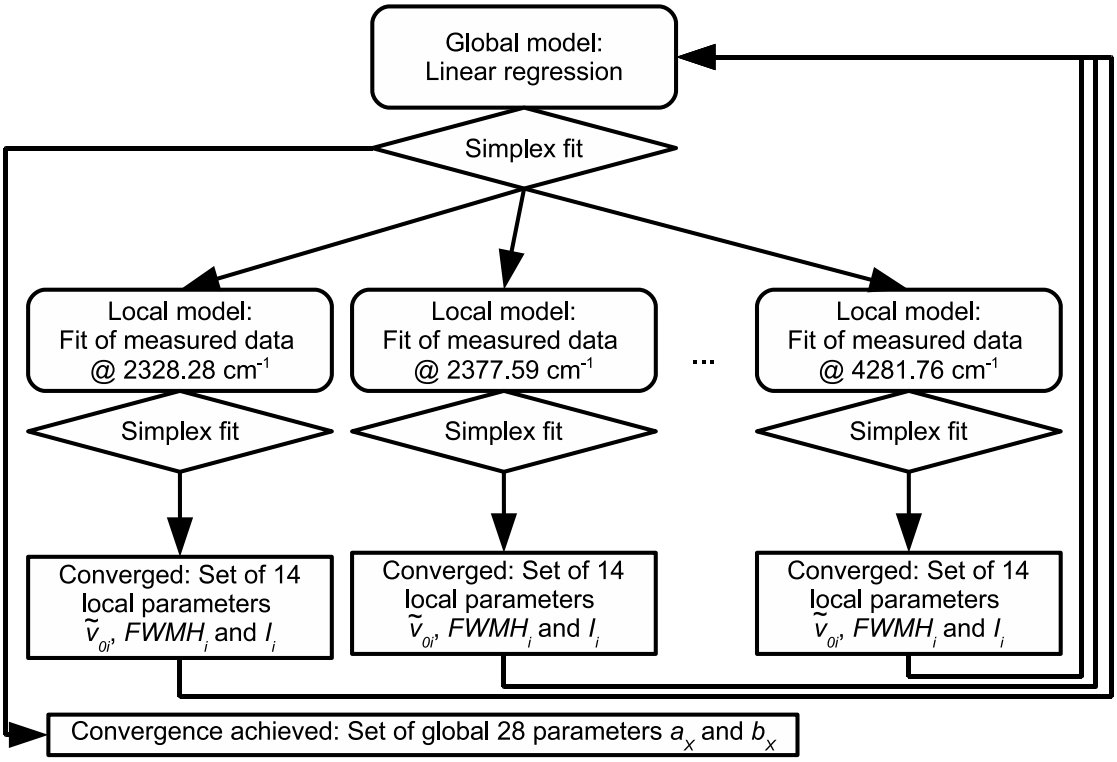

Figure 3.25: Description of the interaction between the local and the global model for the AOTF transfer function fit.

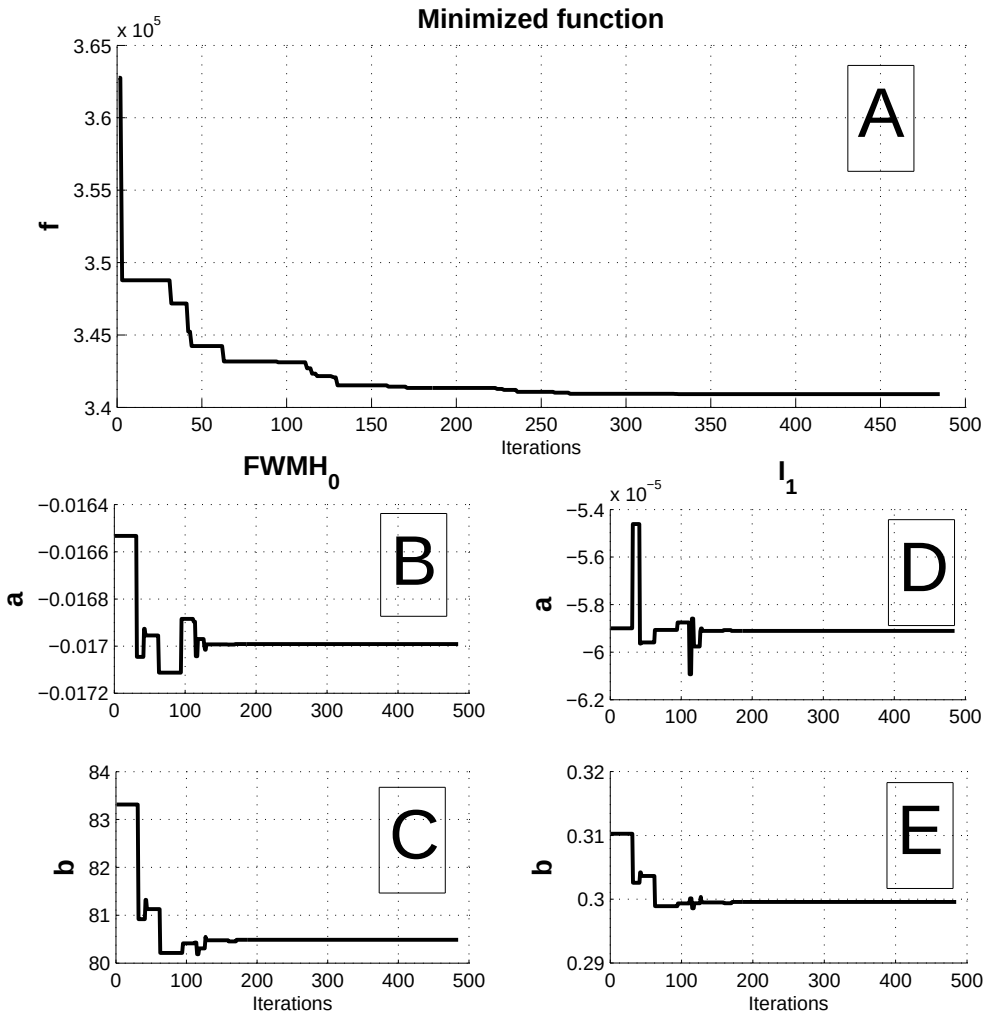

Figure 3.26: Convergence of the global model for bin 1 of binning 2 x 12 for the miniscans 140 to 502. The convergence occurred after 482 steps. Panel A shows the convergence of the function minimized by the Simplex algorithm. Panels B and C show the convergence of parameters $FWMH_{0_a}$ and $FWMH_{0_b}$, and Panels D and E concern the convergence of I_{1_a} and I_{1_b}.

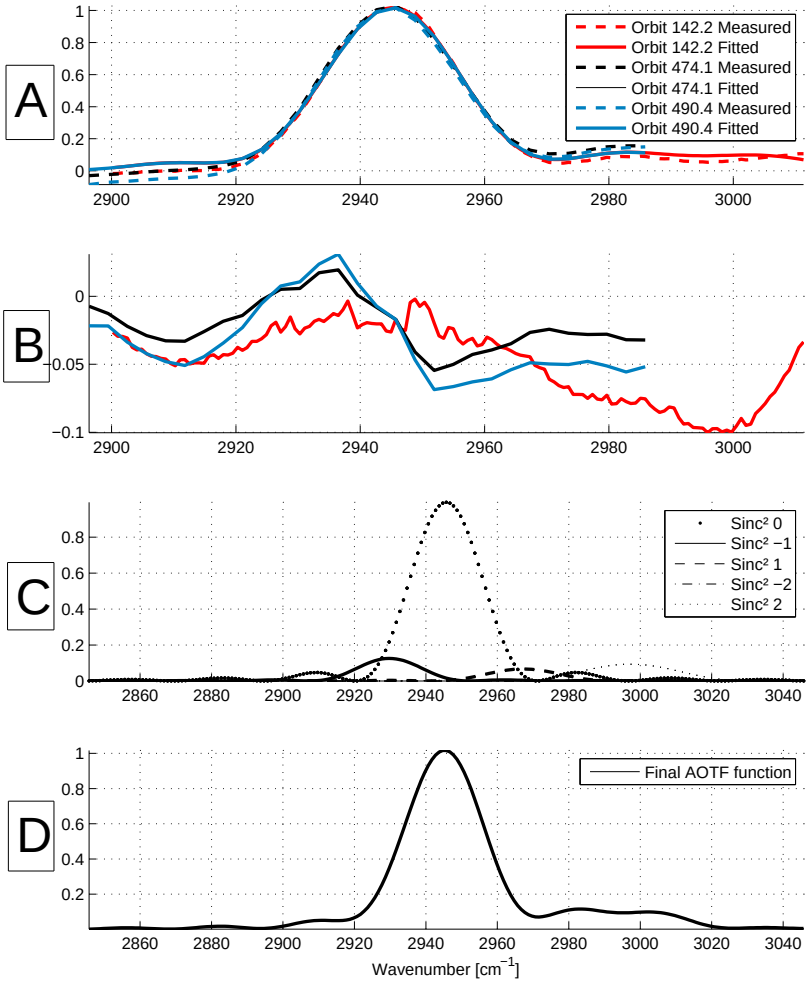

Figure 3.27: Fit of the 2943.70 cm^{-1} solar line. Panel A shows the fit of the solar line at 2943.70 cm^{-1}. This line was scanned three times, during orbits 142.2 (10/09/2006), 474.1 (08/08/2007) and 490.1 (24/08/2007). The measured AOTF transfer functions are plotted as solid lines; the fitted functions are plotted as dashed lines. They depict the models described in Equation (3.29). The y-scale is an arbitrary scale, between 0 and 1. Panel B shows the residuals of the fit of the three solar lines. Panel C shows the 5 sinc-square functions, and Panel D shows the final AOTF transfer function, obtained from the model described in Equation (3.28).

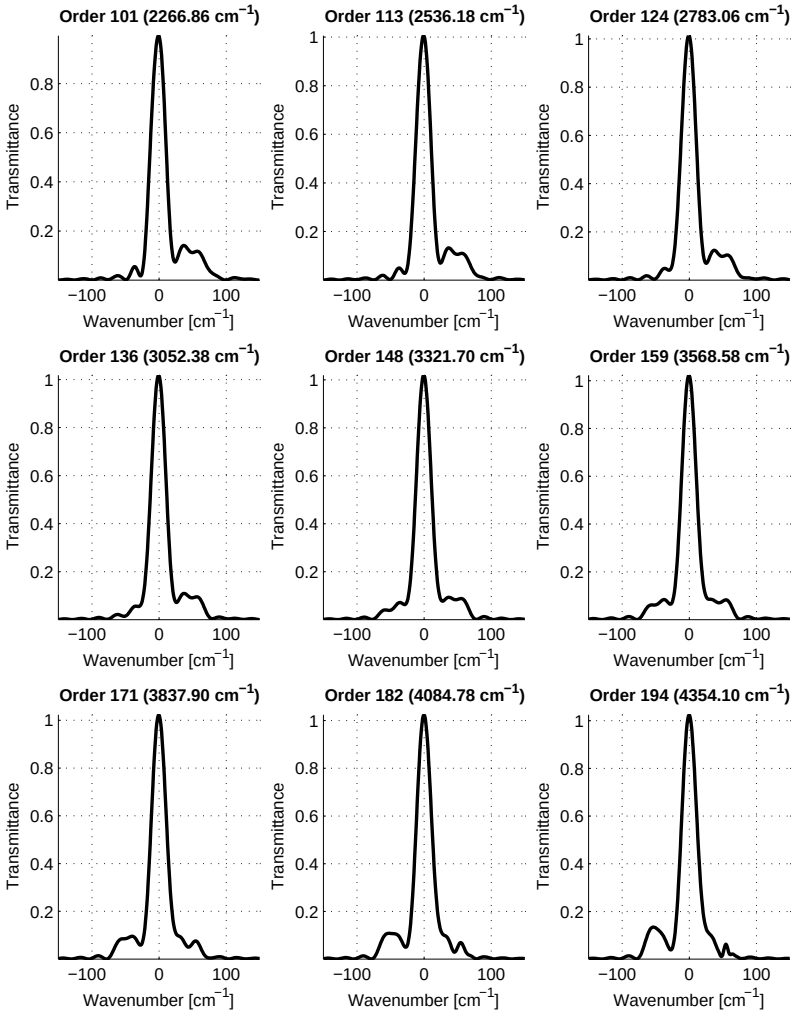

Figure 3.28: AOTF final functions retrieved for bin 1 (binning 2 x 12) for several orders from minsicans between 140 and 502.

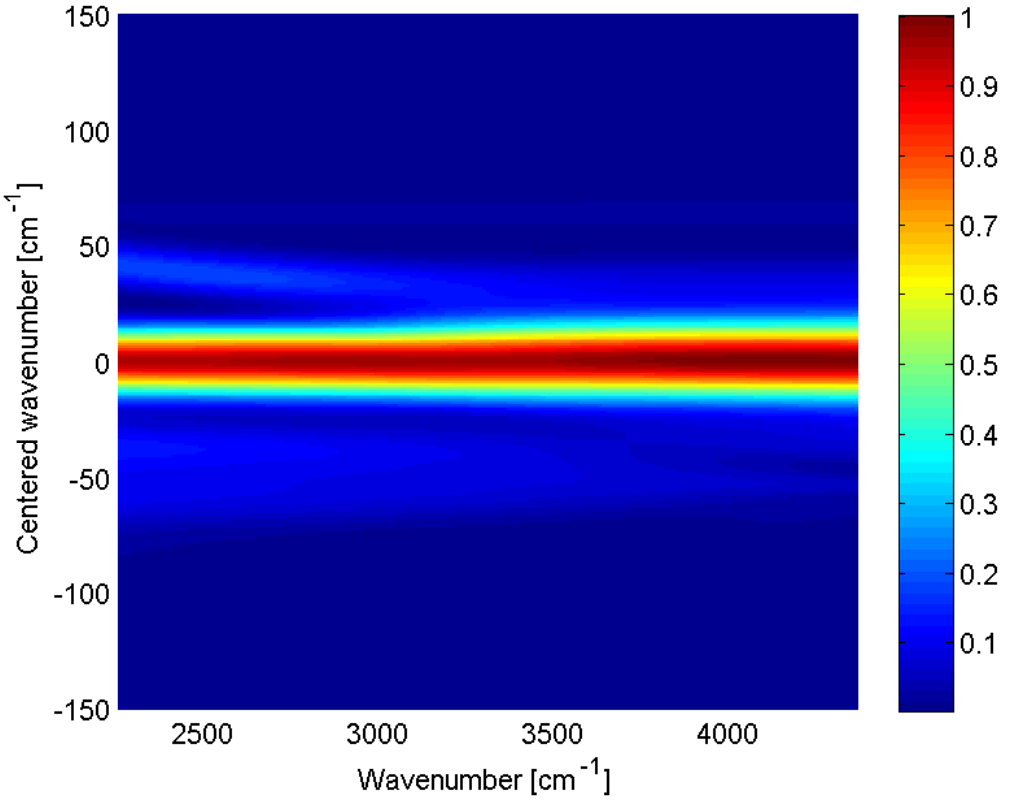

Figure 3.29: 3-D plot of the retrieved AOTF transfer function as a function of the wavenumber, and the central wavenumber, for bin 1 of binning 2 x 12 from minsicans between 140 and 502. View from top.

Chapter 4

The spectral inversion

4.1 Introduction

In this Chapter, we introduce the retrieval procedure that was developed to derive vertical profiles from the SOIR data.

The analysis code is based on the ASIMUT program written in C++ [Vandaele *et al.* (2008)] and was adapted in MATLAB [Mahieux *et al.* (2010)] in order to allow the temperature determination and to improve the treatment of some particular instrumental parameters, like the AOTF transfer function and the wavenumber to pixel relation.

First, the solar occultation geometry is introduced, and the onion peeling approach is described. Then, the retrieval method itself is explained for the retrieval of the vertical density profile of a given species. In the case of some atmospheric compounds, such as carbon dioxide or carbon monoxide, we show how information can be obtained on rotational temperature. The Chapter concludes on a retrieval example, and a sensitivity study on the algorithm parameters.

4.2 Attitude and geometry

4.2.1 Onion peeling method

The solar occultation is the measurement technique used by SOIR to probe the Venus atmosphere. The so-called onion peeling method [1] can be used to invert the problem [Vandaele *et al.* (2008)]. Each measurement can be assigned to a tangent point at the limb, i.e. the point on the line of sight of the instrument for which this axis is tangent to the limb of Venus. Figure 4.1 shows the geometry. The corresponding altitudes are monotonically decreasing in the case of an ingress. These tangent altitudes z_j corresponding to each measurement j define a vertical altitude layering within the atmosphere. The regions between two successive measurement altitudes z_{j-1} and z_j of this scale are called a layer, L_j. The upper boundary of the first layer is arbitrarily fixed. Within each layer, the assumption is made that all the atmospheric parameters, such as the temperature, the total density, the pressure, the volume mixing ratios (vmr) etc., are constant. A ray tracing algorithm deals with the determination of these values from the vertical profiles of the atmospheric parameters in each layer.

The onion peeling method allows to solve the problem by decoupling the absorption along the light path in several absorption portions. This model has the advantage of transforming the problem into the resolution of a non-linear equations system, with the variables being the

1. The onion peeling method is a particular case of the Abel transform, which is an integral transform used in the analysis of spherically symmetric functions.

atmospheric parameters. Note that for a given layer, only the layers located above it have to be considered, and thus have an influence on its atmospheric parameters.

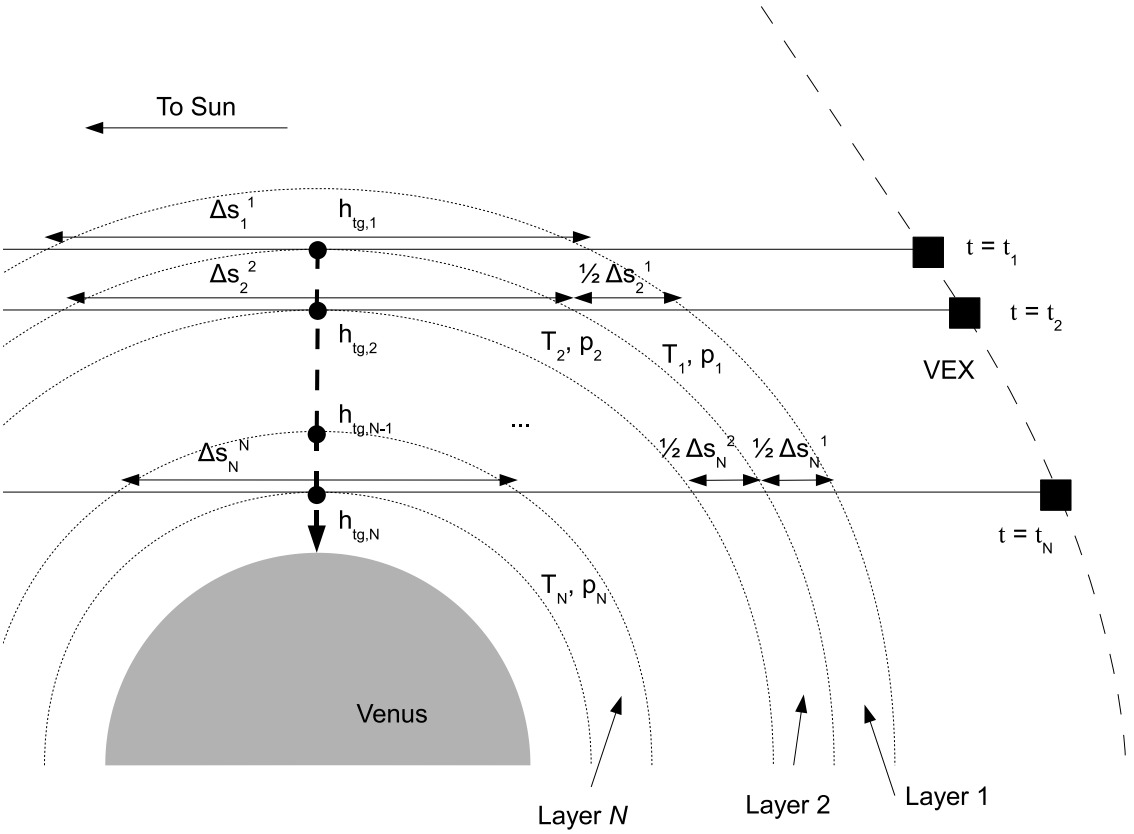

Figure 4.1: Description of the onion peeling method. In the ingress case depicted here, the instrument is taking a measurement every second. The tangent altitudes $h_{tg,j}$ define layers in the atmosphere. The light path is divided into several segments, named $\Delta s_j^{\prime j}$ with j' such that the time corresponds to $t = t'_j$, and j the layer number. In each layer j, the quantities temperature T_j and pressure p_j are assumed to be constant.

4.2.2 Geometry

4.2.2.1 Introduction

To obtain the geometry [2] of the spacecraft, we use the SPICE routines for MATLAB, called MICE, developed by NAIF (the Navigation and Ancillary Information Facility of NASA) [NAIF (2009)]. This tool is used by the whole VEX mission. It gives, from the geometry of the whole spacecraft at any time, the kernels and quaternions. They are calculated at ESAC, the European Space Astronomy Center, located in Villanueva de la Cañada, Spain.

Here is a description of the calculation procedure to compute the tangent altitude.

The binning cases 2 x 16 and 2 x 12 are discussed here.

4.2.2.2 SOIR reference frame

All the vectors presented in this Section are calculated in the SOIR/VEX reference frame, except otherwise stated. The SOIR/VEX reference frame is defined such that the z-axis is aligned

2. The geometry of the spacecraft gathers all the instantaneous characteristics of its positions, velocitys and pointing angles.

towards the pointing direction and the x-axis is parallel to the large side (spectral direction) of the slit. The y-axis is such that the system axis is right handed.

The SOIR reference frame does not correspond to the VEX spacecraft reference frame. The transformation matrix from VEX to SOIR is written as

$$\begin{pmatrix} -1.766 \cdot 10^{-3} & -1.011 \cdot 10^{-3} & 1 \\ 4.967 \cdot 10^{-1} & -8.679 \cdot 10^{-1} & 0 \\ 8.679 \cdot 10^{-1} & 4.967 \cdot 10^{-1} & 2.035 \cdot 10^{-3} \end{pmatrix} \tag{4.1}$$

All the informations concerning the SOIR reference frame can be found in the instrument kernel of SOIR, which may be downloaded from the FTP server of ESA at `ftp://ssols01.esac.esa.int/pub/data/SPICE/VEX/kernels`.

4.2.2.3 Tangent altitude calculation

The exact universal time of the measurement of a given order is needed: t_{VEX} is taken at half-time of the order measurement, so 125 ms after the initial time of each measurement.

In the solar occultation configuration, the calculation of the tangent altitude is straightforward when the pointing angle $\alpha_{pointing}$ and the distance between Venus and VEX $\left\|\overrightarrow{Ven}\right\|$ are known, as depicted in Figure 4.2. $\alpha_{pointing}$is the complement of the angle between the SOIR pointing direction and the vector between VEX and Venus. The tangent altitude is obtained from:

$$h_{tg} = \sin(180^\circ - \alpha_{pointing}) \cdot \left\|\overrightarrow{Ven}\right\| - r_V \tag{4.2}$$

with r_V the Venus radius, 6051.8 km.

The $\alpha_{pointing}$ angle is such that the SOIR instrument points towards the Sun. But it has to be corrected for two effects.

1. The satellite does not point to the center of the Sun. It points to a point located 10' above it, in a direction located in the plane defined by VEX, the center of Venus and the center of the Sun. This configuration is depicted in Figure 4.3. The reason for the depointing comes from the consideration that the refraction of the light beams in the Venus atmosphere has to be considered. This is due to the atmospheric density at the lowest altitudes reached by SOIR. If the instrument points to the center of the Sun, the refracted Sun would exit the pointing direction too early in the occultation [Mahieux *et al.* (2008)]. The refraction displaces the image of the Sun away from the limb. This situation is despicted in Figure 4.5.
2. During the occultations, the spacecraft is set in an inertial mode, in order to follow the target point on the Sun. However, a slight rotation of the slit's FOV around the pointing direction is observed. The angle γ_{slit} associated to this rotation remains small, with values usually lower than 10°, see Figures 4.3 and 4.4. The geometry of VEX is calculated to force the slit FOV to be parallel to the limb of Venus at a tangent altitude of 60 km. Thus, in a given binning case, the pointing angle of one bin center is not the same as the one of the center of the whole slit, and introduces an altitude difference.

In Figure 4.6, let us consider the points (1), (2), (3) and (4), which correspond to the edges of bin 1. The axis system depicted in this Figure is linked to the Venus reference frame, and is such that the z-axis is parallel to the vertical direction, the x-axis is parallel to the limb and the y-axis is parallel to the pointing direction. We decided that the lowest point defines the tangent altitude h_{tg}.

The inclination angle γ_{slit}, depicted in Figures 4.4 and 4.6, is obtained from the relation

$$\gamma_{slit} = \text{sign}\left[\mathbf{R}_{\{VEX\}\to\{Venus\}} \cdot \left(\overrightarrow{Ven} \times \overrightarrow{Sun}\right)\right] \cdot \angle\left(-\overrightarrow{TgPt}, \mathbf{R}^{-1}_{\{VEX\}\to\{Venus\}} \cdot \overrightarrow{1_z}\right) \tag{4.3}$$

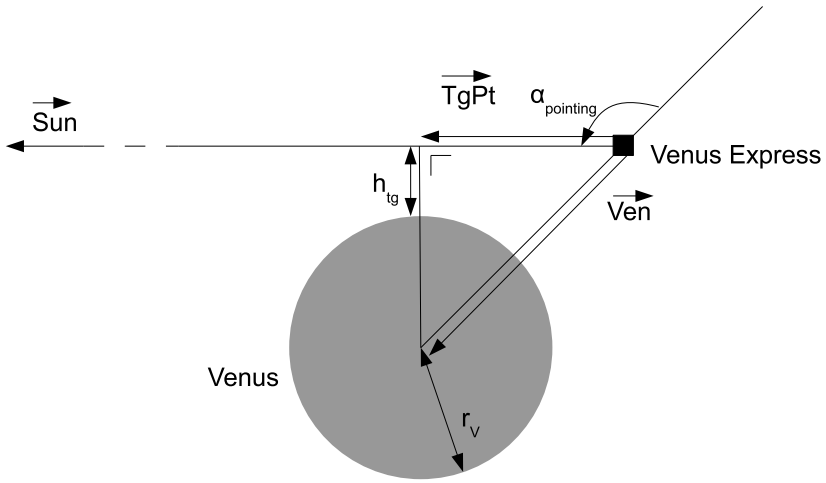

Figure 4.2: Definition of the tangent altitude. All the vectors distances and angles presented in the text are depicted on the Figure: $\overrightarrow{Ven}$ the vector between VEX and Venus, $\overrightarrow{Sun}$ the vector between VEX and the center of the Sun, $\overrightarrow{TgPt}$ the vector between VEX and the tangent point, $\alpha_{pointing}$ the SOIR pointing angle, r_V the Venus radius and h_{tg} the altitude of the tangent point.

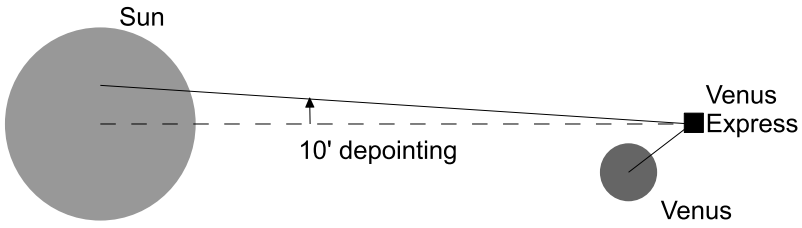

Figure 4.3: Description of the pointing direction of the instrument SOIR, by pointing 10' above the center of the Sun.

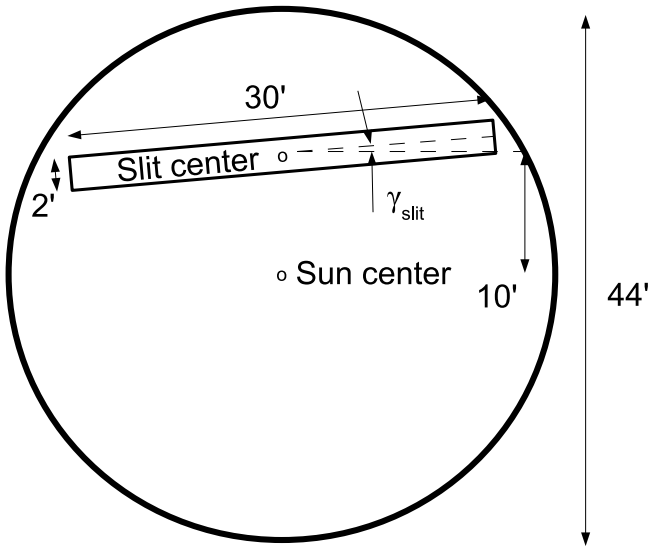

Figure 4.4: Position of the slit in the Sun disk. The slit has a size of 30' by 2', respectively in the spectral and spatial direction. The slit does not point to the Sun center, but 10' above it. It is tilted by an angle of γ_{slit}.

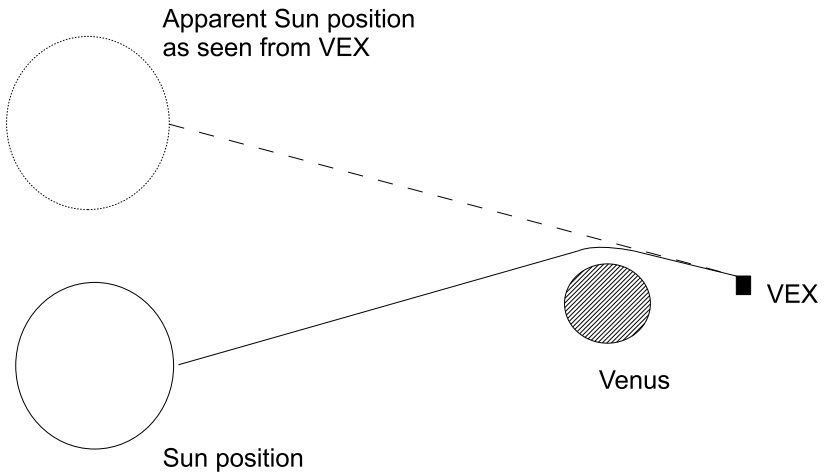

Figure 4.5: Apparent position of the Sun due to atmospheric diffraction. The plain curve shows the Sun light path considering the diffraction it undergoes when crossing the Venus atmosphere. The dashed line shows the apparent Sun light path without considering the atmospheric refraction.

where $\mathbf{R}_{\{VEX\}\to\{Venus\}}$ is the instantaneous rotation matrix from the VEX reference frame to the SOIR reference frame, $\overrightarrow{Sun}$ is the vector from VEX to the Sun in the VEX reference frame, $\overrightarrow{TgPt}$ is the vector from VEX to the tangent point in the VEX reference frame, $\overrightarrow{1_z}$ is the z-direction unit vector in the SOIR reference frame and $\angle$ represents the angle between two vectors. The expression sign $\left[\mathbf{R}_{\{VEX\}\to\{Venus\}} \cdot \left(\overrightarrow{Ven} \times \overrightarrow{Sun}\right)\right]$ gives the sign of the inclination angle, as the function calculating the angle between two vectors always returns values between 0° and 180°. The vectors $\overrightarrow{Ven}$ and $\overrightarrow{Sun}$ are both computed in the VEX reference frame.

For a given bin (1 or 2) and binning case (12 or 16) the pointing angle $\alpha^{bin}_{pointing}$ can now be computed:

$$\alpha^{bin}_{pointing} = \angle\left(\overrightarrow{Ven}, \overrightarrow{Sun}\right) + 10' + \sin(\gamma_{slit}) \cdot \frac{15}{60} \cdot \frac{1}{2} \cdot (-1)^{bin+1} \cdot \frac{binning}{16} \tag{4.4}$$

where *binning* takes the values 12 or 16 depending on the binning case considered. No sign has to be taken into account as we know that this angle has always a value between 0 and 180°.

Equation (4.2) is now written:

$$h^{bin}_{tg} = sin(180° - \alpha^{bin}_{pointing}) \cdot \left\|\overrightarrow{Ven}\right\| - r_V \tag{4.5}$$

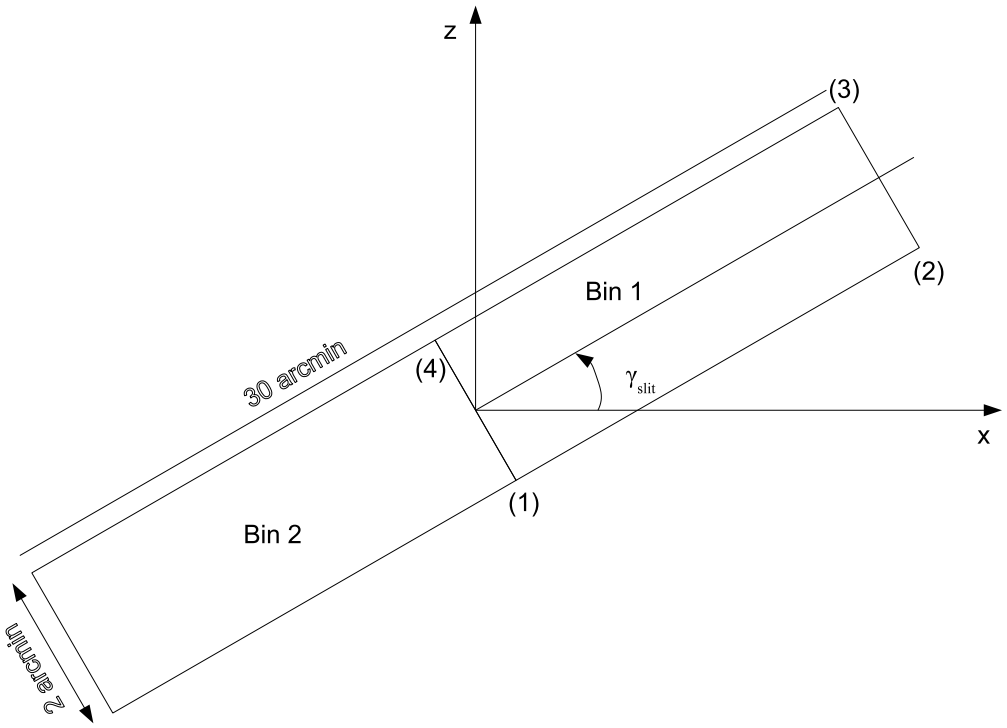

Figure 4.6: Slit inclination to the limb. The x-axis is parallel to Venus limb, the z-axis is the altitude vertical axis. The inclination angle of the slit is γ_{slit}. The points (1), (2), (3) and (4) are edges of bin 1. Point (1) determines the tangent altitude in the presented case, as it is the lowest one. The depicted binning case is 2 x 16.

4.2.2.4 Pointing error

There is a pointing error which comes from the pointing direction uncertainty, resulting from the precision of the star trackers [3] of the spacecraft.

The satellite pointing error is obtained directly from ESOC [4], the European Space Operation and Control of the European Space Agency, located in Darmstadt, Germany, which provides the pointing angle error, from which the altitude error is computed. The largest values are of the order of 500 m when the satellite is far away from the planet, and less than 50 m when the satellite is close to the planet.

4.2.2.5 Doppler effect

The velocity projection to correct for Doppler effect $v_{Doppler}$ (Sections 3.5.3.3 and 4.6) is obtained by projecting the VEX velocity vector on the SOIR optical path. To obtain it, the relative velocity of VEX to the Sun $\overrightarrow{v_{Ven}}$ is projected on the SOIR optical path direction $\overrightarrow{1_z}$:

$$v_{Doppler} = \overrightarrow{v_{Ven}} \cdot \overrightarrow{1_z} \tag{4.6}$$

4.2.2.6 Measurement coordinates and local solar time

The latitude and longitude of the tangent point are also needed. The position vector between Venus and the tangent point is used $\overrightarrow{TgPt_{\{Venus\}}}$, in the Venus reference frame. It comes:

$$\overrightarrow{TgPt} = \left(\frac{\overrightarrow{Sun}}{\left\| \overrightarrow{Sun} \right\|} \cdot \overrightarrow{Ven} \right) \cdot \frac{\overrightarrow{Sun}}{\left\| \overrightarrow{Sun} \right\|} \tag{4.7}$$

$$\overrightarrow{TgPt_{\{Venus\}}} = \overrightarrow{Ven_{\{Venus\}}} - \mathbf{R}_{\{VEX\} \rightarrow \{Venus\}} \cdot \overrightarrow{TgPt} \tag{4.8}$$

where $\overrightarrow{Ven_{\{Venus\}}}$ is the vector between VEX and Venus in the Venus reference frame. The first equation is evaluated in the VEX reference frame, while the second one is in the instantaneous Venus reference frame.

A routine transforming rectangular coordinates to latitude/longitude coordinates is used to obtain the latitude and longitude in degrees.

The local solar time is deduced by calculating the angle between the vector Venus to Sun, the longitude of the tangent point and the data of the observation.

4.2.3 Ray tracing and light refraction in the atmosphere

The ray tracing calculation allows the determination of the tangent height and of the absorption path in each layer, taking into account the refraction of the light beam into the atmosphere. The refraction model is based on the measurements performed during the Magellan mission.

The refraction is calculated as described in Vandaele *et al.* (2008). The model is based on the ray-tracing program FSCATM [5] [Gallery *et al.* (1983)]. Some modifications were included in the implementation, essentially dealing with the determination of the index of refraction of the atmosphere of the planet. Integrated total density, integrated partial density of the fitted species, mean local temperature, integrated local pressure and path length are computed for each layer (see Figure 4.1).

The model assumes a one-dimensional atmosphere, spherically homogeneous, with all parameters varying only with the vertical variable, i.e. the altitude, and also computes the atmospheric

3. A star tracker is an optical device that measures the positions of stars using photocells or a camera in order to locate the spacecraft with precision.

4. ftp://ssols01.esac.esa.int/pub/data/GDP/VEX/ATTDEV/

5. FSCATM is a Fortran program that calculates the integrated amounts, the air mass or the column density, for infrared absorbing gases for an arbitrary slant path through the atmosphere, and includes the effects of both curvature and refraction.

refraction of the light in the atmosphere. The light path is decomposed on a fine grid (50 m steps). The refraction angle is computed at the interface between all of these segments and summed up. The effective temperature, pressure, total density and volume mixing ratio (vmr) are calculated in each small layer so defined, using the Curtis-Godson approximations [6] [Goody & Yung (1995)].

The refraction starts to play a significant role when the tangent altitude reaches 70 km. Above, the air density is too small to really bend the light path.

4.3 Atmospheric equations and model

In this work, we take the temperature and pressure vertical profiles from the VIRA model [7] for altitudes up to 100 km [Seiff *et al.* (1985)]. For higher altitudes (from 140 km and upwards), data were taken from the Hedin model [Hedin *et al.* (1983)] as suggested in [Mueller-Wodarg & Tingle (2009)]. The transition between the two data sets is performed by spline interpolation of the temperature and the pressure is reconstructed through the hydrostatic law.

This model, later called a-priori, depends on the latitude, on the local solar time and on the solar flux. The local solar time is either 06:00 AM or 06:00 PM. The solar flux from the F10.7 reference at 1 AU [8] is taken as 82 W/m^2, corresponding to the mean solar activity.

Figure 4.7 presents the total density (top Panels) and the temperature (bottom Panels) values from this model. The left hand side Panels concern the morning terminator profiles, while the right hand side ones give the evening terminator profiles. The profiles are presented for four different latitudes: 20°, 40°, 60° and 75°.

In the layer j, the density n_j and the pressure p_j may be obtained considering the ideal gas law. In each layer j, we have:

$$p_j = n_j \cdot k_B \cdot T_j \tag{4.9}$$

where k_B is the Boltzmann constant ($1.381 \cdot 10^{23}$ J/K), n_j is the density in the layer j in [molec/m^3], T_j is the temperature in layer j and p_j is the pressure in layer j in [Pa]. The same holds for each molecular species, but then partial density and partial pressure are considered.

The obtained pressure $p(z)$ and density $n(z)$ profiles of each species should verify the hydrostatic equilibrium:

$$dp_{hydro}(z) = -n_{hydro}(z) \cdot MM(z) \cdot g(z) \cdot dz \tag{4.10}$$

$$g(z) = g_0 \cdot \left(\frac{r_V}{r_V + z}\right)^2 \tag{4.11}$$

$$\tag{4.12}$$

with $n_{hydro}(z)$ the hydrostatic density in [mol/m^3], z is the altitude in [m], MM is the molar mass of the considered species or group of species in [kg/m^3], g is the gravity depending on the altitude z in [m/s^2], g_0 is the gravity constant of Venus (8.87 m/s^2) and r_V is the radius of the planet Venus (6051.8 km). This equation can also be written as:

$$p_{hydro}(z) = p_0 \cdot \exp\left(-\int \frac{dz}{H(z)}\right) \tag{4.13}$$

$$H(z) = \frac{R \cdot T(z)}{MM(z) \cdot g(z)} \tag{4.14}$$

$$n_{hydro}(z) = \frac{n_0 \cdot T_0}{T(z)} \cdot \exp\left(-\int \frac{dz}{H(z)}\right) \tag{4.15}$$

6. The Curtis-Godson approximation allows to estimate the pressure, temperature and absorber amount for a uniform path when the absorption is Lorentzian, i.e. the pressure effects are neglected. The mean pressure and temperature are obtained from $\overline{p} = \frac{1}{m}\int p \cdot n \cdot dz$ and $\overline{T} = \frac{1}{m}\int T \cdot n \cdot dz$ with $m = m\int n \cdot dz$, n, T and p the absorber density, temperature and partial pressure vertical profiles and z the altitude [Irwin (2010)].

7. VIRA stands for Venus International Reference Atmosphere. Different VIRA models can be found in the literature.

8. The F10.7 index is a measure of the noise level generated by the sun at a wavelength of 10.7 cm at the Earth's orbit.

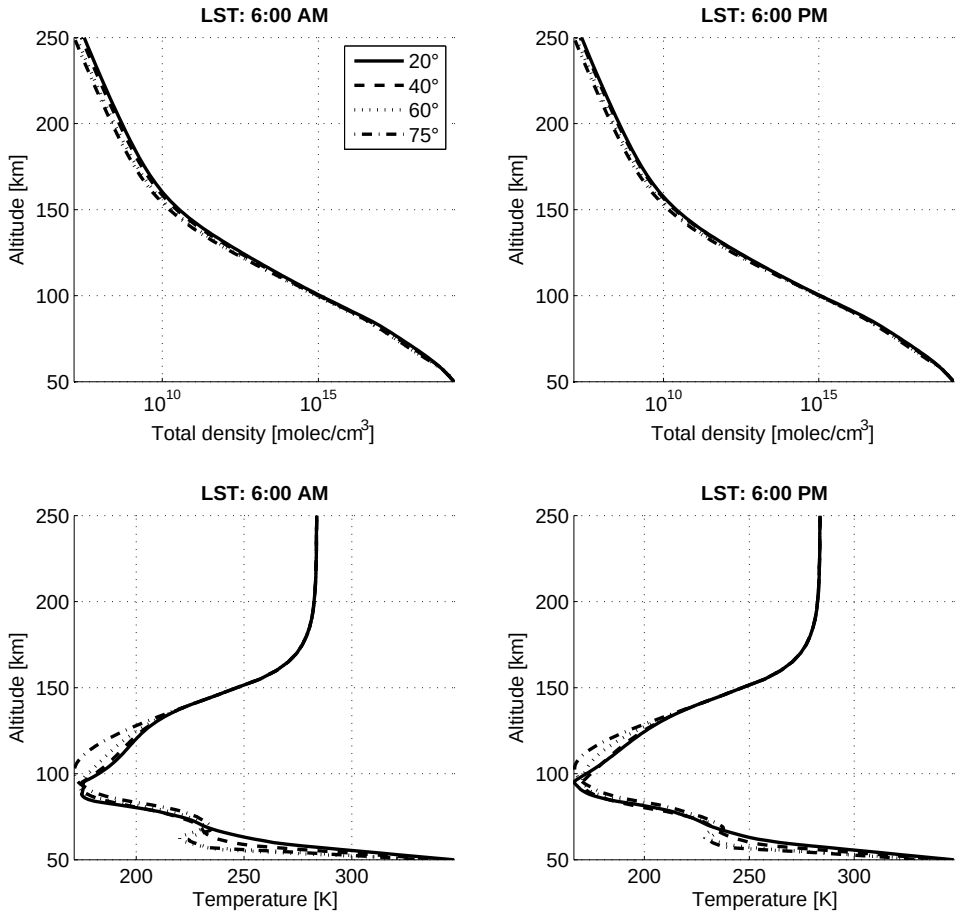

Figure 4.7: Total density (top Panels) and temperature (bottom Panels) of the atmosphere model. The latitude (at 20°, 40°, 60° and 75°) and local solar time (right Panels at 06:00 AM, left Panels at 06:00 PM) dependency is shown.

where $H(z)$ is the scale height [9]. The scale height only depends on the temperature profile. We check later in the text if the temperature profile turns in a hydrostatic density profile matching the retrieved density, see Section 5.4.3. R is the ideal gas constant (8.314 J/mol/K), and is equal to $k_B \cdot N_{Av}$, with k_B the Boltzmann constant ($1.38{\cdot}10^{-23}$ J/K) and N_{Av} the Avogadro number ($6.02{\cdot}10^{23}$ mol^{-1}).

4.4 Slit projection in the atmosphere at the tangent point: the slit height and the layer thickness

Two important characteristics of the geometry are defined here: the slit height and the layer thickness.

Slit height

To obtain the slit height, the tangent altitude of the 4 corners depicted in Figure 4.6 of a half slit is calculated. To account for the duration of a spectrum measurement, which lasts for 250 ms, the 4 corners altitudes are computed at each measurement start and end times. The slit height is obtained as the maximum altitude difference between these two times four computed tangent altitudes (four for the start measurement time, four for the end measurement time). It is proportional to the distance of the satellite to the tangent point. The slit inclination angle γ_{slit} also increases the slit height. The slit height variation with tangent altitude for occultation 341.1 (28/03/2007) is given in Figure 4.8. From this example, we see that this height remains almost constant during an occultation (variations of 80 m, or 4% of the total slit height).

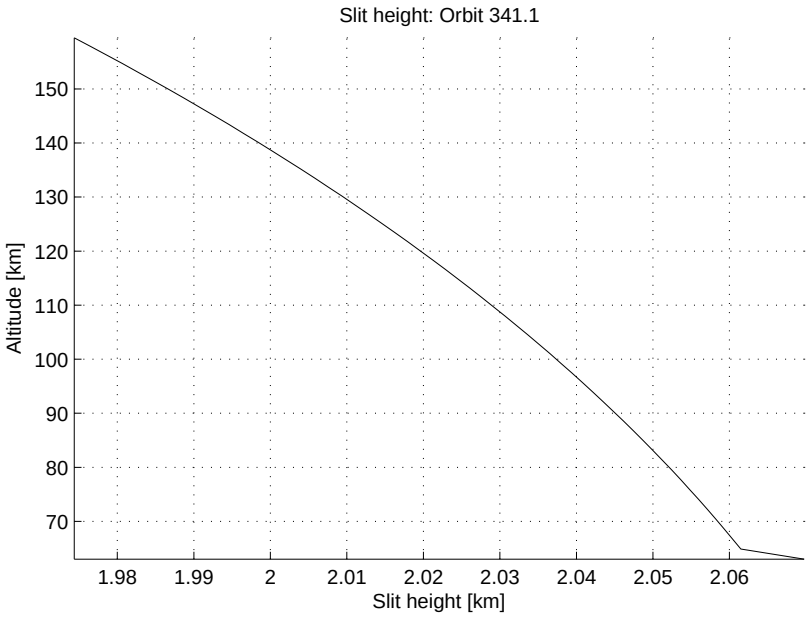

Figure 4.8: Slit height in the atmosphere at the tangent point of orbit 341.1 (28/03/2007) as a function of the altitude.

Layer thickness

The layer thickness is linked to the projection of the SOIR slit in the atmosphere at the tangent point. It is the altitude difference between two successive tangent altitudes, as it is defined in

9. The scale height is the height within which some parameter, such as pressure or density, decreases by a factor 1/e in an isothermal atmosphere. It is a measure of the effective thickness of an atmospheric layer. Definition from Taylor & al. (2000)

Section 4.2.2.3. The layer thickness is related to the velocity vector of the satellite projected in the plane perpendicular to the pointing direction. If the vertical velocity component is small, i.e. the Sun sets (or rises) slowly as seen from the satellite, the altitude difference between two layers is small, typically 500 m. On the contrary, if the vertical velocity component is high, the layers are much thicker, reaching a few kilometers.

Convolution product

Considering the layer thickness and the slit height, several configurations are observed. They are presented for 3 typical configurations corresponding to occultations for which (1) the slit height is smaller than the layer thickness (Figure 4.9), (2) the slit height equals the layer thickness (Figure 4.10) and (3) the slit height is larger than the layer thickness (Figure 4.11).

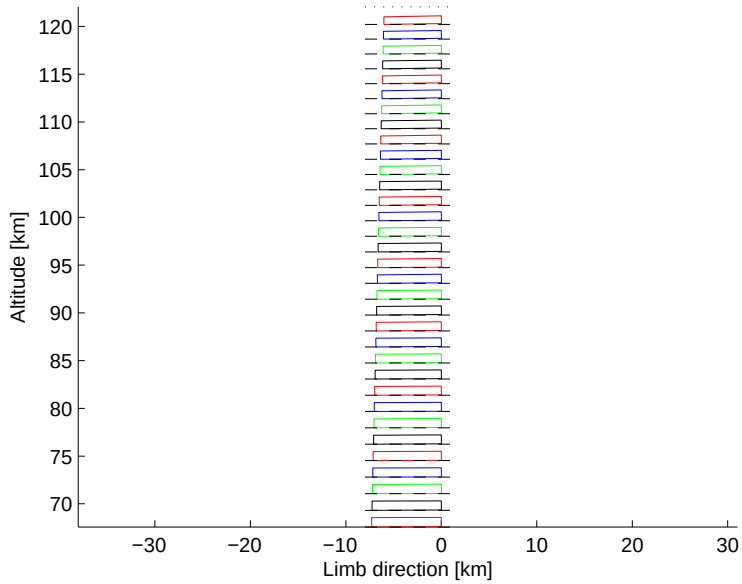

Figure 4.9: Representation of the projection of the slit in the atmosphere, with the layers definition, for orbit 247.1. The layers width are more than twice bigger than the slit height. The distance from VEX to the tangent point was 1687.75 km. At a given time, the slit projection remains entirely within the corresponding layer.

The method, based on the Beer-Lambert law (see next Section), assimilates the detector projection as a point in the atmosphere, which can only be a valid approximation if the slit height is much smaller compared to the layer thickness. This is obviously not the case for most of the measurements.

To account for this, we consider that the atmosphere is vertically scanned by the instrument. Mathematically, it corresponds to a convolution product. We define a function S_{slit} that we use to convolve the vertical profiles. It represents the surface of the slit projected on the altitude axis at each time:

$$S_{slit}(z) = \int_{z_{min}}^{z} slit(x, z) \cdot dx \tag{4.16}$$

where the x-axis and z-axis are the ones shown in Figure 4.6, z_{min} is the bin minimum altitude, and $slit(x, z)$ is the mathematical function corresponding to the slit edges projection.

The convolution function $slit(x, z)$ is a trapezoidal function, which is constructed as depicted in Figure 4.12. The surface under the curve is normalized.

The parameters that have an influence on the shape of the convolution function are:

– the distance between the tangent point and VEX: it results in a wider function for increasing VEX - tangent point distances;

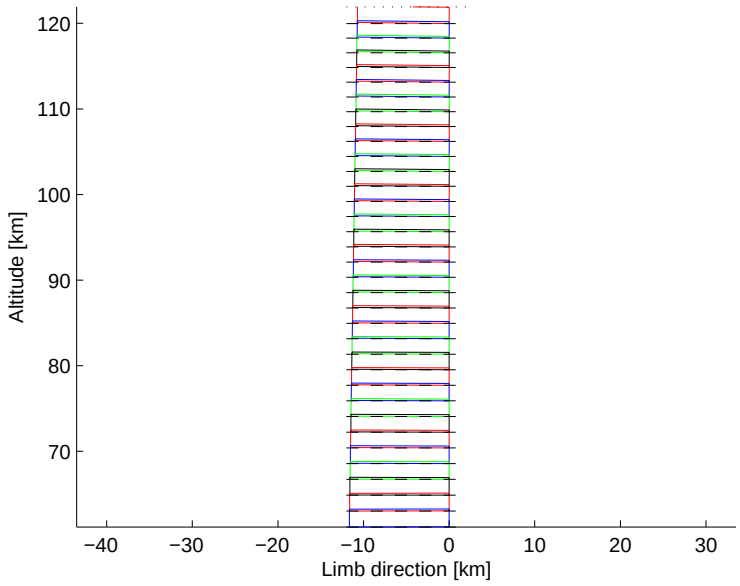

Figure 4.10: Representation of the projection of the slit in the atmosphere, with the layers definition, for orbit 341.1. The width of the layers is equal to the slit height. The distance from VEX to the tangent point was 3541.17 km. At a given time, the slit projection covers entirely the corresponding layer and a portion of the layer above.

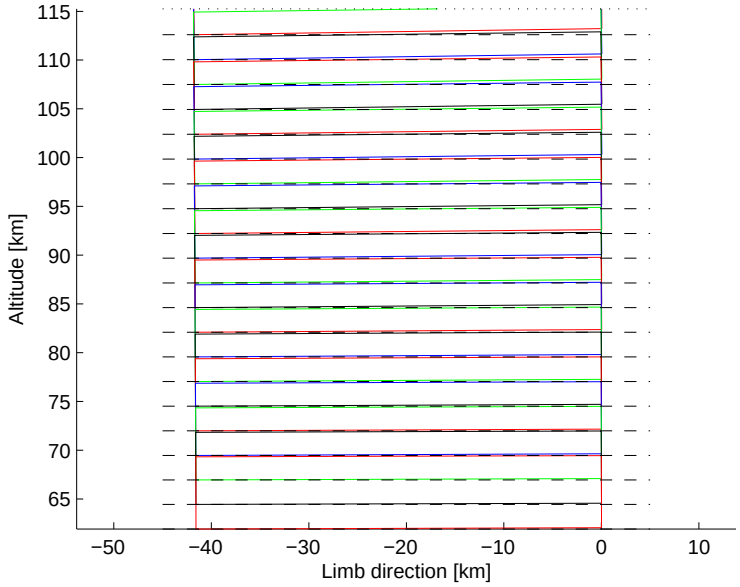

Figure 4.11: Representation of the projection of the slit in the atmosphere, with the layers definition, for orbit 334.1. The layers width are much smaller than the slit height. The distance from VEX to the tangent point was 12,709.41 km. At a given time, the slit projection covers at least three layers.

– the inclination angle: it influences the two wings of the trapeze;

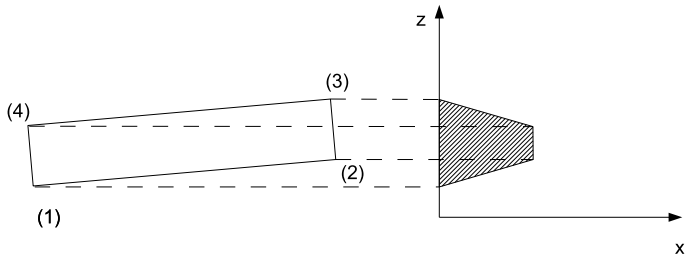

Figure 4.12: Slit function. The function has a trapezoidal shape, and it is the value of the bin surface projected along the vertical axis.

The vertical profiles become:

$$n^*(z) = n(z) \otimes S_{slit}(z) \tag{4.17}$$
$$T^*(z) = T(z) \otimes S_{slit}(z) \tag{4.18}$$
$$p^*(z) = p(z) \otimes S_{slit}(z) \tag{4.19}$$
$$\tag{4.20}$$

where $\otimes$ represents the convolution product, $n(z)$, $T(z)$ and $p(z)$ are the density, temperature and pressure vertical profiles, and $n^*(z)$, $T^*(z)$ and $p^*(z)$ are their convolved profiles. Note that from now on for a sake of simplicity in the notations, we use the $n(z)$, $T(z)$ and $p(z)$ notations, reminding that we should write $n^*(z)$, $T^*(z)$ and $p^*(z)$.

The slit functions for the 3 typical orbits 247.1, 341.1 and 334.1 are presented in Figures 4.13 to 4.15 as a function of altitude.

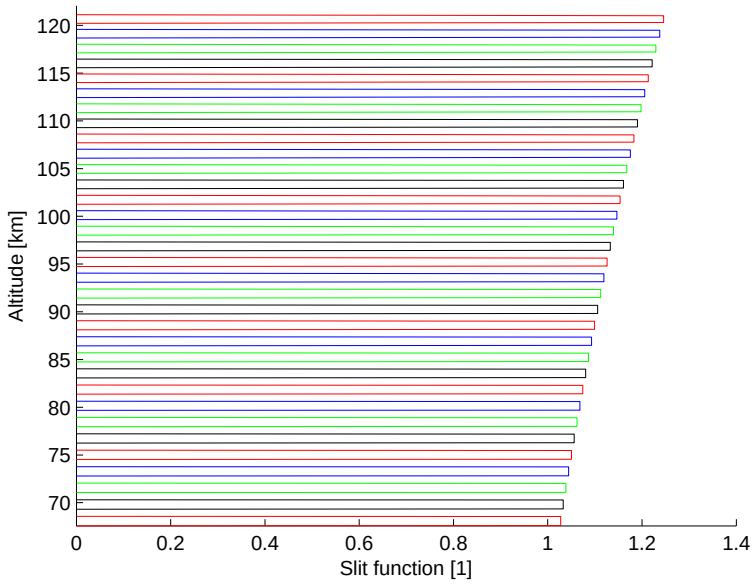

Figure 4.13: Slit function of orbit 247.1 as a function of altitude. The slit function is normalized, such that the surface under each function is 1.

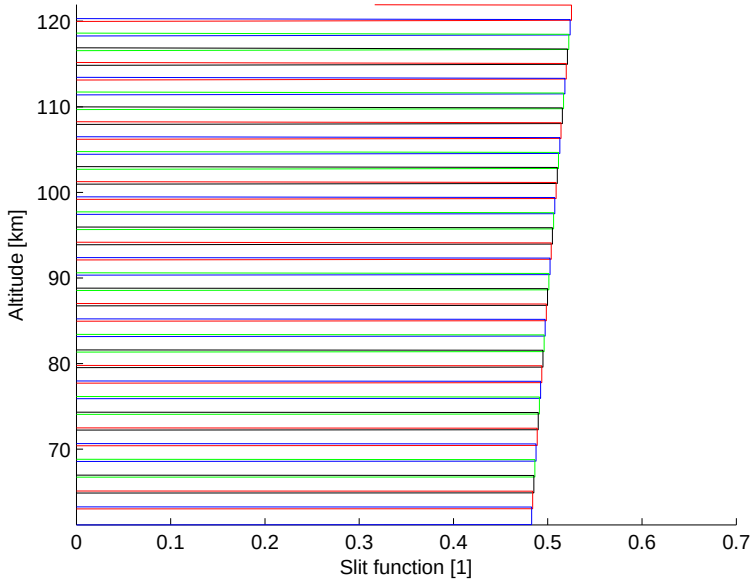

Figure 4.14: Slit function of orbit 341.1 as a function of altitude. The slit function is normalized, such that the surface under each function is 1.

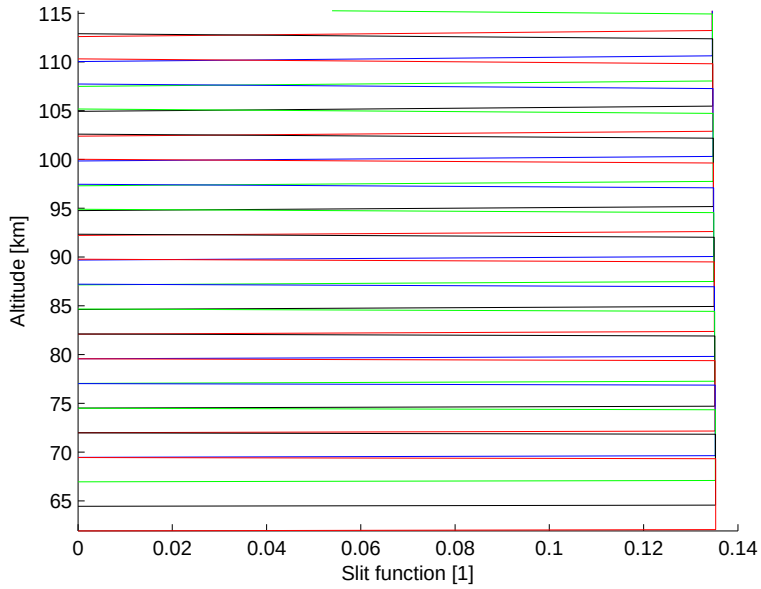

Figure 4.15: Slit function of orbit 334.1 as a function of altitude. The slit function is normalized, such that the surface under each function is 1.

4.5 Spectrum modeling

4.5.1 Absorption Cross Section and transmittance calculation

Molecular absorption cross sections (ACS) in each layer are calculated using a line by line procedure, extensively described in Vandaele *et al.* (2008), using spectroscopic parameters from the Hitran 2008 database [Rothman *et al.* (2009)] adapted for the Venusian CO_2-rich atmosphere. Here is a summary of the procedure.

$ACS(\tilde{\nu}, z)$ is in general the sum of several contributions: the single absorption lines of different gaseous species, the continuum contribution, and the Rayleigh scattering term. We consider here only the first term. The continua and the Rayleigh contribution are both modeled by a unique polynomial, and grouped under the name aerosols absorption.

The ACS depends on the partial and total pressures, as well as the temperature in each layer. The Voigt profile is used to model the line shape from Hui *et al.* (1978).

The line intensity of each single line is read in the database, and corrected for the Venus local atmospheric pressure and temperature conditions. Indeed, in the Hitran database, all the parameters are calculated for Earth conditions, which are a temperature of 296 K and a pressure of 101,320 Pa. The lines are broadened by several effects, and their intensities are a function of the temperature [Bandwell & McCash (1994)]. The relations applied are summarized in Appendix H.

The ACS are precalculated and placed in lookup tables for all isotopologues at different pressure and temperature conditions, by steps of 1 K between 70 and 350 K for the temperature, and by logarithmic steps of a factor 10 between 10^{-4} and 100 mbar for the pressure. Indeed, the effect of temperature is large on the ACS, while the pressure effects are quite low. A pressure change induces a pressure broadening effect, and a slight pressure shift. The pressure broadening effect is not measured by the SOIR instrument, as the width of the atmospheric lines is much lower than the resolution of the instrument by a factor [10] 100 to 10, and does not change the measured intensity of the line. The pressure shift is very small, and is around 10^{-5} cm^{-1} [Rothman *et al.* (2009)]. It is not measured by SOIR either, as the wavenumber precision is equal to the spectral sampling interval (see Section 3.5.3.4).

4.5.2 Transmittance calculation

The transmittance $\mathrm{Tr}_{i,j}$ due to the molecule i in the layer j is calculated using the Beer-Lambert law:

$$\mathrm{Tr}_{i,j} = \exp\left[-n_{i,j} \cdot s_j \cdot ACS\left(n_{i,j}, T_j, p_j\right)\right] \tag{4.21}$$

where $n_{i,j}$ is the density of the molecule i in the layer j, s_j is the path length within the layer j, T_j and p_j are the temperature and the pressure in the layer j and ACS is the absorption cross sections profile of the molecular species. The product $\tau_{i,j} = -n_{i,j} \cdot s_j \cdot ACS\left(n_{i,j}, T_j, p_j\right)$ is called optical depth (OD). The way how n_j, s_j, T_j and p_j are calculated from the ray tracing algorithm was described in Section 4.2.3.

The transmittance $\mathrm{Tr}_{L,Molecular}$ due to the molecular species present along the whole path corresponding to the tangent height L is finally obtained by multiplying the absorbance of all molecules in all the above layers, the most outside layer being layer 1:

$$\mathrm{Tr}_{L,molecular} = \prod_{j=1}^{L} \prod_{i=1}^{n_{molecules}} \mathrm{Tr}_{i,j} \tag{4.22}$$

Aerosols, which are present in the Venus mesosphere up to 90 km [Esposito (1983); Lane & Opstbaum (1983)], also have a characteristic signature. In the infrared region probed by SOIR their signature is rather broad and does not present any fine structures [Wilquet *et al.* (2009)].

10. The synthetic spectrum has a FWHM of about 0.001 cm^{-1} to 0.01 cm^{-1}, while the resolution of SOIR is about 0.15 cm^{-1}.

Their influence on the observed spectra is to decrease the mean transmittance level. This effect is more pronounced as the line of sight goes deeper into the atmosphere.

The impact of aerosols is considered in this work by representing their contribution to the transmission by a second degree polynomial on the wavenumber. For layer L, the aerosol contribution to the transmission can be written as:

$$\mathrm{Tr}_{L,aerosols} = a_L + (\tilde{\nu} - \tilde{\nu}_0) \cdot b_L + (\tilde{\nu} - \tilde{\nu}_0)^2 \cdot c_L \tag{4.23}$$

where a_L, b_L and c_L are the polynomial coefficients, $\tilde{\nu}$ is the wavenumber, $\tilde{\nu}_0$ is the central wavenumber of the scanned order.

The aerosol extinction is calculated from this polynomial approximation using the relation from Bingen *et al.* (2003):

$$\begin{aligned} \beta_N = \quad & -\Bigg(log\left[a_L + (\tilde{\nu} - \tilde{\nu}_0) \cdot b_L + (\tilde{\nu} - \tilde{\nu}_0)^2 \cdot c_L\right] \\ & \qquad + \sum_{j=1}^{N-1} dz_j \cdot \beta_j(\tilde{\nu}, z) \Bigg) / dz_N \end{aligned} \tag{4.24}$$

$$\begin{aligned} dz_j = \quad & 2 \cdot \Bigg[\sqrt{(r_V + z_j)^2 - (r_V + z_{j+2})^2} \\ & - \sqrt{(r_V + z_{j+1})^2 - (r_V + z_{j+2})^2} \Bigg] \end{aligned} \tag{4.25}$$

where N is the layer for which the extinction is calculated, β_j is the extinction of layer j, dz_j is the thickness of layer j, r_V is the radius of Venus and z_j is the altitude of the bottom of layer j.

Although these parameters are calculated during the retrieval procedure, they are not discussed in this text. These results can be found in Wilquet *et al.* (2008, 2011).

Finally, the spectrum I_L, which is compared to the one recorded by the instrument, is the solar spectrum attenuated by the effect of the atmospheric molecular species and aerosols, convolved by the instrumental function (Section 3.5.3.4):

$$I_L = \underbrace{(I_S \cdot \mathrm{Tr}_{L,aerosols} \cdot \mathrm{Tr}_{L,molecular})}_{\text{Synthetic spectrum}} \otimes \underbrace{Gauss(\sigma_{SOIR})}_{\text{Instrument function}} \tag{4.26}$$

with I_S the Sun absorption cross section and $Gauss(\sigma_{SOIR})$ is the instrumental function with a FWHM equal to the spectral resolution function of SOIR.

4.5.3 Order addition

The bandwidth of SOIR's AOTF, used for the diffraction order selection, is larger than the free spectral range of the echelle grating; to correctly simulate the spectra measured by the spectrometer, the contribution of the adjacent orders also has to be taken into account (Section 3.5.4.1). Usually, the three first adjacent orders and the central order are considered to form most of the observed transmittance. In some cases, however, when very strong lines are present in adjacent orders located further away from the central order, it may be necessary to consider a larger number of adjacent orders. This situation has to be evaluated from to case. However it is of common agreement not to consider more than 3 adjacent orders, as the AOTF transfer function is not known further away from the central order, see Section 3.5.4.4.

The contribution from the adjacent orders is calculated using:

$$\mathrm{Tr}_L = \frac{\sum_{p=-n_{orders}}^{n_{orders}} AOTF_p \cdot I_L}{\sum_{p=-n_{orders}}^{n_{orders}} AOTF_p \cdot I_{Sun}} \tag{4.27}$$

where Tr_L is the synthetic transmittance of layer L, n_{orders} is the number of adjacent orders considered, $AOTF_p$ is the values of the AOTF transfer function in the order p and I_L is the convoluted absorbance of the molecules and aerosols absorbing in order p [Mahieux *et al.* (2010)], containing the contribution of all the layers located above it.

The whole procedure for constructing a spectrum is shown in Figure 4.16. In this Figure, Panel A shows the spectrum at infinite resolution of CO_2 in diffraction order 149 and its 3 lower and higher closer diffraction orders (146 to 152). In Panel B, the spectrum is convolved by the SOIR ILP, and the AOTF transfer function is presented. Panel C shows the product of these two curves, and Panel D shows the contribution of each diffraction order taken individually, and reported to the central order 149. Panel E is the final synthetic spectrum, resulting of the sum of the 7 orders contribution, and divided by the solar spectrum which underwent the same procedure (not shown here).

4.6 Retrieval algorithm

4.6.1 Implementation of the optimal estimation method

4.6.1.1 The iterative procedure

The problem

The model of the transmittance in a given layer L is given by:

$$\mathrm{Tr}_L = \frac{1}{\sum_{p=-n_{orders}}^{n_{orders}} BF \cdot AOTF_p \cdot [I_S \otimes Gauss(\sigma_{SOIR})]} \cdot \sum_{p=-n_{orders}}^{n_{orders}} BF \cdot AOTF_p \cdot \left[\left(I_S \cdot \mathrm{Tr}_{L,aero} \cdot \prod_{j=1}^{L} \prod_{i=1}^{n_{molec}} \exp\left[-n_{i,j} \cdot s_j \cdot ACS_{i,j}\right] \right) \otimes Gauss(\sigma_{SOIR}) \right] \tag{4.28}$$

$$\mathrm{Tr}_{L,aero} = a_L + (\tilde{\nu}'_j - \tilde{\nu}_0) \cdot b_L + (\tilde{\nu}'_j - \tilde{\nu}_0)^2 \cdot c_L \tag{4.29}$$

$$ACS_{i,j} = ACS_{i,j}(n_{i,j}, T_j, \tilde{\nu}'_j) \tag{4.30}$$

$$\tilde{\nu}'_j = \tilde{\nu} + d_j \tag{4.31}$$

where Tr_L is the transmittance at the layer L, $AOTF_p$ is the modified AOTF transfer function, adapted on the n_{AOTF} points and translated of a value d_{AOTF}, BF is the blaze function (defined in Section 3.5.2.1), d_j is the wavenumber shift of layer j, $\tilde{\nu}$ is the wavenumber and σ_{SOIR} is the resolution of the instrument.

In the following sections, the indices referring to the considered layer number L will be ignored for the sake of simplicity.

Let us consider the retrieval of the vertical profiles of n_{molec} from a series of $n_{spectra}$ transmittances acquired during one occultation. The $n_{spectra}$ spectra have defined a structured atmosphere composed of $m_{layer} = n_{spectra}$ layers (see Figure 4.1), whose boundaries correspond to the tangent heights of each measurement. The state vector contains all the variables fitted during the retrieval procedure. These variables are the a, b and c parameters of the aerosol contribution (3 x m_{layer} variables), and the logarithm of the molecular densities of the targeted species in all the defined layers ($n_{molec} \times m_{layer}$ variables). The logarithm of the density is used for three reasons:

1. We know, from the hydrostatic equilibrium (Eq. (4.10) and (4.11)), that the density varies exponentially with altitude;
2. The use of the logarithm forbids to have negative densities, as for a given x, $\log(x) > 0$;
3. The matrices expressions used in the algorithm described here are better conditioned.

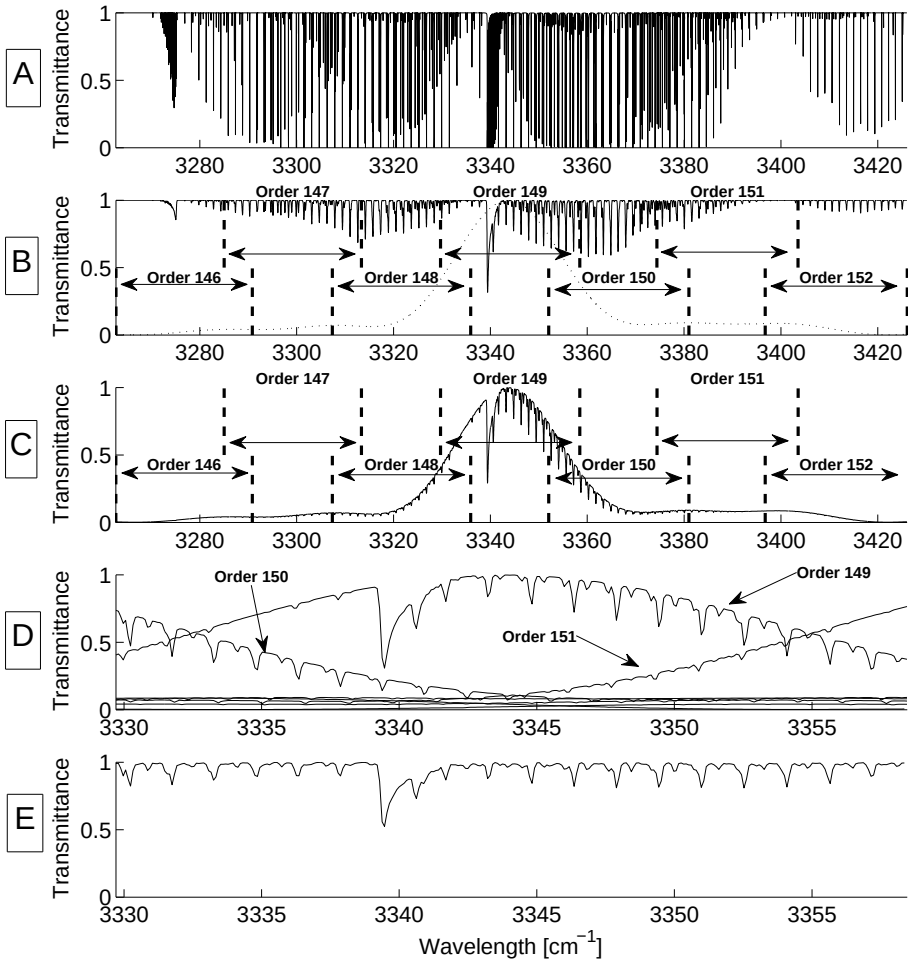

Figure 4.16: Procedure to simulate a SOIR spectrum. Panel A shows the absorption cross section of CO_2 around 3340 cm^{-1}. It is calculated for one layer with atmospheric conditions at 90 km (p = $3{\cdot}10^{-1}$ bar, T = 180 K and a path length of 100 km). Panel B shows the transmittance Tr of these lines, after using the Beer-Lambert law and convolution by the ILP. Panel C is the transmittance Tr after convolution by the instrument function and multiplication by the AOTF transfer function. The different diffraction orders are also indicated. The order overlap is clearly seen. Panel D shows the contribution of the different orders. One can see that the contribution of the adjacent order cannot be neglected. Panel E is the sum of these orders contributions divided by the Sun spectrum measured outside the atmosphere which underwent the same procedure.

The temperature in each layer may also be fitted (m_{layer} variables). Even if the line intensities of all molecules are temperature dependent, the temperature is only fitted for molecules having regularly spaced absorption lines within each branch and absorption lines close to each others, like CO or CO_2.

Moreover a wavenumber shift can be introduced and fitted for each spectrum (m_{layer} variables) to improve the matching of the absorption lines positions from the spectroscopic database and the observed position.

The AOTF transfer function may be fitted too:

- first, a slight variation in transmittance is allowed on several points, usually around 40, to improve the quality of the fit (n_{AOTF} variables);
- second, the AOTF transfer function may also be translated along the wavenumber axis, to correct for possible deviations of the wavenumber - AOTF frequency relation (Section 3.5.4.2) (1 variable).

The method

In order to fit Tr_L to the measured spectra, the Optimal Estimation method (OEM) developed by Rodgers [Rodgers (1990, 2000)] is implemented to invert the observed transmittances. All transmittances are inverted in one go. Some of the basic formula are given below.

In the OEM, the retrieved best estimate $\widehat{x}$ can be seen as a combination of an a-priori estimate of the atmospheric state x_a and the true atmospheric state x:

$$\widehat{x} = x_a + A \cdot (x - x_a) \tag{4.32}$$

where A is the averaging kernel matrix, representing the sensitivity of the retrieved state to the true state

$$A = \frac{\partial \widehat{x}}{\partial x} \tag{4.33}$$

The measurement vector y, which contains the measured spectra, is related to the underlying true atmospheric state by a nonlinear forward model F which contains the a-priori model parameters b and the random spectral measurement noise ϵ

$$y = F(x, b) + \epsilon \tag{4.34}$$

In order to determine the optimal solution to Eq. (4.32) using Newtonian iteration, the forward model must be linearized around a reference state. In this case, the best estimate state is used. From this, a weighting function matrix K is derived. It is the Jacobian matrix of the forward model F to the variables x, $\frac{\partial F}{\partial x}$. Computationally, the averaging kernel matrix A is determined from this weighting function matrix K, the a-priori covariance matrix S_a, and the measurement error matrix S_ϵ:

$$A = \left(S_a^{-1} + K' \cdot S_\epsilon^{-1} \cdot \ K\right) \cdot \ K' \cdot S_\epsilon \cdot \ K \tag{4.35}$$

From this, the iterative equation can be written as:

$$\begin{aligned} x_{k+1} = \quad & x_k + \left(S_a^{-1} + \ K_k^T \cdot S_\epsilon^{-1} \ K_k\right)^{-1} \cdot \\ & \left[\ K_k^T \cdot S_\epsilon^{-1} \cdot (y - F(x_k)) - S_a^{-1} \cdot (x_k - x_a)\right] \end{aligned} \tag{4.36}$$

where x_k are the state vector values at iteration k, S_a is the covariance matrix of the fitted parameters x, S_ϵ is the measurement error matrix, K_k is the Jacobian of the problem at iteration k, y contains the measured spectra, F represents the forward model and x_a is the a-priori state vector. The superscript ^{T} denotes the transposition of a matrix.

From Equation (4.36), it is observed that the a-priori vector x_a influences the solution x along the retrieval procedure, damped by the covariance matrix S_a. The influence of the S_a matrix and of the a-priori vector x_a on the quality and confidence put in the results will be further investigated in Section 4.8.

4.6.1.2 OEM matrices and vectors

Covariance matrix

The covariance matrix S_a contains the allowed variability of each variable:

$$S_a = \epsilon \left\{ (x - x_a) \cdot (x - x_a)^T \right\} \tag{4.37}$$

where x_a is the a-priori state vector and x is the solution of the problem.

The covariance values are constant for the a, b, c, n, T, d, e, f, n_{AOTF} and d_{AOTF}.

Non diagonal terms are added for the covariance of the AOTF transfer function variations. A Gaussian dependence is used to account for correlations between the different points where the AOTF transfer function is fitted and to ensure a final smooth AOTF transfer function. They are defined as:

$$S_a^{\omega}(k, k') = \sqrt{S_a^{\omega}(k, k) \cdot S_a^{\omega}(k', k')} \cdot \exp\left[- \left(\frac{\tilde{\nu}_k - \tilde{\nu}_{k'}}{l_c} \right)^2 \right] \tag{4.38}$$

where S_a^{ω} is the submatrix of S_a corresponding to the AOTF transfer function fit, $\tilde{\nu}_k$ and $\tilde{\nu}_{k'}$ are the wavenumber positions of points k and k', l_c is the correlation length [Vandaele *et al.* (2008)]. The correlation length is chosen arbitrarily to be a fifth of the diffraction order width for the AOTF transfer function.

In the case of the densities, temperature and wavenumber shift variables the user has the choice between two options. Either only diagonal terms are considered, and thus the correlation existing within a vertical profile is expressed through the Jacobian. Indeed, for the solar occultation case, the derivation of the Jacobian matrix is based on the fact that each layer's parameters only depend on the characteristics of the layers located above it. A variation in a given layer only influences the layers located below it. This is the default option. The other option is to use an adaptation of the same formalism as expressed in Equation (4.38), in order to increase the vertical dependence of the variables. Equation (4.38) becomes

$$S_a^{n,T,d}(k, l) = \sqrt{S_a^{n,T,d}(k, k) \cdot S_a^{n,T,d}(l, l)} \cdot \exp\left[- \left(\frac{z_k - z_l}{\overline{\Delta z}} \right)^2 \right] \tag{4.39}$$

where $S_a^{n,T,d}$ is the submatrix of S_a corresponding to the densities, temperature or displacement, z_k and z_l are the altitude of layers k and l respectively, and $\overline{\Delta z}$ is the mean layer thickness. But an increased instability of the algorithm is observed using this option.

S_a is a square matrix of size $(6 + (n_{molec} + 2) \cdot m_{layer} + n_{AOTF})$.

Measurement error matrix

The measurement error matrix S_ϵ contains the errors obtained from the signal to noise ratio.

S_ϵ is not square and has a size of $n_{\tilde{\nu}} \times m_{layer}$, where $n_{\tilde{\nu}}$ is the number of wavenumber points in each interval used for the fit.

Jacobian matrix

The Jacobian matrix K contains the first derivatives of the forward model with relation to all the state vector variables.

The derivatives

$$\frac{\partial \mathrm{Tr}}{\partial a_L}, \frac{\partial \mathrm{Tr}}{\partial b_L}, \frac{\partial \mathrm{Tr}}{\partial c_L}, \frac{\partial \mathrm{Tr}}{\partial n_{i,j}}, \frac{\partial \mathrm{Tr}}{\partial T_j}, \frac{\partial \mathrm{Tr}}{\partial d_j}, \frac{\partial \mathrm{Tr}}{\partial n_{AOTF}}, \frac{\partial \mathrm{Tr}}{\partial d_{AOTF}} \tag{4.40}$$

are easily computed. The four first ones are derived analytically, and the four last ones are calculated numerically.

The sub matrices of K, $\frac{\partial \mathrm{Tr}}{\partial n_{i,j}}$, $\frac{\partial \mathrm{Tr}}{\partial T_j}$ and $\frac{\partial \mathrm{Tr}}{\partial d_j}$ are inferior triangular matrices because of the onion peeling procedure. Indeed, the densities, temperatures and wavenumber displacements in layer j

only depend on the respective values obtained in the layer located above it. This is expressed in Equation (4.28).

$\frac{\partial \mathrm{Tr}}{\partial d_{AOTF}}$ is a vector, as $\frac{\partial \mathrm{Tr}}{\partial a_L}$, $\frac{\partial \mathrm{Tr}}{\partial b_L}$, $\frac{\partial \mathrm{Tr}}{\partial c_L}$ which have non-zero values only for a given layer.

$\frac{\partial \mathrm{Tr}}{\partial n_{AOTF}}$ is a full matrix.

K has a size of $[(6 + (n_{molec} + 2) \cdot m_{layer} + n_{AOTF})] \times [n_{\tilde{\nu}} \cdot m_{layers}]$.

State vectors and forward model vector

The vectors x_k, x_a, $F(x_i)$ and y contain respectively the state vector variables at step k, the a-priori values of the variables x_k, the calculated synthetic transmittance at step k and the $n_{spectra}$ observed spectra. x_k, x_a have a length of $[(6 + (n_{molec} + 2) \cdot m_{layer} + n_{AOTF})]$, while $F(x_i)$ and y have a length of $[n_{\tilde{\nu}} \cdot m_{layers}]$.

4.6.1.3 The retrievals errors and covariance matrices

Retrieval error calculation

The error calculation is done using the relations:

$$\widehat{x} - x = (A - I_n) \cdot (x - x_a) + G \cdot \epsilon \tag{4.41}$$

$$G = \left[(S_a^{-1} + K^T \cdot S_\epsilon^{-1} \cdot K) \cdot K^T \cdot S_\epsilon^{-1}\right]^{-1} \tag{4.42}$$

$$A = G \cdot K \tag{4.43}$$

where $\widehat{x} - x$ is the error vector, x is the solution at convergence and $\widehat{x}$ is the exact solution, I_n is a unity matrix having the same size as A and ϵ is the error vector used to build S_ϵ.

Covariance error calculation

The covariance of the error vector is built by considering two sources, namely the a-priori covariance S_s and the retrieval noise covariance S_m:

$$S_s = (S_a^{-1} + K^T \cdot S_\epsilon^{-1} \cdot K)^{-1} \cdot S_a^{-1} \cdot (S_a^{-1} + K^T \cdot S_\epsilon^{-1} \cdot K)^{-1} \tag{4.44}$$

$$S_m = (S_a^{-1} + K^T \cdot S_\epsilon^{-1} \cdot K)^{-1} \cdot K^T \cdot S_\epsilon^{-1} \cdot K \cdot (S_a^{-1} + K^T \cdot S_\epsilon^{-1} \cdot K)^{-1} \tag{4.45}$$

4.6.1.4 Degrees of freedom and averaging kernels

The degrees of freedom (DOF) represent the number of independent variables of a given OE run. It is an important characteristics as it indicates if the problem is well presented or not. For example, let us say that in a given orbit, a run is made on m_{layer} layers. To ensure a good convergence and a reliable solution, the DOF of the a, b, c, n_j, T, d sets of variables should equal m_{layer}, e, f and d_{AOTF} should equal 1 and n_{AOTF} should equal the number of points on which the AOTF function is fitted. However, we will see that it is not always the case for most of the parameters.

The DOF are obtained by calculating the trace of the submatrices of A concerning the variables cited here above. Indeed, this trace is also equal to the sum of the eigen values. The eigen values of the matrices are equal to the DOF of each set of variable. Their corresponding eigen vectors are named averaging kernels. However, because the eigen values computation time is often very expensive, the vectors corresponding to the variable line or column in the symmetric A matrix is often used as an approximation of the eigen vector. The averaging kernels (AK) teaches what is the influence of a given variable on the other ones.

4.6.1.5 Convergence criteria

The convergence of the OEM algorithm is assumed when the two following criteria are satisfied:

$$\|x_k - x_{k+1}\|^T \cdot \left[\left(S_a^{-1} + K_k^T \cdot S_\epsilon^{-1}\right) \cdot K_k\right]^{-1} \cdot \|x_k - x_{k+1}\| < \quad 10^{-2} \cdot DOF \tag{4.46}$$

$$\|F(x_k) - F(x_{k+1})\| \cdot \left[S_\epsilon \cdot (K_k \cdot S_a \cdot K_k^T + S_\epsilon)^{-1} \cdot S_\epsilon\right]^{-1} \cdot \|F(x_k) - F(x_{k+1})\| < \quad 10^{-2} \cdot n_{\tilde{\nu}} \cdot n_{spectra} \tag{4.47}$$

with n_{pixels} the number of pixels on a spectrum considered during the retrieval procedure.

4.6.1.6 Fitting procedure

For a given occultation and a given diffraction order, the spectroscopic parameters of the different species to retrieve must be supplied, as well as the wavenumber range on which they are fitted. More than one isotopologue for each species may be fitted simultaneously. The altitude range is automatically determined, but may also be imposed by the user (see Section 4.6.2 for description of the procedure).

The algorithm returns the fitted values of all the parameters defined earlier. The user has the choice to use the a-priori atmospheric parameters derived from the atmosphere model, or to use the ones derived from another fitting procedure, for example in the case of a non-CO_2 retrieval, a quasi simultaneous CO_2 inversion.

4.6.2 Predetermination of the optimal altitude range

We developed an automatic procedure to determine the optimal altitude range of a given retrieval. Usually, atmospheric spectra are recorded at tangent altitudes starting around 220 km and down to 60 km. However, the spectra corresponding to the higher altitudes usually do not contain any molecular absorption features, but provide a good indication of the noise level of the measurements. Spectra corresponding to the lowest altitudes are often saturated as detailed in the next sections. We consider here an ensemble of recorded spectra in a given order where a molecular species absorbs.

The first spectrum considered for the retrieval corresponds to the emergence of the monitored absorption structures. Only the wavenumber range on which the retrieval is performed is considered. The maximum (I_{max}), minimum (I_{min}) and mean (I_{mean}) values of the transmittance are computed on this window for each atmospheric spectrum. The depth of the strongest observed line (I_{diff}) is computed by subtracting the minimum value from the maximum value ($I_{max} - I_{min}$). At high altitudes, usually above 180 km, before the emergence of the absorption features, only noise is measured, and I_{diff} provides a majoring value for it. A signal to noise value ($\overline{SNR_{180-200}}$) representative of these high altitudes is calculated by considering the average values of the signal and the noise between 220 km and 180 km, $\overline{I_{mean}}$ and $\overline{I_{diff}}$,

$$SNR_{180-200} = \frac{\overline{I_{mean}}}{\overline{I_{diff}}} \tag{4.48}$$

The first spectrum to consider for the retrieval procedure corresponds to the altitude when the absorption structures are seen above the noise. From trials, a factor of 0.002 is introduced, thus the first spectrum is defined for

$$\frac{\overline{I_{mean}}}{\overline{I_{diff}}} < 0.002 \cdot SNR_{180-200} \tag{4.49}$$

From this altitude on, spectral structures are seen in the spectra.

The lower bound of the altitude range is defined when saturation occurs. The atmospheric absorption lines have transmittances reaching zero values, before convolution by the instrument

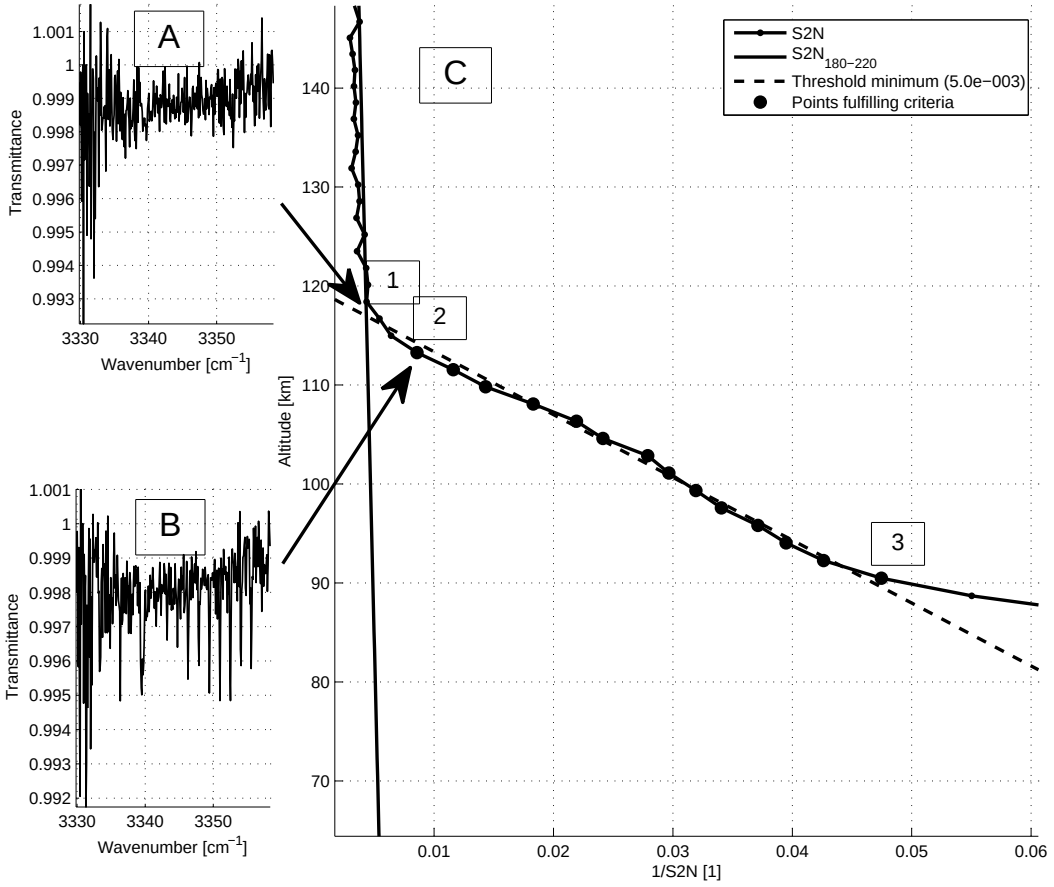

Figure 4.17: Determination of the altitude range. The altitude range is determined by studying the quotient $\frac{I_{mean}}{I_{diff}}$, with I_{mean} being the mean value of the spectrum on the interval fitted, and I_{diff} being the maximum less the minimum value on the interval. The Figure presented on Panel C depicts its variation as a function of altitude. At high altitude, above point 1 - see spectrum in Panel A, $\frac{I_{mean}}{I_{diff}}$ is an upper value of the noise level. When the absorption structures start appearing in the spectra, at point 2 - see spectrum in Panel B, an inflection point is observed in the curve. It is observed that the second inflection point - point 3 - corresponds to the altitude when the absorption lines are completely saturated.

resolution function. From this altitude, the information contained in the spectra become useless, and a reliable retrieval can not be made anymore. This will be detailed in the next Section.

The criteria used for the selection of the first and last spectra are clearly demonstrated when plotting the quantity $\frac{I_{mean}}{I_{diff}}$ as a function of the altitude, as illustrated in Figure 4.17. The slope radically changes at two well defined altitudes. Values of $\frac{I_{mean}}{I_{diff}}$ are almost constant above the altitude of point 2 on Panel C corresponding to the appearance of the absorption features as illustrated by the Panels A and B, corresponding respectively to one spectrum without absorption structures and one with them. The altitude of the last spectrum to be included in the retrieval, point 3 on Panel C, is obtained at the second change in slope. Below this altitude, most of the absorption lines are saturated − at infinite resolution − and the surface under the structures seen in the convolved spectrum recorded by the instrument are no longer proportional to the density of the absorbing species.

4.6.3 Saturation criterium

Saturation may be observed if the transmittance of a spectral line reaches values close to zero. In that case, all the information contained in the observed spectral line is lost, as the shape of the line does not vary with increasing densities. It is not directly observed in the spectra measured by SOIR, as the resolution of the instrument is much larger than the width of the observed spectral lines. This is explained in Figure 4.18. Detection procedures of such events are developed, to avoid meaningless density profiles.

All absorption lines having a transmittance lower than 0.15 before convolution by the ILP are considered as saturated. The transmittance before convolution and order addition $\widetilde{\mathrm{Tr}_L}(\tilde{\nu})$ is defined as:

$$\widetilde{\mathrm{Tr}_L}(\tilde{\nu}) = \prod_{j=1}^{L} \prod_{i=1}^{n_{molec}} \exp\left[-n_{i,j} \cdot s_j \cdot ACS_j\left(n_{i,j}, T_j, \tilde{\nu}_i\right)\right] \tag{4.50}$$

If saturation occurs, two actions are taken:

- all the points $\tilde{\nu}^*$ for which we have $\widetilde{\mathrm{Tr}_L}(\tilde{\nu}) < 0.15$ are removed from the fitted wavenumber range;
- the spectrum of layer j^* at iteration k of the Rodgers algorithm is said to be saturated if more than 40 percent of the absorption lines coming from the central order are saturated, or 40 percent of the detector is covered by saturated lines. In that case, the altitude range is modified to suit the saturation criterion: all the layers j located under and including the current layer are excluded from the retrieval, i.e. for $j^* \leq j \leq m_{layer}$;
- to that end, the corresponding lines and columns are removed from the S_a, K, S_ϵ, Y, F, x_k and x_a matrices or vectors. That condition is evaluated at each step of the OE algorithm.

From these criteria, it is obvious that the number of layers, and thus the size of the system, will be variable along the retrieval, depending on the density profile. This is not a problem because the system is triangular, see Equation (4.28), and the variables in a given layer only depend on the variables of the layers located above itself. Moreover, the convergence of the algorithm is only accepted when the number of layers is stable for more than one iteration in addition to the criteria defined in Section 4.6.1.5.

The aerosol background can be retrieved for the layers in which saturation occurs, if the saturated lines are removed from the wavenumber fitted range. The variables a, b and c of the aerosol background are thus retrieved on the whole occultation, while the density, temperature and displacement are only retrieved in the non saturated altitude range.

4.6.4 Wavenumber scale definition

The pixel to wavenumber scale is defined in Section 3.5.3.3. When the calibration had been performed, the Doppler wavenumber shift induced by the velocity of VEX relative to the Sun had been removed. During solar occultation, the same procedure has to be applied, but by considering

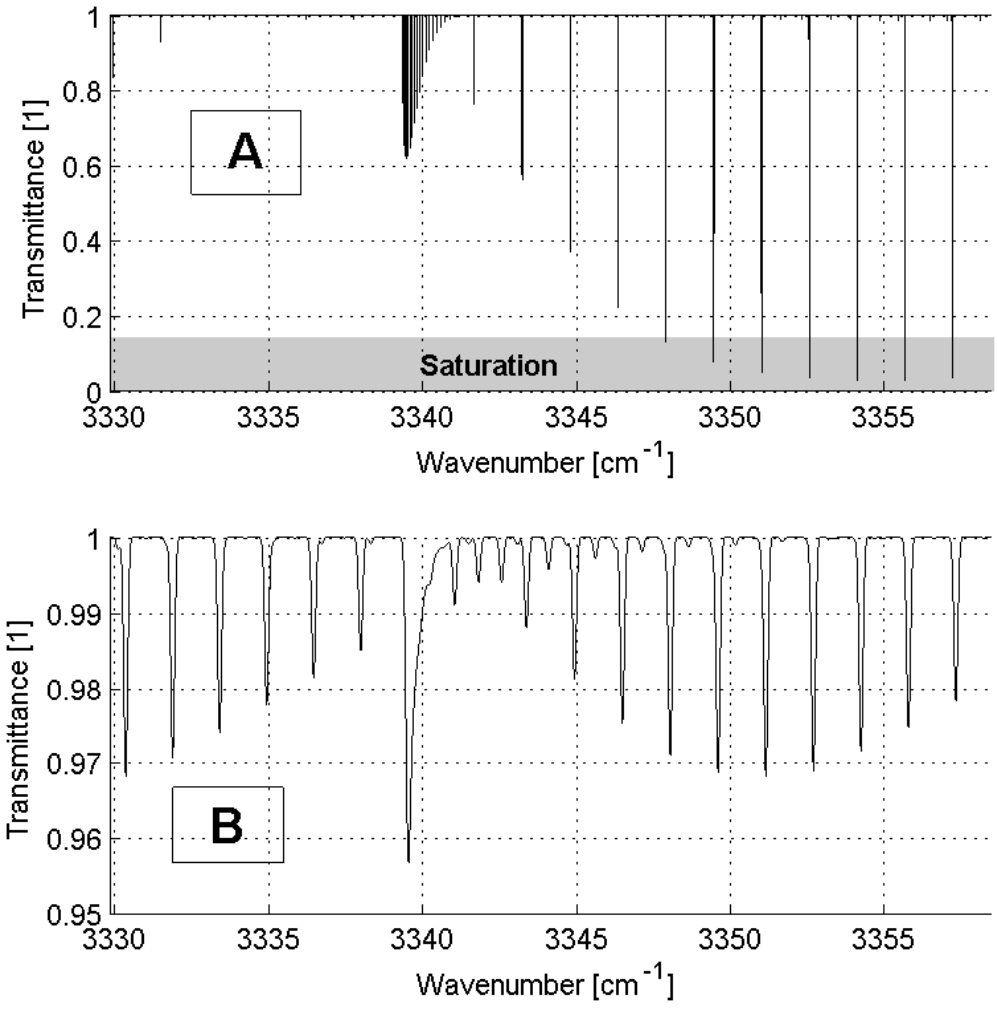

Figure 4.18: Illustration of the line saturation: Panel A shows the spectrum before convolution by the ILP. The gray box at the bottom is the saturation zone. It is clearly seen that some lines are considered as saturated. Panel B is the result after convolution by the ILP, multiplication by the AOTF transfer function, and addition of the adjacent orders. The transmittance only reaches values of 0.97, so 0.03% of absorption. The very large path length ($\approx$ 400 km) in each layer are responsible for this.

the projected velocity of VEX relative to Venus, i.e. the measurement point. The same formula as Eq. (3.20) has to be used to correct for the induced wavenumber shift:

$$\tilde{\nu}' = \tilde{\nu} \cdot \left(1 + \frac{v_{VEX}}{c_{light}}\right) \tag{4.51}$$

with $\tilde{\nu}$ the wavenumber scale from the calibration relations, $\tilde{\nu}'$ the corrected wavenumber scale, v_{VEX} the velocity of VEX relative to Venus projected on the line of sight and c_{light} the light velocity (299,792.458 km/s).

After these corrections, it is observed that small variations remain when considering the coincidence of the observed and database absorption lines. The justification comes from small temperature variations within the instrument that may induce such variations to the calibration described in Section 3.5.3.3. The residual is fitted using the relation:

$$\tilde{\nu}" = \tilde{\nu} + [e + f \cdot (\tilde{\nu} - \tilde{\nu}_0)] \tag{4.52}$$

where e and f are the coefficients of a first order polynomial of the reduced wavenumber $\tilde{\nu} - \tilde{\nu}_0$. These two variables are fitted on the whole occultation, meaning they have the same value for all m_{layer} spectra. For this reason, they are independent of the wavenumber shifts of each layer d_i. From this relation, the $\tilde{\nu}$ variable of Equation (4.28) should be replaced by $\tilde{\nu}"$.

4.6.5 A-priori wavenumber scale

The wavenumber scale described in Section 3.5.3.3 is named reference calibration from now on. A better a-priori of the wavenumber scale is calculated here. The procedure is iterative, and the reference calibration is taken as an initial guess.

First, a spectrum which shows relatively strong absorption lines is selected: it is the first spectrum found 10 km below the highest useful tangent altitude, determined from the procedure described in Section 4.6.2. In this spectrum, the absorption lines are clearly seen, see Panel A of Figure 4.19. The retrieved species are known. The position of all the lines are obtained from the Hitran 2008 spectral database [Rothman *et al.* (2009)].

Five diffraction orders are considered: the central selected one, and then the 2 orders lower and 2 orders above. The apparent position of the absorption lines from the adjacent orders is recalculated using the reference calibration. The pixel position of the observed absorption lines is then matched with the list from the spectral database. The line positions are corrected for the pressure wavenumber shift (see Appendix H for description), even if this one is very small.

By considering the Beer-Lambert law, a relative intensity $\widehat{I}_i^*$ of a given species i with a line intensity I_i at wavenumber $\tilde{\nu}^*$ from the spectral database is computed

$$\widehat{I}_i^* = AOTF(\tilde{\nu}^*) \cdot \exp(-I_i \cdot vmr_i) \tag{4.53}$$

where vmr_i is the volume mixing ratio of the species i.

The values $\widehat{I}_i^*$ are sorted by decreasing values. Finally, they are matched to all the observed minima, as depicted in Panel B of Figure 4.19.

As the diffraction order, the apparent pixel position and the theoretical wavenumber of each matched line are known, the pixel to wavenumber and reciprocal relations can be computed using a first order polynomial

$$p = \quad F_{p\leftrightarrow\omega} = a + \frac{\tilde{\nu}}{n} \cdot b \tag{4.54}$$

$$\frac{\tilde{\nu}}{n} = \quad F'_{\omega\leftrightarrow p} = a' + p \cdot b' \tag{4.55}$$

where $\tilde{\nu}$, n and p are the wavenumber, order and pixel number of each observed absorption line, $F_{p\leftrightarrow\omega}$ and $F'_{\omega\leftrightarrow p}$ are the direct and reciprocal derived polynomials, with coefficients a, b, a' and b' respectively.

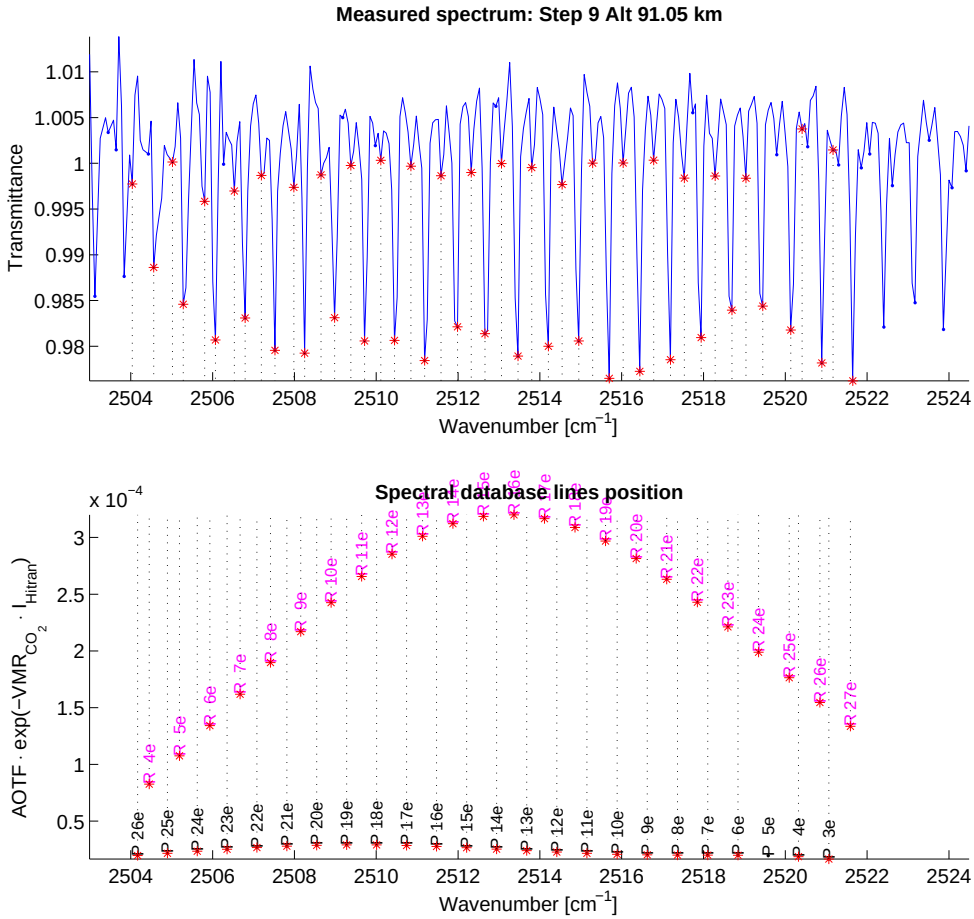

Figure 4.19: Line matching for the pixel to wavenumber calibration for orbit 341.1, order 112, bin 1. Panel A shows the first spectrum 10 km below the first structures appears in the recorded spectra. The minima are listed. They are matched with the spectral database line positions in Panel B. The lines from orders 110, 111, 112, 113 and 114 are considered, but only orders 111 (black) and 112 (purple) present strong absorption lines. They are shown by the red crosses, and correspond to the CO_2 rovibrational transitions. The relative transitions are presented, corrected by Equation (4.53).

Using these two relations, the whole procedure is iteratively applied until the covariance of the linear fit stabilizes. The convergence is very fast, and usually occurs before three steps. The final relations for orbit 341.1, order 112, bin 1 are presented in Figure 4.20. In that case, the convergence occurred in two steps.

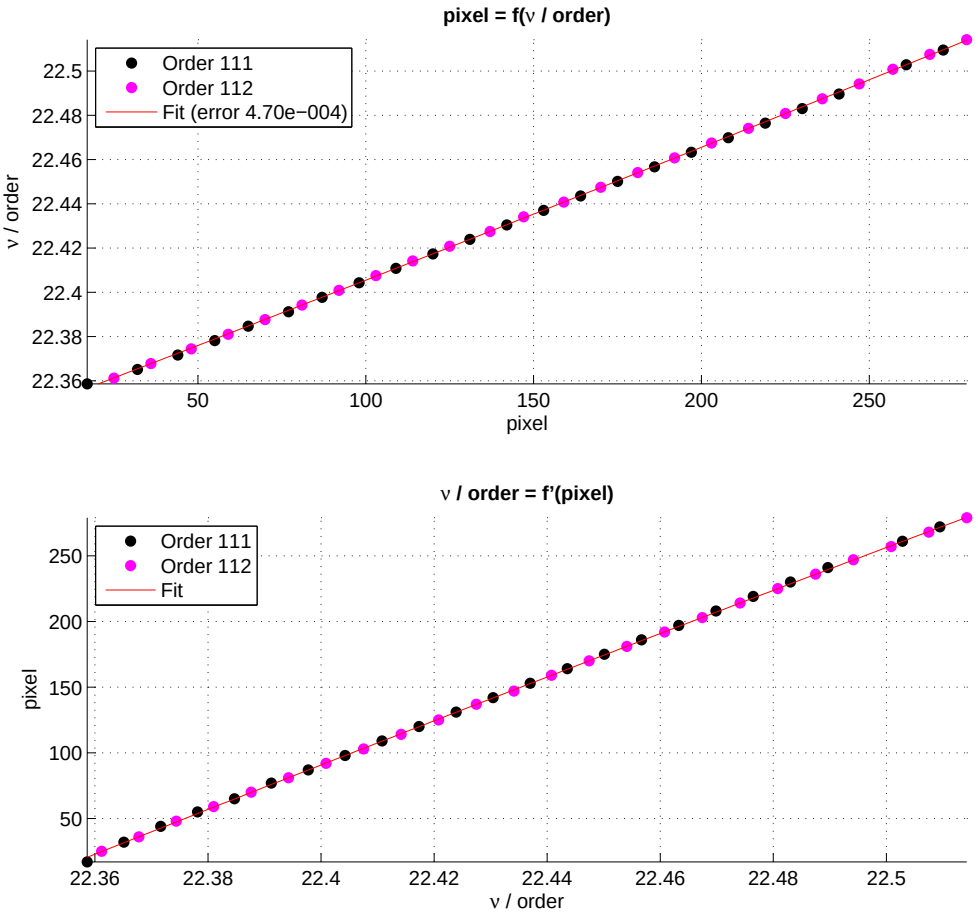

Figure 4.20: Pixel to wavenumber relation obtained from the atmospheric lines for orbit 341.1 order 112 bin 1. The top Panel gives the relation pixel to wavenumber, while the bottom Panel gives its reciprocal. The colors correspond to the order from which the lines come, i.e. 112 as the central order and 111 as order - 1. The error given in the fit is the standard deviation.

4.6.6 A-priori wavenumber shift

An a-priori wavenumber shift on each layer is also calculated. Starting from the obtained calibration functions, the same procedure as the one described in Section 4.6.5 is applied on each spectrum, but the displacement is considered as constant, so the b and b' coefficients of Equations (4.54) and (4.55) are zero. This equation is evaluated in each layer separately.

The a-priori wavenumber shift is given in Figure 4.21. The horizontal bars are the standard deviations. They have a mean value of 0.032 cm^{-1}, which is within the range of a pixel spectral width: between 0.032 and 0.035 cm^{-1} in order 112 (see Figure 3.18).

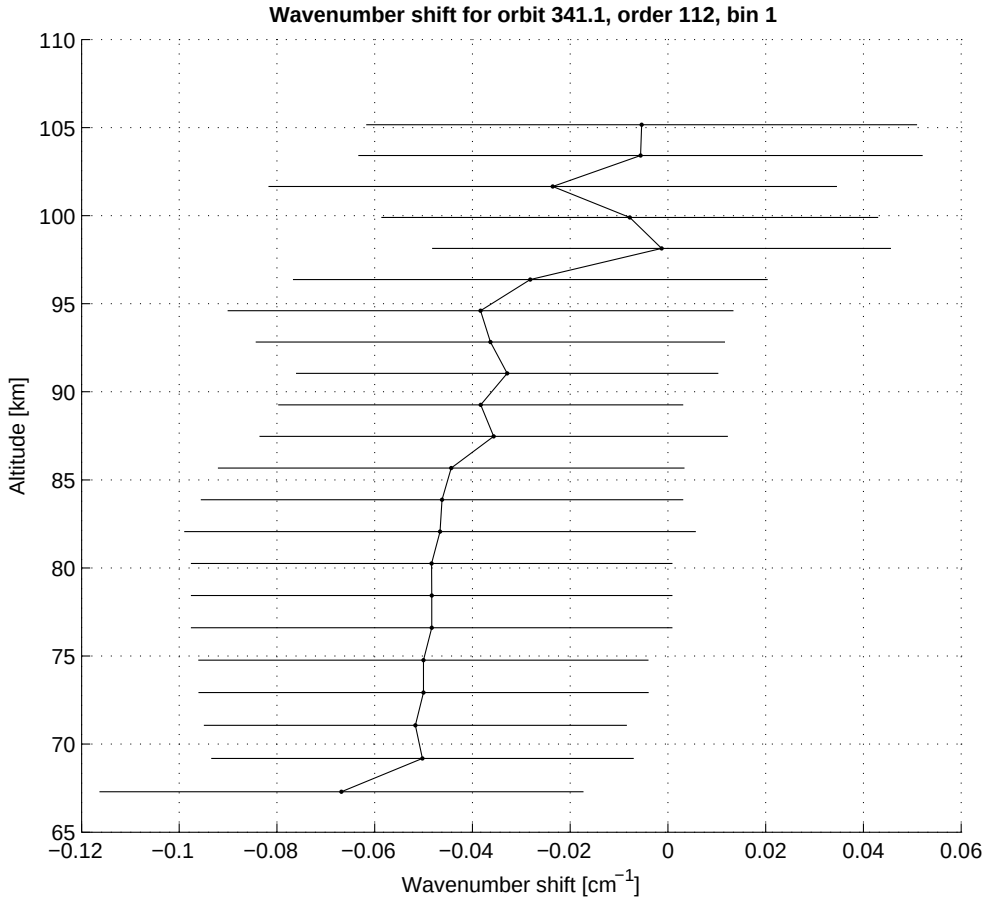

Figure 4.21: A-priori wavenumber shift for orbit 341.1 order 112. The horizontal bars are the standard deviation from the fit described in Section 4.6.6.

4.6.7 A-priori density profile

A method is designed in order to find a robust a-priori for the density profile. Indeed, it is observed that the VIRA model often fails as an a-priori, for example for CO_2 retrievals, as the densities can have values from one hundred times lower to ten times higher for a given altitude than the VIRA model. It can be even more drastic for other species. The major drawback to that situation is that it slows down the algorithm, as the solution is much further from the a-priori.

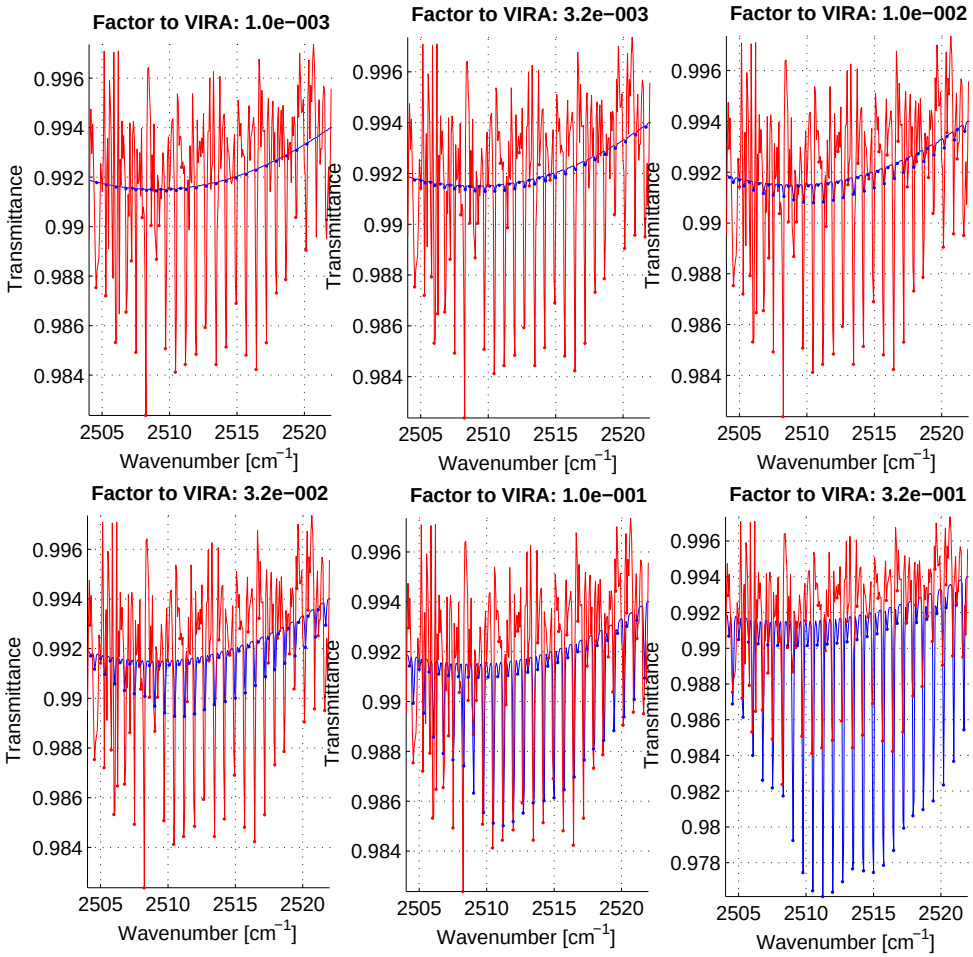

Figure 4.22: Calculation of the a-priori density coefficient for orbit 341.1, order 112, bin 1. The spectrum is simulated for different density coefficients value that multiply the VIRA profile. Its value is given as the title of each subgraph. The measured spectrum is plotted in red, while the simulated spectra are plotted in blue. The red and blue points are the ones used to calculate the coefficient.

The method is applied on the first useful spectrum, obtained from the procedure described in Section 4.6.2. In this spectrum, we suppose that some weak absorption lines are present, even if most of the signal is made of noise. The baseline of the spectrum $a_1+(\tilde{\nu}-\tilde{\nu}_0)\cdot b_1+(\tilde{\nu}-\tilde{\nu}_0)^2\cdot c_1$ can be roughly determined using a polynomial fit (see Equation (4.28)). The depth of each measured absorption lines can be easily calculated. They are all put in a vector $\mathrm{Tr}_{measured}$. We now evaluate Equation (4.28) for different regularly spaced densities. Such as in Sections 4.6.5 and 4.6.6, the measured and observed lines are matched to each other. But this time, their transmittances are compared. The difference

$$\phi_{n_\alpha} = \sum_{i=1}^{L_{lines}} D_{i,n_\alpha}^{calculated} - D_i^{measured} \tag{4.56}$$

is calculated, where

$$D_{i,n_\alpha}^{calculated} = 1 - \mathrm{Tr}_{i,n_\alpha}^{calculated} \quad (4.57)$$

$$D_i^{measured} = a_1 + (\tilde{\nu} - \tilde{\nu}_0) \cdot b_1 + (\tilde{\nu} - \tilde{\nu}_0)^2 \cdot c_1 - \mathrm{Tr}_i^{measured} \quad (4.58)$$

with n_α the set of density coefficients to the VIRA model, ϕ_{n_α} the coefficient for n_α, $\mathrm{Tr}_{i,n_\alpha}^{calculated}$ the calculated transmittance for n_α, $\mathrm{Tr}_i^{measured}$ the measured transmittance. In each spectrum, L_{lines} are observed. For the best value, the sum is zero. An interpolation gives this best coefficient value.

The procedure is shown in Figures 4.22 and 4.23. Figure 4.22 shows the comparison between the measured spectrum (blue) and the synthetic spectra (red) calculated for different densities. The dots on each curve of each Panel show the local minima that correspond to known absorption lines from the simulated orders. The mean depth, i.e. the transmittance, is calculated from the depth of all the points (see equations above), and the difference is plotted in Figure 4.23. The zero value of the curve corresponds to the best estimate using the described procedure.

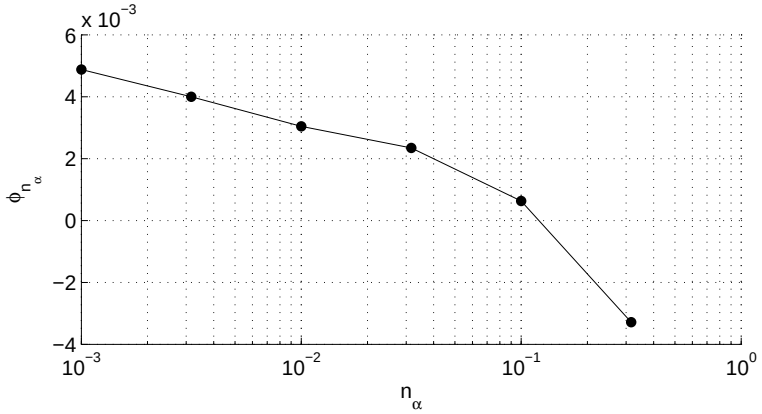

Figure 4.23: Calculation of the a-priori density coefficient for orbit 341.1, order 112, bin 1. The graph shows the evolution of the quotient ϕ_{n_α}. The a-priori value is obtained when it crosses the x-axis: 0.1348 in this case.

4.6.8 Non local thermodynamical effects

Local thermodynamical equilibrium (LTE) needs to be satisfied in order to assimilate the rotational temperature to the kinetic temperature, which may not be necessarily the case [Gilli *et al.* (2009)]. However, the non-LTE effects only weakly affect cold bands [11] [Edwards *et al.* (1998); López Valverde *et al.* (2010)].

Indeed, when a species like CO_2 is excited by radiation, the translational, rotational and vibrational spectroscopic levels of the molecular system adjust to equilibrium at very different rates. The translational and rotational levels return to equilibrium with shorter time constants than the vibrational levels. It implies that in the upper atmosphere, the translational and rotational levels are in LTE while the vibrational levels may not be. The rotational temperature that is obtained from an absorption band can thus be assimilated to the kinetic temperature [López Valverde (2010); López Valverde *et al.* (2010)].

However, the vibrational levels of the different bands may not be at equilibrium [Edwards *et al.* (1998)]. This situation finds its origin in the atmosphere dynamics and chemistry. This non equilibrium situation is the result of the solar radiation pumping by the species at high altitude on the day side of the planet. The subsolar to antisolar atmospheric circulation at high altitude induced by the temperature difference between the dayside and nightside thermosphere transports these excited species. It induces a difference in the vibrational partition sum $Q_v(T)$ to

11. A cold band is vibrational transition starting from the ground state.

the Boltzmann law: some vibrational levels are more populated than they should be if they were in LTE, i.e. their vibrational temperature are slightly different.

In the present study, $Q_v(T)$ is obtained from tables coming from Hitran 2008 [Rothman *et al.* (2009)]. But a good approach to obtain the $Q_v(T)$ value for CO_2 is [López Puertas (2010)]:

$$Q_v(T) = \prod_{i=1,2,3} \frac{1}{\left(1 - \exp\left(\frac{-E_i}{k_B \cdot T_v}\right)\right)^{l_i}} \tag{4.59}$$

where E_i is the energy of the CO_2 main isotopologue at vibrational level v_i, considering that the three vibrational modes are independent, T_v is the vibrational temperature and k_B is the Boltzmann constant. If only the v_2 vibrational mode 01001 [12] (band center at ≈ 667 cm^{-1}) is considered, we have

$$Q_{v_2}(T) = \frac{1}{\left(1 - \exp\left(\frac{-E_2}{k_B \cdot T_v}\right)\right)^2} \tag{4.60}$$

If we take typical values for the kinetic and for the CO_2 (01000) vibrational temperatures at Venus, we see that the differences are always larger than 8 to 10 %, see Table 4.1.

Altitude	Kinetic temperature	Vibrational temperature	$Q_{v_2}^{NLTE}$	$Q_{v_2}^{LTE}$	$\frac{Q_{v_2}^{NLTE}}{Q_{v_2}^{LTE}}$
[km]	[K]	[K]	[1]	[1]	[1]
100	190	190	1.01294	1.01294	100%
140	240	180	1.00975	1.03773	97.3038%
160	300	160	1.00499	1.08692	92.4622%

Table 4.1: Calculation of the LTE and non-LTE partition sums for different conditions on Venus, from López Puertas (2010).

If the non-LTE effect is neglected, the densities retrieved by SOIR overestimate the atmospheric densities by at most 10%.

In regard to what is described here above, we do not include for the moment any non LTE effect in the SOIR retrievals. The effect on our retrieval should remain weak, as the density error mentioned is larger than the retrievals error bars. This aspect will be developed in future studies.

4.6.9 Temperature dependence

SOIR spectra are sensitive to the atmospheric temperature through its influence on the intensities of the absorption lines of, for example, CO or CO_2. The temperature influences the overall shape of one specific vibrational band, as shown in Figure 4.24. If the temperature increases, the position of the band absorption maximum moves to higher J values, as the distribution of the line intensities for the different rotational transition changes. From the overall shape, temperature can then be derived even if some of the information contained in this shape disappears because of the curvature of the AOTF transfer function, as illustrated in Figure 4.24.

This approach leads to the determination of the rotational temperature of the gas.

The shape of the AOTF function thus influences the temperature retrieval, as a good knowledge of the function is needed in order to correctly build the synthetic spectrum. However, the correction of the AOTF function using the n_{AOTF} points as described in Section 4.6.1 only locally modifies the transfer function, and thus not the overall shape.

12. These notation are given in the Hitran format for CO_2 [Rothman & Young (1981)]. The four digits represent the different quantum numbers: $v_1 v_2 l_2 v_3 R$. The v_i are the vibrational quantum numbers and l_i is the vibrational angular momentum quantum number. R is a ranking index between 1 and $v_1 + 1$.

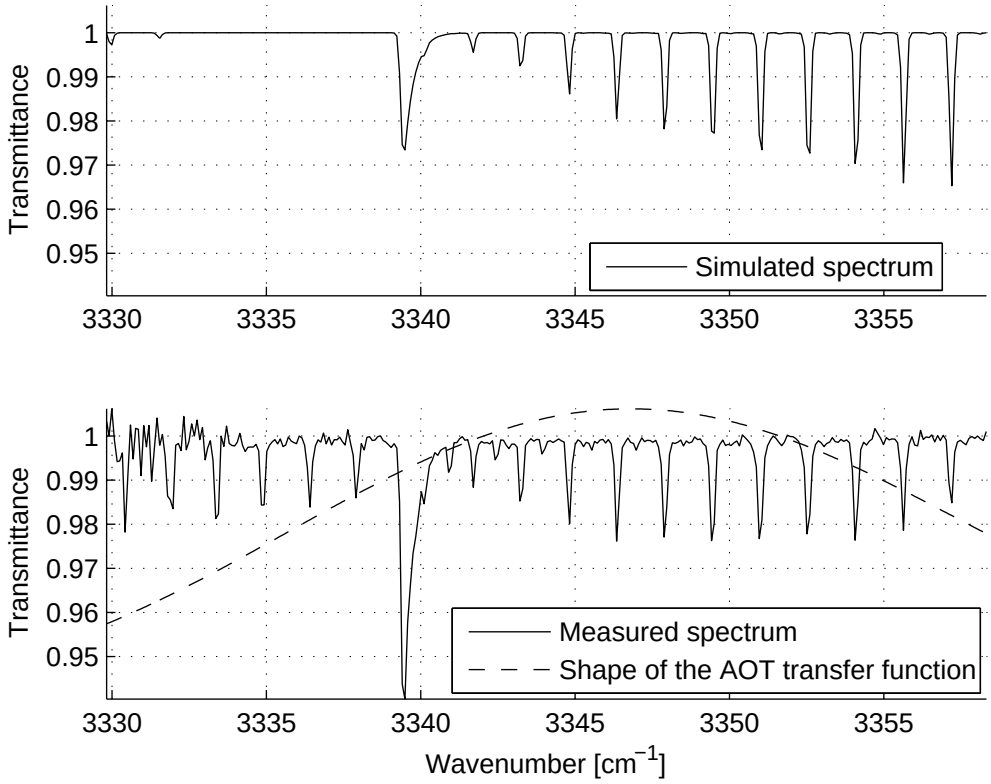

Figure 4.24: Temperature dependency. This Figure shows that the temperature information is lost because of the shape of the AOTF transfer function. The top Panel is a CO_2 spectrum in diffraction order 149, simulated for a layer (atmospheric conditions: altitude of 110 km, pressure of 0.152 Pa, temperature of 181.2 K, total density of 0.1 $\times 10^4$ mol/m^3, volume mixing ratio of 0.965, path length of 200 km), but without order addition nor contribution of the AOTF transfer function. The maximum is to the right of the spectral window. The bottom Panel shows the measured spectrum, and the shape of the AOTF function. It is clearly seen that the maximum of absorption of the band is located around 3347 cm^{-1}. The maximum value of the AOTF has been somewhat increased in order to better see its maximum. It is obvious that the maximum of the measured transmittance is displaced closer to the maximum of the AOTF transfer function.

4.6.10 Combination of the profiles obtained from the two bins

For each measurement, we have two data sets, each corresponding to one bin. During an occultation, the two bins scan almost the same portion of atmosphere. For this reason, the results are combined in order to improve the accuracy of the vertical profiles, and their errors. The following relations are applied:

$$n = \exp\left(\frac{\log(n_1)}{\delta n_1} + \frac{\log(n_2)}{\delta n_2}\right) / \left(\frac{1}{\delta n_1} + \frac{1}{\delta n_2}\right) \quad (4.61)$$

$$T = \left(\frac{T_1}{\delta T_1} + \frac{T_2}{\delta T_2}\right) / \left(\frac{1}{\delta T_1} + \frac{1}{\delta T_2}\right) \quad (4.62)$$

$$\delta n = \sqrt{\delta n_1^2 + \delta n_2^2} \quad (4.63)$$

$$\delta T = \sqrt{\delta T_1^2 + \delta T_2^2} \quad (4.64)$$

with n and T the density and rotational temperature profiles, δn and δT the retrieval errors on these profiles, and the subscripts 1 and 2 referring to the vertical profiles obtained from the measurements on bins 1 and 2.

4.7 Example of retrieval

We give here an example of retrieval, to illustrate the OEM algorithm. The orbit 341.1 (28/03/2007) order 149 bin 1 is studied. Its characteristics are summarized in Table 4.2.

Variable name	Unit	Value
Latitude	^{o}	82.06
Longitude	^{o}	348.23
LST	hour	17.3
Projected speed	km/s	-8.76
AOTF frequency	kHz	19869
Binning case	-	2 x 12
Start time	HH:MM:SS	6:20:01 AM
End time	HH:MM:SS	6:29:54 AM
Orbit case		Egress
Resolution	cm^{-1}	0.1628

Table 4.2: Characteristics of the orbit 341.1, order 149. The latitude, the longitude, the LST and the velocity of the spacecraft projected on the line of sight are given at a tangent altitude of 120 km.

The diffraction order 149 (3329.8 - 3358.3 cm^{-1}) corresponds to a spectral interval in which the main isotopologue $^{16}O^{12}C^{16}O$ presents a relatively strong absorption band. The isotopologues $^{16}O^{13}C^{16}O$ and $^{16}O^{12}C^{18}O$ also present weaker absorption bands. As mentioned in Vandaele *et al.* (2008), this band allows us to cover tangent altitudes from about 75 km up to 120 km. But saturation of the lines generally restricts the minimum altitude to approximately 100 km. To simulate this order, the adjacent orders +3 and -3 are taken into account, ranging from 3262.8 cm^{-1} to 3426.1 cm^{-1}. The strongest band in intensity, which is included in the simulation, is the 21102-00001 vibrational transition, having a maximal intensity of $4.75 \cdot 10^{-24}$ cm^{-1}/(molecule cm^{-2}). The synthetic spectra comprise 362 lines in total: a cut-off at 10^{-27} cm^{-1}/(molecule cm^{-2}) is defined. The covered rotational transitions range from the P80e to the P2e and R2e to R82e. Figure 4.25 shows the strongest absorption band in diffraction orders 146 to 152 and the wavenumber coverage of this order measurement, while Figure 4.26 shows all the absorption bands that are calculated in this region. In this Figure, the colors correspond to the isotopologues.

The spectra at level 0.3 were given in Figure 3.10 (see page 31).

Two spectral windows are defined: the spectrum are fitted in the ranges 3334 to 3338 cm^{-1} and 3341 to 3358 cm^{-1}, in order not to fit the Q branch that is not resolved using the SOIR instrument.

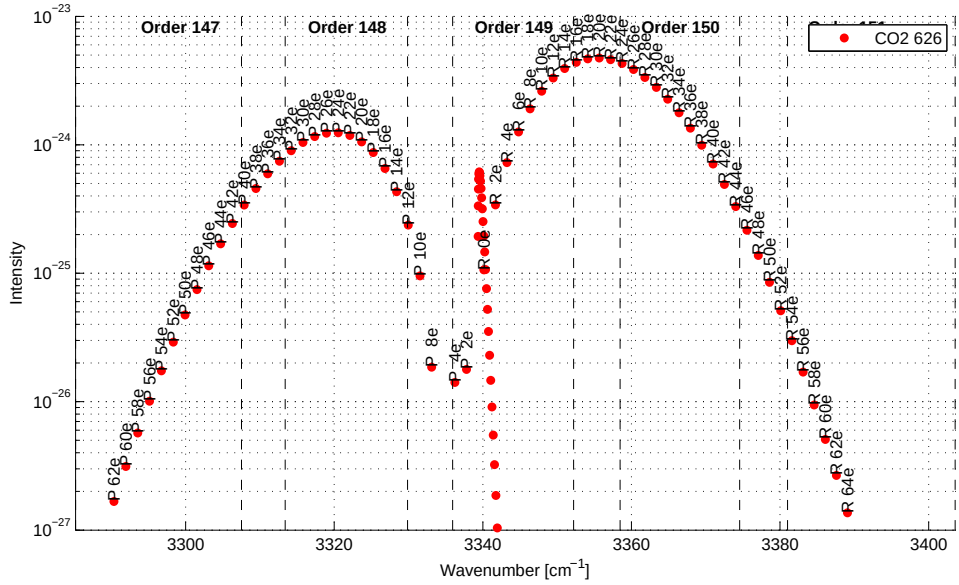

Figure 4.25: Absorption lines of the strongest vibrational band of the main isotopologue of CO_2, $^{16}O^{12}C^{16}O$, in the orders 146 to 152. Only the main absorption transition is presented: 21102-00001 and is cut at 10^{-27} cm^{-1}/(molecule cm^{-2}). The rotational transitions are also indicated for P and R branches. The line intensities are calculated for a pressure and temperature observed at 120 km on Venus (from the Hedin model): $2{\cdot}10^{-4}$ bar and 186 K.

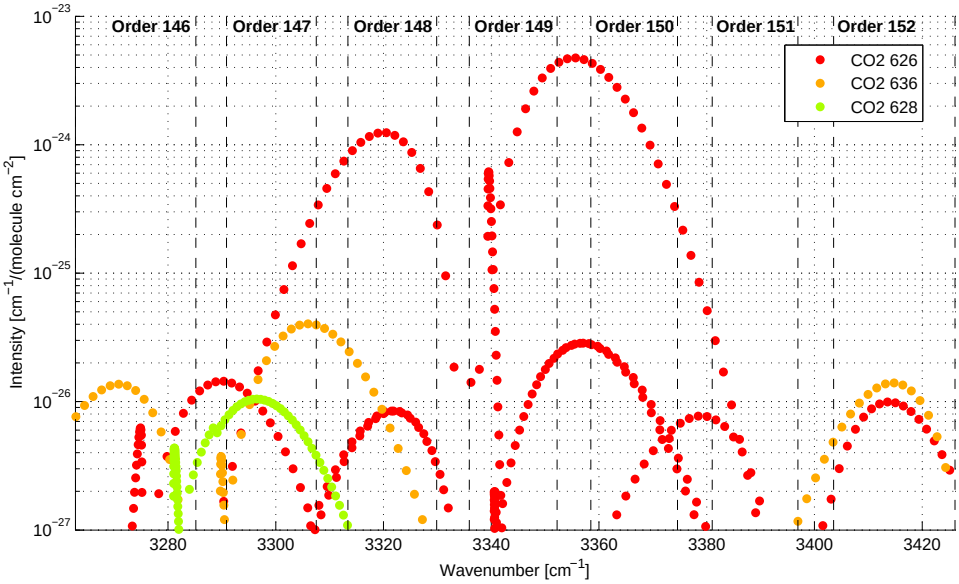

Figure 4.26: Absorption lines of all the vibrational band of all the isotopologues of CO_2 in the orders 146 to 152. They are cut at 10^{-27} cm^{-1}/(molecule cm^{-2}). The line intensities are calculated for a pressure and temperature observed at 120 km on Venus (from the Hedin model): $2{\cdot}10^{-4}$ bar and 186 K.

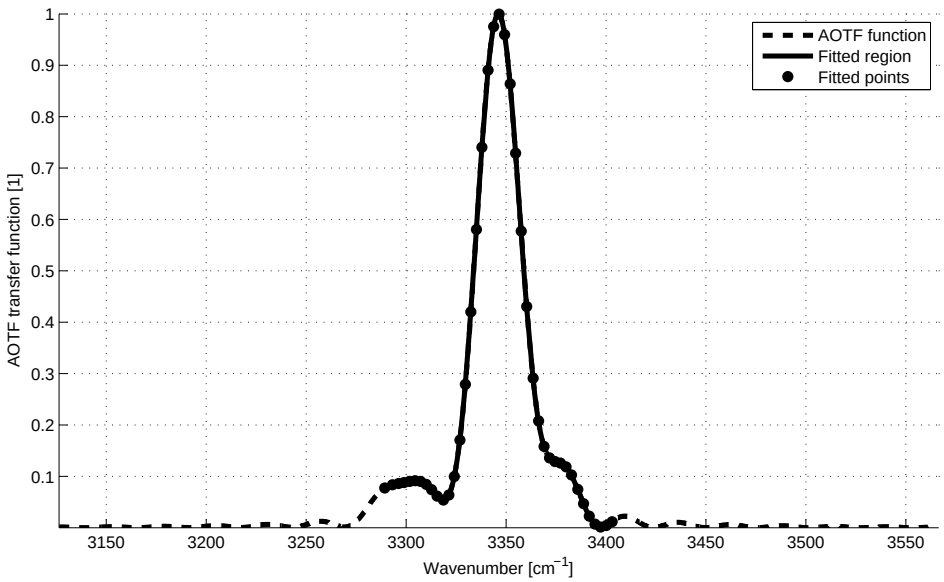

Figure 4.27: AOTF function before the retrieval of orbit 341.1 order 149 bin 1. The dashed curve is the initial function, the plain curve is the fitted function. The large points represent the positions of the fitted values of the AOTF. The fitted AOTF function is interpolated between these points.

The AOTF function is fitted on 40 equally spaced points, see Figure 4.27.

The useful altitude range for the retrieval extends from 104.5 km up to 118.3 km, resulting from the saturation criteria developed before: the layers below 104.5 km are removed because some of the lines were saturated, and were not fulfilling the saturation criteria described in Section 4.6.3.

The vertical profiles for the CO_2 density and the temperature are given in Panels A and B of Figure 4.28. The density profile is slightly higher than the a-priori, and 4 times lower than the model. The temperature profile is colder than the model, of maximum 8 K. The error bars on the parameters are shown as the horizontal bars.

The wavenumber displacement shift is given in Panel C of the same Figure.

The background parameters fit are given in Panels D, E and F of Figure 4.28.

The root mean square (RMS) [13] is plotted in Panel G.

Figure 4.29 illustrates the quality of the fit, which is performed only on a portion of the recorded spectra shown as the green curve. The blue curves are the measured spectra. The red curves are the regions that are not fitted in this order:

- the wavenumbers corresponding to the first and last pixels, as the noise is very large in this region: it can be easily seen when looking at level 0.2 data (see Figure 3.9 on page 30 for orbit 341.1). The signal is very low in these regions.
- the Q branch is not fitted (3338 to 3341 cm^{-1}), because it is not resolved with the SOIR resolution, as previously said.

The averaging kernels for the fitted parameters are presented in Figure 4.31. As expected, the averaging kernels corresponding to the background parameters (a, b, and c, not shown for the latter) are only defined at the level to which they correspond. The averaging kernels or the CO_2 concentrations have maximum values increasing while going deeper in the atmosphere, because there is more spectroscopic information present in the spectra: the path length is longer and the density is higher for low altitude measurements. It may also be observed that the highest altitude

13. The root mean square between the synthetic spectrum $\widetilde{\mathrm{Tr}}$ and the observed spectrum Tr is calculated as $RMS = \sqrt{\sum_{\tilde{\nu}_i} \left| \mathrm{Tr}(\tilde{\nu}_i)^2 - \widetilde{\mathrm{Tr}}(\tilde{\nu}_i)^2 \right|}$.

kernels are also defined at the surrounding altitudes, corresponding to the fact that they influence as well the layers located below them.

Figure 4.30 gives the result of the AOTF fit. The functions adaptation on the side lobes is quite important. It will be shown in Section 4.8.4 how important is this fit.

The error covariances matrices are calculated for the baseline parameters a, b and c, the CO_2 density, the rotational temperature and the AOTF fitted values. The a-priori covariance is presented in Figure 4.32, and the retrieval covariance noise in Figure 4.33. The error covariances of a, b and c parameters are diagonal matrices, as the parameter of a given layer does not depend on the other layers parameters. The influence of the other layers on the density and temperature parameters is observed in their error covariance matrices by showing non-zero values outside the diagonal: the upper layers have an influence on the lower layers, coming from the onion peeling method.

As explained in Section 4.6.10, the vertical profiles obtained from the two bins are combined, to enhance the accuracy of the results. We first compare the vertical density and temperature profiles obtained from bins 1 and 2 to the result of the combination. They are presented in Figure 4.34. The density and temperature profiles obtained from both bins are close to each others, such as the combinations. The error bars are slightly larger, to account for the error bars of the initial fits, as it can be seen in Figure 4.35.

Combinations of the wavenumber shifts are also calculated, as the results are independent of the calibrations. On the other hand, no combination can be done on the parameters of the baseline, as their values are linked to instrument calibrations.

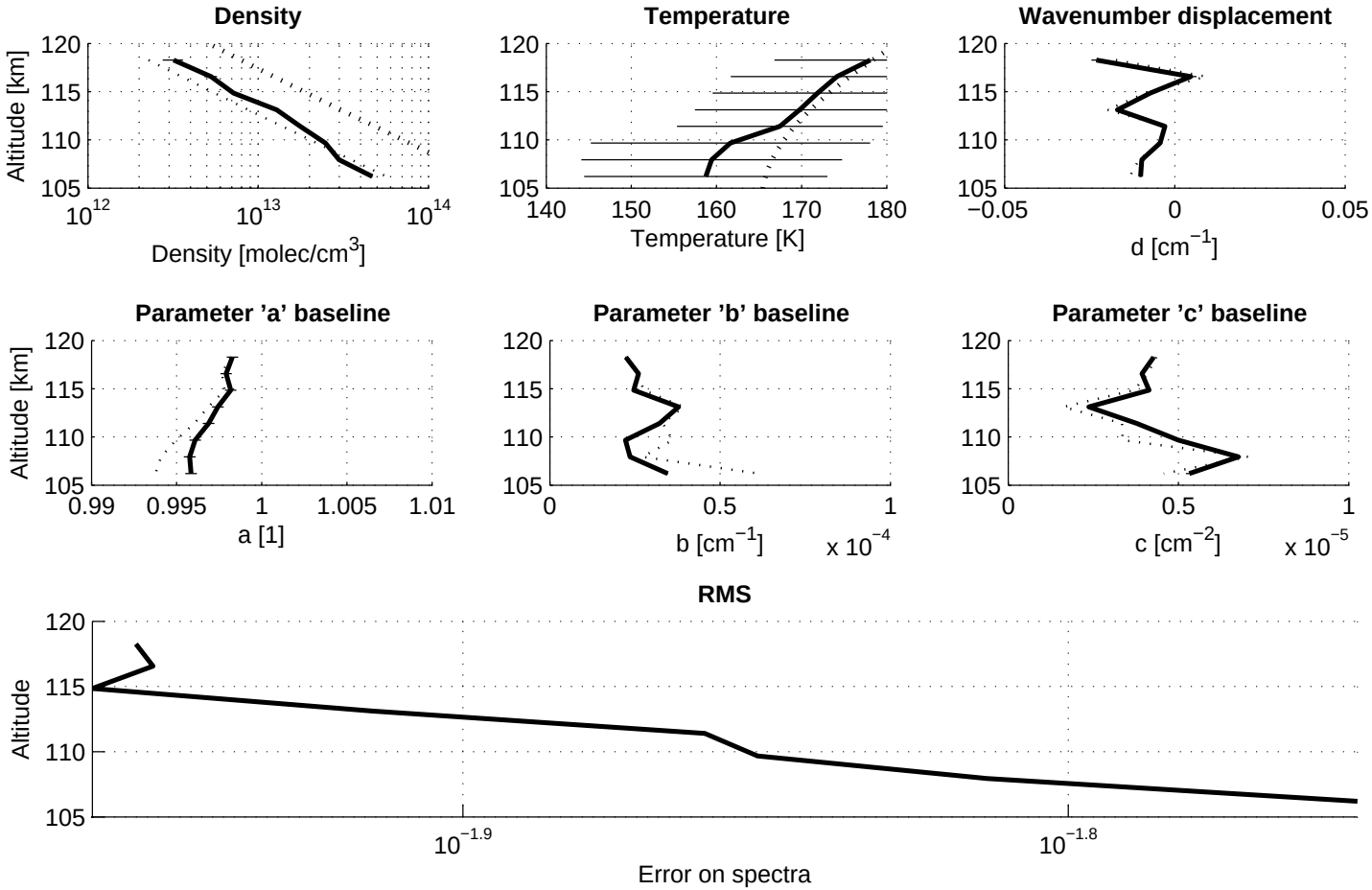

Figure 4.28: Vertical profiles resulting from the retrieval of orbit 341.1 order 149 bin 1. The thick plain curves are the results of the fit. The thick doted lines are the model values and the thin doted lines are the a-priori values. The Panel A is the density profile, the horizontal bars are the error bars. Panel B gives the fitted temperature. Panel C shows the wavenumber shift. Panels D, E and F are the background parameters. Panel G gives the RMS.

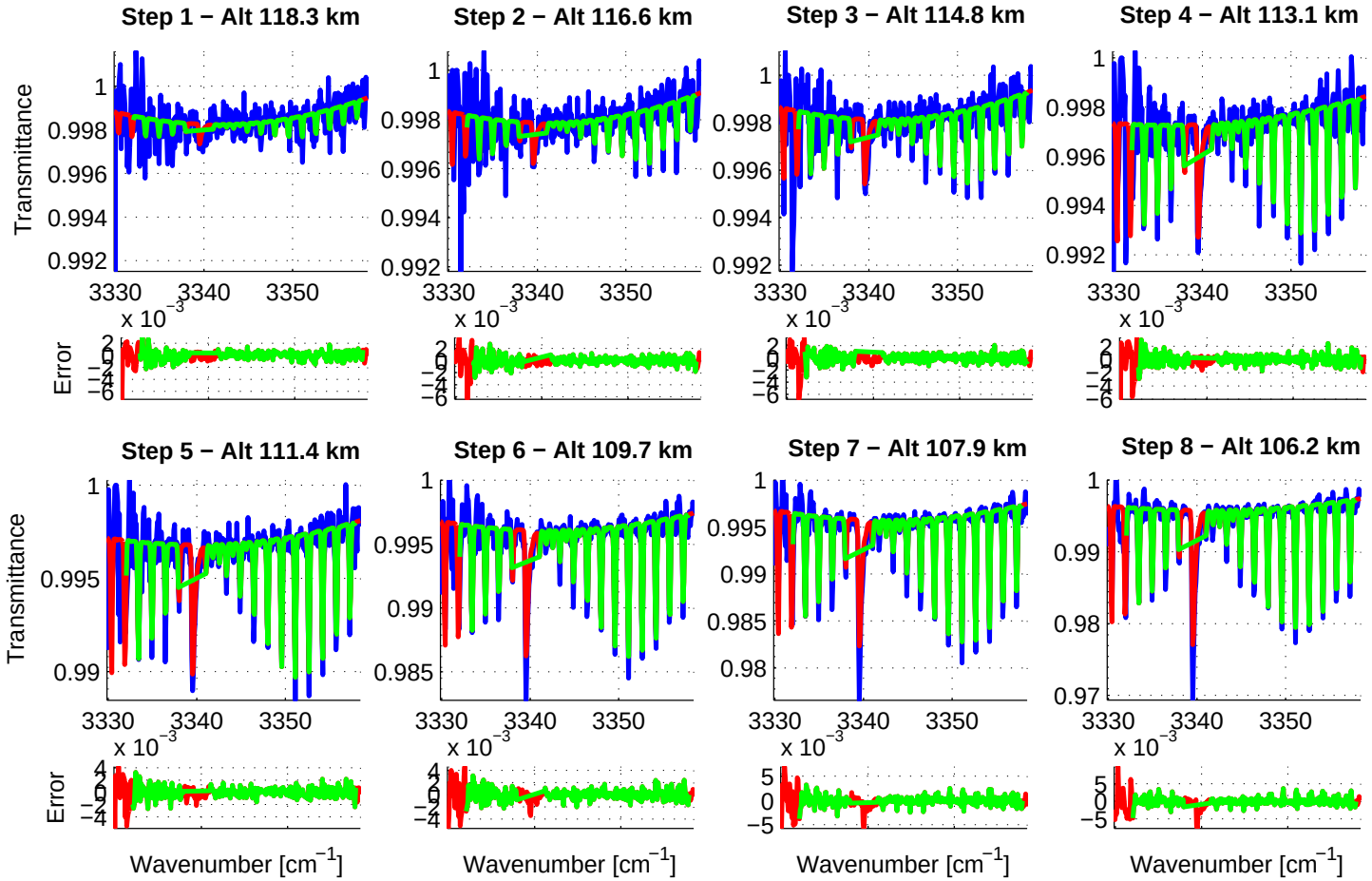

Figure 4.29: Illustration of the quality of the spectral fit obtained during the CO_2 retrieval of orbit 341, order 149. For each altitude, the top Panel compares the observed (blue) and fitted (green) transmittances, and the bottom Panel illustrates the residuals (observed - fitted transmittances). Also in the top Panel, red represents the calculated transmittance outside the fitting wavenumber range.

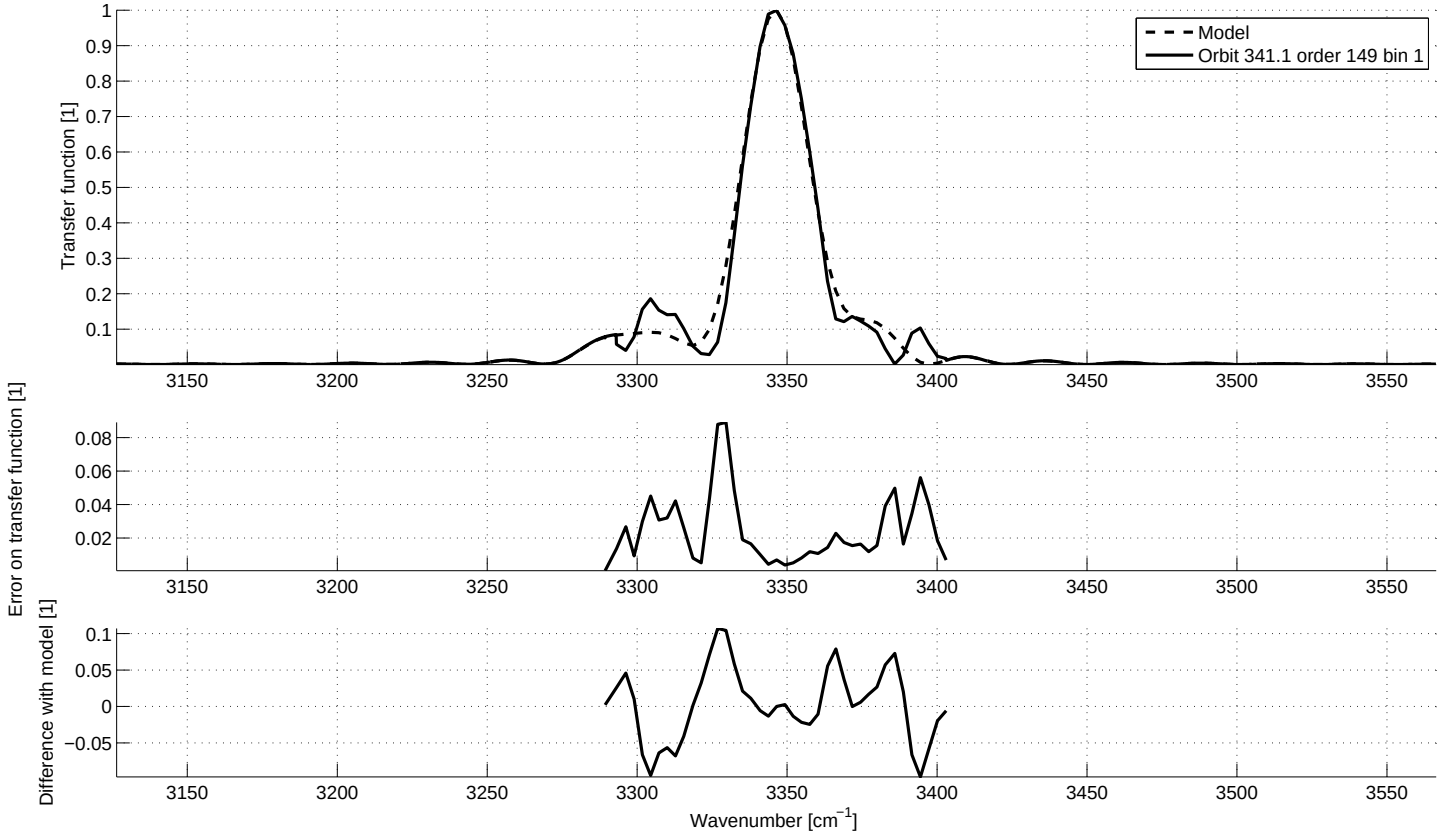

Figure 4.30: Result of the AOTF fit of orbit 341.1 order 149 bin 1. The top Panel gives the fit: the dashed curve is the model, described in Section 3.5.4.4; the plain curve is the result of the fit. The intermediate Panel gives the error on the fit, and the bottom Panel gives the difference between the fit and the model.

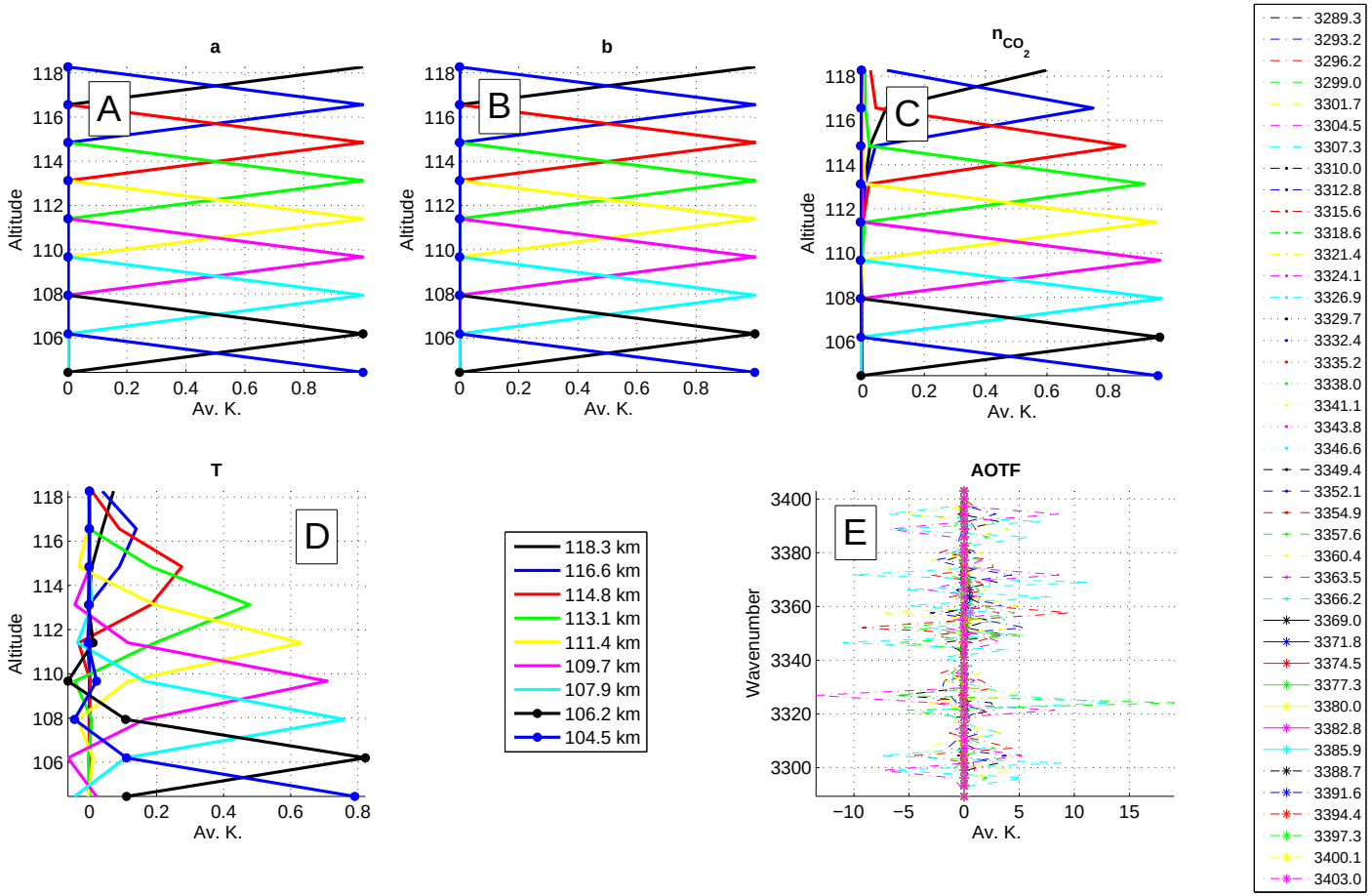

Figure 4.31: Averaging kernels of the last step of the Optimal Estimation algorithm from the retrieval of CO_2 of orbit 341, order 149 bin 1: (a) aerosols a parameter; (b) aerosols b parameter; (c) CO_2 density vertical profile; (d) rotational temperature vertical profile and (e) AOTF fit. The averaging kernels show the area of dependency of each single variable.

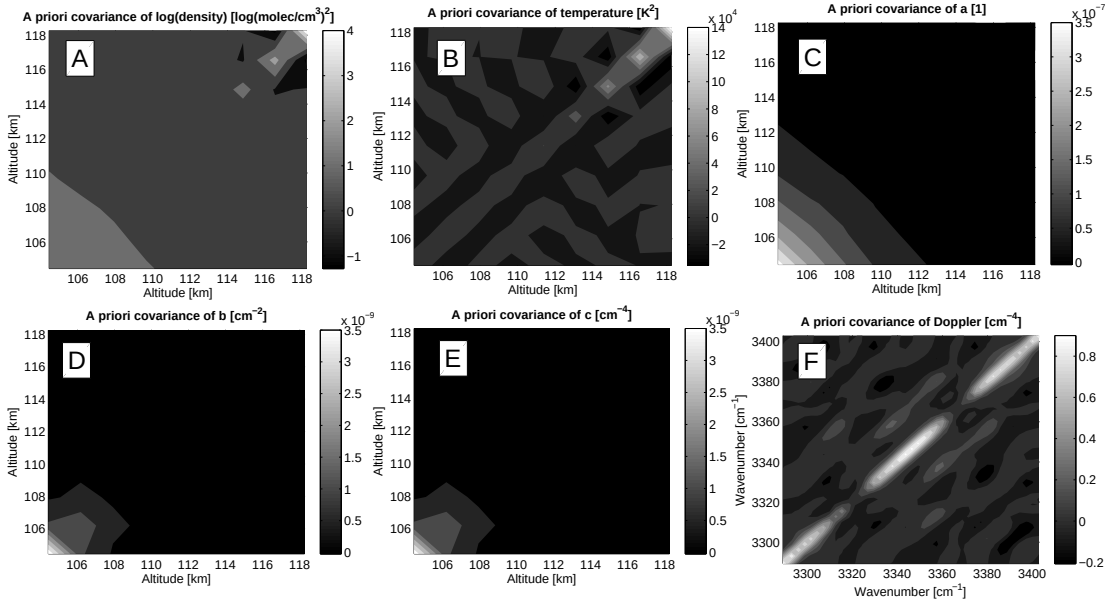

Figure 4.32: A-priori covariance of the Optimal Estimation algorithm from the retrieval of CO_2 of orbit 341, order 149 bin 1: (a) aerosols a parameter; (b) aerosols b parameter; (c) aerosols c parameter; (d) CO_2 vertical densities; (e) rotational temperature vertical profile and (f) AOTF fit.

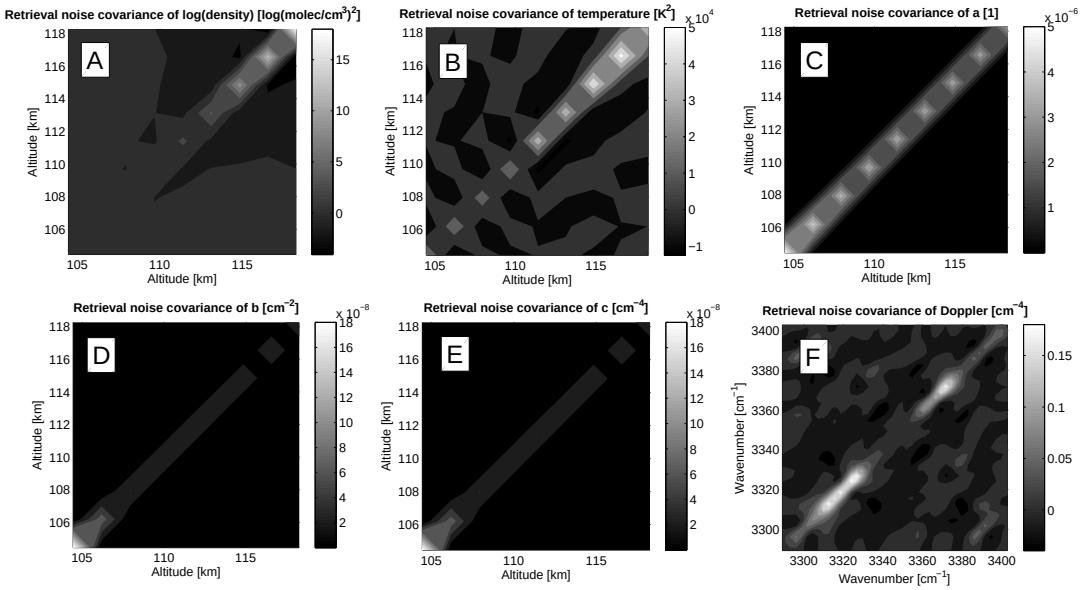

Figure 4.33: Retrieval noise covariance of the Optimal Estimation algorithm from the retrieval of CO_2 of orbit 341, order 149 bin 1: (a) aerosols a parameter; (b) aerosols b parameter; (c) aerosols c parameter; (d) CO_2 vertical densities; (e) rotational temperature vertical profile and (f) AOTF fit.

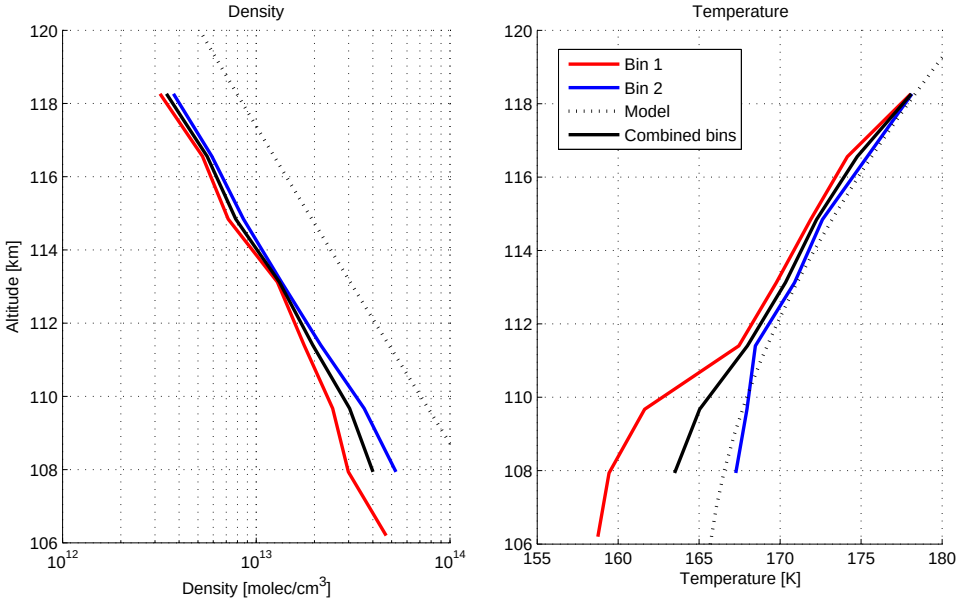

Figure 4.34: Vertical density (left) and temperature (right) profiles from both bins of orbit 341.1. The red curves are the profiles obtained from bin 1, while the blue one is the results from bin 2. The black plain line is the result of the combination, while the black dashed line is the model from VIRA (see Section 4.3).

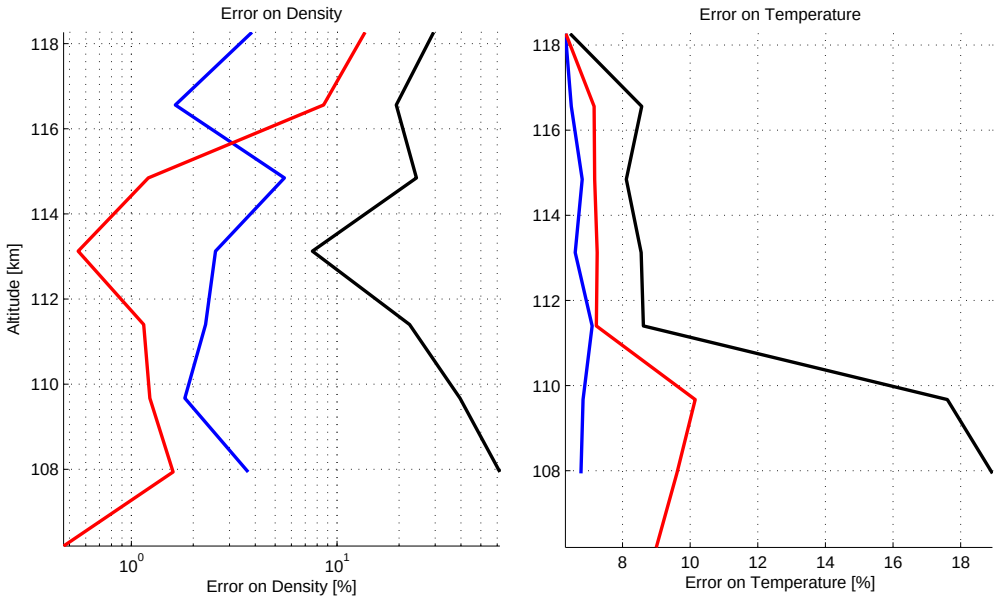

Figure 4.35: Error on the density (left) and temperature (right) profiles in percents of the retrieved densities. The red line is the error on the fit obtained from bin 1, the blue ones concern bin 2, and the black lines concern the combination.

4.8 Algorithm sensitivity study

4.8.1 Introduction

The sensitivity of the algorithm is studied, in order to evaluate the critical parameters, and to obtain their best values.

The sensitivity to the following parameters are studied:
– the covariances, i.e. the values of the S_a matrix
– the a-priori, i.e. the values of x_a
– the AOTF function fit
– the temperature fit
– the wavenumber displacement fit
– the number of adjacent orders to include in the fit

The whole sensitivity study is performed on the orbit 361.1, order 149, bin 1, measured on the 17/04/2007, while deriving CO_2 vertical profiles. It is used as an example in Section 4.7.

4.8.2 Sensitivity to the covariance matrix

4.8.2.1 Introduction

The covariance matrix is one of the most important parameters of the OEM. It defines the allowed variation of each parameter around its a-priori value.

The parameters that are tested are:
– the baseline parameters a, b and c
– the density logarithm $\log n$
– the temperature T
– the wavenumber displacement d
– the wavenumber scale parameters e and f
– the AOTF fit n_{AOTF} and the AOTF maximum position d_{AOTF}

To determine the best parameters value, the covariances are changed to a set of possible values. All the tested combinations are listed in Table 4.3. The vertical profiles, the root mean square of the fits (RMS), the degrees of freedom (DOF) of each variable and the number of convergence steps will guide us in the choice of the best covariance parameters.

Case	Sa_a	Sa_b	Sa_c	Sa_n	Sa_t	$Sa_{n_{AOTF}}$	$Sa_{d_{AOTF}}$	Sa_e	Sa_f	Sa_d
1	**1**	0.01	0.001	5	200	1	5	5	0.005	0.1
2	**0.3**	0.01	0.001	5	200	1	5	5	0.005	0.1
3	**0.1**	0.01	0.001	5	200	1	5	5	0.005	0.1
4	**0.01**	0.01	0.001	5	200	1	5	5	0.005	0.1
5	**0.001**	0.01	0.001	5	200	1	5	5	0.005	0.1
1	0.3	**1**	0.001	5	200	1	5	5	0.005	0.1
2	0.3	**0.1**	0.001	5	200	1	5	5	0.005	0.1
3	0.3	**0.01**	0.001	5	200	1	5	5	0.005	0.1
4	0.3	**0.001**	0.001	5	200	1	5	5	0.005	0.1
5	0.3	**0.0001**	0.001	5	200	1	5	5	0.005	0.1
1	0.3	0.01	**0.01**	5	200	1	5	5	0.005	0.1
2	0.3	0.01	**0.001**	5	200	1	5	5	0.005	0.1
3	0.3	0.01	**0.0001**	5	200	1	5	5	0.005	0.1
4	0.3	0.01	**0.00001**	5	200	1	5	5	0.005	0.1
1	0.3	0.01	0.001	**10**	200	1	5	5	0.005	0.1
2	0.3	0.01	0.001	**5**	200	1	5	5	0.005	0.1
3	0.3	0.01	0.001	**4**	200	1	5	5	0.005	0.1
4	0.3	0.01	0.001	**3**	200	1	5	5	0.005	0.1
5	0.3	0.01	0.001	**2**	200	1	5	5	0.005	0.1
6	0.3	0.01	0.001	**1**	200	1	5	5	0.005	0.1
7	0.3	0.01	0.001	**0.5**	200	1	5	5	0.005	0.1
8	0.3	0.01	0.001	**0.1**	200	1	5	5	0.005	0.1
1	0.3	0.01	0.001	5	**500**	1	5	5	0.005	0.1
2	0.3	0.01	0.001	5	**200**	1	5	5	0.005	0.1
3	0.3	0.01	0.001	5	**100**	1	5	5	0.005	0.1
4	0.3	0.01	0.001	5	**10**	1	5	5	0.005	0.1
1	0.3	0.01	0.001	5	200	**10**	5	5	0.005	0.1
2	0.3	0.01	0.001	5	200	**5**	5	5	0.005	0.1
3	0.3	0.01	0.001	5	200	**1**	5	5	0.005	0.1
4	0.3	0.01	0.001	5	200	**0.5**	5	5	0.005	0.1
5	0.3	0.01	0.001	5	200	**0.01**	5	5	0.005	0.1
6	0.3	0.01	0.001	5	200	**0.001**	5	5	0.005	0.1

Table 4.3: List of all the studied cases for the covariance sensitivity. The bold values are the tested values. The square root of the covariances are given.

Case	Sa_a	Sa_b	Sa_c	Sa_n	Sa_t	$Sa_{n_{AOTF}}$	$Sa_{d_{AOTF}}$	Sa_e	Sa_f	Sa_d
1	0.3	0.01	0.001	5	200	**10**	5	5	0.005	0.1
2	0.3	0.01	0.001	5	200	**5**	5	5	0.005	0.1
3	0.3	0.01	0.001	5	200	**1**	5	5	0.005	0.1
4	0.3	0.01	0.001	5	200	**0.5**	5	5	0.005	0.1
5	0.3	0.01	0.001	5	200	**0.01**	5	5	0.005	0.1
6	0.3	0.01	0.001	5	200	**0.001**	5	5	0.005	0.1
1	0.3	0.01	0.001	5	200	1	**10**	5	0.005	0.1
2	0.3	0.01	0.001	5	200	1	**5**	5	0.005	0.1
3	0.3	0.01	0.001	5	200	1	**0.1**	5	0.005	0.1
4	0.3	0.01	0.001	5	200	1	**0.01**	5	0.005	0.1
1	0.3	0.01	0.001	5	200	1	5	**10**	0.005	0.1
2	0.3	0.01	0.001	5	200	1	5	**5**	0.005	0.1
3	0.3	0.01	0.001	5	200	1	5	**1**	0.005	0.1
4	0.3	0.01	0.001	5	200	1	5	**0.1**	0.005	0.1
5	0.3	0.01	0.001	5	200	1	5	**0.01**	0.005	0.1
6	0.3	0.01	0.001	5	200	1	5	**0.001**	0.005	0.1
1	0.3	0.01	0.001	5	200	1	5	5	**1**	0.1
2	0.3	0.01	0.001	5	200	1	5	5	**0.1**	0.1
3	0.3	0.01	0.001	5	200	1	5	5	**0.01**	0.1
4	0.3	0.01	0.001	5	200	1	5	5	**0.001**	0.1
5	0.3	0.01	0.001	5	200	1	5	5	**0.0001**	0.1
1	0.3	0.01	0.001	5	200	1	5	5	1	**10**
2	0.3	0.01	0.001	5	200	1	5	5	0.1	**1**
3	0.3	0.01	0.001	5	200	1	5	5	0.01	**0.1**
4	0.3	0.01	0.001	5	200	1	5	5	0.001	**0.01**
5	0.3	0.01	0.001	5	200	1	5	5	0.0001	**0.001**

Table 4.3 (Continued)

4.8.2.2 Baseline parameters covariances

The a parameter

The a parameter is the constant term of the baseline polynomial fit. Because a transmittance is fitted, it may vary between 0 and 1.

Five different values are tested for the covariance square root on the baseline a parameter: 1, 0.3, 0.1, 0.01, 0.001. The vertical profiles resulting from the fit are presented in Figure 4.36, while the DOF and number of the number of iterations are given in Table 4.4.

The too low value of the square root covariance (case 5) induces a higher RMS, and reduces the degrees of freedom of the a variable. No convergence is achieved for this particular case. Case 5 presents different vertical profiles than the other ones. If we consider the other cases, there is no change of the DOF. All the other parameters are almost invariant: the density, temperature, wavenumber displacement and background parameters are equivalent, and the RMS too.

The number of iterations is constant for cases 1 to 3, and increases for cases 4 and 5, because the problem is probably too constrained.

A good compromise would be to take 0.3 as square root covariance for the a parameter, as it does not reduce the DOF of the variable, shows a good RMS and allow a good fit even if the a-priori is bad.

Case	a	b	c	n	T	$e+f$	n_{AOTF}	d	d_{AOTF}	Iterations
1	5.000	4.994	4.991	4.352	3.274	0.180	5.654	0.071	0.000	3
	5	5	5	5	5	2	49	5	1	
2	5.000	4.994	4.991	4.352	3.274	0.180	5.654	0.071	0.000	3
	5	5	5	5	5	2	49	5	1	
3	4.997	4.993	4.991	4.352	3.277	0.180	5.654	0.071	0.000	3
	5	5	5	5	5	2	49	5	1	
4	5.654	5.919	5.989	5.063	3.612	0.254	6.085	0.087	0.005	4
	6	6	6	6	6	2	49	6	1	
5	1.615	10.127	10.983	7.963	4.462	0.638	14.507	0.177	0.000	21
	11	11	11	11	11	2	49	11	1	

Table 4.4: DOF and convergence steps of the Sa_a covariance sensitivity test. The case, the degrees of freedom of the a, b, c (baseline parameters), $\log n$ (density logarithm), T (temperature), e, f (wavenumber scale), n_{AOTF} (AOTF function fit), d_{AOTF} (AOTF wavenumber scale fit) and the number of iterations are given. For each case, the first line gives the DOF while the second gives the number of variables of each parameter, i.e. the maximum value of the DOF.

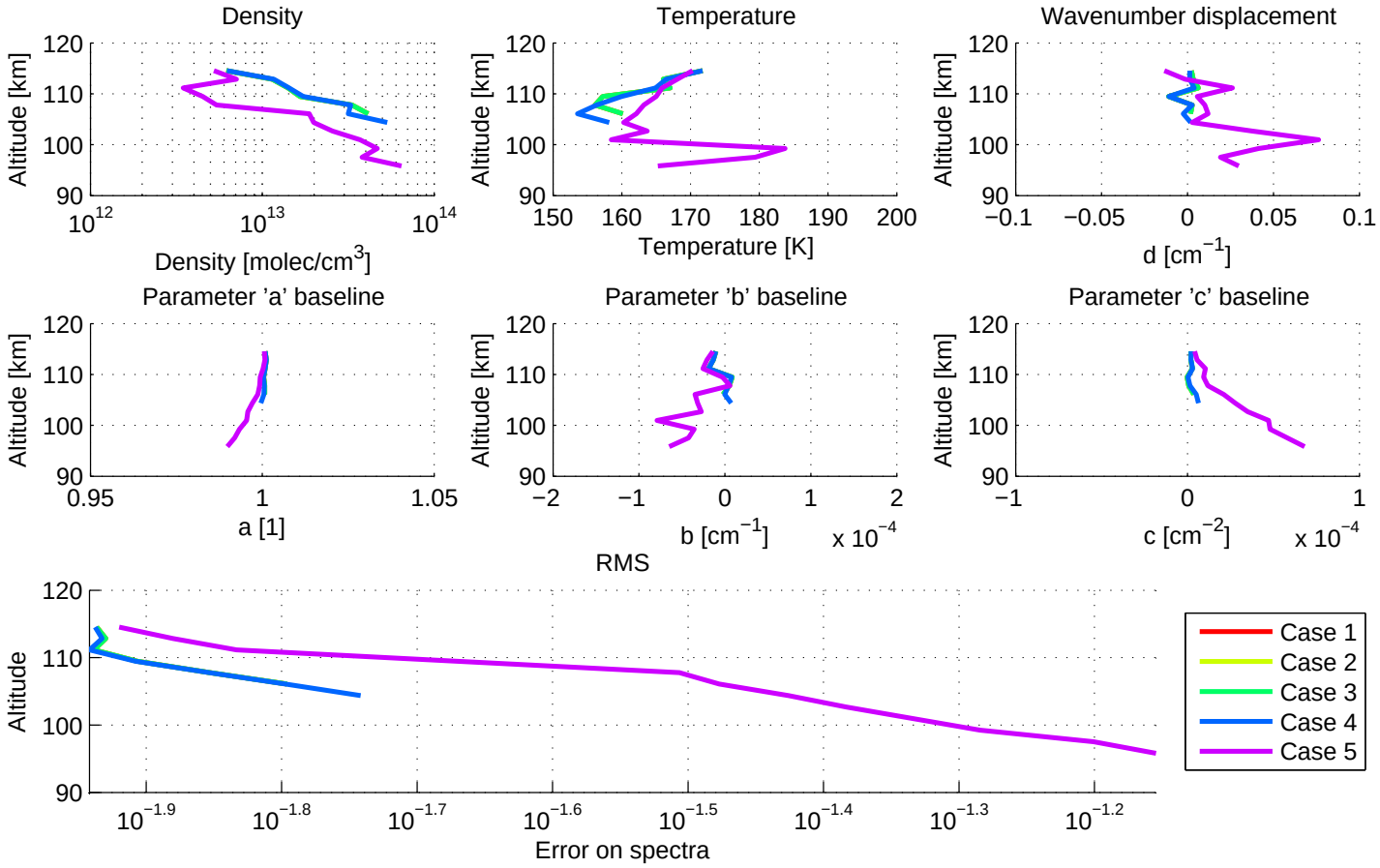

Figure 4.36: Density, temperature, wavenumber displacement and background vertical profiles and RMS for the Sa_a covariance sensitivity test.

The b parameter

The b parameter is the coefficient of the linear term of the baseline polynomial fit. It may take any value, positive or negative, but should remain close to zero.

Five different values are tested for the square root covariance on the baseline b parameter: 1, 0.1, 0.01, 0.001, 0.0001 [cm]. The vertical profiles resulting from the fit are presented in Figure 4.37, while the DOF and number of the number of iterations are given in Table 4.5.

The density, wavenumber displacement and baseline a parameter are invariant to the Sa_b changes, the temperature profile and b and c profiles are slightly changed. The too low values of the square root covariance (cases 4 and 5) reduce the degrees of freedom of the b variable. The RMS is almost constant for the five cases, slightly better for cases 1, 2 and 3. The number of iterations is constant for all cases.

We choose 0.01 cm as square root covariance for the b parameter.

Case	a	b	c	n	t	$e+f$	n_{AOTF}	d	d_{AOTF}	Iterations
1	5.000	5.000	4.994	4.352	3.274	0.180	5.654	0.071	0.000	3
	5	5	5	5	5	2	49	5	1	
2	5.000	5.000	4.994	4.352	3.274	0.180	5.654	0.071	0.000	3
	5	5	5	5	5	2	49	5	1	
3	5.000	4.994	4.991	4.352	3.274	0.180	5.654	0.071	0.000	3
	5	5	5	5	5	2	49	5	1	
4	5.000	4.463	4.715	4.353	3.272	0.180	5.663	0.070	0.000	3
	5	5	5	5	5	2	49	5	1	
5	5.000	1.242	3.113	4.345	2.977	0.203	5.562	0.084	0.001	3
	5	5	5	5	5	2	49	5	1	

Table 4.5: DOF and convergence steps of the Sa_b covariance sensitivity test. The case, the degrees of freedom of the a, b, c (baseline parameters), $\log n$ (density logarithm), T (temperature), e, f (wavenumber scale), n_{AOTF} (AOTF function fit), d_{AOTF} (AOTF wavenumber scale fit) and the number of iterations are given. For each case, the first line gives the DOF while the second gives the number of variables of each parameter, i.e. the maximum value of the DOF.

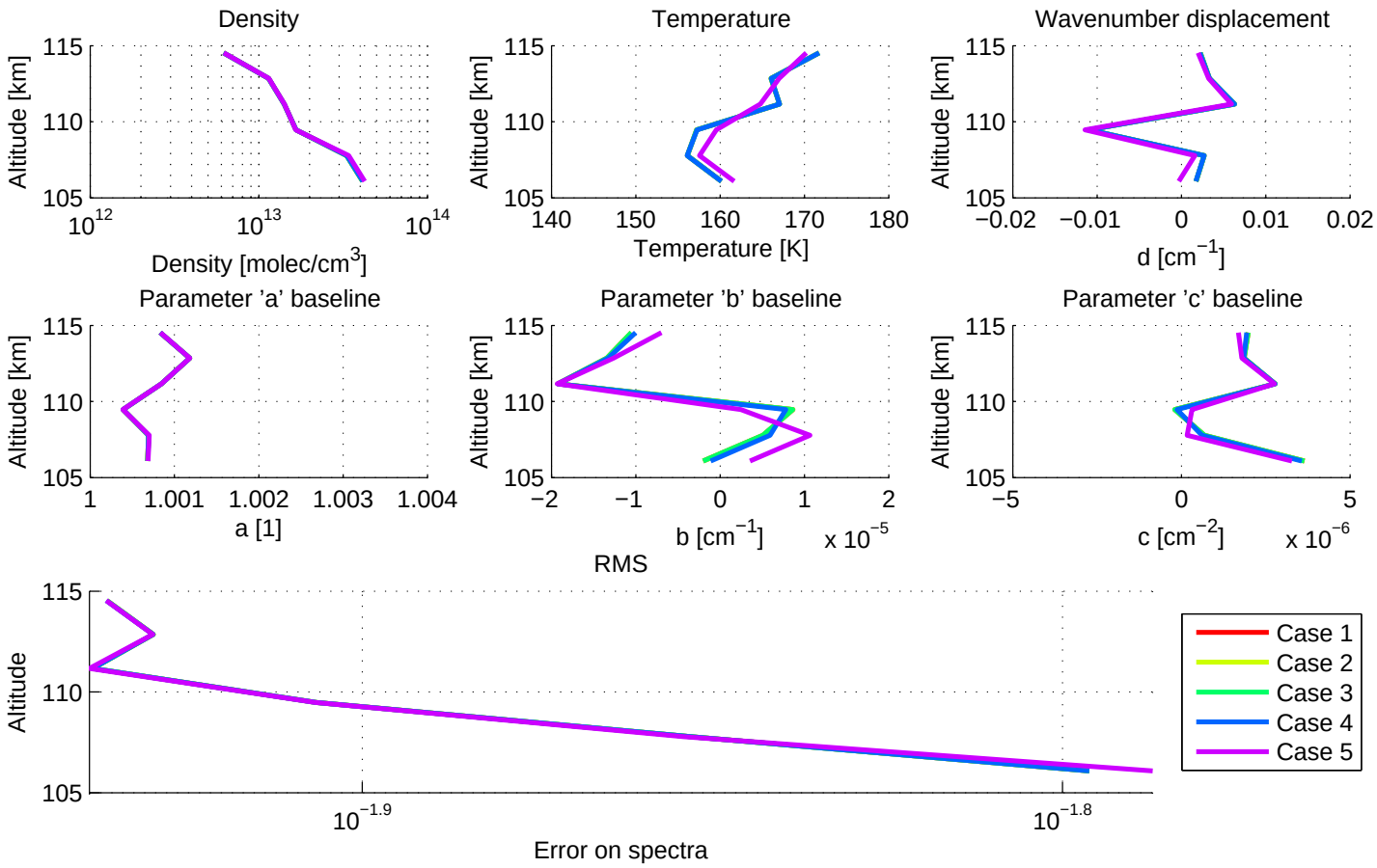

Figure 4.37: Density, temperature, wavenumber displacement and background vertical profiles and RMS for the Sa_b covariance sensitivity test.

The c parameter

The c parameter is the coefficient of the square term of the baseline polynomial fit. It may take any value, positive or negative, but should remain close to zero.

Four different values are tested for square root covariance on the the baseline c parameter: 0.01, 0.001, 0.0001, 0.00001 [cm^2]. The vertical profiles resulting from the fit are presented in Figure 4.38, while the DOF and the number of iterations are given in Table 4.6.

The too low values of the square root covariance (cases 3 and 4) induce a higher RMS, and reduce the degrees of freedom of the c variable. If we consider the two other cases, the DOF are almost constant for c. For the two cases, all the other parameters are almost invariant: the density, temperature, wavenumber displacement and background parameters are equivalent, such as the RMS. The number of iterations is constant for all cases, except for case 4, for which it is slightly higher.

A good compromise would be to take 0.001 cm^2 as square root covariance for the c parameter, as it does not reduce the DOF of the variable and shows a good RMS.

Case	a	b	c	n	t	$e+f$	n_{AOTF}	d	d_{AOTF}	Iterations
1	5.000	4.994	4.997	4.358	3.274	0.180	5.654	0.071	0.000	3
	5	5	5	5	5	2	49	5	1	
2	5.000	4.994	4.991	4.352	3.274	0.180	5.654	0.071	0.000	3
	5	5	5	5	5	2	49	5	1	
3	5.000	4.994	4.505	3.845	3.172	0.188	6.164	0.073	0.000	3
	5	5	5	5	5	2	49	5	1	
4	5.000	4.997	2.144	1.465	3.085	0.128	5.592	0.073	0.005	4
	5	5	5	5	5	2	49	5	1	

Table 4.6: DOF and convergence steps of the Sa_c covariance sensitivity test. The case, the degrees of freedom of the a, b, c (baseline parameters), $\log n$ (density logarithm), T (temperature), e, f (wavenumber scale), n_{AOTF} (AOTF function fit), d_{AOTF} (AOTF wavenumber scale fit) and the number of iterations are given. For each case, the first line gives the DOF while the second gives the number of variables of each parameter, i.e. the maximum value of the DOF.

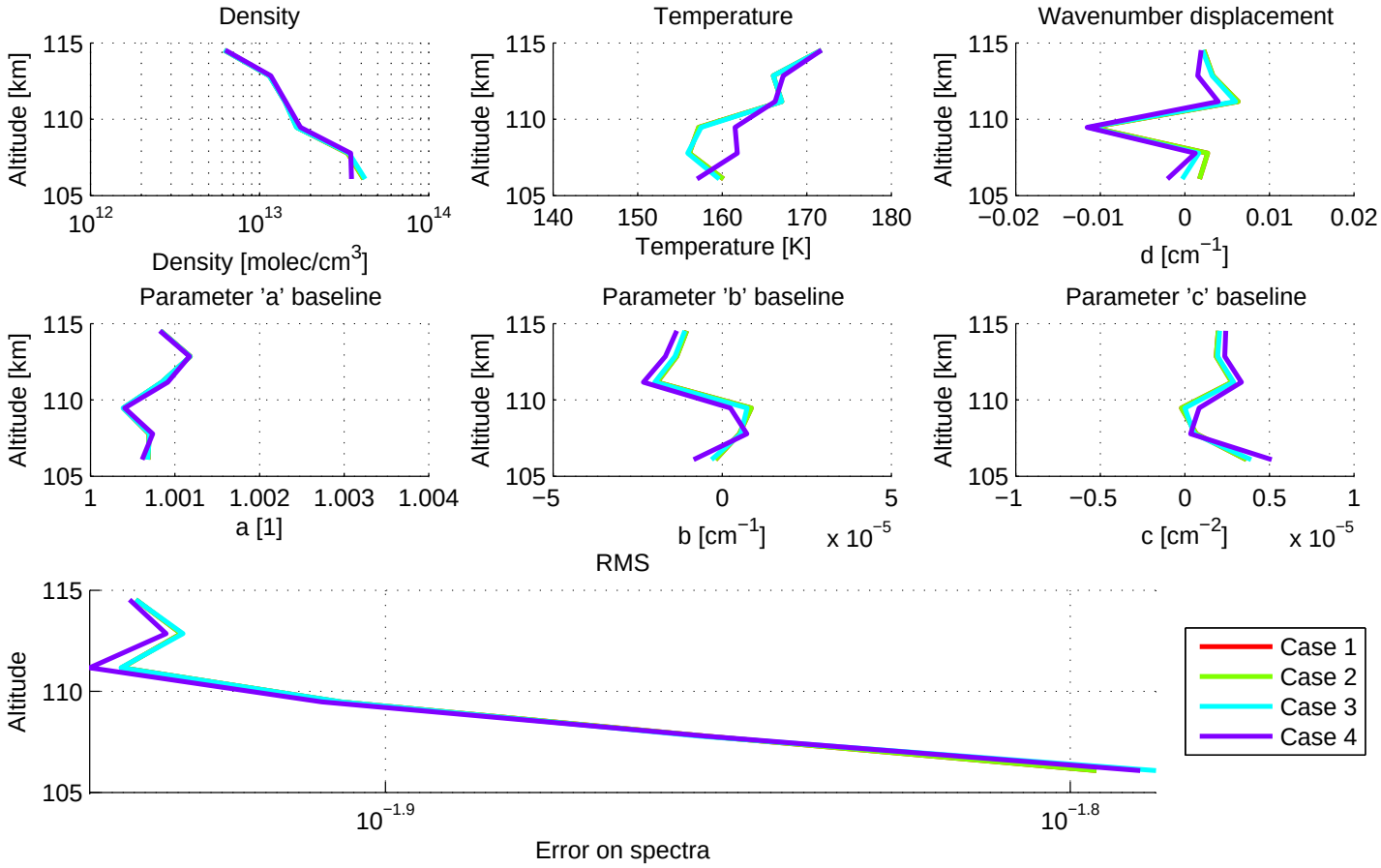

Figure 4.38: Density, temperature, wavenumber displacement and background vertical profiles and RMS for the Sa_c covariance sensitivity test.

4.8.2.3 Density logarithm covariance

Eight different values are tested for the square root covariance on the density logarithm $\log n$ parameter: 10, 5, 4, 3, 2, 1, 0.5, 0.1. The vertical profiles resulting from the fit are presented in Figure 4.39, while the DOF and the number of iterations are given in Table 4.7.

The density DOF regularly decreases with lower density logarithm square root covariances. The RMS also gets better and lower for higher density logarithm square root covariances. The best RMS are obtained for cases 1, 2 and 3. It is observed on the vertical profiles of the different variables $\log n$, T, a, b and c, for which the too low square root covariances forbid the profiles to undergo too large changes, and thus to get closer to the solution. Case 1 seems to introduce large variation in the density profile that can be attributed to instabilities. They are less observed for cases 2 and 3.

The number of iterations is constant for all cases. For cases 5 to 8, six layers are fitted without saturation, because the problem is too constrained, and prohibits to reach larger density values.

We decided to take 5 as square root covariance for the $\log n$ parameter, to ensure a good fit and to damp the possible instabilities.

Case	a	b	c	n	t	$e+f$	n_{AOTF}	d	d_{AOTF}	Iterations
1	5.000	4.994	4.991	4.812	3.689	0.164	5.451	0.067	0.004	3
	5	5	5	5	5	2	49	5	1	
2	5.000	4.994	4.991	4.347	3.214	0.242	6.589	0.070	0.000	3
	5	5	5	5	5	2	49	5	1	
3	5.000	4.994	4.991	3.986	3.396	0.226	5.443	0.072	0.001	3
	5	5	5	5	5	2	49	5	1	
4	5.000	4.994	4.991	3.634	2.944	0.104	6.133	0.131	0.000	3
	5	5	5	5	5	2	49	5	1	
5	6.000	5.992	5.989	3.626	2.305	0.604	6.789	0.115	0.000	3
	6	6	6	6	6	2	49	6	1	
6	6.000	5.992	5.989	3.158	1.054	0.143	7.109	0.057	0.001	3
	6	6	6	6	6	2	49	6	1	
7	6.000	5.992	5.989	3.033	0.172	0.079	7.260	0.016	0.001	3
	6	6	6	6	6	2	49	6	1	
8	6.000	5.992	5.989	2.996	0.052	0.077	7.286	0.016	0.000	3
	6	6	6	6	6	2	49	6	1	

Table 4.7: DOF and convergence steps of the Sa_n covariance sensitivity test. The case, the degrees of freedom of the a, b, c (baseline parameters), $\log n$ (density logarithm), T (temperature), e, f (wavenumber scale), n_{AOTF} (AOTF function fit), d_{AOTF} (AOTF wavenumber scale fit) and the number of iterations are given. For each case, the first line gives the DOF while the second gives the number of variables of each parameter, i.e. the maximum value of the DOF.

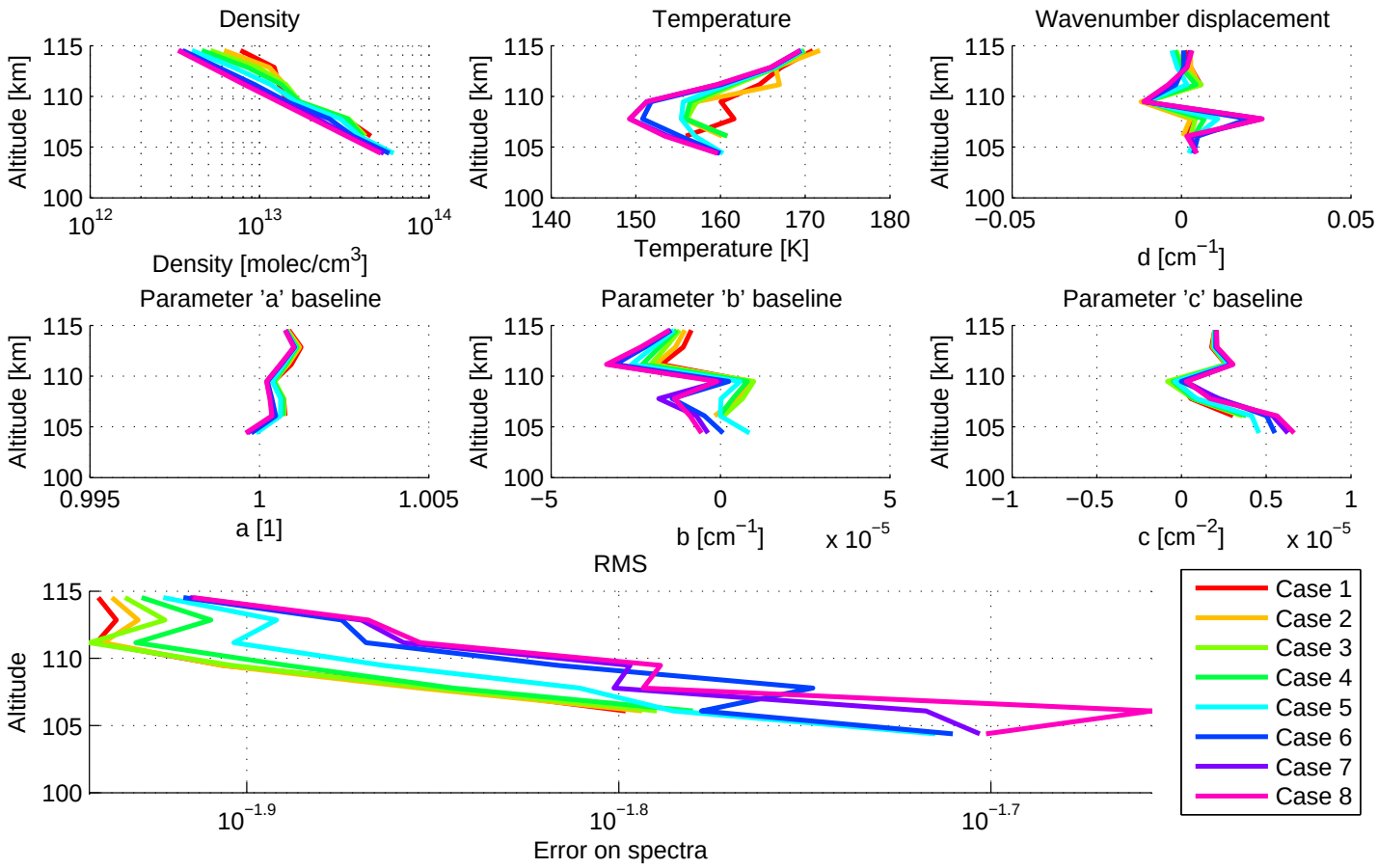

Figure 4.39: Density, temperature, wavenumber displacement and background vertical profiles and RMS for the Sa_n covariance sensitivity test.

4.8.2.4 Temperature covariance

Four different values are tested for the square root covariance on the temperature T parameter: 500, 200, 100, 10 [K]. The vertical profiles resulting from the fit are presented in Figure 4.40, while the DOF and the number of iterations are given in Table 4.8.

The temperature variable DOF are almost constant for the 4 cases. Only the temperature profiles are modified, all the other profiles are almost unchanged. The variations in the temperature profile are in the 40 K for case 1 compared to the other cases. Temperature variations in the order of 20 K on a 2 km altitude difference are observed, which seems rather large, and can be assimilated to instabilities within the algorithm. The RMS is slightly better for cases 1 and 2.

The number of iterations is constant for all cases.

We decided to take 200 K as square root covariance for the T parameter, to allow a valid fit while removing too large temperature variations within the different layers, and to reduce as much as possible the dependence of the a-priori temperature profile on the retrieved temperature profile.

Case	a	b	c	n	t	$e+f$	n_{AOTF}	d	d_{AOTF}	Iterations
1	5.000	4.994	4.991	4.334	3.400	0.614	6.985	0.072	0.002	3
	5	5	5	5	5	2	49	5	1	
2	5.000	4.994	4.991	4.352	3.274	0.180	5.654	0.071	0.000	3
	5	5	5	5	5	2	49	5	1	
3	5.000	4.994	4.991	4.344	3.169	0.056	5.129	0.093	0.002	3
	5	5	5	5	5	2	49	5	1	
4	5.000	4.994	4.991	4.324	3.209	0.001	5.099	0.099	0.001	3
	5	5	5	5	5	2	49	5	1	

Table 4.8: DOF and convergence steps of the Sa_n covariance sensitivity test. The case, the degrees of freedom of the a, b, c (baseline parameters), $\log n$ (density logarithm), T (temperature), e, f (wavenumber scale), n_{AOTF} (AOTF function fit), d_{AOTF} (AOTF wavenumber scale fit) and the number of iterations are given. For each case, the first line gives the DOF while the second gives the number of variables of each parameter, i.e. the maximum value of the DOF.

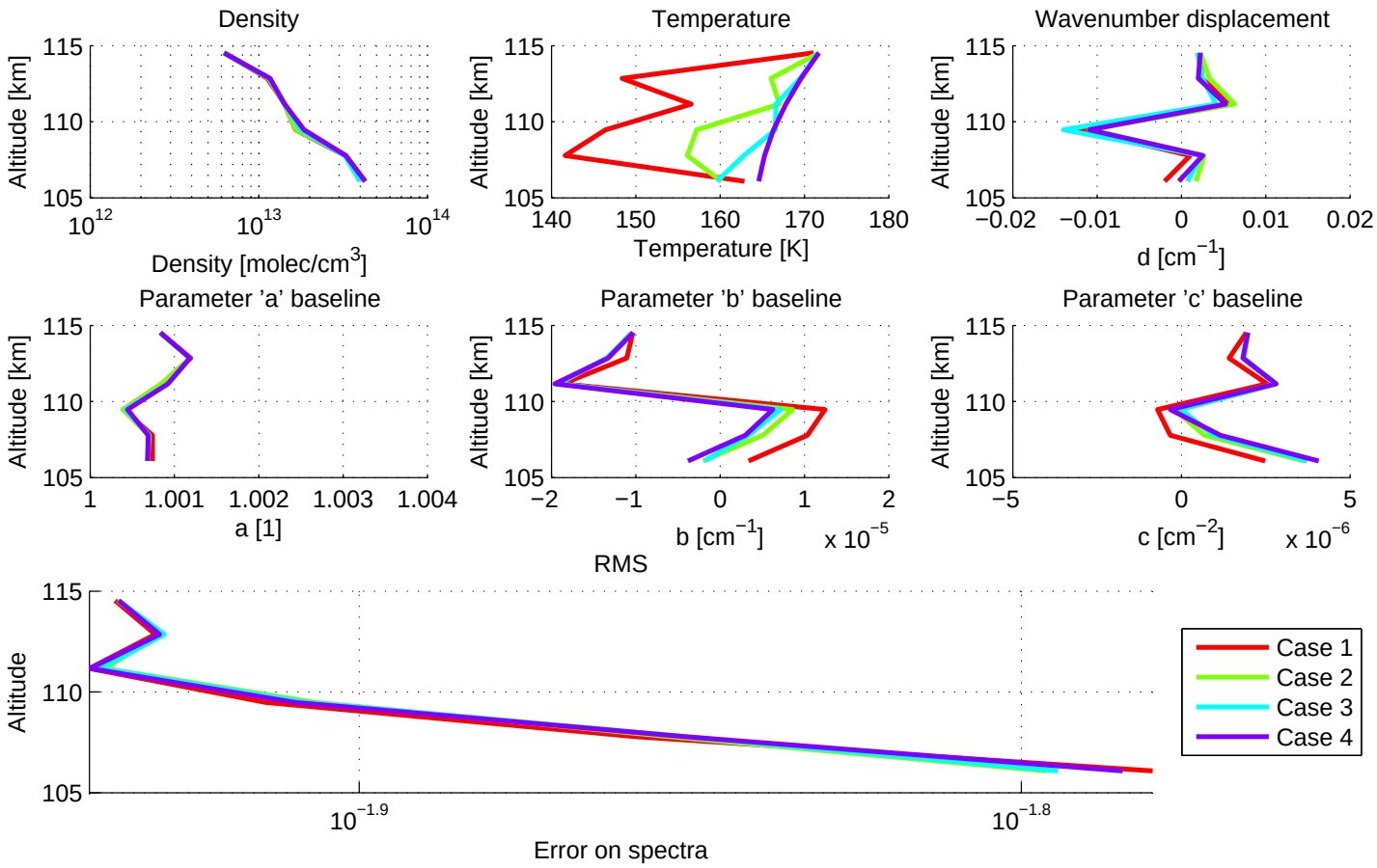

Figure 4.40: Density, temperature, wavenumber displacement and background vertical profiles and RMS for the Sa_t covariance sensitivity test.

4.8.2.5 AOTF parameters covariances

The AOTF fit covariance

The n_{AOTF} parameter fits the shape of the AOTF transfer function at several points.

Six different values are tested for the square root covariance on the AOTF fit n_{AOTF} parameter: 10, 5, 1, 0.5, 0.01, 0.001. The vertical profiles resulting from the fit are presented in Figure 4.41, while the DOF and the number of iterations are given in Table 4.9. The fitted AOTF function is plotted in Figure 4.42.

The best RMS is obtained for case 1. The wavenumber displacement and the background a profiles are not influenced. All the other profiles are mostly the same. Concerning the AOTF transfer function itself, cases 1 and 2 induce very large corrections, to the point that it completely looses its sinc square shape. Case 3 slightly modifies the transfer function, but keeps the main shape, and enhances the RMS.

The number of iterations is constant (3) except for case 1 (4).

We decided to take 1 as square root covariance for the n_{AOTF} parameter. Indeed, this value prevent from too large excursions of the AOTF transfer function, while sensibly enhancing the quality of the fits.

This test shows how important a good knowledge of the AOTF transfer function is to obtain a meaningful fit.

Case	a	b	c	n	t	$e+f$	n_{AOTF}	d	d_{AOTF}	Iterations
1	5.000	4.994	4.991	4.348	3.204	0.173	8.539	0.277	0.001	4
	5	5	5	5	5	2	49	5	1	
2	5.000	4.994	4.991	4.348	3.070	0.155	7.347	0.359	0.013	3
	5	5	5	5	5	2	49	5	1	
3	5.000	4.994	4.991	4.352	3.274	0.180	5.654	0.071	0.000	3
	5	5	5	5	5	2	49	5	1	
4	5.000	4.994	4.991	4.348	3.231	0.210	4.573	0.029	0.001	3
	5	5	5	5	5	2	49	5	1	
5	5.000	4.994	4.991	4.353	3.243	0.113	4.411	0.000	0.000	3
	5	5	5	5	5	2	49	5	1	
6	5.000	4.994	4.991	4.353	3.243	0.113	4.411	0.000	0.000	3
	5	5	5	5	5	2	49	5	1	

Table 4.9: DOF and convergence steps of the $Sa_{n_{AOTF}}$ covariance sensitivity test. The case, the degrees of freedom of the a, b, c (baseline parameters), $\log n$ (density logarithm), T (temperature), e, f (wavenumber scale), n_{AOTF} (AOTF function fit), d_{AOTF} (AOTF wavenumber scale fit) and the number of iterations are given. For each case, the first line gives the DOF while the second gives the number of variables of each parameter, i.e. the maximum value of the DOF.

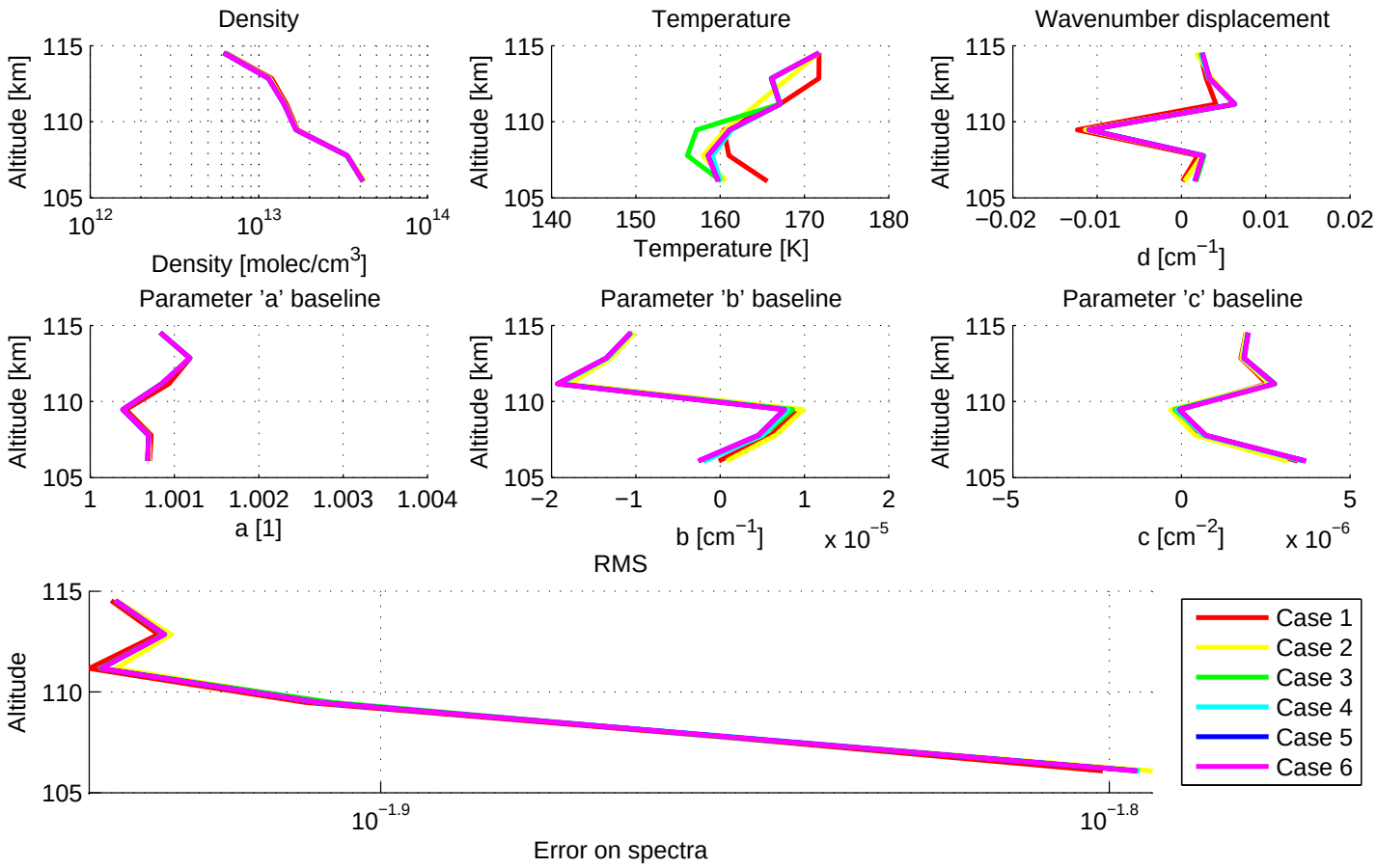

Figure 4.41: Density, temperature, wavenumber displacement and background vertical profiles and RMS for the $Sa_{n_{AOTF}}$ covariance sensitivity test.

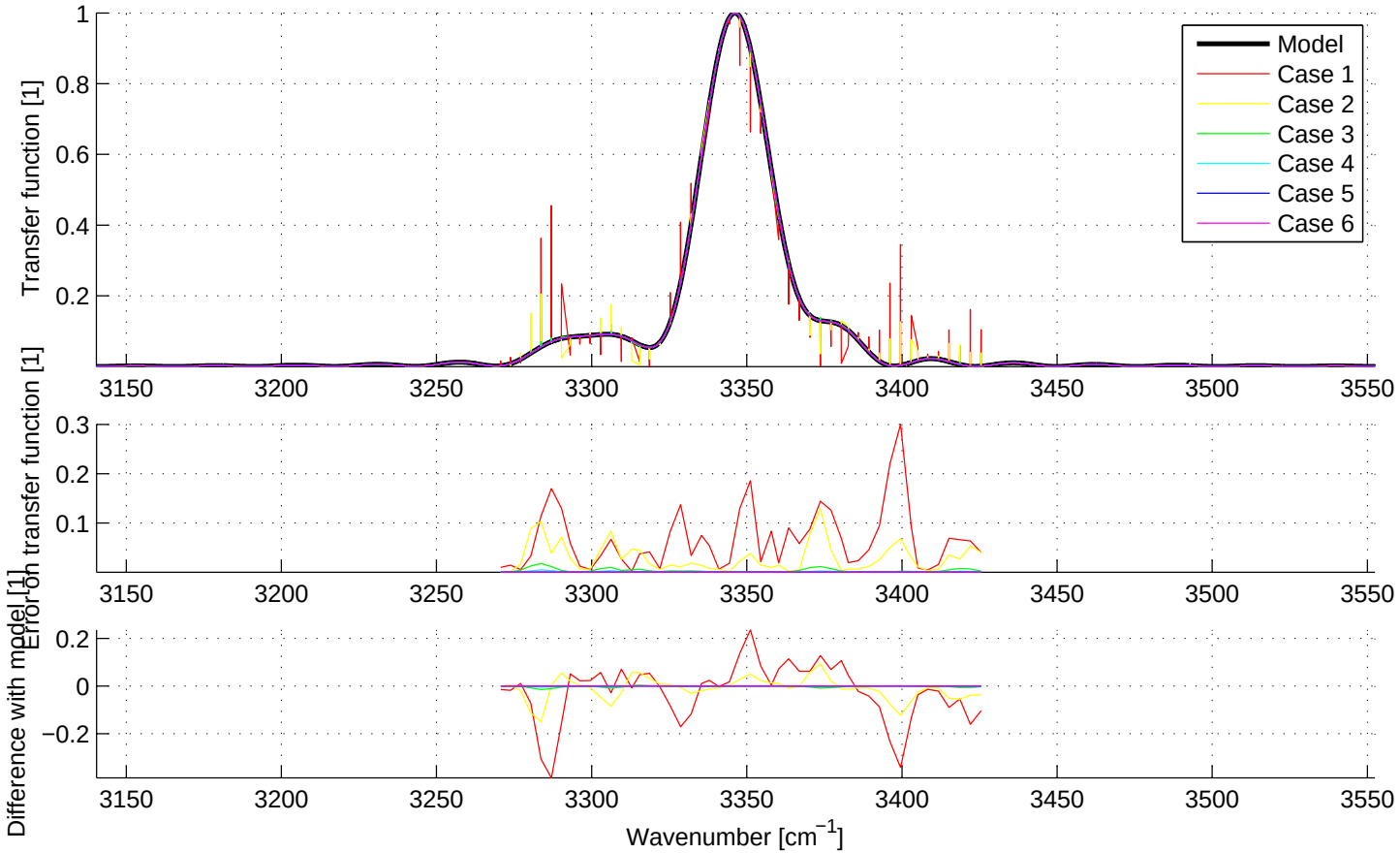

Figure 4.42: AOTF fitted function for the $Sa_{n_{AOTF}}$ covariance sensitivity test. The top Panel shows the retrieved AOTF function. The black line is the a-priori AOTF function. The central Panel gives the error on the retrieved AOTF function for the different cases. The bottom Panel shows the difference between the a-priori and the fitted AOTF transfer function.

The AOTF displacement covariance

The d_{AOTF} parameter allows a wavenumber displacement of the whole AOTF transfer function.

Four different values are tested for the square root covariance on the AOTF displacement fit d_{AOTF} parameter: 10, 5, 0.1, 0.01 [cm^{-1}]. The vertical profiles resulting from the fit are presented in Figure 4.43, while the DOF and the number of iterations are given in Table 4.11. The fitted AOTF function is plotted in Figure 4.44. The values obtained from the fit for d_{AOTF} are summarized in Table 4.10.

The best RMS is obtained for case 3. All the profiles are mostly the same. The fitted values are negligible for cases 3 and 4, while noticeable changes are obtained for cases 1 and 2.

We decided to take 5 cm^{-1} as square root covariance for the d_{AOTF} parameter, as it the lowest value that is tested for which a consequent displacement is obtained.

The changes due to this fit do not seem to be relevant in the case of orbit 361.1. However, it has been noted in some other occultations that the AOTF transfer function could be displaced of a few tenth of cm^{-1}, in order to enhance the quality of the fit. For this reason, the variable d_{AOTF} is systematically fitted.

Case	d_{AOTF}	Error on d_{AOTF}
1	2.81E-01	3.32E-02
2	6.47E-02	2.15E-02
3	-2.57E-05	5.53E-05
4	-2.54E-07	5.50E-07

Table 4.10: Values of the fitted parameters d_{AOTF} for the AOTF displacement covariance sensitivity test. The first column is the case, the second column is the fitted value, the third one is the error obtained from the OE algorithm. The values are given in cm^{-1}.

Case	a	b	c	n	t	$e+f$	n_{AOTF}	d	d_{AOTF}	Iterations
1	5.000	4.994	4.991	4.337	3.221	0.201	6.361	0.066	0.000	3
	5	5	5	5	5	2	49	5	1	
2	5.000	4.994	4.991	4.352	3.274	0.180	5.654	0.071	0.000	3
	5	5	5	5	5	2	49	5	1	
3	5.000	4.994	4.991	4.337	3.157	0.231	5.365	0.078	0.001	3
	5	5	5	5	5	2	49	5	1	
4	5.000	4.994	4.991	4.337	3.157	0.231	5.365	0.078	0.001	3
	5	5	5	5	5	2	49	5	1	

Table 4.11: DOF and convergence steps of the $Sa_{d_{AOTF}}$ covariance sensitivity test. The case, the degrees of freedom of the a, b, c (baseline parameters), $\log n$ (density logarithm), T (temperature), e, f (wavenumber scale), n_{AOTF} (AOTF function fit), d_{AOTF} (AOTF wavenumber scale fit) and the number of iterations are given. For each case, the first line gives the DOF while the second gives the number of variables of each parameter, i.e. the maximum value of the DOF.

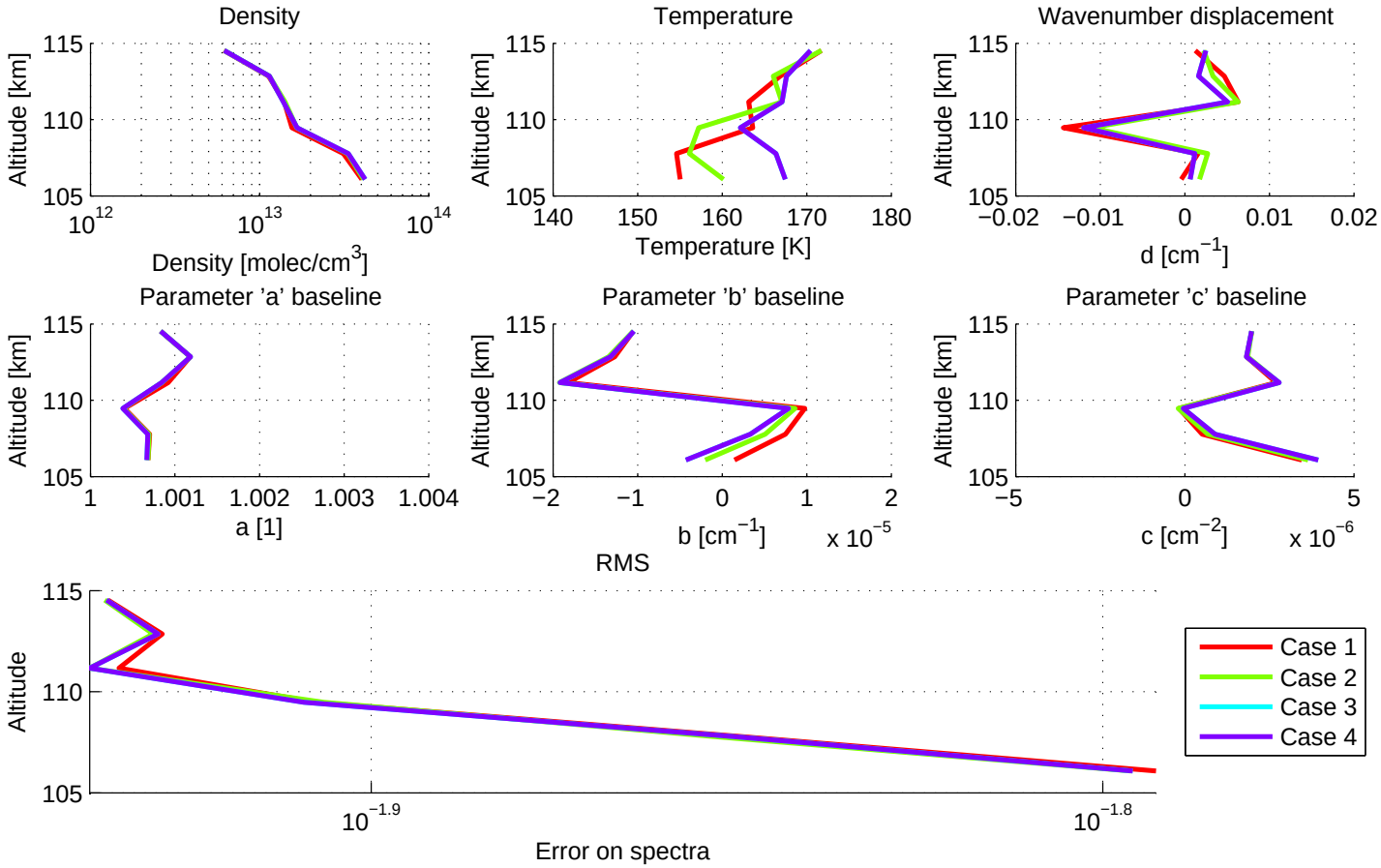

Figure 4.43: Density, temperature, wavenumber displacement and background vertical profiles and RMS for the $Sa_{d_{AOTF}}$ covariance sensitivity test.

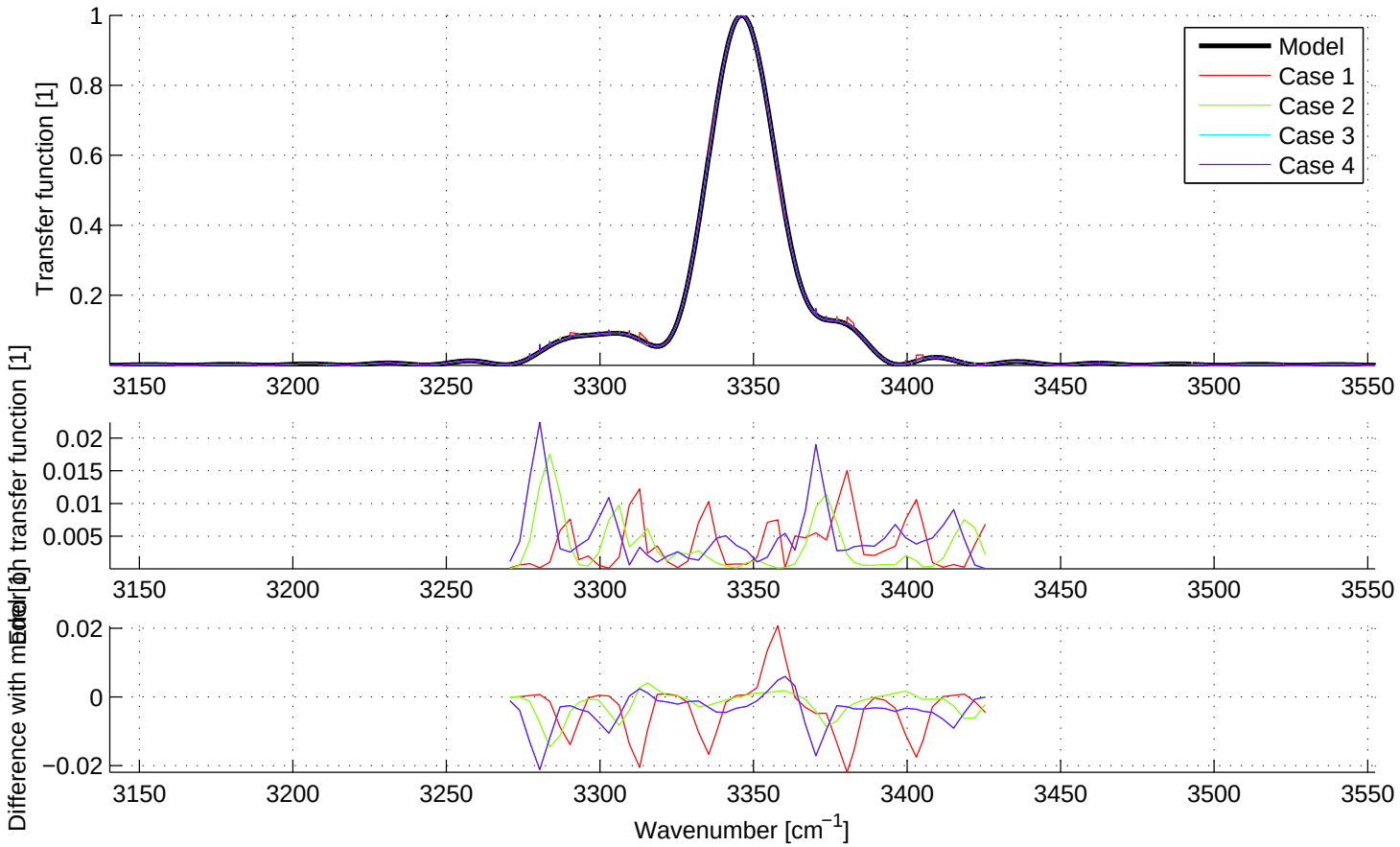

Figure 4.44: AOTF fitted function for the $Sa_{d_{AOTF}}$ covariance sensitivity test. The top Panel shows the retrieved AOTF function. The black line is the a-priori AOTF function. The central Panel gives the error on the retrieved AOTF function for the different cases. The bottom Panel shows the difference between the a-priori and the fitted AOTF transfer function.

4.8.2.6 Wavenumber scale relation covariances

The e variable

The e variable is the constant term of the wavenumber scale fit.

Six different values are tested for the square root covariance on the wavenumber scale e parameter: 10, 5, 1, 0.1, 0.01, 0.001 [cm^{-1}]. The vertical profiles resulting from the fit are presented in Figure 4.45, while the DOF and the number of iterations are given in Table 4.13. The values of the fitted parameters are given in Table 4.12.

The vertical profiles are not sensitive to the Sa_e variations, except the temperature profile. The number of iterations is constant (except for case 6), as the DOF are. The RMS is slightly better for case 4.

The fitted value is constant for square root covariances larger than 5 (cases 1 and 2). For this reason, we decided to take 5 cm^{-1} as square root covariance for the e parameter.

Case	e	Error on e
1	2.13E-02	2.70E-03
2	2.13E-02	2.71E-03
3	2.09E-02	2.61E-03
4	1.60E-02	5.59E-04
5	6.50E-04	3.08E-04
6	4.80E-06	9.97E-07

Table 4.12: Values of the fitted parameters e wavenumber scale covariance sensitivity test. The first column is the case, the second column is the fitted value, the third one is the error obtained from the OE algorithm. The values are given in cm^{-1}.

Case	a	b	c	n	t	$e+f$	n_{AOTF}	d	d_{AOTF}	Iterations
1	5.000	4.994	4.991	4.352	3.275	0.180	5.652	0.071	0.000	3
	5	5	5	5	5	2	49	5	1	
2	5.000	4.994	4.991	4.352	3.274	0.180	5.654	0.071	0.000	3
	5	5	5	5	5	2	49	5	1	
3	5.000	4.994	4.991	4.351	3.234	0.174	6.263	0.073	0.000	3
	5	5	5	5	5	2	49	5	1	
4	5.000	4.994	4.991	4.317	3.122	0.254	5.848	0.073	0.001	3
	5	5	5	5	5	2	49	5	1	
5	6.000	5.992	5.989	5.264	3.615	0.209	7.140	0.077	0.006	3
	6	6	6	6	6	2	49	6	1	
6	6.000	5.992	5.989	5.287	3.506	0.255	6.194	0.076	0.006	4
	6	6	6	6	6	2	49	6	1	

Table 4.13: DOF and convergence steps of the Sa_e covariance sensitivity test. The case, the degrees of freedom of the a, b, c (baseline parameters), $\log n$ (density logarithm), T (temperature), e, f (wavenumber scale), n_{AOTF} (AOTF function fit), d_{AOTF} (AOTF wavenumber scale fit) and the number of iterations are given. For each case, the first line gives the DOF while the second gives the number of variables of each parameter, i.e. the maximum value of the DOF.

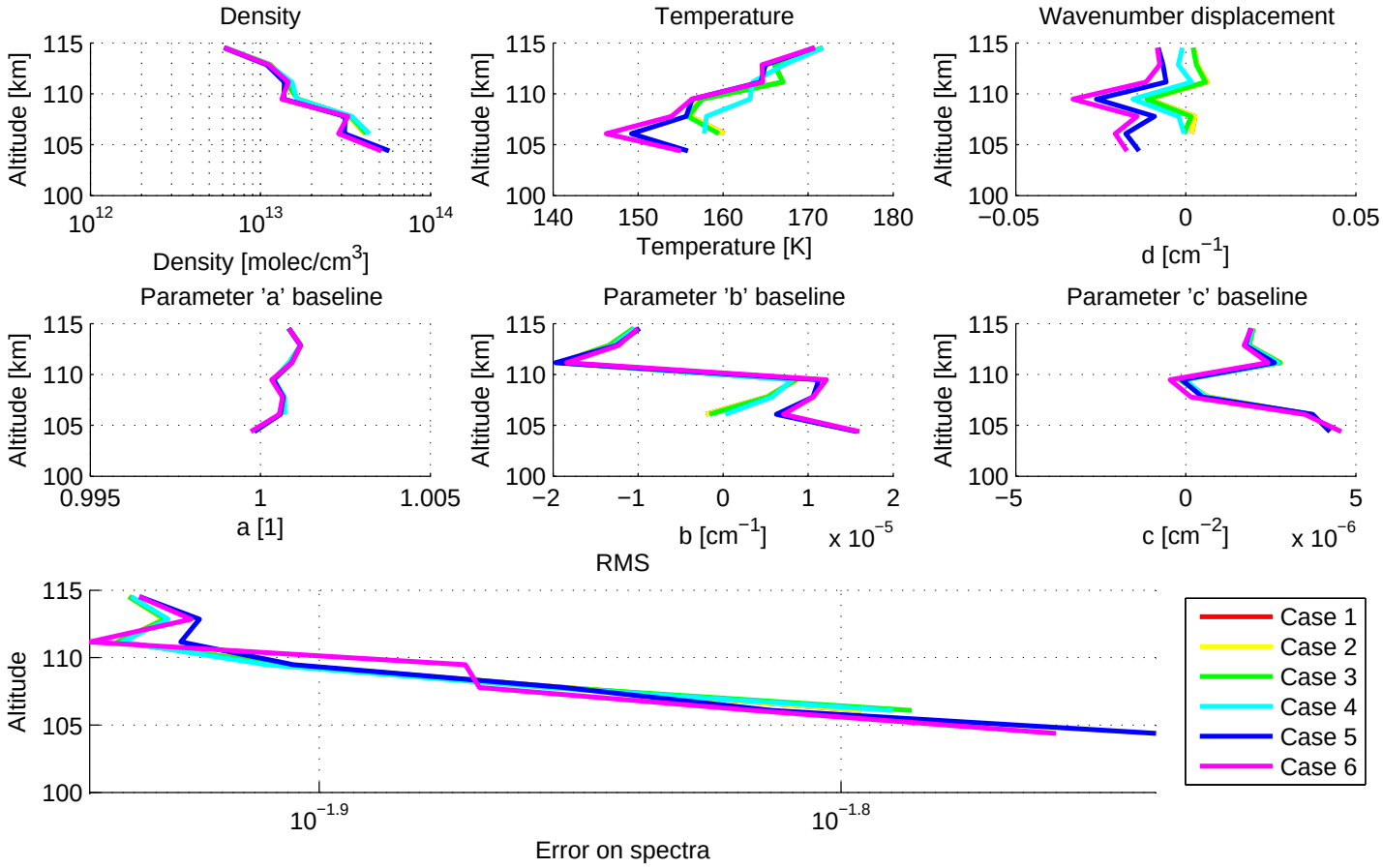

Figure 4.45: Density, temperature, wavenumber displacement and background vertical profiles and RMS for the Sa_e covariance sensitivity test.

The f variable

The f variable is the linear term factor of the wavenumber scale fit.

Five different values are tested for the square root covariance on the wavenumber scale f parameter: 1, 0.1, 0.01, 0.001, 0.0001 [1]. The vertical profiles resulting from the fit are presented in Figure 4.46, while the DOF and the number of iterations are given in Table 4.15. The values of the fitted parameters are given in Table 4.14.

The vertical profiles are quasi not sensitive to the Sa_f variations. The number of iterations slightly increases for cases 1 and 2, and the DOF are roughly constant. The RMS is slightly better for cases 1 and 2.

The fitted value is constant for square root covariances larger than 0.1 (cases 1 and 2). For this reason, we decided to take 0.1 as square root covariance for the f parameter.

Case	f	Error on f
1	1.24E-03	3.43E-05
2	1.24E-03	3.83E-05
3	8.77E-04	4.23E-04
4	2.10E-05	2.03E-05
5	2.14E-07	2.08E-07

Table 4.14: Values of the fitted parameters f wavenumber scale covariance sensitivity test. The first column is the case, the second column is the fitted value, the third one is the error obtained from the OE algorithm. The values are given without units.

Case	a	b	c	n	t	$e+f$	n_{AOTF}	d	d_{AOTF}	Iterations
1	6.000	5.992	5.989	5.079	3.575	0.209	7.094	0.084	0.009	4
	6	6	6	6	6	2	49	6	1	
2	6.000	5.992	5.989	5.077	3.586	0.232	7.103	0.084	0.009	4
	6	6	6	6	6	2	49	6	1	
3	5.000	4.994	4.991	4.360	3.156	0.177	6.189	0.072	0.000	3
	5	5	5	5	5	2	49	5	1	
4	5.000	4.994	4.991	4.346	3.347	0.141	6.576	0.077	0.000	3
	5	5	5	5	5	2	49	5	1	
5	5.000	4.994	4.991	4.346	3.099	0.110	6.148	0.072	0.000	3
	5	5	5	5	5	2	49	5	1	

Table 4.15: DOF and convergence steps of the Sa_f covariance sensitivity test. The case, the degrees of freedom of the a, b, c (baseline parameters), $\log n$ (density logarithm), T (temperature), e, f (wavenumber scale), n_{AOTF} (AOTF function fit), d_{AOTF} (AOTF wavenumber scale fit) and the number of iterations are given. For each case, the first line gives the DOF while the second gives the number of variables of each parameter, i.e. the maximum value of the DOF.

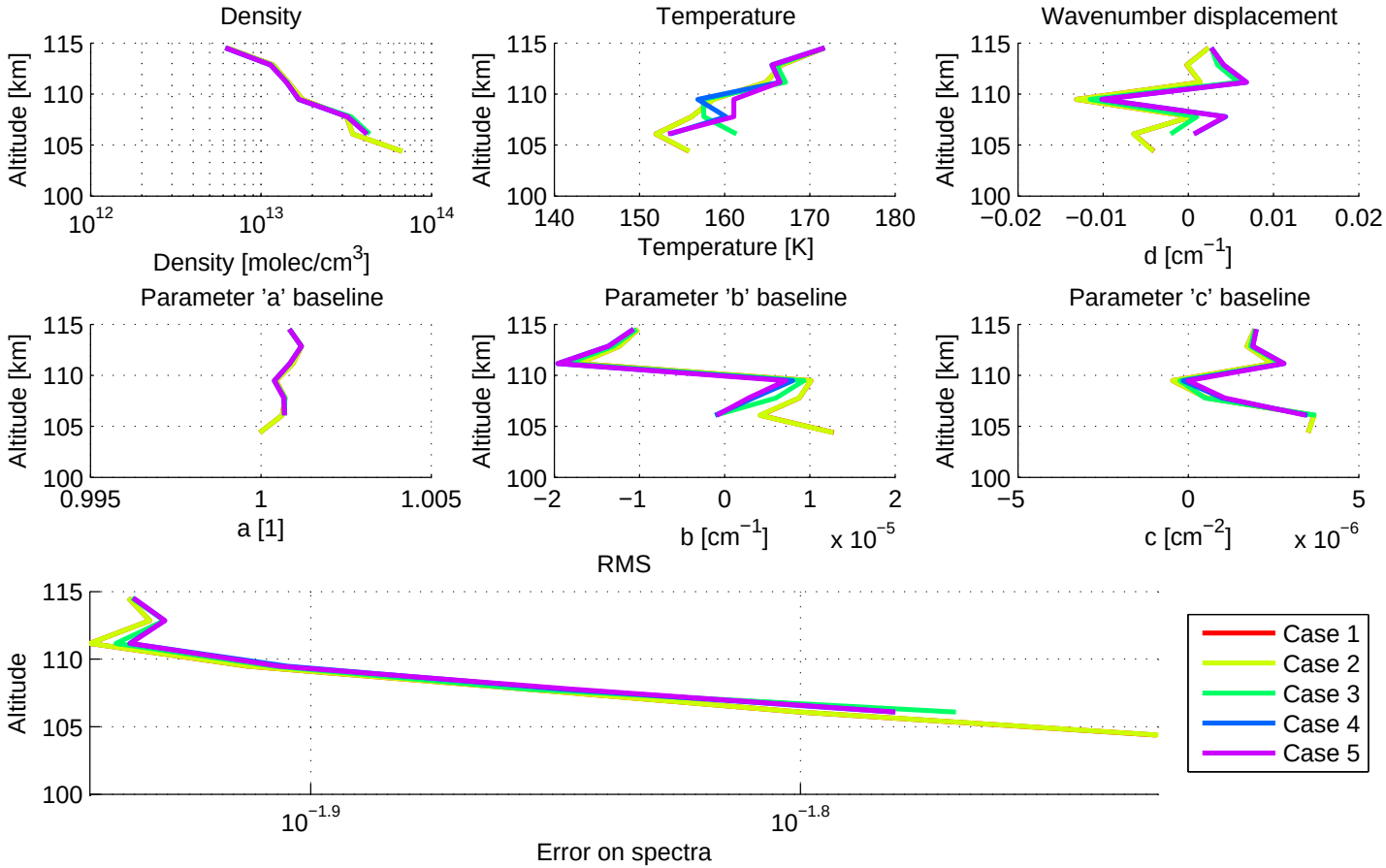

Figure 4.46: Density, temperature, wavenumber displacement and background vertical profiles and RMS for the Sa_f covariance sensitivity test. In the density and temperature Panels, the black line is the a-priori.

4.8.2.7 Wavenumber scale covariances

The d parameters are the wavenumber scale displacement introduced in each layer to correct for the possible Doppler shifts.

Five different values are tested for the square root covariance on the wavenumber scale d parameter: 10, 1, 0.1, 0.01, 0.001 [cm^{-1}]. The vertical profiles resulting from the fit are presented in Figure 4.47, while the DOF and the number of iterations are given in Table 4.16.

The vertical profiles depend on the value of Sa_d. The DOF are slightly variable. It may be hard to elect the best candidate. However, cases 2 and 3 show a lower RMS.

We decided to take 0.01 cm^{-1} as square root covariance for the d parameter.

Case	a	b	c	n	t	$e+f$	n_{AOTF}	d	d_{AOTF}	Iterations
1	6.000	5.992	5.989	5.211	3.555	0.193	10.679	0.095	0.000	4
	6	6	6	6	6	2	49	6	1	
2	6.000	5.992	5.989	5.111	3.443	0.668	11.070	0.083	0.000	4
	6	6	6	6	6	2	49	6	1	
3	5.000	4.994	4.991	4.360	3.156	0.177	6.189	0.072	0.000	3
	5	5	5	5	5	2	49	5	1	
4	6.000	5.992	5.989	5.320	3.779	0.435	4.650	0.085	0.004	3
	6	6	6	6	6	2	49	6	1	
5	7.000	6.991	6.987	6.238	4.076	0.357	3.802	0.103	0.000	4
	7	7	7	7	7	2	49	7	1	

Table 4.16: DOF and convergence steps of the Sa_d covariance sensitivity test. The case, the degrees of freedom of the a, b, c (baseline parameters), $\log n$ (density logarithm), T (temperature), e, f (wavenumber scale), n_{AOTF} (AOTF function fit), d_{AOTF} (AOTF wavenumber scale fit) and the number of iterations are given. For each case, the first line gives the DOF while the second gives the number of variables of each parameter, i.e. the maximum value of the DOF.

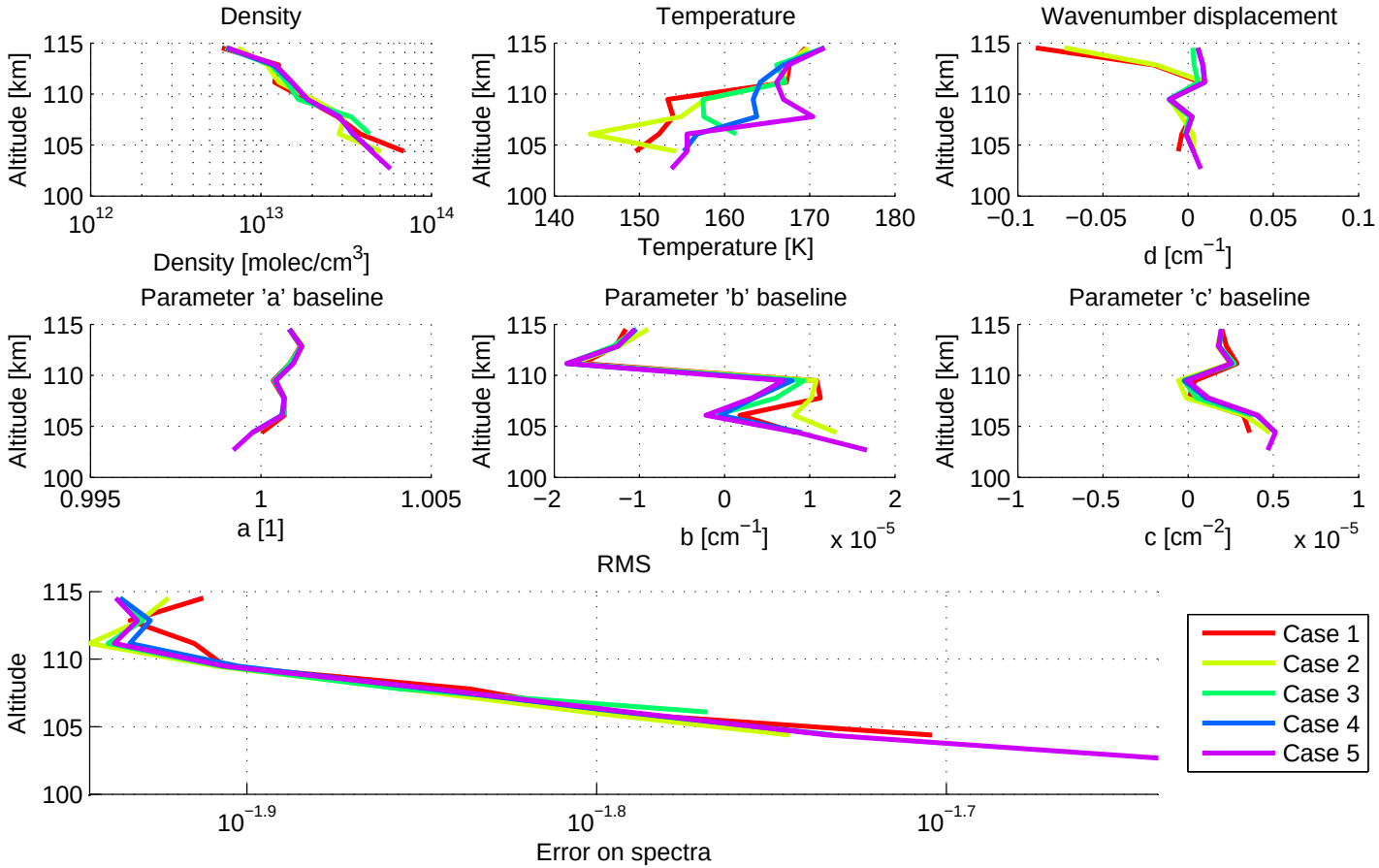

Figure 4.47: Density, temperature, wavenumber displacement and background vertical profiles and RMS for the Sa_d covariance sensitivity test. In the density and temperature Panels, the black line is the a-priori.

4.8.3 Sensitivity to the a-priori value

We study here the influence of the temperature and density a-priori, to evaluate the robustness of this fit with respect to the a-priori. The different cases are summarized in Table 4.17. The linear density guess has been described in Section 4.6.7.

Case	A-priori density	Linear density guess	A-priori temperature
1	Model	Yes	Model
2	Model	No	Model
1	Model	Yes	Model - 20
2	Model	Yes	Model - 10
3	Model	Yes	Model
4	Model	Yes	Model + 10
5	Model	Yes	Model + 20

Table 4.17: Description of the test cases for the a-priori density and temperature influence study.

4.8.3.1 Density

Two different cases are studied, see the first 2 lines of Table 4.17. They study the influence of the density guess (see Section 4.6.7): with the density initial guess in case 1, and without in case 2. The vertical profiles are presented in Figure 4.48, and the DOF are presented in Table 4.18. The vertical profiles are very similar, but the RMS is slightly better when the linear density guess is performed. The linear density guess of case 1 resulted in a factor 0.268 of the initial density profile. It allowed the a-priori density profile to get close enough to the solution to allow the convergence.

Case	a	b	c	n	t	$e+f$	n_{AOTF}	d	d_{AOTF}	Iterations
1	7.000	6.994	6.992	6.218	3.945	0.386	8.918	0.118	0.008	4
	7	7	7	7	7	2	49	7	1	
2	7.000	6.994	6.992	6.366	4.102	0.446	9.042	0.203	0.002	5
	7	7	7	7	7	2	49	7	1	

Table 4.18: DOF and convergence steps for the a-priori density influence study. The case, the degrees of freedom of the a, b, c (baseline parameters), $\log n$ (density logarithm), T (temperature), e, f (wavenumber scale), n_{AOTF} (AOTF function fit), d_{AOTF} (AOTF wavenumber scale fit) and the number of iterations are given. For each case, the first line gives the DOF while the second gives the number of variables of each parameter, i.e. the maximum value of the DOF.

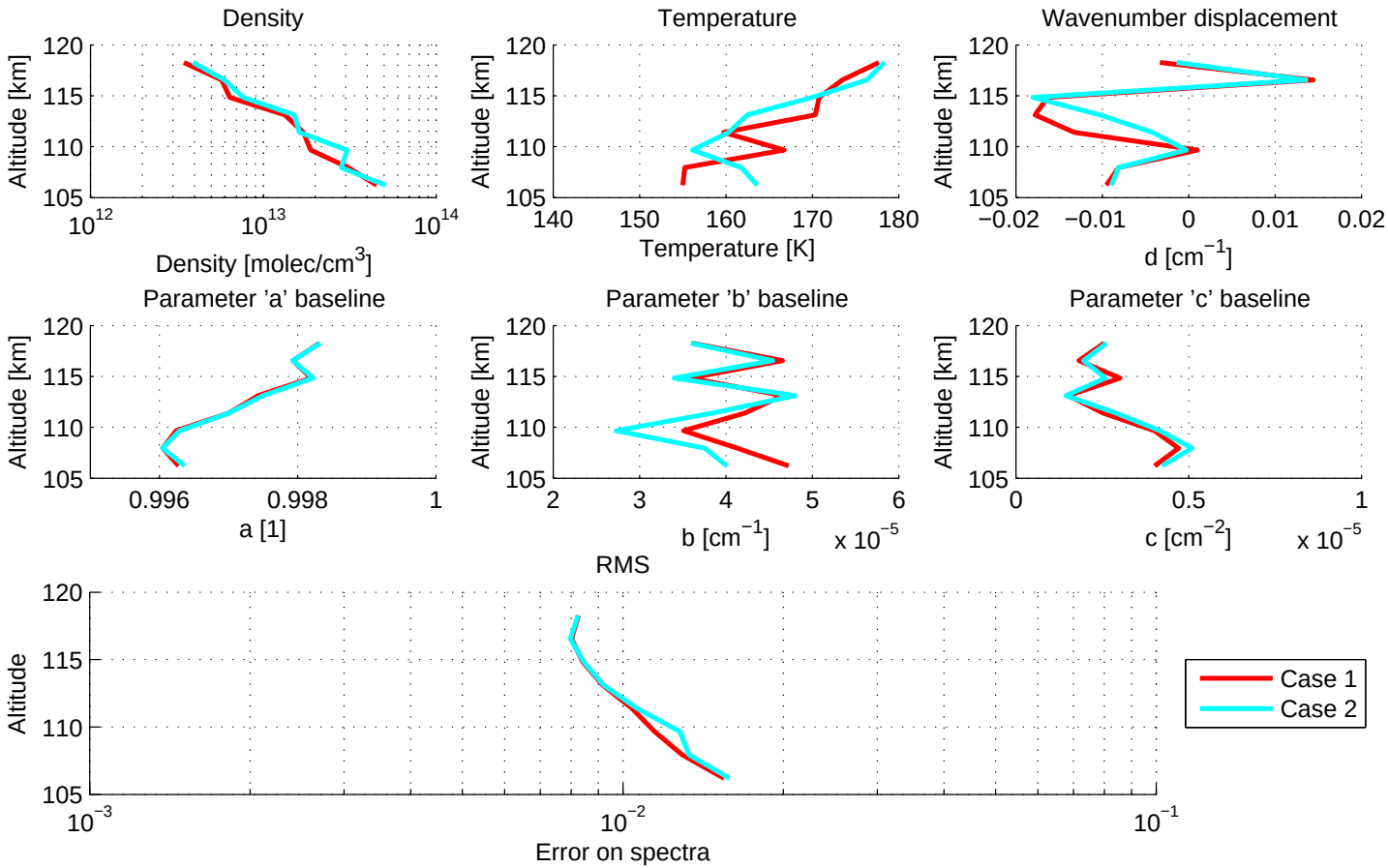

Figure 4.48: Vertical profiles and RMS for the a-priori density fit. Density, temperature, wavenumber displacement and background vertical profiles and RMS for the a-priori density influence fit.

4.8.3.2 Temperature

Five different values to the temperature a-priori are tested for the temperature a-priori sensitivity test: -20, -10, 0, 10, 20. They are listed in the 5 bottom lines of Table 4.17. The vertical profiles resulting from the fit are presented in Figure 4.49, while the DOF and the number of iterations are given in Table 4.19.

The density and background parameters profiles are slightly sensitive to the a-priori temperature variations. The temperature profiles are very variable. It suggests that the SOIR data and the algorithm are not robust in terms of temperature with respect to the a-priori temperature. That could be foreseen from what is explained in Section 4.6.9: the temperature fit enhances the quality of the results, but the shape of the AOTF function influences the precision on the results. From the DOF and the number of iterations, no conclusion can be drawn.

A lower limit of 20 K should be taken for the error bars on the temperature obtained from the OEM in order to consider the dependency of the retrieved temperature profile to the a-priori temperature profile.

Case	a	b	c	n	t	$e+f$	n_{AOTF}	d	d_{AOTF}	Iterations
1	7.000	6.994	6.992	6.452	3.941	0.191	9.198	0.139	0.000	5
	7	7	7	7	7	2	49	7	1	
2	7.000	6.994	6.992	5.988	4.053	0.389	8.330	0.141	0.000	3
	7	7	7	7	7	2	49	7	1	
3	7.000	6.994	6.992	6.218	3.945	0.386	8.918	0.118	0.008	4
	7	7	7	7	7	2	49	7	1	
4	7.000	6.994	6.992	6.188	3.969	0.291	8.288	0.178	0.000	3
	7	7	7	7	7	2	49	7	1	
5	8.000	7.993	7.991	7.421	4.235	0.482	10.240	0.234	0.000	4
	8	8	8	8	8	2	49	8	1	

Table 4.19: DOF and convergence steps for the a-priori temperature influence study. The case, the degrees of freedom of the a, b, c (baseline parameters), $\log n$ (density logarithm), T (temperature), e, f (wavenumber scale), n_{AOTF} (AOTF function fit), d_{AOTF} (AOTF wavenumber scale fit) and the number of iterations are given. For each case, the first line gives the DOF while the second gives the number of variables of each parameter, i.e. the maximum value of the DOF.

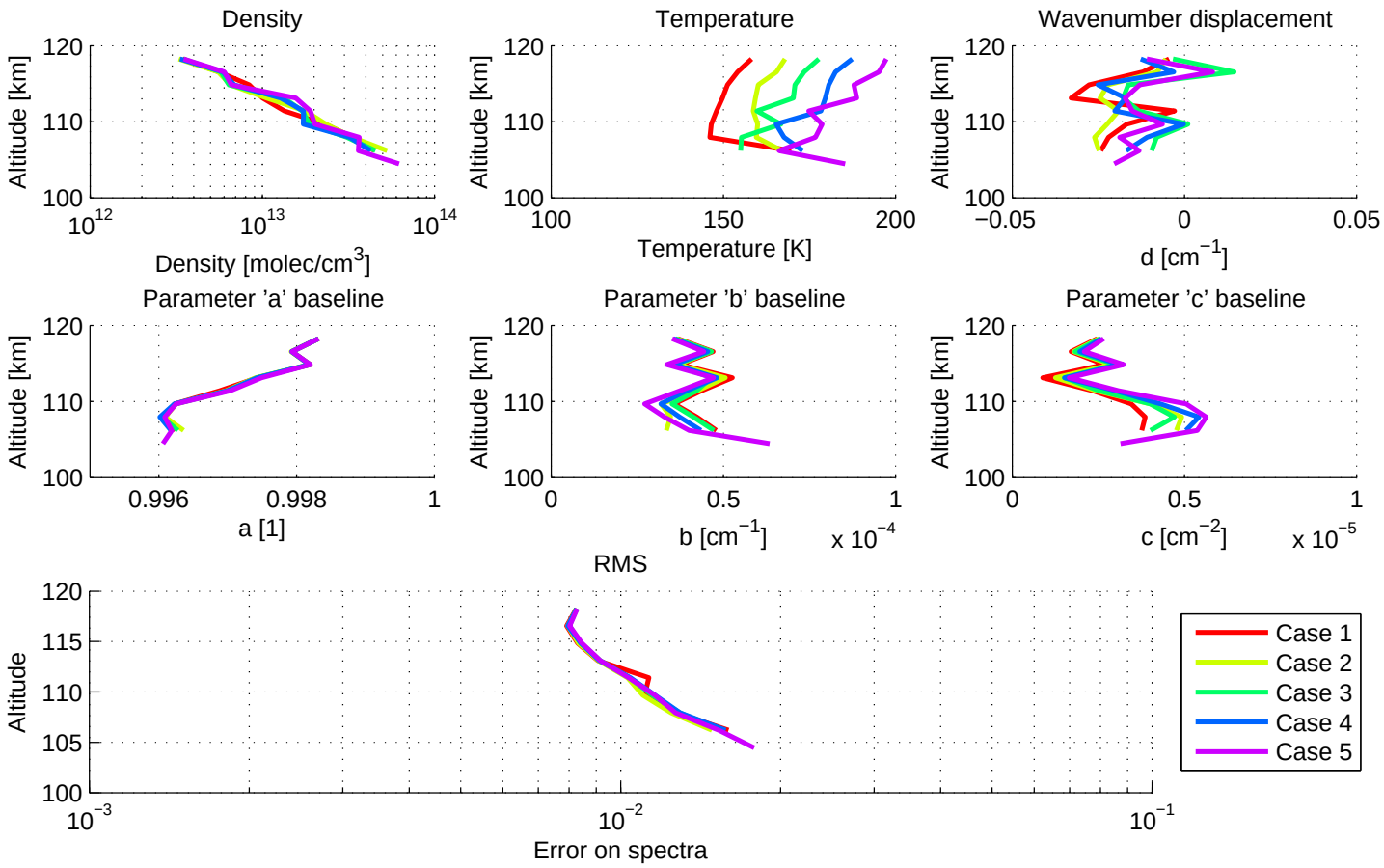

Figure 4.49: Density, temperature, wavenumber displacement and background vertical profiles and RMS for the a-priori temperature influence fit.

4.8.4 Sensitivity to the AOTF function parameters

We study here the influence of the AOTF parameters fit: the AOTF transmittance fit (n_{AOTF}) and the maximum wavenumber fit (d_{AOTF}). Four cases are defined and are summarized in Table 4.20. The vertical profiles resulting from the 4 cases are presented in Figure 4.50, while the DOF and the number of iterations are given in Table 4.21.

The vertical profiles are influenced by the the different cases, mostly the temperature profile. We see that the RMS are all in the same range. Fitting the AOTF decreases the temperature and the wavenumber shift d DOF.

The fit of AOTF function does not seem to influence the fit in the present example. However, it seems in other retrievals that the fit enhances the quality of the solution.

Case	AOTF fit	AOTF maximum displacement fit
1	Yes	Yes
2	No	Yes
3	Yes	No
4	No	No

Table 4.20: List of the cases for the AOTF fit influence study.

Case	a	b	c	n	t	$e+f$	n_{AOTF}	d	d_{AOTF}	Iterations
1	7.000	6.994	6.992	6.218	3.945	0.386	8.918	0.118	0.008	4
	7	7	7	7	7	2	49	7	1	
2	7.000	6.994	6.992	6.496	3.920	0.318		3.042	0.207	6
	7	7	7	7	7	2		7	1	
3	7.000	6.994	6.992	6.273	3.967	0.200	8.584	0.126		4
	7	7	7	7	7	2	49	7		
4	7.000	6.994	6.992	6.141	3.918	0.396		2.842		6
	7	7	7	7	7	2		7		

Table 4.21: DOF and convergence steps for the AOTF fit influence study. The case, the degrees of freedom of the a, b, c (baseline parameters), $\log n$ (density logarithm), T (temperature), e, f (wavenumber scale), n_{AOTF} (AOTF function fit), d_{AOTF} (AOTF wavenumber scale fit) and the number of iterations are given. For each case, the first line gives the DOF while the second gives the number of variables of each parameter, i.e. the maximum value of the DOF.

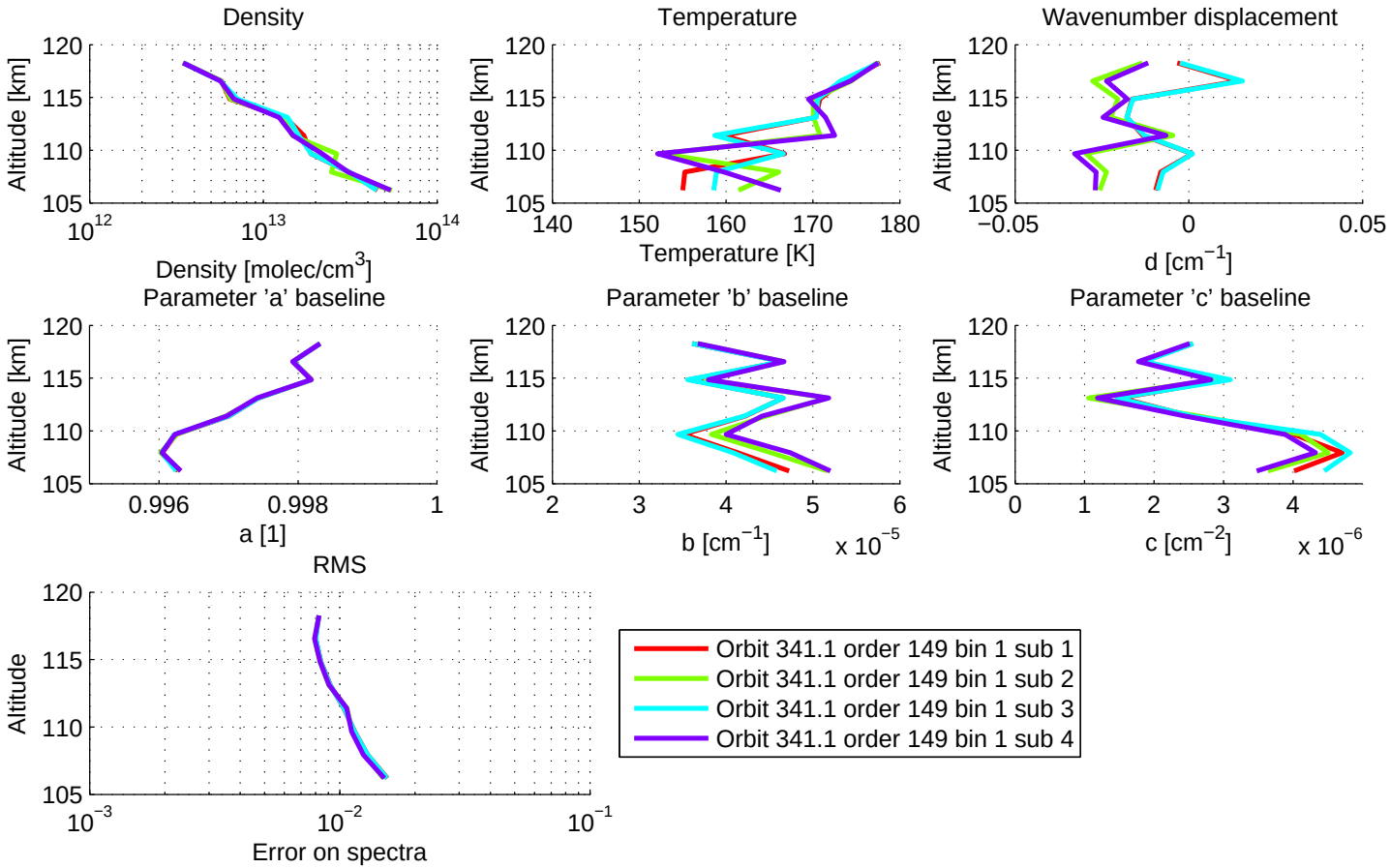

Figure 4.50: Density, temperature, wavenumber displacement and background vertical profiles and RMS for the study of the influence of the AOTF fit. The *sub* in reference corresponds to the case.

4.8.5 Sensitivity to the temperature fit

It is stated in Section 4.6.9 that the temperature dependence is quite weak, because the AOTF function strongly influences the shape of the rotational bands in our spectra. Moreover, it has been shown in Section 4.8.3.2 that the sensitivity to the a-priori temperature is high. This study aims to prove the usefulness of the temperature fit. The two cases are summarized in Table 4.22: with and without the temperature fit.

The vertical profiles and the RMS of the two cases are presented in Figure 4.51, and the DOF and number of iterations in Table 4.23. We see that the DOF of the two retrievals are almost the same, and thus are not influenced by the temperature fit. The vertical profiles are also mostly constant. But, when we take a look at the RMS, we see that there is an slight improvement. From this study, we conclude that the temperature fit at least enhances the quality of the fit. However, special care should be taken when considering the temperature profiles, as explained before in the text.

Case	Temperature fit
1	Yes
2	No

Table 4.22: List of the cases for the temperature fit influence study.

Case	a	b	c	n	t	$e+f$	n_{AOTF}	d	d_{AOTF}	Iterations
1	7.000	6.994	6.992	6.218	3.945	0.386	8.918	0.118	0.008	4
	7	7	7	7	7	2	49	7	1	
2	7.000	6.994	6.992	6.316		1.951	9.864	0.110	0.000	4
	7	7	7	7		2	49	7	1	

Table 4.23: DOF and convergence steps for the temperature fit influence study. The case, the degrees of freedom of the a, b, c (baseline parameters), $\log n$ (density logarithm), T (temperature), e, f (wavenumber scale), n_{AOTF} (AOTF function fit), d_{AOTF} (AOTF wavenumber scale fit) and the number of iterations are given. For each case, the first line gives the DOF while the second gives the number of variables of each parameter, i.e. the maximum value of the DOF.

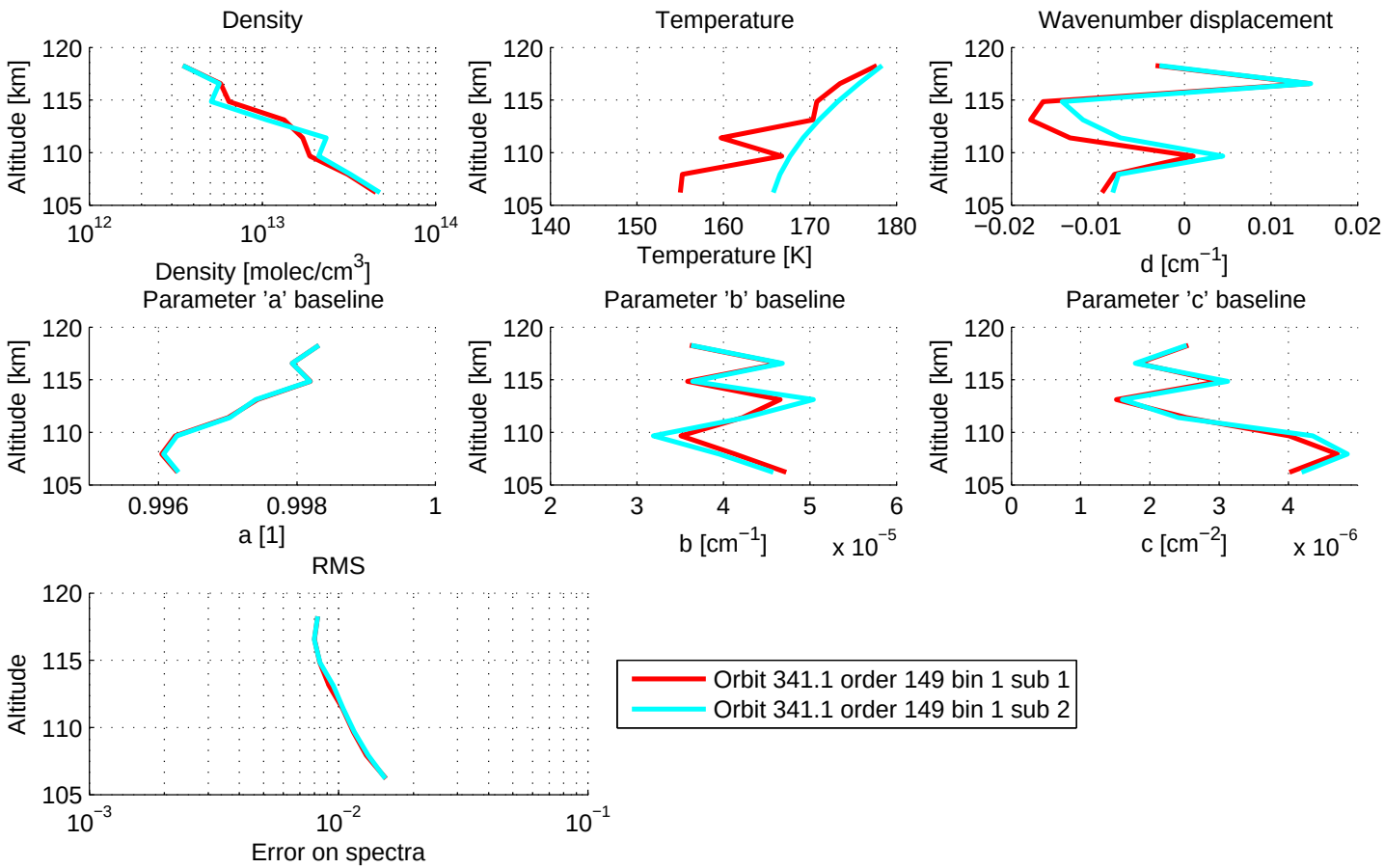

Figure 4.51: Density, temperature, wavenumber displacement and background vertical profiles and RMS for the study of the influence of the temperature fit. The *sub* in reference corresponds to the case.

4.8.6 Sensitivity to the wavenumber displacement fit

In this Section, we test the influence of the wavenumber displacement fit d. Two cases are defined, see Table 4.24, with and without the fit. The vertical profiles are given in Figure 4.52 and the DOF and number of iterations in Table 4.25.

For both cases, the a-priori as taken from what is described in Section 4.6.6.

We see that the density and temperature profiles are almost not sensible, either the background parameters. The wavenumber displacement profile is slightly shifted. The error bars are lower. The RMS is smaller for the all altitudes. The DOF of the density and the temperature are slightly lower in case 1 while the DOF of the AOTF fits are higher.

We can conclude from the slightly better RMS that the wavenumber shift fit enhances the quality of the fit.

Case	Displacement fit
1	Yes
2	No

Table 4.24: List of the cases for the wavenumber displacement fit influence study.

Case	a	b	c	n	t	$e+f$	n_{AOTF}	d	d_{AOTF}	Iterations
1	7.000	6.994	6.992	6.218	3.945	0.386	8.918	0.118	0.008	4
	7	7	7	7	7	2	49	7	1	
2	7.000	6.994	6.992	6.316		1.951	9.864	0.110	0.000	4
	7	7	7	7		2	49	7	1	

Table 4.25: DOF and convergence steps for the wavenumber displacement fit influence study. The case, the degrees of freedom of the a, b, c (baseline parameters), $\log n$ (density logarithm), T (temperature), e, f (wavenumber scale), n_{AOTF} (AOTF function fit), d_{AOTF} (AOTF wavenumber scale fit) and the number of iterations are given. For each case, the first line gives the DOF while the second gives the number of variables of each parameter, i.e. the maximum value of the DOF.

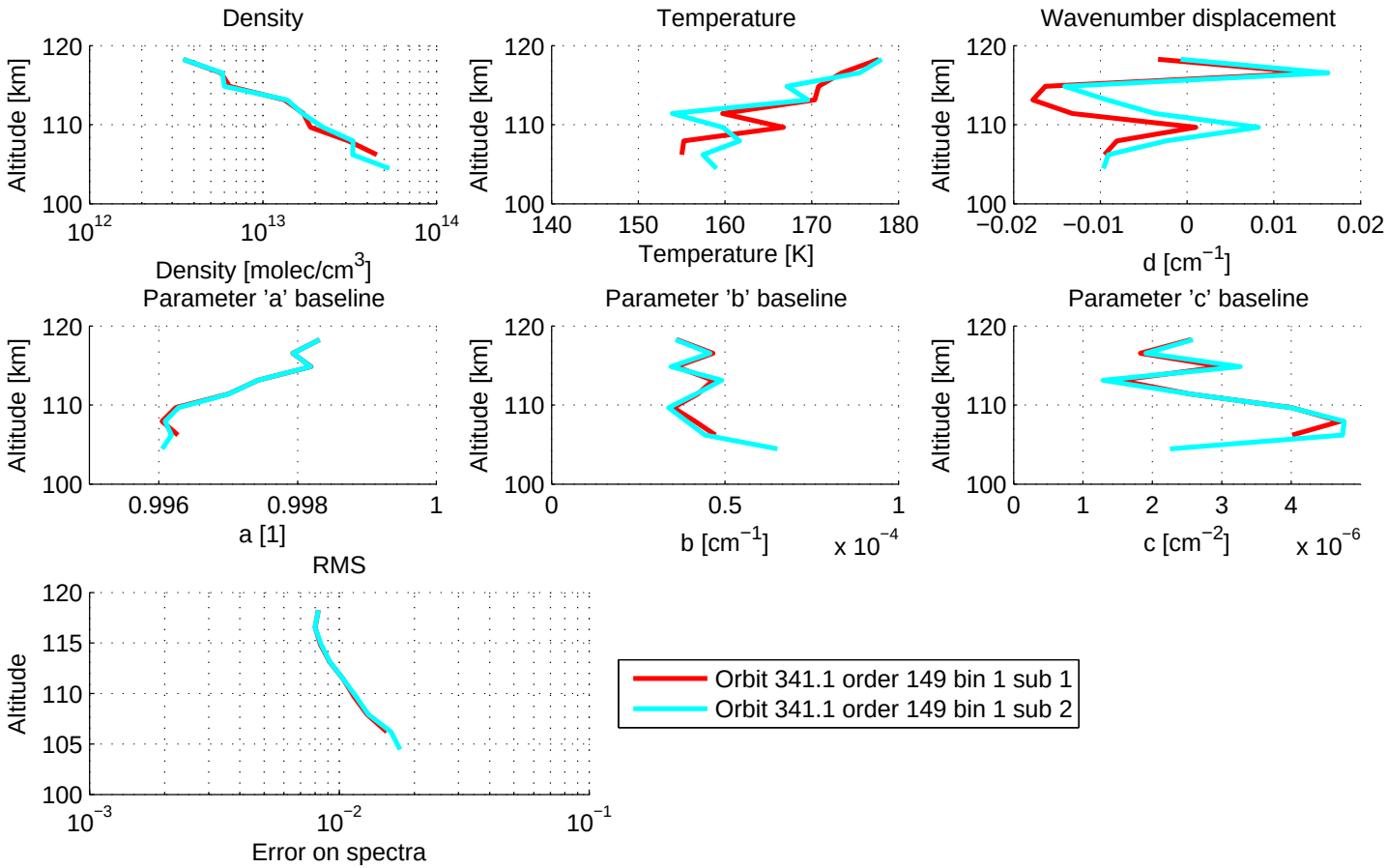

Figure 4.52: Density, temperature, wavenumber displacement and background vertical profiles and RMS for the study of the influence of the wavenumber displacement fit. The *sub* in reference corresponds to the case.

4.8.7 Sensitivity to the number of adjacent orders

The number of adjacent orders to take into account is difficult to determine.

On one hand, if the number of orders is too low, absorption lines coming from adjacent orders are not simulated by the algorithm, and may be wrongly associated by the OEM to other lines, which may give, in turn, wrong vertical profiles.

One the other hand, if the number of orders is too high, at first, the algorithm runs very slowly, because too many lines are simulated. Also, we know that the AOTF transfer function becomes unknown when going too far from its maximum (Section 3.5.4.4).

The aim is thus to find the correct number of orders to include in the simulation. This kind of sensitivity test has to be run on each order, for each kind of fitted species.

We tried with 0, 1, 2, 3, 4 and 5 couples of adjacent orders - 1, 3, 5, 7, 9 and 11 orders in total. The different cases are summarized in Table 4.26. The DOF and number of iterations are confined in Table 4.27 and the vertical profiles in Figure 4.53.

When looking at the RMS Panel of Figure 4.53, we can directly reject case 1: the RMS is much higher. When the number of adjacent orders takes higher values, the RMS is reduced. When looking at the other vertical profiles, without considering case 1, we see that the density profile slightly increases with higher values of the adjacent orders number until cases 5 and 6, for which the density profiles becomes more unstable. The other profiles are also somewhat changed. There is no large difference between case 2 and case 6 in terms of density and temperature profiles. The number of steps before convergence is better for cases 4 to 6.

There is no clear change in the DOF.

3 adjacent orders are chosen to simulate the spectra measured in order 149.

However, as stated before, such an analysis should be performed systematically for each spectral main order window.

Case	Number of adjacent orders
1	0
2	1
3	2
4	3
5	4
6	5

Table 4.26: List of the cases for the number of adjacent orders influence study.

Case	a	b	c	n	t	$e+f$	n_{AOTF}	d	d_{AOTF}	Iterations
1	9.000	8.992	8.990	7.963	4.523	0.923	11.780	0.000	0.000	9
	9	9	9	9	9	2	19	9	1	
2	8.000	7.993	7.991	6.227	4.152	0.494	14.031	1.867	0.213	9
	8	8	8	8	8	2	43	8	1	
3	8.000	7.993	7.991	6.543	4.022	0.424	14.504	0.926	0.145	5
	8	8	8	8	8	2	45	8	1	
4	7.000	6.994	6.992	6.218	3.945	0.386	8.918	0.118	0.008	4
	7	7	7	7	7	2	49	7	1	
5	8.000	7.993	7.991	7.418	4.083	0.530	11.976	1.504	0.075	4
	8	8	8	8	8	2	48	8	1	
6	8.000	7.993	7.991	7.367	4.065	0.437	14.520	0.247	0.000	4
	8	8	8	8	8	2	53	8	1	

Table 4.27: DOF and convergence steps for the number of adjacent orders influence study. The case, the degrees of freedom of the a, b, c (baseline parameters), $\log n$ (density logarithm), T (temperature), e, f (wavenumber scale), n_{AOTF} (AOTF function fit), d_{AOTF} (AOTF wavenumber scale fit) and the number of iterations are given. For each case, the first line gives the DOF while the second gives the number of variables of each parameter, i.e. the maximum value of the DOF.

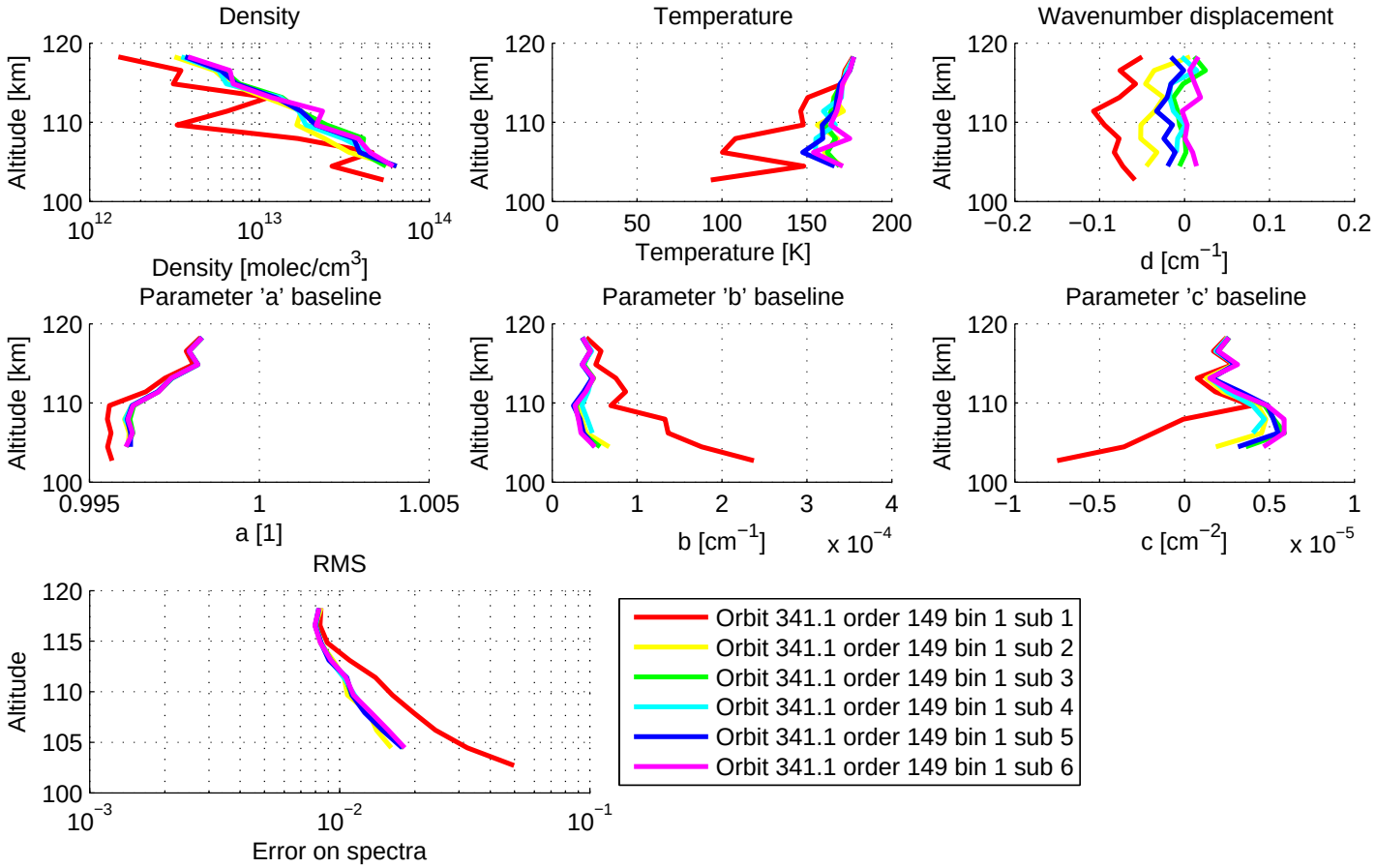

Figure 4.53: Density, temperature, wavenumber displacement and background vertical profiles and RMS for the study of the number of adjacent orders influence. The *sub* in reference corresponds to the case.

4.9 Temperature retrieval attempt using the Boltzmann law

In this Section, we look into another formulation to use the Boltzmann law to derive the temperature profile. Hence, the sections devoted to the study of the temperature parameters (Sections 4.8.2.4, 4.8.3.2 and 4.8.5) showed that the influence of the a-priori on the retrieved temperature profile remains large, even if attempts were made to weaken this effect. We used the so-called Boltzmann plot to obtain temperature profiles.

Each absorption line corresponds to a transition between two rovibrational levels. Within one rovibrational band, each transition corresponds to a vibrational transition between the two same vibrational levels, while the two rotational levels vary. The final rotational level is denoted J' [Bandwell & McCash (1994)].

We know that a rovibrational band in absorption is represented by a Boltzmann distribution:

$$I_{P(J")} \propto I_0 \cdot \tilde{\nu}_{J" \to J'} \cdot (2 \cdot J") \cdot \exp \frac{-h \cdot c_{light} \cdot B" \cdot J" \cdot (J" - 1)}{k_B \cdot T_{rot}} \tag{4.65}$$

where J' and $J"$ denote the higher and lower rotational J-levels of the transition, $P(J")$ is the line labeling, $I_{P(J")}$ is the intensity of the line, I_0 is the database line intensity, h, c_{light}, k_B are the Planck, velocity of light and Boltzmann constants, $B"$ is the rigid rotator constant of the molecule vibrational transition and T_{rot} is the rotational temperature.

When looking at this formula, it is easy to obtain a relation that gives the rotational temperature. If the equation is written in the following way

$$\log \left(\frac{I_{P(J")}}{\tilde{\nu}_{J" \to J'} \cdot (2 \cdot J")} \right) = \alpha + \beta \cdot \frac{-h \cdot c_{light} \cdot B" \cdot J" \cdot (J" + 1)}{k_B} \tag{4.66}$$

the value of the slope β is the inverse of T_{rot}. We decide to call the temperature profile obtained by this method the Boltzmann temperature.

This method is applied to the SOIR spectra, as the number of absorption lines seen in an order can be very large. We unfortunately see that the method completely fails. Two options were indeed considered: using the Boltzmann plot during the retrieval process to obtain temperature profiles, or deriving the Boltzmann temperature on the converged solution. The first option turned the algorithm to very unstable solutions, most of the time forbidding convergence to be achieved. The results of the second method are presented later in this section.

The method implies a precise knowledge of the quantity $I_{P(J")}$. But with the SOIR spectra, that quantity is rather hard to obtain. We know that this value is equal to the surface under the absorption lines, and is constant whatever the resolution of the instrument. The value is modulated by the AOTF transfer function, and thus could be easily reconstructed, using the AOTF function itself, but changes the surface under each absorption line. The order overlapping adds many more absorption lines in the spectra, that sometimes overlap each other, and makes the determination of $I_{P(J")}$ even harder. The contribution of these adjacent orders needs thus to be carefully removed. Finally, it is often hard to precisely determine the baseline value at the absorption line wavenumber during a fit.

The method is applied on the retrieval described in Section 4.7. The spectra and the application of relation (4.66) are presented in Figures 4.54 (determinations of $I_{P(J")}$) and 4.55 (regressions). The points from equation (4.66) do not perfectly align on a straight line inf Figure 4.55.

The vertical profiles are presented in Figure 4.56. The horizontal bars on the Boltzmann temperature are the errors calculated on the linear coefficient of the fit (the inverse of it, in fact). We observed a very large difference between the OEM fitted temperature and the Boltzmann temperature, which reaches much higher values, and has larger excursions. The method does not calculate reliable values.

The same conclusions are drawn for many other orbits. Moreover, the temperature for simultaneous measurements of the same vibrational band in two different orders often leads to very different profiles.

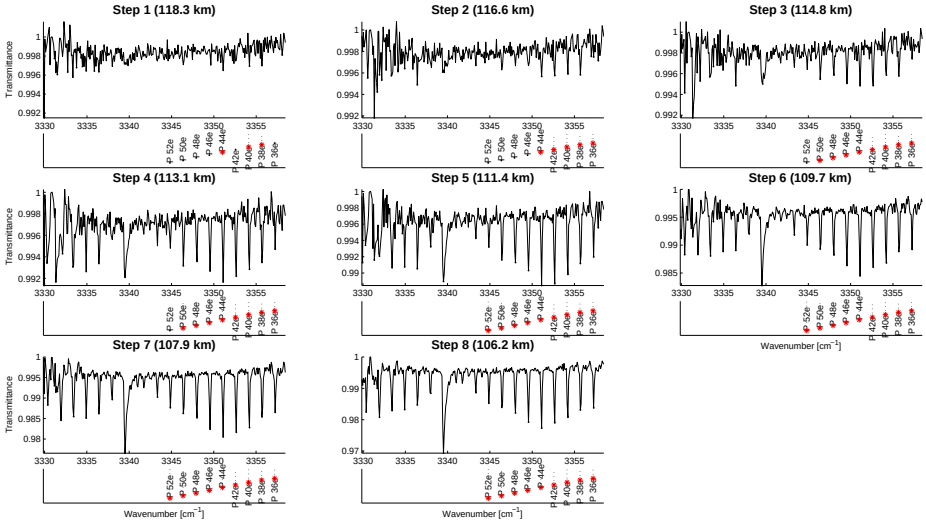

Figure 4.54: Fitted spectra of orbit 341.1 order 149 bin 1. In each upper Panel, the measured spectrum and the detected absorption lines are denoted by the black dots. In each lower Panel, the database rotational transitions are presented. The ones that are matched with a measured absorption line are marked by a red star.

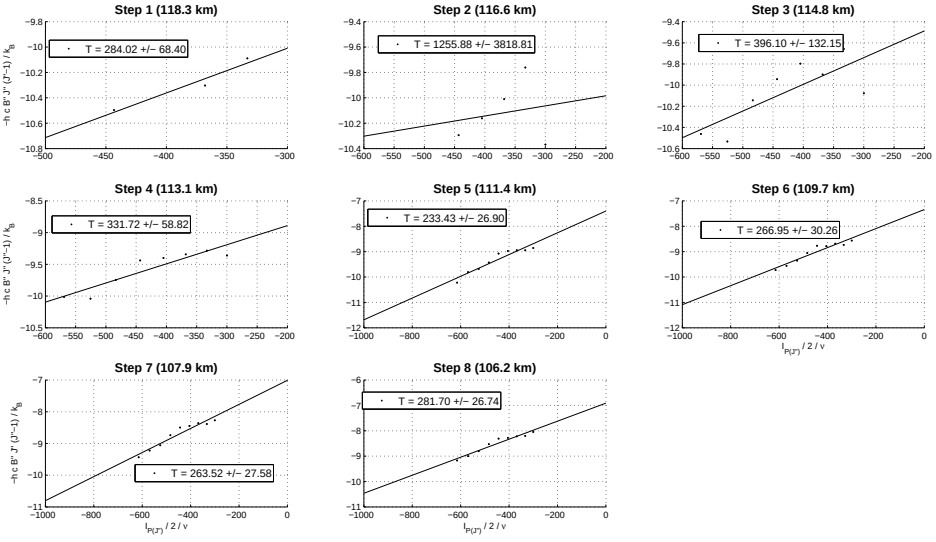

Figure 4.55: Determination of the rotational temperature using the Boltzmann equation (4.66) for orbit 341.1 order 149 bin 1. In each Panel, the dots are the points calculated using equation (4.66), the lines are the fits. The measured temperature and its error are given in each legend Panel.

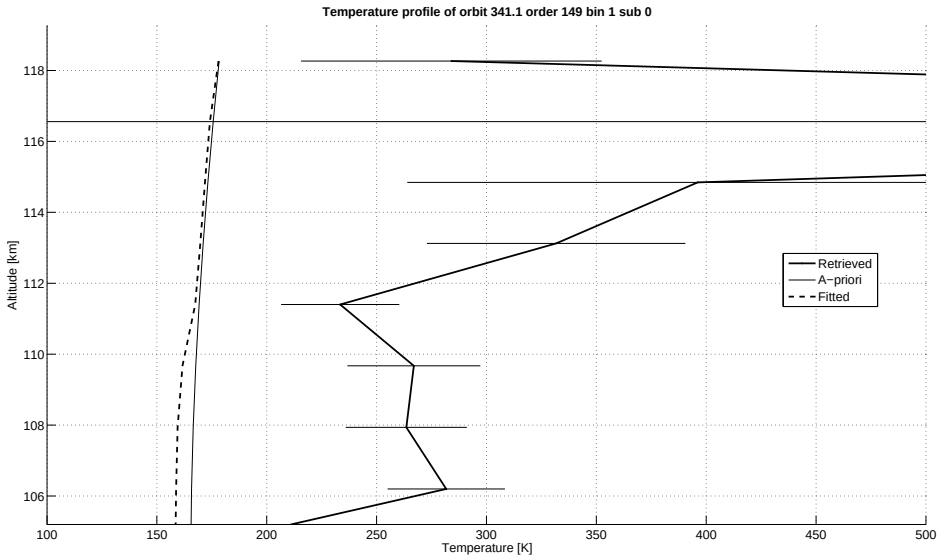

Figure 4.56: Comparison of the temperature profiles obtained for the retrieval of orbit 341.1 order 149 bin 1. The a-priori or model, the OEM fitted temperature and the Boltzmann temperature are presented.

4.10 Systematic errors

4.10.1 Introduction

In this Section, we consider the whole data set that will be further described in Chapter 5. Density and rotational temperature profiles are obtained for many species from the two bins. They simultaneously record almost identical portions of the atmosphere.

The errors that are obtained from the OE algorithm are linked to the retrieval error. Their values often seem small. We derive here a way to evaluate a statistical error. During an observation, the almost same portion of air is measured by the two bins of the SOIR detector. We use this approach to evaluate the statistical error, by comparing the temperature profiles deduced from the two sets of spectra, measured on each bin.

We will interpret this in the following paragraphs.

4.10.2 Altitude error

The altitude error from the pointing precision of the satellite is described in Section 4.2.2.4. The values are of a few hundreds of meters.

The difference between the density profiles can be interpreted as an altitude bias. This bias is evaluated on the whole dataset as the altitude difference measured for the same retrieved density. The systematic altitude error is calculated as the standard deviation of the measured bias. It equals 2.02 km. More than 2281 points are considered.

The results are presented in Figure 4.57. The latitude possible trend is investigated: the black line illustrates the linear fit of the data. From that fit, the trend is inexistent.

4.10.3 Density error

The systematic density error is calculated here on the logarithm of the density, which is actually fitted during the inversion precess. It is linked to the systematic altitude error. Indeed, the two

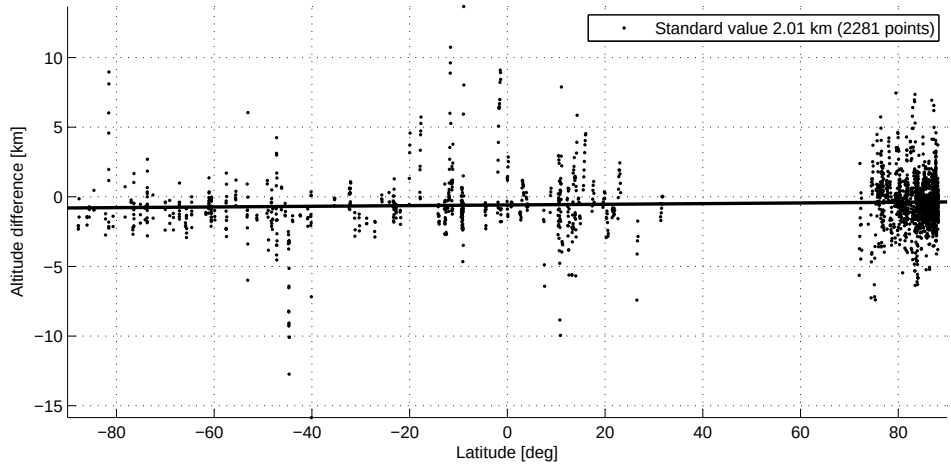

Figure 4.57: Evaluation of the altitude error from the altitude difference between the density fits of the two bins of the whole dataset as a function of the latitude of the measurement. The black line is the linear fit of the data. No trend as a function of latitude is observed.

density curves are parallel, and it is not possible to discriminate without uncertainty between a density and a altitude systematic error. To ensure a good relevance of our data set, we consider both in the present study. The density logarithm difference between the two bins for a same altitude is calculated. The results are given in Figure 4.58. The resulting standard deviation equals 0.93 %, and is calculated on 2517 points.

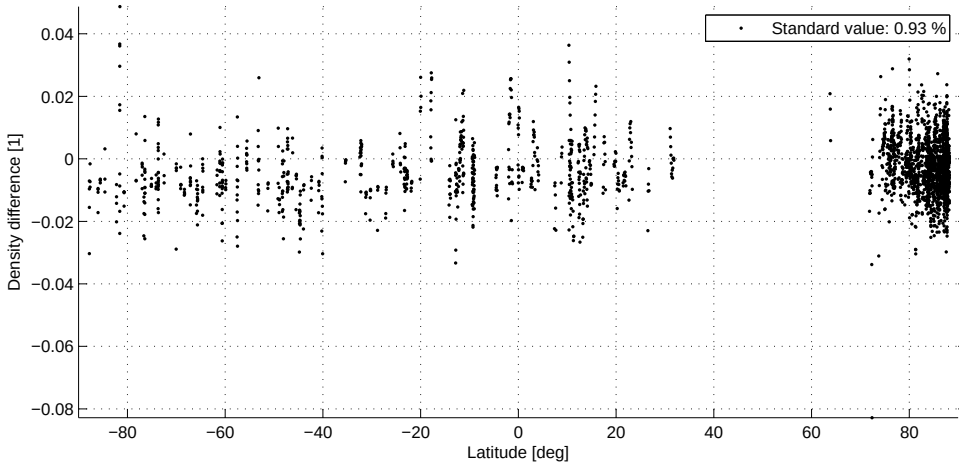

Figure 4.58: Evaluation of the density error from the density logarithm difference between the density logarithm fits of the two bins at the same altitudes of the whole dataset as a function of the latitude of the measurement.

4.10.4 Temperature error

Finally, the temperature error is studied in the same way as the density error. This difference in retrieved temperature profiles finds its origin from several characteristics: the a-priori value of the temperature, and the AOTF transfer function. For this last point, we consider that the knowledge of the AOTF transfer function is not perfect and introduces a bias. Considering all the temperature profiles that are obtained up to now, we estimated the standard deviation of the temperature difference.

The temperature difference between the two bins for each measurement is calculated. The values are plotted in Figure 4.59. The derived temperature standard deviation equals to 11.03 K, and is calculated on 2517 points.

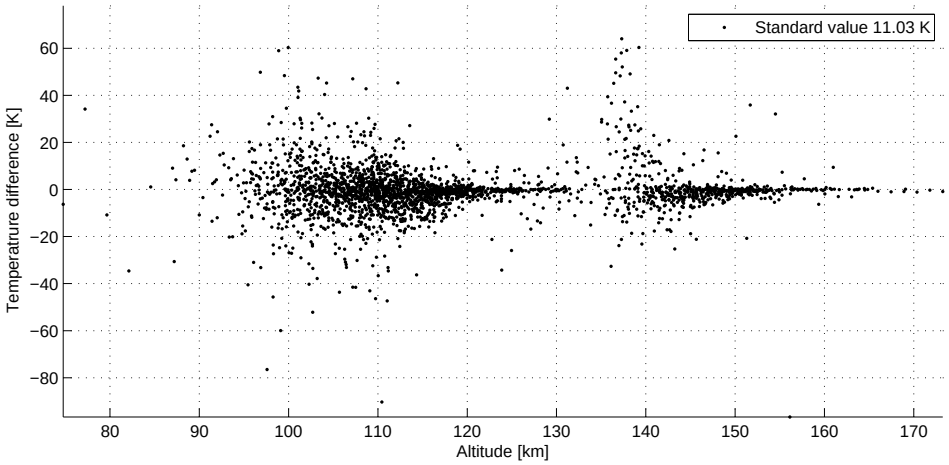

Figure 4.59: Evaluation of the temperature error from the temperature difference between the temperature fits of the two bins at the same altitudes of the whole dataset as a function of the latitude of the measurement.

Chapter 5

CO_2 density and temperature profiles

5.1 Introduction

325 successful occultations have been performed since the beginning of the mission on January the 1st, 2011. In each of these, 4 different diffraction orders were measured. If we consider that each measurements was recorded by the two bins, a total of 2600 sets of spectra are in the SOIR database. The list of orbits is given in Appendix K, together with the relevant orbital data.

Several species and their isotopologues present in the Venus atmosphere are detected in the SOIR spectra, such as $^{12}C^{16}O_2$, $^{13}C^{16}O_2$, $^{16}O^{12}C^{18}O$ [Mahieux *et al.* (2010, 2011a)], $^1H_2^{16}O$, $^1H^{16}O^2H$ [Fedorova *et al.* (2008)], $^{12}C^{16}O$, $^{13}C^{16}O$ [Vandaele *et al.* (2008)], $^1H^{35}Cl$, $^1H^{37}Cl$ [Bertaux *et al.* (2006); Vandaele *et al.* (2008)], $^1H^{19}F$ [Bertaux *et al.* (2006); Vandaele *et al.* (2008)] and $^{32}S^{16}O_2$ [Belyaev *et al.* (2008, 2011)]. H_2SO_4 in the aerosols content has also been observed, under $H_2SO_4 \cdot 2H_2O$ [Wilquet *et al.* (2008, 2011)]. The diffraction orders where each species presents absorption lines are given in Appendix L.

For some compounds like OCS, H_2CO, CH_4, OH, HI and HBr, only detection limits can be determined. The absorption structure of the species is not observable in the spectra, because the signature is below the noise level. A detection limit of a species gives therefore an upper boundary of the molecule density at different altitudes.

The OE algorithm described previously was run on almost the whole data set where CO_2 absorbs. About 70% of the CO_2 dataset is available, or roughly 600 vertical profiles. They cover almost 200 orbits.

In this Chapter, we will describe the need to define occultation seasons, give an overview of the CO_2 spectroscopy and discuss some CO_2 vertical profiles. Finally an overview of the CO_2 density and rotational vertical profiles will be presented and future work will be discussed.

5.2 Occultation season definition

There is no true seasons on Venus because its rotation axis is tilted by 179° to the ecliptic, relative to the North polar axis. In order to study SOIR results, a time reference frame corresponding to the spacecraft orbit is defined and is called the occultation season.

The measurement period analyzed here starts in May 2006 and ends in December 2010. This period is divided into VEX occultation seasons (OS). These represent the time it takes VEX to cover all latitudes on the terminator, or for the VEX orbital plane to accomplish half a rotation around the planet (in terms of local solar time). It is an intrinsic characteristic of the VEX orbit. One OS lasts for roughly 100 Earth days. They are listed in Table 5.1, accompanied with the number of CO_2 order measurement occurrences.

The occultation seasons have a well defined and reproducible pattern when the orbit number is plotted as a function of the latitude. This pattern is divided in two different branches: the morning terminator and the evening terminator branches. They are seen in Figure 5.1. There is an explicit function between the orbit number and the latitude for a given terminator.

The OS are defined in order to allow us to study the time variations of the retrieved atmospheric profiles. It will be used in Section 5.5.

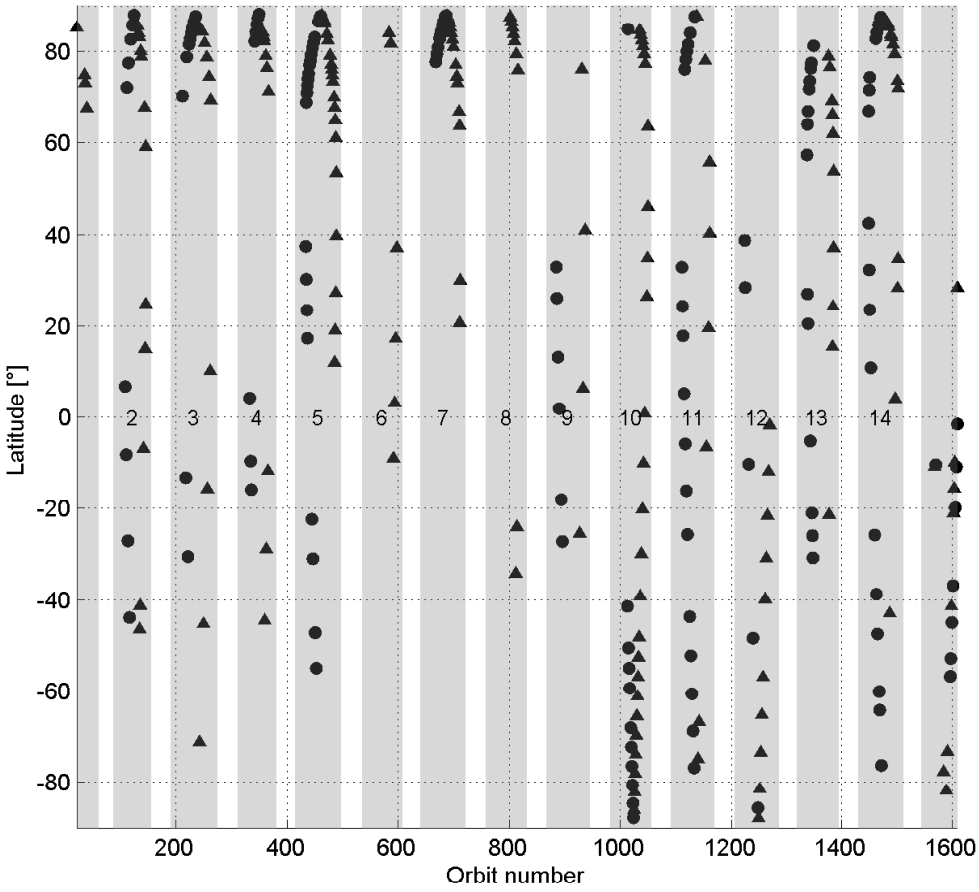

Figure 5.1: Map of all the occultations, as a function of the orbit number and the latitude. The occultation seasons are also depicted. All the orbits are presented. The ◯ are the morning terminator measurements while the △ are the evening terminator ones.

OS		1	2	3	4	5	6	7	8	9	10	11	12	13	14	15
Orbit	Start	23	87	189	310	414	534	639	757	866	981	1090	1204	1316	1427	1541
	End	60	155	274	380	497	607	721	831	944	1055	1169	1285	1392	1509	1616
Date	Start	14/05/06	17/09/06	27/10/06	25/02/07	09/06/07	07/10/07	20/01/08	17/05/08	03/08/08	27/12/08	15/04/09	06/08/09	27/11/09	18/03/10	30/07/10
	End	20/06/06	24/10/06	20/01/07	06/05/07	29/08/07	18/12/07	11/04/08	30/07/08	19/11/08	11/03/09	02/07/09	27/10/09	11/02/10	08/06/10	13/09/10
Order	104	0	0	0	0	0	0	0	0	0	0	0	1	1	0	0
	105	0	1	1	0	0	2	15	0	0	0	0	1	0	0	0
	108	1	1	1	0	2	0	0	0	0	0	0	0	0	0	0
	109	2	0	0	0	0	0	0	0	0	0	0	0	2	0	0
	110	1	0	1	0	0	0	0	0	0	0	0	1	0	0	0
	111	0	0	4	0	8	3	0	0	0	0	0	0	0	3	0
	112	0	0	4	5	12	3	15	0	2	0	4	0	0	5	0
	116	0	0	0	0	0	0	0	0	0	1	1	0	1	2	0
	117	0	0	0	0	0	0	1	0	0	1	0	0	1	3	0
	123	0	5	2	0	1	0	0	0	0	2	0	0	0	0	0
	124	0	0	0	0	1	0	0	0	0	2	0	0	0	0	0
	125	0	0	0	0	15	0	0	0	0	2	0	0	0	8	3
	140	0	0	0	0	0	0	0	0	0	0	0	1	1	0	0
	141	0	0	0	0	0	0	0	0	0	0	1	1	1	7	4

Table 5.1: VEX occultation season definition. For each season, the first and last orbit number, as well as its corresponding day are given. Only the orders where a CO_2 isotopologue absorbs are given.

OS		1	2	3	4	5	6	7	8	9	10	11	12	13	14	15
Orbit	Start	23	87	189	310	414	534	639	757	866	981	1090	1204	1316	1427	1541
	End	60	155	274	380	497	607	721	831	944	1055	1169	1285	1392	1509	1616
Date	Start	14/05/06	17/09/06	27/10/06	25/02/07	09/06/07	07/10/07	20/01/08	17/05/08	03/08/08	27/12/08	15/04/09	06/08/09	27/11/09	18/03/10	30/07/10
	End	20/06/06	24/10/06	20/01/07	06/05/07	29/08/07	18/12/07	11/04/08	30/07/08	19/11/08	11/03/09	02/07/09	27/10/09	11/02/10	08/06/10	13/09/10
Order	142	0	0	0	0	1	0	0	0	0	0	0	0	2	0	0
	143	0	0	0	0	1	0	0	0	0	0	0	0	1	0	0
	144	0	0	0	0	1	0	0	0	0	0	0	0	2	0	0
	145	0	0	0	0	3	0	0	0	0	1	0	3	0	0	0
	146	0	2	0	0	0	0	0	0	0	1	1	0	0	0	0
	147	0	3	0	2	0	2	0	0	0	1	1	0	0	0	0
	148	0	2	1	0	0	0	0	0	0	1	1	1	15	9	2
	149	0	2	1	16	17	6	27	9	10	29	20	16	11	7	1
	150	0	0	0	0	0	0	0	1	0	0	0	1	7	8	0
	151	0	0	0	0	1	0	0	0	0	0	0	0	1	0	0
	152	0	0	0	0	0	0	0	1	0	0	0	0	1	0	0
	153	0	0	0	0	0	0	0	0	0	0	1	0	2	0	0
	154	0	0	0	0	0	0	0	0	0	0	1	0	0	0	0
	155	0	0	0	0	0	0	0	0	2	0	0	0	0	0	2
	156	0	0	0	0	0	0	0	0	0	0	1	0	0	4	1

Table 5.1 (Continued)

OS		1	2	3	4	5	6	7	8	9	10	11	12	13	14	15
Orbit	Start	23	87	189	310	414	534	639	757	866	981	1090	1204	1316	1427	1541
	End	60	155	274	380	497	607	721	831	944	1055	1169	1285	1392	1509	1616
Date	Start	14/05/06	17/09/06	27/10/06	25/02/07	09/06/07	07/10/07	20/01/08	17/05/08	03/08/08	27/12/08	15/04/09	06/08/09	27/11/09	18/03/10	30/07/10
	End	20/06/06	24/10/06	20/01/07	06/05/07	29/08/07	18/12/07	11/04/08	30/07/08	19/11/08	11/03/09	02/07/09	27/10/09	11/02/10	08/06/10	13/09/10
Order	157	0	0	0	0	0	0	0	0	0	0	1	0	0	0	0
	158	0	0	0	0	0	0	0	0	0	0	1	0	0	0	0
	159	0	0	0	0	0	0	0	0	0	0	1	0	0	0	0
	160	0	0	0	0	0	0	0	0	0	0	1	0	1	3	0
	161	0	0	0	0	0	1	0	0	0	0	3	0	0	0	0
	162	0	0	0	0	0	1	0	0	0	0	3	0	0	0	0
	163	0	0	0	0	0	0	0	0	0	0	1	0	0	0	0
	164	0	0	0	0	0	0	0	0	0	0	1	1	0	0	0
	165	0	0	0	0	0	0	0	0	0	0	1	1	1	3	2
	166	1	0	0	2	0	0	27	0	0	0	8	3	0	4	1
	177	0	0	0	0	0	0	0	1	0	0	1	0	0	0	0
	178	0	0	0	0	0	0	1	0	0	0	1	0	0	0	0
	179	0	0	0	0	1	0	0	0	0	0	1	0	1	0	2
Total		5	7	13	7	40	10	59	1	2	8	30	10	10	38	12

Table 5.1 (Continued)

5.3 Spectroscopy

CO_2 is the main species present in the mesosphere of Venus, and one of the main component in the Venus thermosphere. The Hitran 2008 [Rothman *et al.* (2009)] database [1] lists 10 isotopologues of CO_2. The eight more abundant ones are considered in this work, even if only the three main ones are clearly observed: $^{16}O^{12}C^{16}O$, $^{16}O^{13}C^{16}O$ and $^{16}O^{12}C^{18}O$. The other ones have not been unambiguously observed, because they are hidden by stronger bands belonging to the three main isotopologues. They are still taken into account in the ACS calculation.

In the wavenumber range measured by SOIR, two strong absorption transitions are observed: at 3725 cm^{-1} and 2350 cm^{-1}, or 2.7 μm and 4.24 μm. Weaker bands are also observed. It will be seen in the next sections that this allows us to retrieve CO_2 densities from 85 km up to 185 km of altitude. The CO_2 absorption bands observed by SOIR are depicted in Figure 5.2, and the studied bands are listed in Table 5.2.

All the absorption lines with an intensity larger than 10^{-27} $cm^{-1}/(molecule\ cm^{-2})$ are considered.

Number	Isotopologue	Vibrational band	Orders	Number of orbits
1	$^{16}O^{13}C^{16}O$	21102-00001	145, 146	10
2	$^{16}O^{12}C^{18}O$	30002-00001	177, 178	3
3	$^{16}O^{12}C^{16}O$	00021-01101	179	5
4	$^{16}O^{12}C^{16}O$	10011-10002	108, 109	7
5	$^{16}O^{12}C^{18}O$	20003-00001	110, 111, 112, 113	69
6	$^{16}O^{12}C^{18}O$	20002-00001	115, 116, 117, 118	12
7	$^{16}O^{12}C^{16}O$	21103-00001	140, 141, 142, 143	18
8	$^{16}O^{12}C^{16}O$	21102-00001	147, 148, 149, 150	199
9	$^{16}O^{13}C^{16}O$	10012-00001	155, 156, 157, 158	10
10	$^{16}O^{12}C^{16}O$	10012-00001	159, 160, 161, 162	11
11	$^{16}O^{12}C^{16}O$	10011-00001	164, 165, 166, 167	54
12	$^{16}O^{12}C^{16}O$	00011-00001	104, 105, 106, 107	25

Table 5.2: List of the strongest vibrational bands that are observed in the SOIR spectra and that are used to retrieve CO_2 densities and rotational temperatures. The concerned isotopologue, the vibrational band definition expressed in the Hitran notations, the diffraction orders where the vibrational bands are observed and the number of orbits during which these orders were measured are given. They are sorted in terms of vibrational band intensity, starting from the weakest one to the strongest one. p=10^{-3} mbar, T=185 K.

1. The line intensities of the isotopologues given in the Hitran database are respectively multiplied by their Earth isotopic ratio. This is taken into account in the Asimat algorithm.

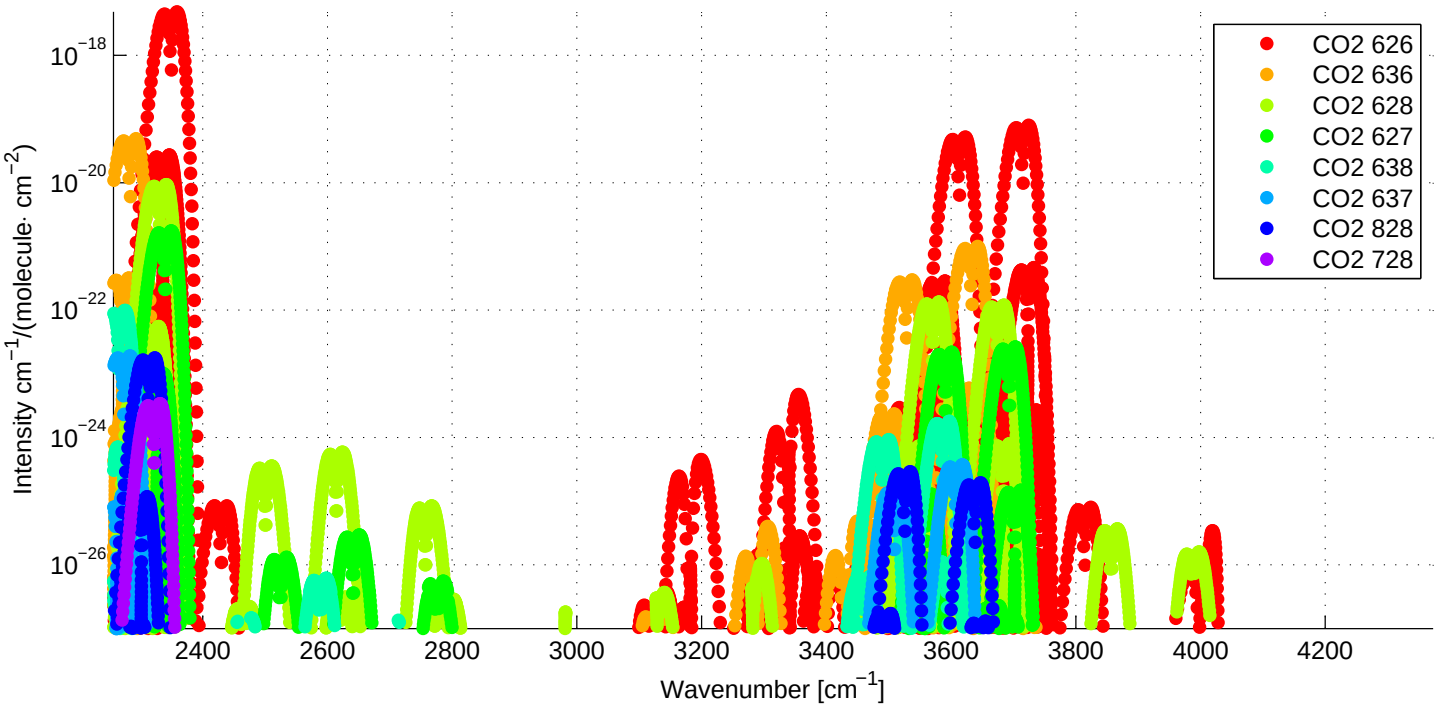

Figure 5.2: Carbon dioxide lines listed in Hitran 2008 in the SOIR wavenumber range. All the isotopologues that absorb in the SOIR wavenumber range with intensities larger than 10^{-27} cm^{-1}/(molecule cm^{-2}) are presented, even if only the three main ones can unambiguously be detected. The intensities are presented at the atmospheric conditions that are encountered on Venus at an altitude of 100 km, the temperature and pressure conditions are derived from the Hedin model. p=10^{-3} mbar, T=185 K.

5.4 Vertical profiles discussion

5.4.1 Description

Nine orbits located at morning and evening terminator and at different latitudes are selected and presented in this Section [Mahieux *et al.* (2011b)]. Amongst them, two orbits are investigated in detail in the next sections.

A map presenting the location of the selected orbits is presented in Figure 5.3. The orbits' characteristics are given in Table 5.3.

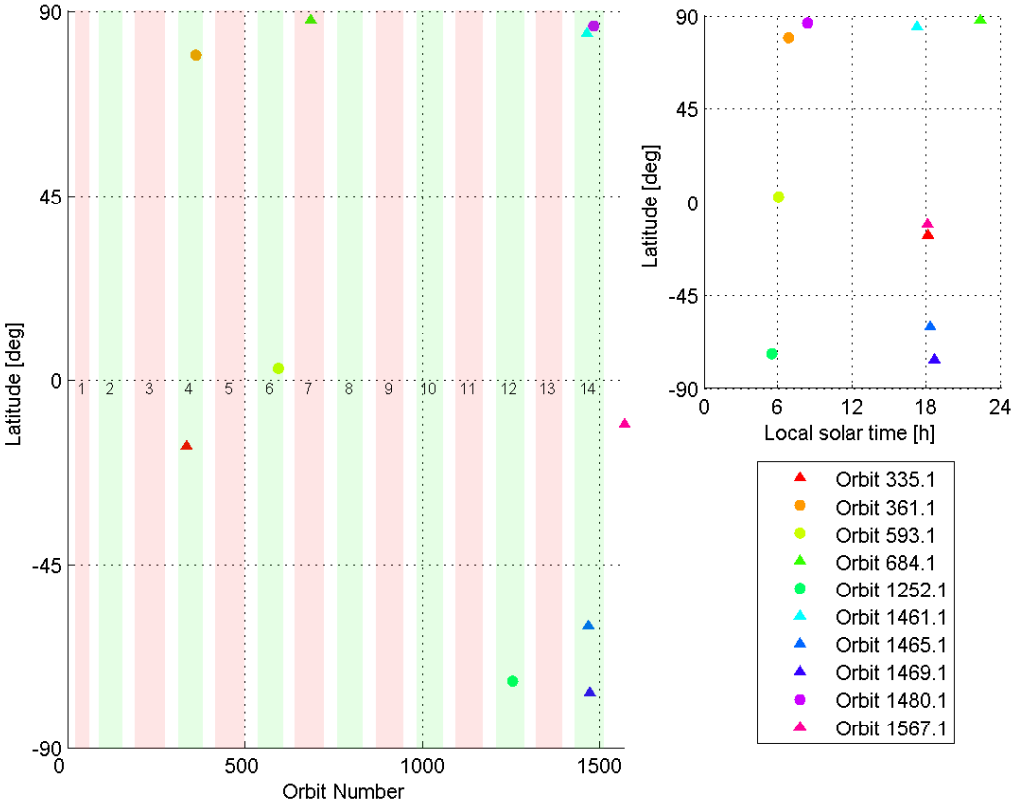

Figure 5.3: Coordinates and LST maps of the orbits presented in the text. The circles refer to the measurements at the morning terminator, the triangles at the evening terminator. The numbers in the coordinate maps as the color boxes correspond to the OS.

Orbit number	Date DD/MM/YYYY	Orders				Latitude deg	Longitude deg	LST hour	Min alt. km	Max alt. km
335.1	22/03/2007	149	166	*112*	-	-15.96	318.5	18	80	145
361.1	17/04/2007	149	166	*112*	-	78.82	208	6.8	90	150
593.1	5/12/2007	149	162	*112*	-	3	214.9	6	95	155
684.1	25/01/2010	105	149	166	*112*	87.52	256.97	21.9	110	175
1461.1	21/04/2010	*117*	148	165	160	84	202.9	17.2	100	155
1465.1	25/04/2010	149	160	166	*111*	-60	200.2	18.2	95	160
1469.1	29/04/2010	148	156	166	***112***	-76.2	207.5	18.6	100	160
1480.1	10/05/2010	141	150	**156**	165	86.9	37	8.2	95	150
1567.1	5/08/2010	141	149	**156**	166	-11.7	159.44	18	100	160

Table 5.3: Characteristics of the selected orbits. The orbit number, the Earth date, the four measured orders, and the coordinates of the measurements are presented. The orders in bold concern measurements on the second isotopologue $^{16}O^{13}C^{16}O$, the ones in italics concern the third isotopologue $^{16}O^{12}C^{18}O$ and ones without any typesetting are from the main isotopologue $^{16}O^{12}C^{16}O$.

The vertical densities are presented in Figure 5.4 for the morning terminator measurements and in Figure 5.6 for the evening ones. The rotational temperature profiles are presented in Figures 5.5 and 5.7 for each terminator. As previously explained in Chapter 4, for each order measurement during a solar occultation, the density and rotational temperature profiles are obtained from the CO_2 rotational lines of a given vibrational transition. The vertical profiles are given as the color curves in the Figures 5.4 to 5.7.

We consider here that the CO_2 isotopic ratios are the same as on Earth [Bézard *et al.* (1987); Clancy & Muhleman (1991)]. A paper [Mahieux *et al.* (2011a)] is currently under review to demonstrate that the SOIR observations are in accordance with this observation. We are not discussing this topic in thee present work.

It was observed that isotopic fractioning [Banks & Kockarts (1973)] takes place above the homopause, which is located around 130 km [Clancy & Muhleman (1983); von Zahn *et al.* (1980)]. This effect is small, and we neglect it in the present study.

The orbits that are selected only concern the three main isotopologues, $^{16}O^{12}C^{16}O$, $^{16}O^{13}C^{16}O$ and $^{16}O^{12}C^{18}O$.

The profiles presented here extend from 80 km up to 175 km. The model is derived from Hedin *et al.* (1983), and is presented as the black dashed curve in Figures 5.4 to 5.7. The density profiles are all lower than the density model. At lower altitude (below 100 km), the difference between the presented profiles ranges from a factor 1 to 10, while at higher altitude, the factor goes from 10 to 100. Compared to the model between 120 km and 130 km, all the profiles present a density reduction. The model is given as the dashed black curves in the Figures 5.4 to 5.7. From the nine vertical profiles given here, it seems that the dispersion in terms of density is larger at dusk than at dawn. However, only 3 morning occultations for 6 evening occultations are presented, which may turn into bad conclusions. When considering the whole data set, no difference is observed. Also, fore some vertical profiles, discontinuities in the vertical profiles are observed (see orbit 1469.1 for example). They are not explained up to now, and will need further investigations to be done in a near future.

The temperature profiles also show some variations, within 20 K. The fact that all the temperature profiles do not show any variation at given altitudes, for example at 170 and 130 km, is suspicious. It is explained from the fact that too few information concerning the temperature could be extracted from the spectra, and resulted in the algorithm to remain on the model. The large error bars resulting from the study presented in Section 4.10.4 accounts for this effect.

Some values from the literature are also plotted in the Figures. These values originate from Earth based measurements and in-situ measurements. Clancy *et al.* (2008) measured the CO line profile temperature using sub-mm telescopes around 100 km of altitude. Three data sets are presented here at 40° S, the Equator and 40° N, taken in evening conditions. The three data sets agree with our retrieved rotational temperatures, to within the error bars.

The density values from von Zahn *et al.* (1980) are taken from the US Pioneer Venus (1978-1992) NMBS experiment measurements, during morning conditions and close to the Equator (7° N). Their density is larger than our retrievals by a factor 2. It should be noted that the local solar time is slightly different, as our measurements took place at exactly 6.00AM, and their measurements at 8.30AM, so later in the day. This explains the difference observed, with higher densities than the ones observed by SOIR at the terminator. It is indeed known that the atmosphere undergoes a contraction at the terminator, with larger densities on the dayside compared to the nightside at the same altitude [Bougher *et al.* (2006)] (see Section 2.3). The values reported by Fox & Kasprzak (2007) and references therein were obtained from the Pioneer Venus ONMS instrument, at dusk and dawn and reported at an altitude of 165 km. The local solar time is not exactly 6.00AM or 6.00PM. This dataset illustrates the density variations measured during the Pioneer era: in the dataset reported in the Figures 5.4 and 5.6, there is a factor 3 to 4 between the highest and the lowest measurement points.

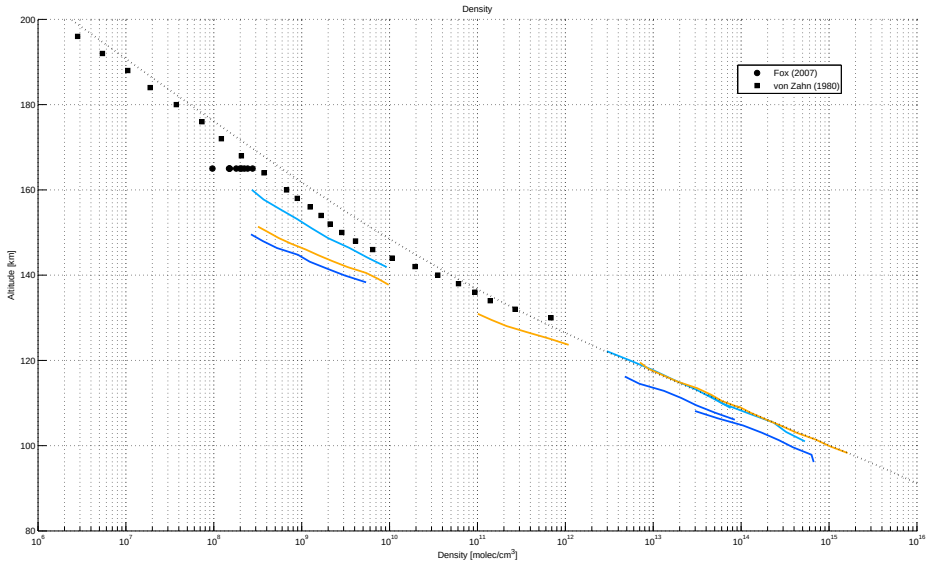

Figure 5.4: Vertical density profiles from the morning terminator measurements: orbits 361.1 (in dark blue), 593.1 (in light blue), and 1480.1 (in orange). The error bars are not displayed to ensure readability. Their mean value is 10%. The Hedin model is the thick dashed black line. The literature data are given as the markers in the density Panel: the circles are data from Fox & Kasprzak (2007) and the squares from von Zahn *et al.* (1980).

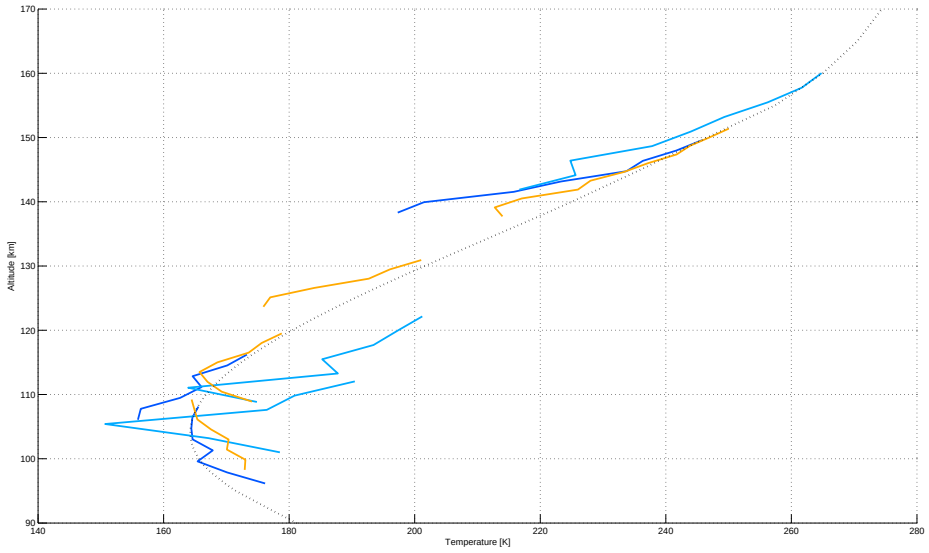

Figure 5.5: Vertical rotational temperature profiles from the morning terminator measurements: orbits 361.1 (in dark blue), 593.1 (in light blue), and 1480.1 (in orange). The error bars are not displayed to ensure readability. Their mean value is 10%. The Hedin model is the thick dashed black line.

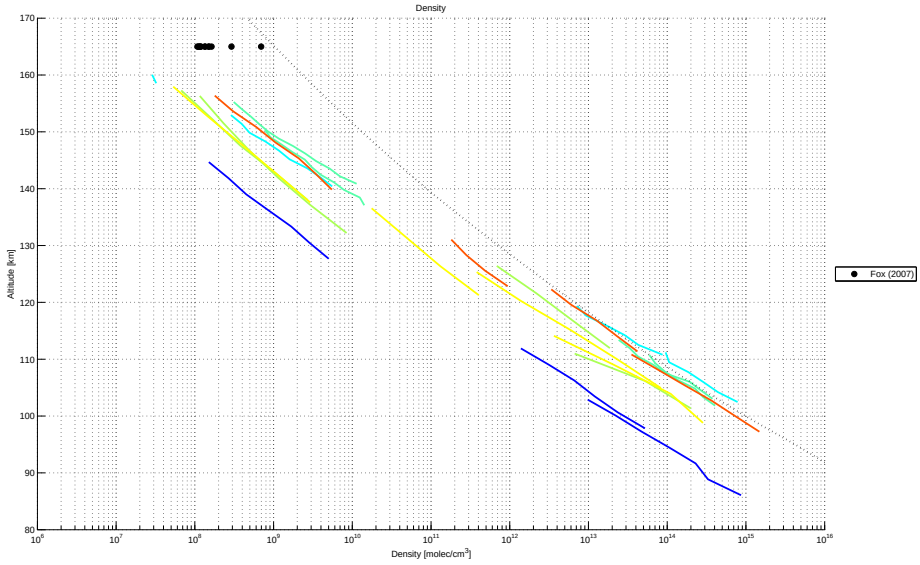

Figure 5.6: Vertical density profiles from the evening terminator measurements: orbits 335.1 (in dark blue), 684.1 (in light blue), 1461.1 (in dark green), 1465.1 (in light light green), 1469.1 (in yellow) and 1567 (in red). The error bars are not displayed to ensure readability. Their mean value is 10%. The Hedin model is the thick dashed black line. The literature data are given as the markers: the circles are from Fox & Kasprzak (2007).

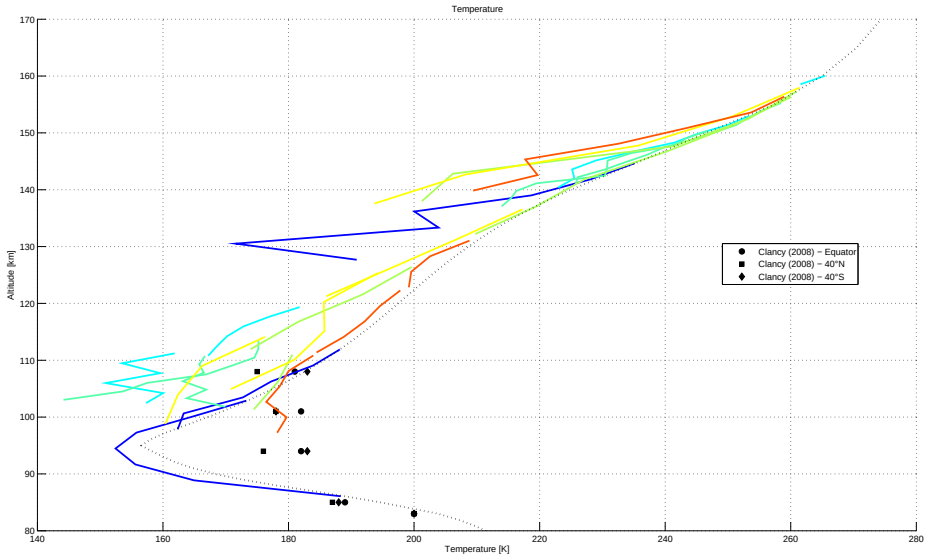

Figure 5.7: Vertical rotational temperature profiles from the evening terminator measurements: orbits 335.1 (in dark blue), 684.1 (in light blue), 1461.1 (in dark green), 1465.1 (in light light green), 1469.1 (in yellow) and 1567 (in red). The error bars are not displayed to ensure readability. Their mean value is 10%. The Hedin model is the thick dashed black line. The literature data are given as the markers: the markers are from Clancy *et al.* (2008), separated in three groups as a function of latitude: 40° N, Equator and 40° S.

5.4.2 Lapse rate and static stability

The lapse rate[2] Γ of all these profiles are analyzed here, knowing that [Petty (2008)]:

$$\Gamma = -\frac{dT}{dz} \tag{5.1}$$

where T is the temperature and z the altitude.

The static stability S compares the lapse rate to the adiabatic lapse rate Γ_d. The adiabatic lapse rate is calculated as

$$\Gamma_d = \frac{g}{c_p} \tag{5.2}$$

where c_p is the specific heat capacity of the considered gas, in this case CO_2 and g the acceleration due to gravity.

The static stability is expressed as

$$S = \Gamma - \Gamma_d = -\frac{dT}{dz} - \frac{g}{c_p} \tag{5.3}$$

If the lapse rate is locally larger than adiabatic lapse rate, then the atmosphere is said to be unstable, as any local rising motion of the atmosphere will be such that that portion will keep rising (S>0). On the contrary, if $\Gamma < \Gamma_d$ (S<0), the atmosphere is said to be stable, and the previous situation will not be observed.

The static stability is calculated for the selected orbits and is presented in Figures 5.8 and 5.9 for the morning and evening terminator respectively. At the morning terminator, the atmosphere is stable down to around 115 km, while at the evening terminator, the atmosphere becomes unstable below 110 km.

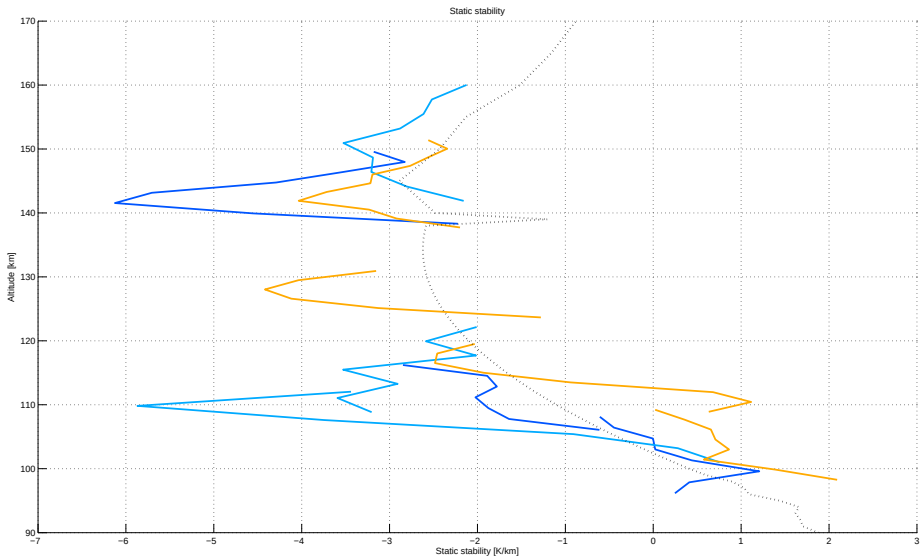

Figure 5.8: Static stability of the morning terminator measurements: orbits 361.1 (in dark blue), 593.1 (in light blue), and 1480.1 (in orange). The static stability from the VIRA model is given as the dotted black line.

2. The lapse rate is the derivative of the temperature with respect to the altitude.

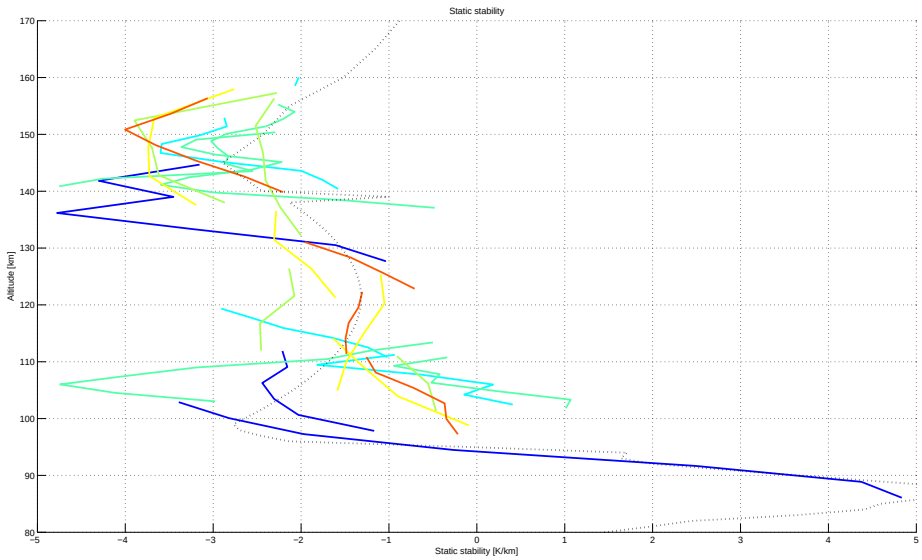

Figure 5.9: Static stability of the evening terminator measurements: orbits 335.1 (in dark blue), 684.1 (in light blue), 1461.1 (in dark green), 1465.1 (in light light green), 1469.1 (in yellow) and 1567 (in red). The static stability from the VIRA model is given as the dotted black line.

5.4.3 Comparison to the hydrostatic profiles

5.4.3.1 Introduction

The aim of this Section is to verify if the profiles determined using SOIR data do follow the hydrostatic law.

The hydrostatic equilibrium (HE) described by the hydrostatic equation and the ideal gas law have already been defined and discussed in Section 4.3 and are described by the equations [Chamberlain & Hunten (1987)]:

$$n_{CO_2}^{hydro}(z) = n_0 \cdot \exp\left(-\int_{z_0}^{z} \frac{dz}{H_{CO_2}}\right) \tag{5.4}$$

$$H_{CO_2} = \frac{k_B \cdot T(z) \cdot N_{Av}}{MM_{CO_2} \cdot g(z)} \tag{5.5}$$

where z is the altitude, $n_{CO_2}^{hydro}(z)$ is the hydrostatic density profile, n is the density profile, H_{CO_2} is the scale height, k_B is the Boltzmann constant and N_{Av} is the Avogadro number. The $_0$ refers to the reference altitude and density. In this case, we chose it as the lowest altitude where we have SOIR measurements.

The comparison between the measured density and the hydrostatic density obtained from equations (5.4) and (5.5) is investigated for the two orbits 1480.1 and 1567.1 that took place at 86.9° and -11.7° at the morning and evening terminator respectively. Results are presented in the left Panels of Figures 5.10 for the orbit 1480.1 and Figure 5.11 for orbit 1567.1. The scale height is given in the right Panels of both Figures 5.10 and 5.11 for the two orbits. First of all, it is clearly observed that the hydrostatic density is different from the retrieved density for both orbits. The error envelopes are given in both Figures by the dashed black lines. It is observed that the retrieved densities are almost entirely comprised within this envelope, except at low altitudes. These results are not convincing as the differences between the hydrostatic profiles and the retrieved profiles are large, sometimes by a factor 10.

The scale height is increasing regularly with altitude, and takes comparable values for both orbits.

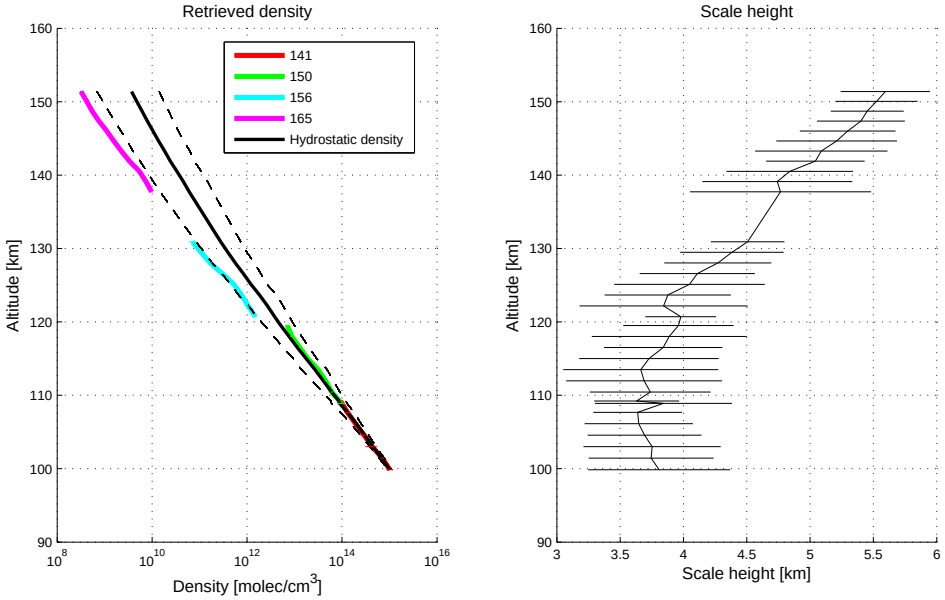

Figure 5.10: Comparison between the retrieved and the hydrostatic density in the left Panel for orbit 1480.1. The dashed curves are the error envelopes of the hydrostatic density. The hydrostatic density is obtained from equation (5.4) and from the retrieved rotational temperature profile. The scale height is given in the right Panel.

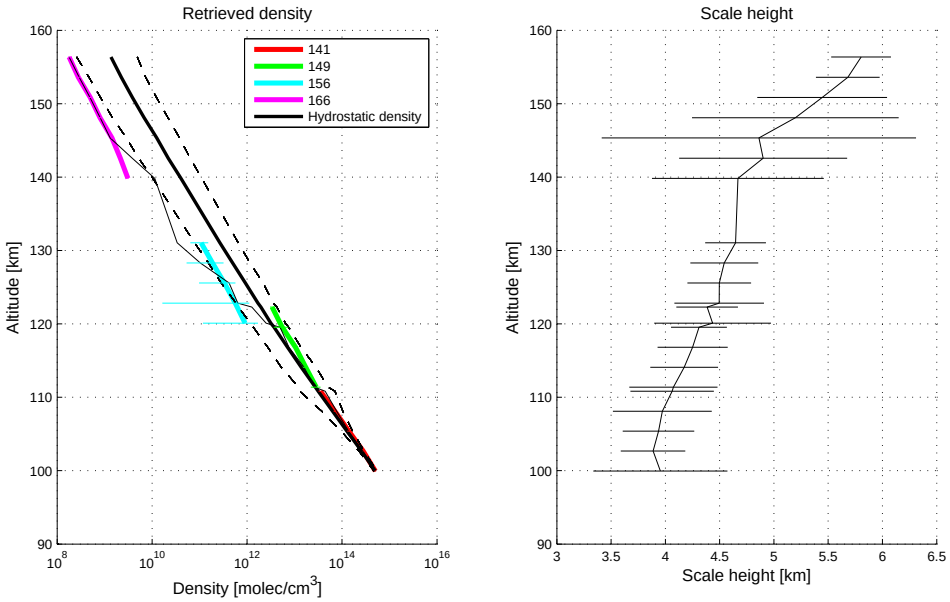

Figure 5.11: Comparison between the retrieved and the hydrostatic density in the left Panel for orbit 1567.1. The dashed curves are the error envelopes of the hydrostatic density. The hydrostatic density is obtained from equation (5.4) and from the retrieved rotational temperature profile. The scale height is given in right Panel.

In the next paragraphs, we investigate in detail the observed variations from the HE. Indeed, three independent variables play a role in the hydrostatic equation: the density $n_{CO_2}^{hydro}$, the temperature T and the local acceleration g. We propose several options that could explain the observed differences, by supposing that one of these variables is incorrect or wrongly attributed:

1. the CO_2 vmr is not constant with altitude, as explained in Section 2.3.4, i.e. the retrieved density n and the hydrostatic density $n_{CO_2}^{hydro}$ are not the same;
2. the temperature profile is different to the one retrieved using the OE method (Section 5.4.3.3), i.e. the rotational temperature is not equal to the hydrostatic/kinetic temperature;
3. the local acceleration is not only equal to the gravity field (Section 5.4.3.4), i.e. the fluid is in a vertical acceleration;
4. the atmosphere is not in HE (Section 5.4.3.5), i.e. one of the hypotheses on which the law is based are not satisfied.

We investigate all these options in the following paragraphs.

5.4.3.2 Volume mixing ratio

In this paragraph, we investigate the fact that the retrieved density is not the density that appears in the hydrostatic equation.

It is known that the CO_2 vmr decreases with increasing altitude [Keating *et al.* (1980); von Zahn *et al.* (1980); Hedin *et al.* (1983); Keating *et al.* (1985)]. The vmr is equal to 96.5% below altitudes of 100 km [Hedin *et al.* (1983)] and starts to decrease in the upper atmosphere. At very high altitude, CO and O become the principal compounds of the atmosphere. It is known that CO_2 photodissociates at high altitude due to solar UV on the dayside of the planet [Fox & Black (1989); Gérard *et al.* (2009)], which means that a CO_2 sink is present at these altitudes.

We propose two options: to compare the retrieved CO_2 density with the hydrostatic density in order to deduce a vmr, or two use the CO and atomic oxygen vertical profiles, produces of the CO_2 photodissociation, from the VIRA model to explain if it modifies the difference mentioned here above.

So, firstly we evaluate the CO_2 vmr considering the quotient between the CO_2 retrieved density and the CO_2 hydrostatic density obtained from the rotational temperature:

$$vmr_i^{retrieved}(z) = \alpha_i \cdot \frac{n_{CO_2,i}(z)}{n_{CO_2}^{hydro}(z)} \tag{5.6}$$

where z the altitude, $vmr_i^{retrieved}$ is the vmr calculated from the density profile $n_{CO_2,i}$ obtained from order i and the hydrostatic density profile $n_{CO_2}^{hydro}$ and α_i is a correction coefficient obtained to ensure that the CO_2 vmr equals to 0.965 at low altitude.

We decided to fit this vmr value using a least square algorithm by the following model:

$$vmr_{CO_2}(z) = 0.965 \textbf{ if } \quad z < z^* \tag{5.7}$$

$$vmr_{CO_2}(z) = 0.965 \cdot \exp\left(-a \cdot (z - z^*)^2 - b \cdot (z - z^*)\right) \textbf{ if } \quad z \geq z^* \tag{5.8}$$

with z^* an altitude level at which the inflection occurs and a and b the coefficient of a second degree polynomial. The polynomial is chosen with no constant term to ensure continuity in the vmr slope with respect to the altitude. The results of this calculation are presented in Figures 5.12 and 5.13 for orbits 1480.1 and 1567.1 respectively. The values of the model parameters are given in Table 5.4.

In these Figures, $vmr_i^{retrieved}$ are the color curves and vmr_{CO_2} is the black dotted curve. The error bars on $vmr_i^{retrieved}$ are the black horizontal lines. The curves do not match well at all, but the values remain within the error bars for both orbits. If we assume that this approach is correct and if we compare the values of z^* between the two occultations, we see that z^* is higher of 10 km for the polar measurement (orbit 1480.1) than for the mid-latitudes one (orbit 1657.1). The CO_2

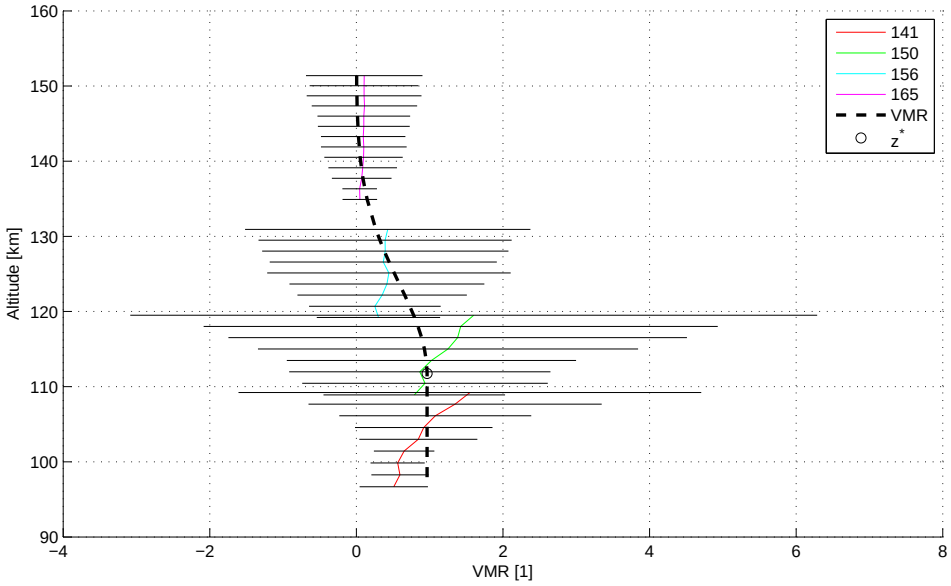

Figure 5.12: Calculation of the CO_2 volume mixing ratio of orbits 1480.1. The volume mixing ratio is obtained by dividing the retrieved density by the hydrostatic density obtained from equation (5.4). This vmr is fitted by the model described in equations (5.7) and (5.8) and is given by the dashed curve. The z^* altitude is represented by the circle in both Panels.

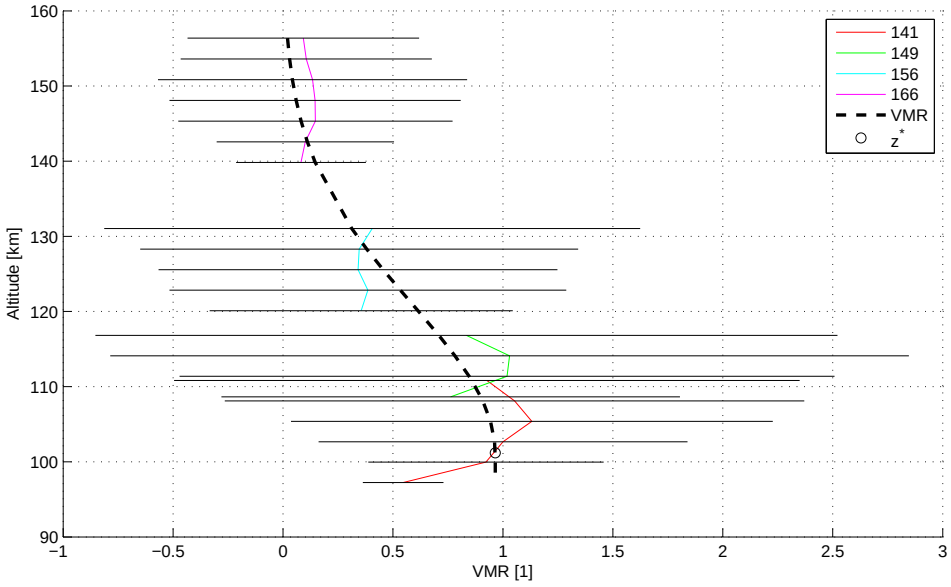

Figure 5.13: Calculation of the CO_2 volume mixing ratio of orbits 1567.1. The volume mixing ratio is obtained by dividing the retrieved density by the hydrostatic density obtained from equation (5.4). This vmr is fitted by the model described in equations (5.7) and (5.8) and is given by the dashed curve. The z^* altitude is represented by the circle in both Panels.

Orbit	z^* [km]	a [1]	b [km^{-1}]
1480.1	111.76	3.50E-03	2.34E-14
1567.1	101.19	1.26E-03	2.34E-14

Table 5.4: Values of the vmr model parameters described by equations (5.7) and (5.8) for orbits 1480.1 and 1567.1.

vmr reduces also much faster with altitude for the polar orbit than for the mid-latitudes one, as it can be seen through the values of a (see Table 5.4).

We are not satisfied with this approach. The values of the vmr are too different from the ones obtained using the fits by the model and the slopes of each single profile are incoherent with the overall shape of the profile.

We will consider the second option: to use CO and O vertical profiles from the VIRA model in the hydrostatic equilibrium equation.

Indeed, the hydrostatic equation represents the equilibrium between the pressure at a given level and the column of fluids above it. The hydrostatic equation can be written in its integral form as:

$$p_{hydro}(z) = -\int_{z_0}^{z} n(z) \cdot MM \cdot g(z) \cdot dz \tag{5.9}$$

If more than one specie is considered, the $n(z) \cdot MM$ factor becomes $\sum_{i=1}^{N_{species}} n_i(z) \cdot MM_i$, with the summation on all the species considered. In this case, CO_2, CO and O are taken into account, as they are species of the same chemistry cycle (see Section 2.3.4). Figures 5.14 and 5.15 show for orbit 1480.1 and 1567.1 respectively the correction to the vertical density profiles if the CO and O vertical profiles from VIRA are considered. The density profiles considering the products of CO_2 are much closer to the hydrostatic profile. However the coincidence is not perfect.

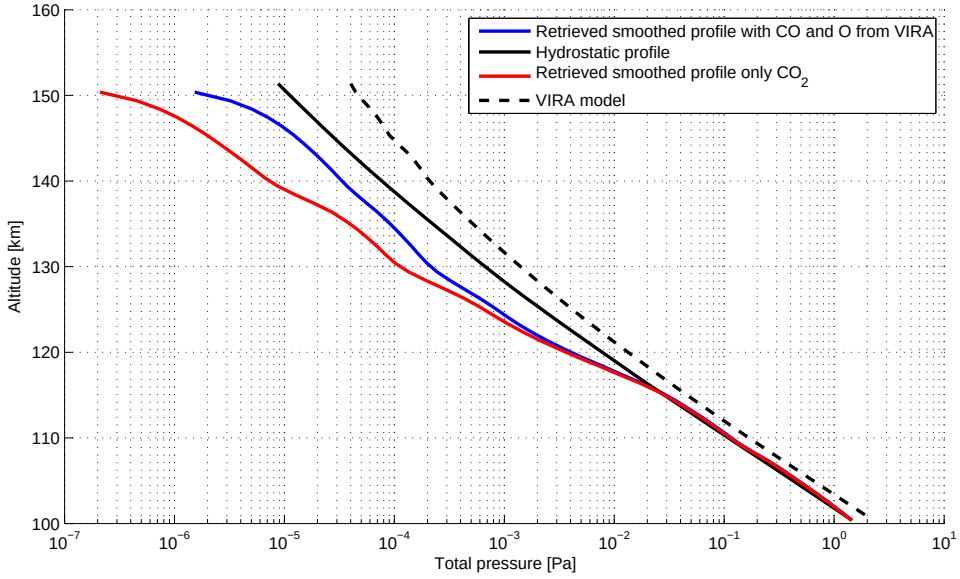

Figure 5.14: Comparison between the hydrostatic pressure profile and the retrieved pressure profiles (that have been combined and smoothed into one single profile), with a vertical pressure profile representing the CO_2, CO and O species. The VIRA model is also given.

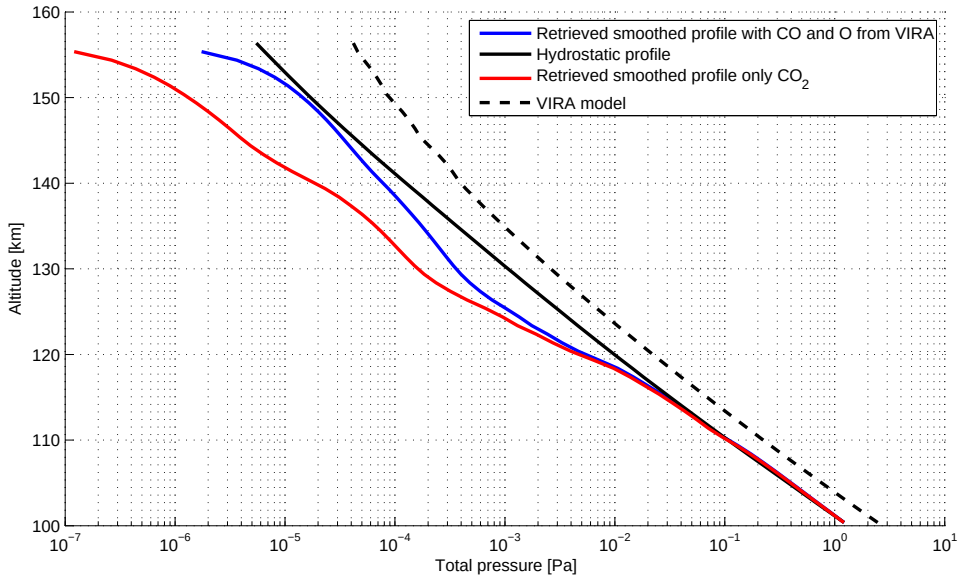

Figure 5.15: Comparison between the hydrostatic pressure profile and the retrieved pressure profiles (that have been combined and smoothed into one single profile), with a vertical pressure profile representing the CO_2, CO and O species. The VIRA model is also given.

We will consider other hypotheses in the next sections to find other explanations for the divergence from HE.

5.4.3.3 Temperature profile

In this Section, we consider that the rotational temperature profile can not be assimilated to the kinetic temperature - despite our assumptions in the non LTE Section (Section 4.6.8).

We derive the temperature profile from the HE law described by the equations (4.10) and (4.11) that was described in Section 4.3. From these equations, the following differential equation comes:

$$\frac{dT^{hydro}(z)}{dz} + T^{hydro}(z) \cdot \frac{d \log n_{CO_2}(z)}{dz} + \frac{MM_{CO_2} \cdot g(z)}{R} = 0 \tag{5.10}$$

where $T^{hydro}(z)$ is the hydrostatic temperature profile and $n_{CO_2}(z)$ the retrieved CO_2 density vertical profile.

The temperature profile comparison is given in Figures 5.16 and 5.17 for orbits 1480.1 and 1567.1, where the initial temperature of the differential equation is taken as the temperature of the highest point of the profiles from each orbit. The error envelopes are also presented in the Figures; they are obtained considering Equation (5.10) for $n_{CO_2}(z) + \Delta n_{CO_2}(z)$ and $n_{CO_2}(z) - \delta n_{CO_2}(z)$, with $\delta n_{CO_2}(z)$ the error on $n_{CO_2}(z)$.

The error bars from the two curves do not cover each other.

The hydrostatic temperature derived using equation (5.10), that would be attributed to the kinetic temperature, is very different to the rotational temperature. Indeed, it is explained in Section 4.6.8, from discussions with López Valverde (2010) and López Puertas (2010), that the rotational and kinetic temperatures should coincide, as the rotational temperature was derived from cold CO_2 vibrational bands.

The hydrostatic temperature calculated over the covered altitude range reach extreme values, ranging between 50 and 400 K for the polar 1480.1 occultation and between 100 and 300 K for the mid-latitudes 1567.1 orbit. The temperature gradients are also large for both orbits, with values of 62.5 K/km for orbit 1480.1 in the 130 - 140 km region.

We do not believe that the temperature profile difference could be an explanation. An option to verify this assumption would be to impose the hydrostatic temperature profiles in the OE method, instead of retrieving the rotational temperature. This approach was tested and the results of the fits were very bad. The spectra are poorly fitted and the root mean square is thus much larger than the one obtained when the temperature is directly fitted.

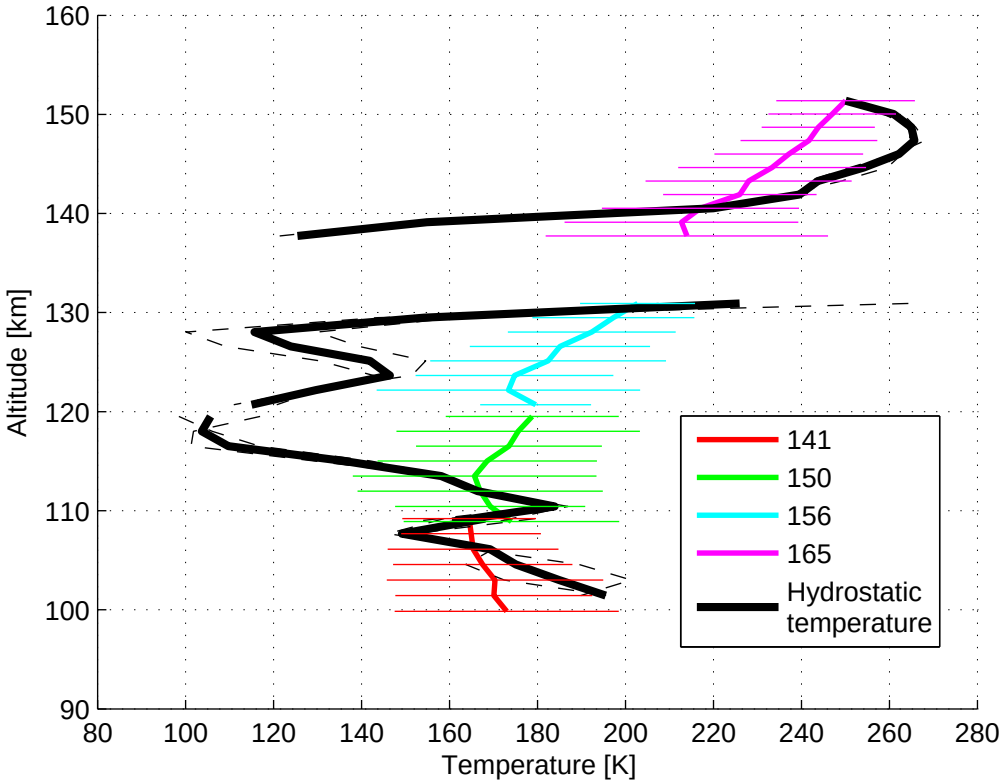

Figure 5.16: Comparison between the retrieved rotational temperature and the hydrostatic temperature for orbit 1480.1. The color curves are the retrieved temperature profiles from the 4 orders of the SOIR data, the black plain curve is the hydrostatic temperature obtained from the retrieved density profiles. The error bars on the measured temperature are given by the horizontal color lines, while the error on the calculated hydrostatic temperature is given as an envelope around the hydrostatic temperature (dashed lines).

5.4.3.4 Vertical acceleration

Another explanation could come from the acceleration term g in the hydrostatic equations (5.4) and (5.5). The acceleration that is used only accounts for the gravitational acceleration $g^{gravitational}(z)$. We introduce another term to evaluate a total acceleration $g(z)$ that would account for the local vertical dynamic acceleration of the fluid $\eta(z)$:

$$g(z) = g^{gravitational}(z) + \eta(z) \tag{5.11}$$

We investigate whether this could explain the differences observed between the hydrostatic and retrieved profiles.

The local acceleration can be obtained from equations (4.10), (4.11) and (5.11):

$$\eta(z) = -T_{CO_2}(z) \cdot R \cdot \frac{d\log(T_{CO_2}(z) \cdot n_{CO_2}(z))}{dz} \cdot \frac{R}{MM_{CO_2}} - g^{gravitational}(z) \tag{5.12}$$

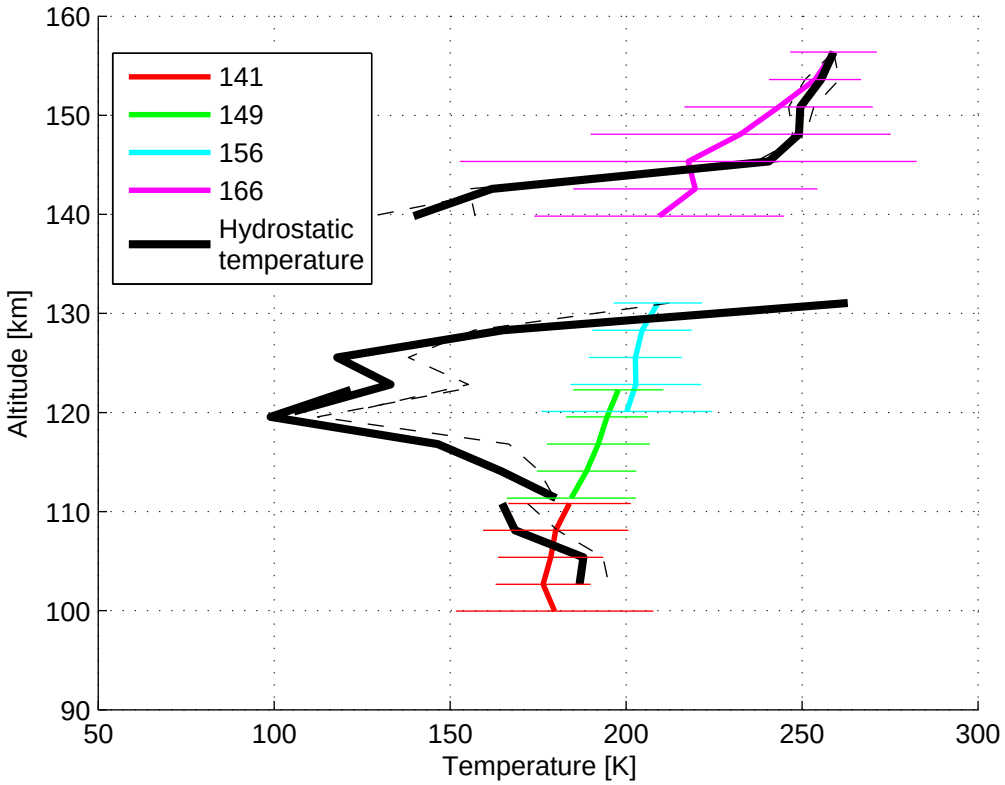

Figure 5.17: Comparison between the retrieved rotational temperature and the hydrostatic temperature for orbit 1567.1. The color curves are the retrieved temperature profiles from the 4 orders of the SOIR data, the black plain curve is the hydrostatic temperature obtained from the retrieved density profiles. The error bars on the measured temperature are given by the horizontal color lines, while the error on the calculated hydrostatic temperature is given as an envelope around hydrostatic temperature (dashed lines).

with $n_{CO_2}(z)$ and $T_{CO_2}(z)$ the CO_2 retrieved density and rotational temperatures vertical profiles.

The results of the calculation are presented in Figures 5.18 and 5.19 for orbits 1480.1 and 1567.1 respectively.

The residual accelerations obtained using equation (5.12) are all positive, with sometimes very large values. This means that the atmosphere would undergo a strong downwelling towards the planet. The largest values are observed at high altitude, reaching 5 to 6 m/s^2, and decreasing while going down in altitude to a minimum below 110 km. Note that the error bars contain the zero acceleration, starting from 120 km and going down in altitude.

This explanation seems to be the most convincing one, as a strong density drop at the terminator at a constant altitude, seen as a contraction of the atmosphere, is predicted in many models [Bougher *et al.* (1997a); Dickinson & Ridley (1975); Fox & Kasprzak (2007)]. The large vertical accelerations observed at high altitude and decreasing with altitude indicate that the fluid is literally falling, and that the effect is damped at lower altitudes. The acceleration argument is also in accordance with the lapse rate results, which showed that the atmosphere is unstable below 120 km.

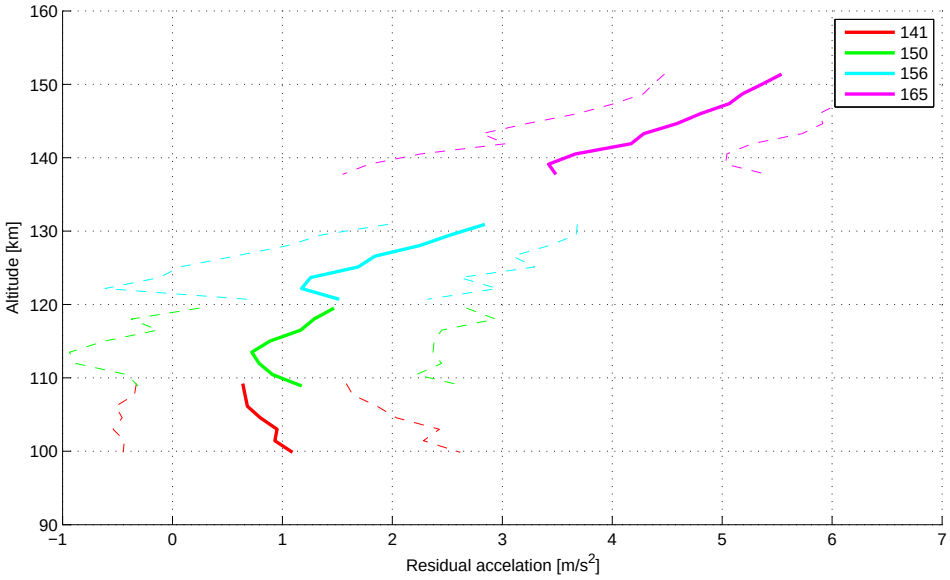

Figure 5.18: Calculation of the residual acceleration from the hydrostatic law for orbit 1480.1. The residual acceleration is given as the color curves for each order's density, and the error bars are given as the envelope around these curves (dotted curves).

5.4.3.5 Validity of the hydrostatic law

The final option that we considered is based on the fact that, if the hydrostatic law is valid, then its hypothesis must be fulfilled. It is that the volume of fluid should not be in an accelerated motion or in a constant motion. We know for example that the hydrostatic equation is not valid on Earth in strong convection atmospheric features, like thunderstorms [Petty (2008)], where the acceleration of the fluid is too large to assume hydrostatic equilibrium. From the accelerations that are derived in the previous paragraph, we wonder if the hydrostatic equation could still be valid: the strong density gradient predicted at the terminator may forbid the use of the HE equation and thus the results at the terminator should be considered with care.

Concerning the ideal gas equation, we do not consider any correction terms, as the pressure remains low enough at the altitudes considered and as the temperature is not too low: it is always above 150 K. However, corrected laws will be probably investigated in future work.

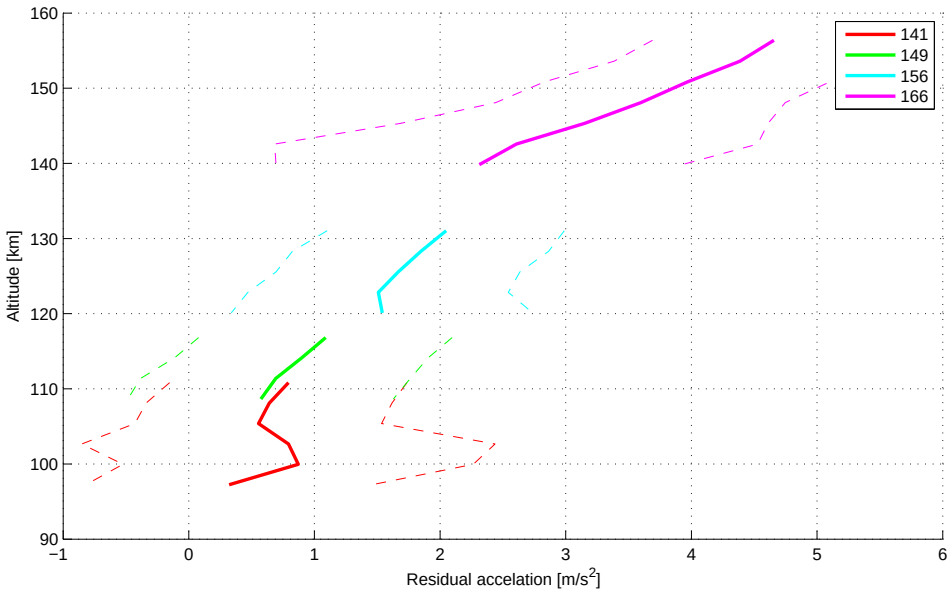

Figure 5.19: Calculation of the residual acceleration from the hydrostatic law for orbit 1567.1. The residual acceleration is given as the color curves for each order's density, and the error bars are given as the envelope around these curves (dotted curves).

5.4.3.6 Conclusion

The hydrostatic law is not fulfilled within the error bars of the density profiles and of the rotational temperature profiles derived from the SOIR data.

Four different hypotheses are presented and analyzed to explain this difference. The most convincing ones are to suppose that the atmosphere encounters a strong contraction at the terminator, and to consider CO_2 photodissociation into CO and O. But the derived vertical accelerations are very large, and reach 6 m/s^2 above 160 km, which suggests that the two effects should be combined in order to better understand the physics occurring at the terminator. This work will be presented in a paper under preparation [Mahieux *et al.* (2011a)].

It is in accordance with the atmosphere dynamics at these altitudes, i.e. the subsolar to antisolar circulation [Bougher *et al.* (2006); Clancy *et al.* (2008); Lellouch *et al.* (1994)], see Section 2.3.3.

The onion peeling algorithm transforms a 3D problem into a 1D problem, by assuming a spherical symmetry of the atmosphere. But it is shown and explained here that there is an asymmetry between the day and night atmosphere at high altitude. This effect is not yet introduced into the retrieval procedure, as it requires comparisons with dynamical models. This exercise will also be done in a future work in collaboration with teams developing models.

5.4.4 Comparison with ground based temperature measurements

In this Section, we report a comparison done by Krötz *et al.* (2011) of their temperature measurements with the SOIR rotational temperatures during OS 10 to 13 (March 2009 to February 2010, see Table 5.1). Krötz *et al.* (2011) used the Cologne Tunable Heterodyne[3] Infrared Spectrometer (THIS) at the NOAO McMath Telescope at Kitt Peak (Hawaii, USA). The description of the technique can be found in Sonnabend *et al.* (2010). The FOV of THIS is 1.7 arcsec.

Their values are limited to a local time range of 1.5 hours from the terminator into the day side, and take place at an altitude of 110 km. The comparison between the SOIR data at 110 km ± 3 km and THIS is presented in Figure 5.20.

3. Heterodyning is the generation of new frequencies by mixing two signals at different frequencies.

In general, it appears that the IR heterodyne values from THIS are slightly warmer than the SOIR values. This can be explained by the differences in the FOV of the two instruments and the assumption that the day side is warmer than the night side. The latitudinal dependence of temperature is well reproduced for both measurements.

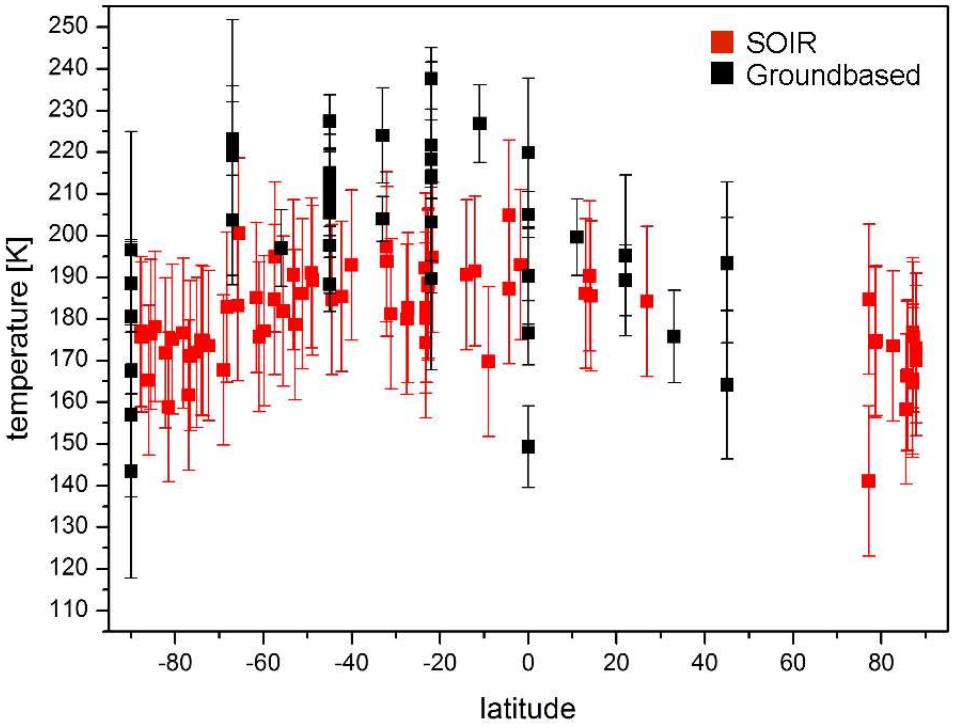

Figure 5.20: Comparison between the SOIR rotational temperature and the THIS temperature measurements during OS 10 to 13 at morning and evening terminator (within 1.5 h to the terminator) at 110 km ± 3 km, from Krötz *et al.* (2011)

5.5 Whole data set: future prospects

The entire available CO_2 dataset has been investigated: it includes 288 different density and temperature profiles coming from 188 orbits from all latitudes and morning and evening terminator, covering an altitude range from 90 to 175 km. The results from the two bins are combined, as explained in Section 4.6.10. They are presented in Figure 5.21 for the density, and in Figure 5.22 for the rotational temperature.

In these Figures, the colors are linked to the time, i.e. the orbit number, from dark blue for the first measured orbit (number 35.1) to red for the last one (number 1685.1). The error bars are not plotted, to ensure readability. The error bars on the density range between 1% and 20%, while the error bars on the temperature vary between 5 K and 30 K.

Large variations are observed in the density and temperature profiles. These variations occur as a function of time as well as a function of latitude. A factor 100 between the lowest and the highest density is observed at 110 km of altitude, and a factor 10 at 150 km. The temperature differences range between 46 K at 110 km and 15 K at 150 km altitude. These large variations had already been observed by the different missions to Venus [Bougher *et al.* (1997a); Zasova *et al.*

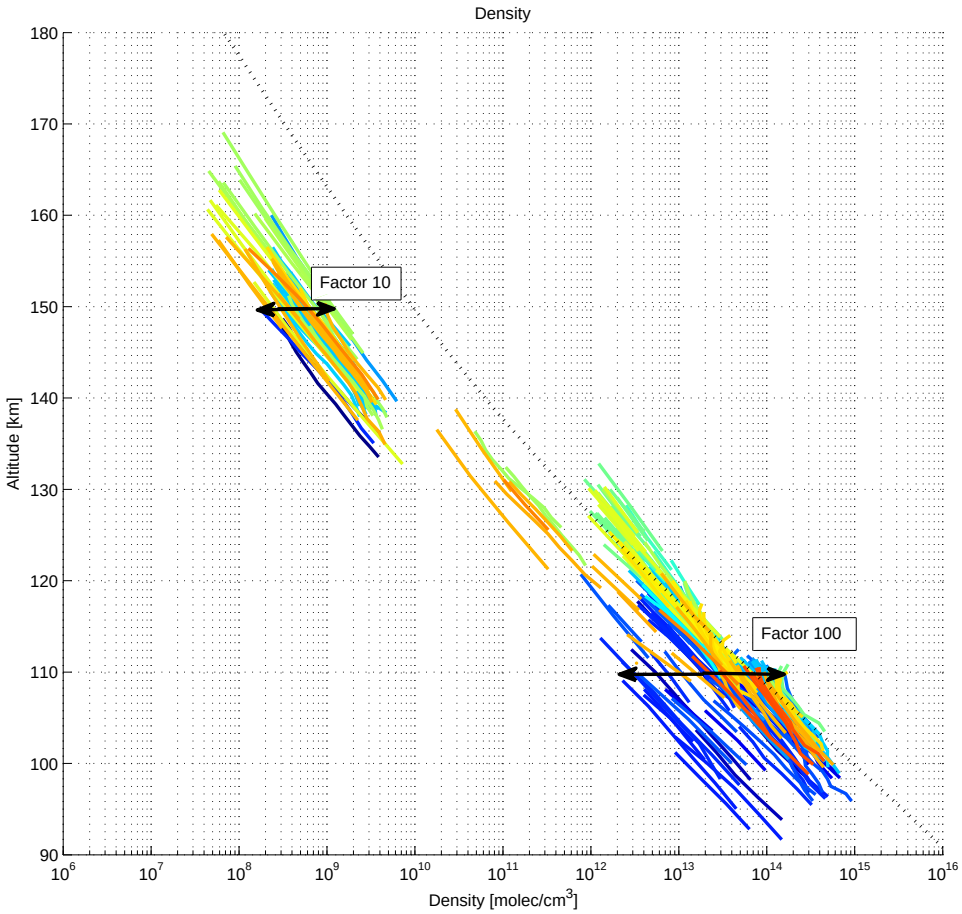

Figure 5.21: The density profiles obtained from the available data set, i.e. 288 CO_2 profiles from 188 orbits, are presented. The variations at 110 and 150 km of altitude are also given. The colors correspond to the orbit number (blue are the first ones, red are the last ones). The dotted black curve is the VIRA model.

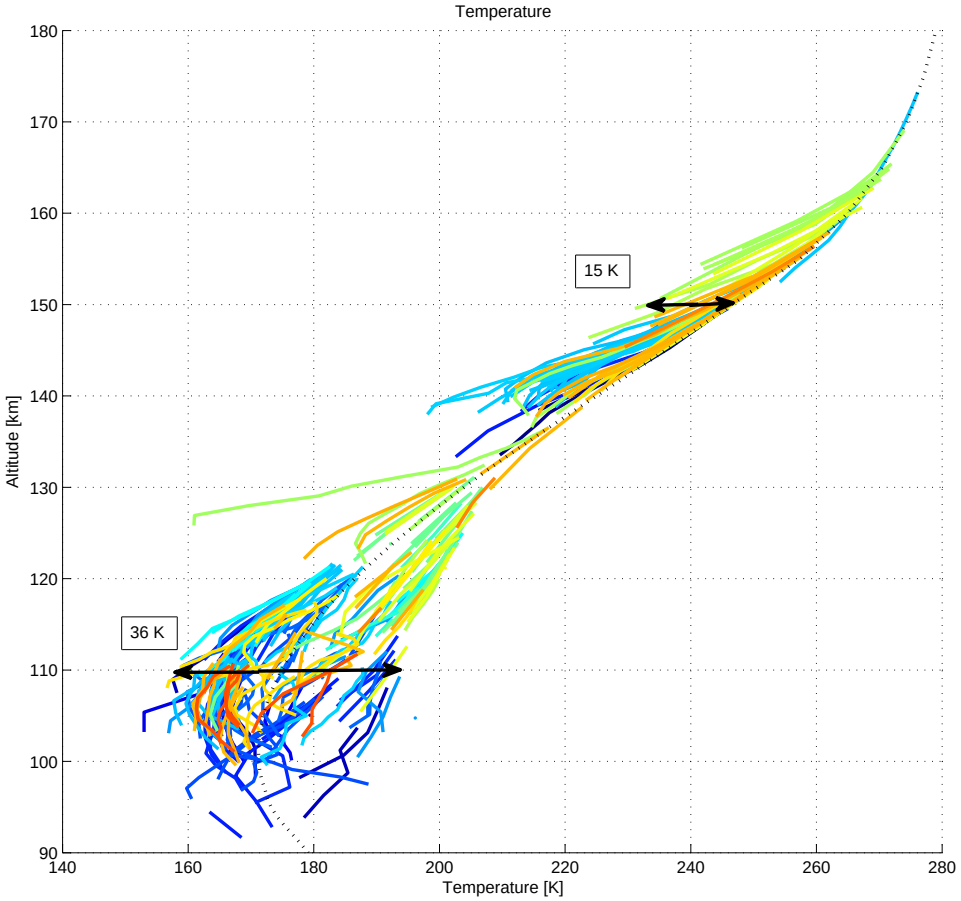

Figure 5.22: The rotational temperature profiles obtained from the available data set, i.e. 288 CO_2 profiles from 188 orbits, are presented. The variations at 110 and 150 km of altitude are also given. The colors correspond to the orbit number (blue are the first ones, red are the last ones).

(2006)]. But the variations observed at the terminator seem to be larger than the ones observed at other local solar times.

In a near future, the dataset will be studied in terms of latitude and time variations, by studying the temperature and density at different altitude levels. For the latitude variations, this work could be done by considering the different OS separately, in order to avoid the time variations. For the time variations, different latitude groups could be created and the variations from OS to OS studied.

A preliminary example of such analysis is given in Figure 5.23 (density) and Figure 5.24 (rotational temperature) for OS 7. In these Figures, three altitude levels are selected: 105, 115 and 150 km. The colors are linked to the time: from blue (orbit 667.1) to red (orbit 710.2). Variations, which seem to have a periodic behavior, as a function of latitude are observed, for both density and rotational temperature. The properties of these variations will be one of the subjects of future studies with the SOIR instrument.

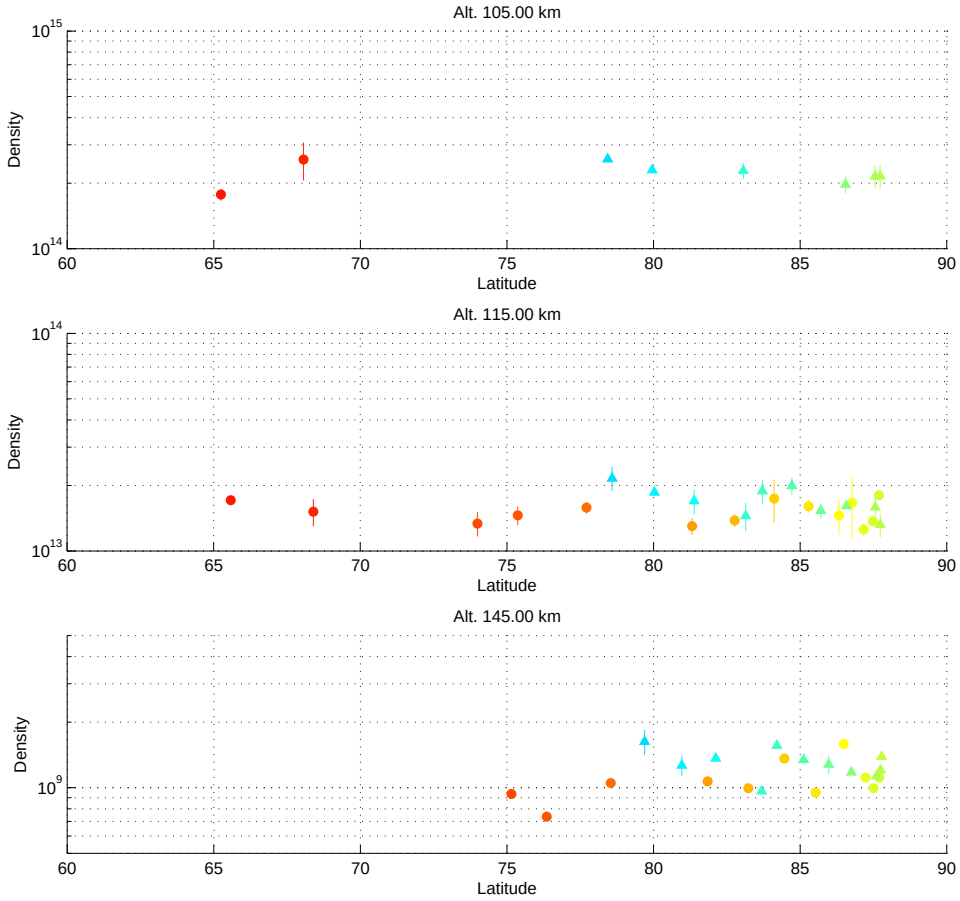

Figure 5.23: CO_2 latitudinal density variations during OS 7 presented at three altitudes: 105, 115 and 145 km. The vertical bars correspond to the error bars obtained from the OEM fits. The latitude extend between 60° N and 90° N. The circles correspond to the morning terminator measurements and the triangles to the evening ones.

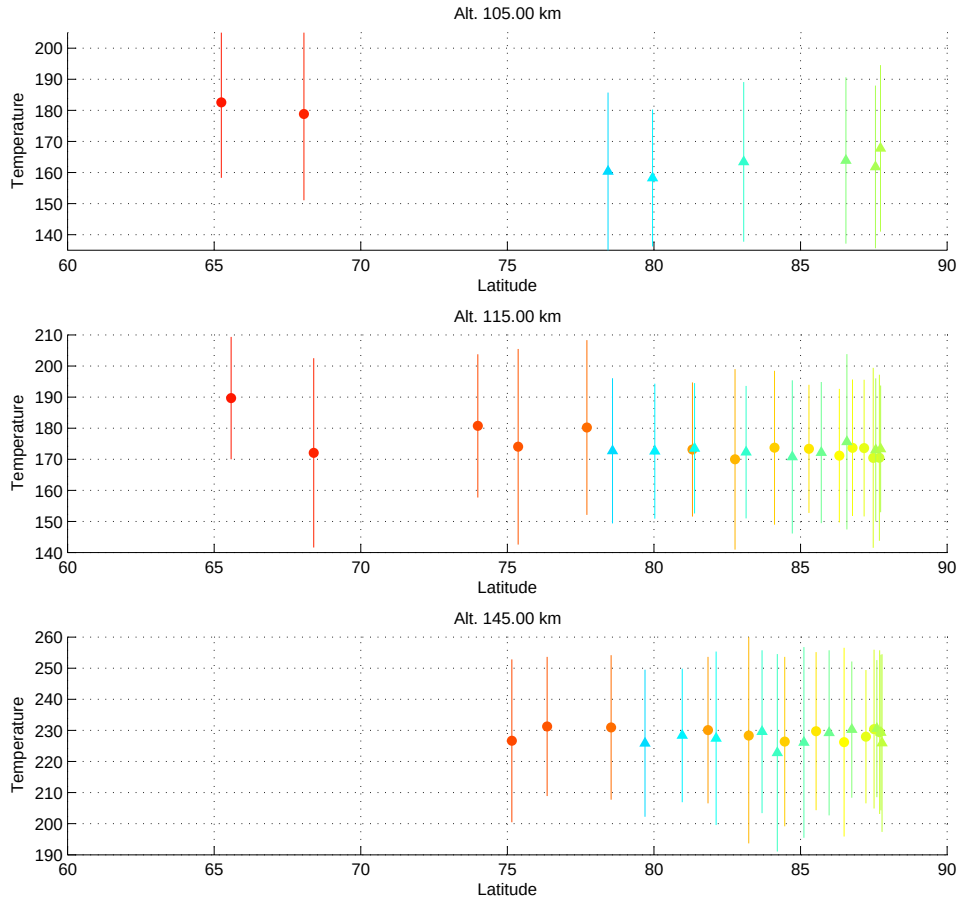

Figure 5.24: CO_2 latitudinal rotational temperature variations during OS 7 presented at three altitudes: 105, 115 and 145 km. The vertical bars correspond to the error bars obtained from the OEM fits. The latitude extend between 60° N and 90° N. The circles correspond to the morning terminator measurements and the triangles to the evening ones.

Chapter 6

Conclusion and future prospects

6.1 Conclusions

The capabilities of the SOIR instrument to measure high resolution vertical profiles at the Venus terminator, between 70 and 180 km, at all latitudes have been demonstrated in this work, considering the particular case of the main Venus atmospheric constituent: CO_2.

In the present manuscript, the different calibrations that the SOIR instrument underwent have been described. They covered the three main optical elements of the instrument: the AOTF, the echelle grating and the detector [Mahieux *et al.* (2008)]. Special attention has been paid to the study of the AOTF transfer function, for which a new dedicated determination method was developed [Mahieux *et al.* (2009)]. This method proved its efficiency in terms of quality of the spectra (signal to noise, line separation, etc) and in terms of scientific results, such as the vertical CO_2 density, temperature and aerosols content profiles.

Asimat, a dedicated algorithm for the spectral inversion of the SOIR acquired data, has also been developed [Mahieux *et al.* (2010)]. Even if the instrument was initially designed to measure density profiles, successful direct rotational CO_2 temperature profiles are also retrieved from the occultation data, which offer unforeseen possibilities. Before SOIR, most of the temperature measurements obtained were limited to given altitude regions, and temperature vertical profiles could only be obtained from expensive atmospheric probes. The fact that rotational temperature are directly derived from the spectra offers possibilities to obtain more information concerning the dynamics occurring at the measurement points.

The temperature vertical profiles obtained by SOIR have been compared to simultaneous ground-based measurements of the Venus' terminator. The results obtained by Krötz *et al.* (2011); Sonnabend *et al.* (2008) using IR spectroscopy agree very well with the ones obtained by SOIR at an altitude of 110 km.

The data obtained by SOIR are limited to the Venus terminator. At first glance, this can be seen as a serious drawback. However this represents a prodigious challenge, as flows from day to night sides are suspected to occur, but have almost never been directly observed up to now. It is supposed that the atmosphere encounters a serious contraction at these local solar times, which has impacts on the density profiles [Mahieux *et al.* (2011b)]. These dynamics are poorly understood, and SOIR data should definitively help to understand these phenomena. Some hypotheses concerning the CO_2 dynamics have been presented in this work, but more study needs to be carried out to further understanding.

The simultaneous retrieval of four different diffraction orders is a major advantage: it allows the retrieval of the same specie vertical profiles at different altitude levels from different absorption bands, and thus to construct vertical profiles covering wide altitude ranges. Also, if different species absorb in the studied orders, it offers the possibility to calculate precise vmr vertical profiles to the CO_2 density, as major atmospheric compound. This motivated the initial study of the CO_2

vertical profiles, as most of the available data in the literature usually consider volume mixing ratios and not volume densities in terms of molec/cm^3.

6.2 Parallel studies

Some results concerning CO_2 have been presented here, but vertical profiles of many other compounds are also retrieved, such as H_2O [Fedorova *et al.* (2008)], CO, HCl, HF [Vandaele *et al.* (2008)], SO_2 [Belyaev *et al.* (2008, 2011)] and their principal isotopologues, and detection limits of other species are also calculated. Results similar to those shown here for CO_2 can be obtained. The study of some of these species will help understand some key chemistry aspects of the Venus atmosphere, such as the deuterium hydrogen ratio [Bertaux *et al.* (2006)], the CO photochemistry, the role of HCl in the sulfur cycle, etc., by giving information to the different models of the Venusian atmosphere chemistry that are developed by different institutes [Mills *et al.* (2007)].

The CO_2 isotopic ratios of the three main isotopologues are also currently investigated, and compared to the literature. The values are comparable to what is observed on Earth [Mahieux *et al.* (2011a)].

Also, unforeseen CO_2 weak absorption bands have been detected by the SOIR instrument [Bertaux *et al.* (2008); Wilquet *et al.* (2008)], and others have been discovered [Robert *et al.* (2011)].

The aerosol compounds are also deeply studied using the SOIR data [Wilquet *et al.* (2011)], and sometimes combined with SPICAV/IR and SPICAV/UV data [Wilquet *et al.* (2009)]. The particle size distribution, spatial, latitudinal and temporal distribution are studied, with the excellent vertical resolution of SOIR from 100 km down to 65 km.

6.3 Future prospects

Some aspects of future work have been given in the previous Chapter: the understanding of the latitudinal and temporal variations of CO_2.

Future work should also concentrate on the exploitation of the SOIR CO_2 data to better understand the terminator's dynamics. Long term studies of the dynamics over the 4 years of data accumulated up to now should help to understand which phenomena occur at these particular locations. A complete study of the other compounds data sets should complete the work of the coming years.

Simultaneous ground-based campaigns are also foreseen, such as the one described in the previous Section, which will allow us to compare our data to other instruments data, and therefore to validate the method and analysis described in this work.

We are also focusing for the moment on the search for new species in our spectra, such as HBr and HI, that should be observed by SOIR if they are present in the atmosphere.

Bibliography

Ackerman, A. A., & Knox, J. A. 2007. *Meteorology : Understanding the atmosphere*. Thomson Brooks/Cole.

Bandwell, C. N., & McCash, E. M. 1994. *Fundamentals of molecular spectroscopy*. Fourth edn. London: McGraw-Hill book company.

Banks, P. M., & Kockarts, G. 1973. *Aeronomy Part B*. Aeronomy, vol. 2. New York: Academic Press.

Barabash, S., Sauvaud, J.-A., Gunell, H., Andersson, H., Grigoriev, A., Brinkfeldt, K., Holmstrom, M., Lundin, R., Yamauchi, M., Asamura, K., Baumjohann, W., Zhang, T.L., Coates, A.J., Linder, D. R., Kataria, D.O., Curtis, C.C., Hsieh, K. C., Sandel, B.R., Fedorov, A., Mazelle, C., Thocaven, J.-J., Grande, M., Koskinen, H.E.J., Kallio, E., Sales, T., Riihela, P., Kozyra, J., Krupp, N., Woch, J., Luhmann, J., McKenna-Lawler, S., Orsini, S., Cerulli-Irelli, R., Mura, M., Milillo, M., Maggi, M., Roelof, E., Brandt, P., Russell, C.T., Szego, K., Winningham, J.D., Frahm, R.A., Scherrer, J., Sharber, J.R., Wurz, P., & Bochsler, P. 2007. The Analyser of Space Plasmas and Energetic Atoms (ASPERA-4) for the Venus Express mission. *Planet. Space Sci.*, **55**(12), 1772–1792.

Belyaev, D., Korablev, O., Fedorova, A., Bertaux, J.-L., Vandaele, A. C., Montmessin, F., Mahieux, A., Wilquet, V., & Drummond, R. 2008. First observations of SO_2 above Venus' clouds by means of solar occultation in the infrared. *J. Geophys. Res.*, **113**, doi:10.1029/2008JE003143.

Belyaev, D., Montmessin, F., Bertaux, J.-L., Mahieux, A., Fedorova, A., Korablev, O., Marcq, E., Y.Yung, & Zhang, X. 2011. Vertical profiling of SO_2 and SO above Venus' clouds by SPICAV/SOIR solar occultations. *Icarus*, **(submitted)**.

Bertaux, J.-L., Fonteyn, D., Korablev, O., Chassefière, E., Dimarellis, E., Dubois, J.P., Hauchecorne, A., Cabane, M., Rannou, P., Levasseur-Regourd, A.C., Cernogora, G., Quémerais, E., Hermans, C., Kockarts, G., Lippens, C., De Mazière, M., Moreau, D., Muller, C., Neefs, B., Simon, P.C., Forget, F., Hourdin, F., Talagrand, O., Moroz, V.I., Rodin, A.V., Sandel, B., & Stern, A. 2000. The study of the Martian atmosphere from top to bottom with SPICAM Light on Mars Express. *Planet. Space Sci.*, **48**(12-14), 1303–1320.

Bertaux, J.-L., Korablev, O., Perrier, S., Quémerais, E., Montmessin, F., Leblanc, F., Lebonnois, S., Rannou, P., Lefèvre, F., Forget, F., Fedorova, A., Dimarellis, E., Reberac, A., Fonteyn, D., Chaufray, J.Y., & Guibert, S. 2006. SPICAM on Mars Express: Observing modes and overview of UV spectrometer data and scientific results. *J. Geophys. Res.*, **111**(E10S90).

Bertaux, J.-L., Nevejans, D., Korablev, O., Villard, E., Quémerais, E., Neefs, E., Montmessin, F., Leblanc, F., Dubois, J.P., & Dimarellis, E. 2007. SPICAV on Venus Express: Three spectrometers to study the global structure and composition of the Venus atmosphere. *Planetary and Space Science*, **55**(12), 1673–1700.

Bertaux, J.-L., Vandaele, A. C., Wilquet, V., Montmessin, F., Dahoo, R., Villard, E., Korablev, O., & Fedorova, A. 2008. First observation of 628 CO_2 isotopologue band at 3.3 μm in the atmosphere of Venus by solar occultation from Venus Express. *Icarus*, **195**(1), 28–33.

Bézard, B., Baluteau, J.P., Marten, A., & Coron, N. 1987. The $^{12}C/^{13}C$ and $^{16}O/^{18}O$ ratios in the atmosphere of Venus from high-resolution 10-μm spectroscopy. *Icarus*, **72**(3), 623–634.

Bingen, C., Vanhellemont, F., & Fussen, D. 2003. A new regularized inversion method for the retrieval of stratospheric aerosol size distributions apllied to 16 years of SAGE II data (1984-2000): method, results and validation. *Annales Geophysicae*, **21**, 797–804.

Bougher, S. W. 1995. Comparative thermospheres: Venus and Mars. *Advances in Space Research*, **15**(4), 21–45.

Bougher, S. W., Alexander, M.J., & Mayr, H.G. 1997a. *Upper atmosphere dynamics: Global circulation and gravity waves*. Vol. 1. Tucson: The University of Arizona Press. Pages 259–291.

Bougher, S. W., Hunten, D.M., & Phillips, R.J. 1997b. Venus II: Geology, Geophysics, Atmosphere, and Solar Wind Environment. *The University of Arizona Press*.

Bougher, S. W., Rafkin, S., & Drossart, P. 2006. Dynamics of the Venus upper atmosphere: Outstanding problems and new constraints expected from Venus Express. *Planetary and Space Science*, **54**(13-14), 1371–1380.

Chamberlain, J. W., & Hunten, D.M. 1987. *Hydrodynamics of atmospheres*. New York: Academic Press. Pages 71–117.

Chang, I.C., Pellegrino, Berg, N., & J. 1996. *Acousto-optic signal processing: theory and implementation*. New York: Marcel Dekker.

Clancy, R. T., & Muhleman, D. O. 1983. A measurement of the ^{12}CO / ^{13}CO ratio in the mesosphere of Venus. *Astrophys. J.*, **273**, 829–936.

Clancy, R. T., & Muhleman, D. O. 1991. Long-term (1979-1990) changes in the thermal, dynamical and compositional structure of the Venus mesosphere as inferre from microwave spectral line observations of ^{12}CO, ^{13}CO, and $C^{18}O$. *Icarus*, **89**(1), 129–146.

Clancy, R. T., Sandor, B. J., & Moriarty-Schieven, G. H. 2008. Venus Upper Atmospheric CO, Temperature, and Winds across the Afternoon/Evening Terminator from June 2007 JCMT Submillimeter Line Observations. *Planet. Space Sci.*, **56**(10), 1344–1354.

Collard, & al., et. 1993. Latitudinal distribution of carbon monoxide in the deep atmosphere of Venus. *Planet. Space Sci.*, **41**, 487.

Crisp, D., Allen, D.A., Grinspoon, D.H., & Pollack, J.B. 1991. The dark side of Venus: Near infrared images and spectra from the Anglo-Australian Observatory. *Science*, **253**(5025).

de Bergh, C. 1995. Isotopic ratios in planetary atmospheres. *Adv. Space Res.*, **15**(3), 427–440.

de Bergh, C., Moroz, V.I., Taylor, F.W., Crisp, D., Bézard, B., & Zasova, L.V. 2006. The composition of the atmosphere of Venus below 100 km altitude: An overview. *Planetary and Space Science*, **54**(13-14), 1389–1397.

Deming, D., Espenak, F., Jennings, D. E., Kostiuk, T., Mumma, M. J., & Zipoy, D. 1983. Observations of the 10-micron natural laser emission from the mesospheres of Mars and Venus. *Icarus*, **55**, 356–368.

Dickinson, R.E., & Ridley, E. C. 1975. A Numerical Model for the Dynamics and Composition of the Venusian Thermosphere. *Journal of the Atmospheric Sciences*, **32**, 1219–1231.

Donahue, T.M., Grinspoon, D.H., Hartle, R.E., & Hodges Jr., R.R. 1997. Ion/Neutral Escape of Hydrogen and Deuterium: Evolution of Water. *Venus II: Geology, Geophysics, Atmosphere, and Solar Wind Environment/ Bougher, Hunten & Phillips Ed.*, 385–414.

Drossart, P., Bézard, B., Encrenaz, T., Lellouch, E., Roos, M., Taylor, F.W., Collard, A.D., Calcutt, S.B., Pollack, J., Grinspoon, D.H., Carlson, R.W., Baines, K.H., & Kamp, L.W. 1993. Search for spatial variations of the H_20 abundance in the lower atmosphere of Venus from NIMS-Galileo. *Planetary and Space Science*, **41**(7), 495–504.

Drossart, P., Piccioni, G., Adriani, A., Angrilli, F., Arnold, G., Baines, K.H., Bellucci, G., Benkhoff, J., Bézard, B., Bibring, J.-P., Blanco, A., Blecka, M.I., & Carlson, R.W. 2007. Scientific goals for the observation of Venus by VIRTIS on ESA/Venus Express mission. *Planet. Space Sci.*, **55**(12), 1653–1672.

Edwards, D.P., López Puertas, M., & Gamache, R.B. 1998. The non-LTE correction to the vibrational component of the internal partition sum for atmospheric calculations. *J. Quant. Spectrosc. Radiat. Transfer*, **59**(3-5), 423–436.

Engman, S., & Lindblom, P. 1982. Blaze characteristics of echelle gratings. *Applied Optics*, **21**(23), 4356–4362.

Esposito, L.W. 1983. *The clouds and hazes on Venus.* Univ. of Arizona. Pages 484–564.

Esposito, L.W., Bertaux, J.-L., Krasnopolsky, V., Moroz, V.I., & Zasova, L.V. 1997. *Chemistry of lower atmosphere and clouds.* Univ. of Arizona Press. Pages 415–458.

Fedorova, A., Korablev, O., Vandaele, A. C., Bertaux, J.-L., Belyaev, D., Mahieux, A., Neefs, E., Wilquet, V., Drummond, R., Montmessin, F., & Villard, E. 2008. HDO and H_2O vertical distribution and isotopic ratio in the Venus mesosphere by SOIR spectrometer on board Venus Express. *J. Geophys. Res.*, doi:10.1029/2008JE003146.

Fegley Jr., B. 2004. *Encyclopedia of paleoclimatology and ancient environments: Venus.* Vol. 21. Springer. Pages 1–56.

Formisano, V., Angrilli, F., Arnold, G., Atreya, S., Baines, K.H., Bellucci, G., Bézard, B., Billebaud, F., Biondi, D., Blecka, M.I., Colangeli, L., Comolli, L., Crisp, D., D Amore, M., Encrenaz, T., Ekonomov, A.P., Esposito, F., Fiorenza, C., Fonti, S., Giuranna, M., Grassi, D., Grieger, B., Grigoriev, A., Helbert, J., Hirsch, H., Ignatiev, N., Jurewicz, A., Khatuntsev, I., Lebonnois, S., Lellouch, E., Mattana, A., Maturilli, A., Mencarelli, E., Michalska, M., López Moreno, J., Moshkin, B., Nespoli, F., Nikolsky, Yu., Nuccilli, F., Orleanski, P., Palomba, E., Piccioni, G., Rataj, M., Rinaldi, G., Rossi, M., Saggin, B., Stam, D., Titov, D., Visconti, G., & Zasova, L. 2006. The Planetary Fourier Spectrometer (PFS) onboard the European Venus Express mission. *Planetary and Space Science*, **54**(13-14), 1298–1314.

Fox, J. L., & Black, J.H. 1989. Photodissociation of CO in the thermosphere of Venus. *Geophys. Res. Letter*, **16**(4), 291–294.

Fox, J.L., & Kasprzak, W.T. 2007. Near-terminator Venus ionosphere: Evidence for a dawn/dusk asymmetry in the thermosphere. *J. Geophys. Res.*, **112**(E09008).

Gallery, W.O., Kneizys, F.X., & Clough, S.A. 1983. *Air mass computer program for atmospheric transmittance/radiance calculation: FSCATM.* Tech. rept. ERP-828/AFGL-TR-83-0065. Air Force.

Garcia, R. F., Drossart, P., Piccioni, G., López Valverde, M.A., & Occhipinti, G. 2009. Gravity waves in the upper atmosphere of Venus revealed by CO_2 nonlocal thermodynamic equilibrium emissions. *J. Geophys. Res.*, **114**, E00B32.

Gel'man, B., Zolotukhin, V., Lamonov, N., Levchuk, B., Lipatov, A., Mukhin, L., Nenarokov, D., Rotin, V., & Okhotnikov, B. 1980. An analysis of the chemical composition of the atmosphere of Venus on an AMS of the Venera-12 using a gas chromatograph. *Cosmic Res.*, **17**, 585–589.

Gérard, J.-C., Hubert, B., Shematovich, V.I., Bisikalo, D.V., & Gladstone, G.R. 2008. The Venus ultraviolet oxygen dayglow and aurora: Model comparison with observations. *Planet. Space Sci.*, **56**(3-4), 542–552.

Gérard, J.-C., Saglam, A., Piccioni, G., Drossart, P., Montmessin, F., & Bertaux, J.-L. 2009. Atomic oxygen distribution in the Venus mesosphere from observations of O_2 infrared airglow by VIRTIS-Venus Express. *Icarus*, **199**, 264–272.

Gilli, G., López Valverde, M.A., Drossart, P., Piccioni, G., Erard, S., & Cardesin-Moinelo, A. 2009. Limb observations of CO_2 and CO non-LTE emissions in the Venus atmosphere by VIRTIS/Venus Express. *J. Geophys. Res.*, **114**(E00B29), doi:10.1029/2008JE003112.

Glenar, D.A., Hillman, J.J., Saif, B., & Bergstralh, J. 1994. Acousto-optic imaging spectropolarimetry for remote sensing. *Applied Optics*, **33**(31), 7412–7424.

Goody, R.M., & Yung, Y.L. 1995. *Atmospheric Radiation: Theoretical Basis*. Oxford University Press.

Gottlieb, Milton S. 1994. *Acousto-optical Tunable filter*. New-York: Marcel Dekker. Pages 197–283.

Grinspoon, D.H. 1993. Implications of the high D/H ratio for the sources of water in Venus' atmosphere. *Nature*, **363**, 428–431.

Hase, F., Wallace, L., McLeod, S., Harrison, J. J, & Bernath, P. 2009. The ACE-FTS atlas of the infrared solar spectrum. *Journal of Quantitative Spectroscopy and Radiative Transfer*, **doi:10.1016/j.jqsrt.2009.10.020**.

Häusler, B., Pätzold, M., Tyler, G.L., Simpson, R.A., Bird, M.K., Dehant, V., Barriot, J.-P., Eidel, W., Mattei, R., Remus, S., Selle, J., Tellmann, S., & Imamura, T. 2006. Radio science investigations by VeRa onboard the Venus Express spacecraft. *Planet. Space Sci.*, **54**(13-14), 1315–1335.

Hedin, A.E., Niemann, H.B., & Kasprzak, W.T. 1983. Global empirical model of the Venus thermosphere. *J. Geophys. Res.*, **88**(A1), 73–83.

Hsieh, Chih-Cheng, Wu, Chung-Yu, Jih, Far-Wen, & Sun, Tai-Ping. 1997. Focal-Plane-Arrays and CMOS Readout Techniques of Infrared Imaging Systems. *IEEE Transactions on circuits and systems for video technology*, **7**(4), 594–605.

Hui, A.K., Armstrong, B.H., & Wray, A.A. 1978. Rapid computation of the Voigt and complex error functions. *J. Quant. Spectrosc. Radiat. Transfer*, **19**(5), 509–516.

Ignatiev, N.I., Moroz, V.I., Moshkin, B.E., Ekonomov, A.P., Gnedykh, V.I., Grigoriev, A.V., & Khatuntsev, I.V. 1997. Water vapour in the lower atmosphere of Venus: A new analysis of optical spectra measured by entry probes. *Advances in Space Research*, **19**(8), 1159–1168.

Irwin, P.G.J. 2010. *Atmospheric Radiation: Molecules, Aerosols & Clouds*.

Jacquinet-Husson, N., Scott, N., Chédin, A., Garceran, K., Armante, R., Chursin, A.A., Barbe, A., Birk, M., Brown, L.R., Camy-Peyret, C., Claveau, C., Clerbaux, C., Coheur, P.F., Dana, V., Daumont, L., Debacker-Barilly, M.R., Flaud, J.M., Goldman, A., Hamdouni, A., Hess, M., Jacquemart, D., Köpke, P., Mandin, J.Y., Massie, S., Mikhailenko, S., Nemtchinov, V., Nikitin, A., Newnham, D., Perrin, A., Perevalov, V.I., Régalia-Jarlot, L., Rublev, A., Schreier, F., Schult, I., Smith, K.M., Tashkun, S.A., Teffo, J.L., Toth, R.A., Tyuterev, Vl.G., Vander Auwera, J., Varanasi, P., & Wagner, G. 2005. The 2003 edition of the GEISA/IASI spectroscopic database. *J. Quant. Spectrosc. Radiat. Transfer*, **95**(4), 429–467, doi:10.1016/j.jqsrt.2004.12.004.

Jenkins, J. M., Kolodner, M. A., Butler, B. J., Suleiman, S. H., & Steffes, P. G. 2002. Microwave remote sensing of the temperature and distribution of sulfur compounds in the lower atmosphere of Venus. *Icarus*, **158**, 312–328.

Kasprzak, W.T., Niemann, H.B., Hedin, A.E., Bougher, S. W., & Hunten, D.M. 1993. Neutral Composition Measurements by the Pioneer Venus Neutral Mass Spectrometer During Orbiter Re-Entry. *Geophys. Res. Lett.*, **20**(23), 2747–2750.

Kasprzak, W.T., Keating, G.M., Hsu, N.C., Stewart, A.I.F., Colwell, W.B., & Bougher, S.B. 1997. *Solar activity behavior of the ionosphere*. Vol. 1. Tucson: The University of Arizona Press. Pages 225–257.

Keating, G.M., Nicholson III, J.Y., & Lake, L.R. 1980. Venus Upper Atmosphere Structure. *Journal of Geophysical Research*, **85**(A13), 7941–7956.

Keating, G.M., Bertaux, J.-L., Bougher, S. W., Craven, T.E., Dickinson, R.E., Hedin, A.E., Krasnopolsky, V.A., Nagy, A.F., Nicholson, J.Y., Paxton, L.J., & von Zahn, U. 1985. Models of Venus Neutral Upper Atmosphere : Structure and Composition. *Advances in Space Research*, **5**(11), 117–171.

Krötz, P., Sonnabend, G., Schmülling, F., Kostiuk, T., Goldstein, J., Sornig, M., Stupar, D., Livengood, T., Hewagama, T., Fast, K., & Mahieux, A. 2011. Observations of Venus Upper Atmosphere Temperatures from Ground Based High-Resolution Spectroscopy of CO_2. *Icarus*, **(submitted)**.

Lane, W.A., & Opstbaum, R. 1983. High altitude Venus haze from Pioneer Venus limb scans. *Icarus*, **54**(1), 48–58.

Lellouch, E., Goldstein, J., Rosenqvist, J., Bougher, S. W., & Paubert, G. 1994. Global circulation, thermal structure and Carbon Monoxide distribution in Venus' mesosphere in 1991. *Icarus*, **110**, 315–339.

Lellouch, E., Clancy, T., Crisp, D., Kliore, A.J., Titov, D., & Bougher, S. W. 1997. *Monitoring of mesospheric structure and dynamics*. Vol. 1. Tucson: The University of Arizona Press. Pages 295–324.

Limaye, S.S., Grund, C.J., & Burre, S.P. 1982. Zonal mean circulation at the cloud level on Venus: Spring and Fall 1979 OCPP observations. *Icarus*, **51**, 416–439.

López Puertas, Manuel. 2010. *Private communication*.

López Valverde, M.A. 2010. *Private communication*.

López Valverde, M.A., Drossart, P., Carlson, R., Mehlman, R., & Roos-Serote, M. 2007. Non-LTE infrared observations at Venus: From NIMS/Galileo to VIRTIS/Venus Express. *Planet. Space Sci.*, **55**, 1757–1771.

López Valverde, M.A., López Puertas, M., Funke, B., Gilli, G., Garcia-Comas, M., Drossart, P., Piccioni, G., & Formisano, V. 2010. Modeling the atmospheric limb emission of CO_2 at 4.3 μm in the terrestrial planets. *Planet. Space Sci.*

Mahieux, A., Berkenbosch, S., Clairquin, R., Fussen, D, Mateshvili, N., Neefs, E, Nevejans, D., Ristic, B., Vandaele, A. C., Wilquet, V., Belyaev, D., Fedorova, A., Korablev, O., Villard, E., Montmessin, F., & Bertaux, J.-L. 2008. In-flight performance and calibration of SPICAV/SOIR on-board Venus Express. *Applied Optics*, **47**(13), 2252–65.

Mahieux, A., Wilquet, V., Drummond, R., Belyaev, D., Fedorova, A., & Vandaele, A.C. 2009. A New Method for Determining the transfer function of an Acousto Optical Tunable Filter. *Optics Express*, **17**, 2005–2014.

Mahieux, A., Vandaele, A.C., Drummond, R., Robert, S., Wilquet, V., Fedorova, A., & Bertaux, J.-L. 2010. Densities and temperatures in the Venus mesosphere and lower thermosphere retrieved from SOIR on board Venus Express. Part I. Retrieval technique. *J. Geophys. Res.*, **115**(E12014).

Mahieux, A., Vandaele, A. C., Robert, S., Wilquet, V., Drummond, R., & Bertaux, J.-L. 2011a. Carbon dioxide isotopologue ratios in the Venus atmosphere from SOIR results on board Venus Express. *Icarus*, **(submitted)**.

Mahieux, A., Vandaele, A. C., Wilquet, V., Robert, S., Drummond, R., Fedorova, A., & Bertaux, J.-L. 2011b. Densities and temperatures in the Venus mesosphere and lower thermosphere retrieved from SOIR on board Venus Express. Part II. CO_2 densities and temperatures. *J. Geophys. Res.*, **(in preparation)**.

Marcq, E., Bézard, B., Encrenaz, T., & Birlan, M. 2005. Latitudinal variations of CO and OCS in the lower atmosphere of Venus from near-infrared nightside spectro-imaging. *Icarus*, **179**(2), 375–386.

Marcq, E., Encrenaz, T., Bézard, B., & Birlan, M. 2006. Remote sensing of Venus' lower atmosphere from ground-based IR spectroscopy: Latitudinal and vertical distribution of minor species. *Planetary and Space Science*, **54**(13-14), 1360–1370.

Markiewicz, W.J., Titov, D.V., Ignatiev, N., Keller, H.U., Crisp, D., Limaye, S.S., Jaumann, R., Moissl, R., Thomas, N., Esposito, L., Watanabe, S., Fiethe, B., Behnke, T., Szemerey, I., Michalik, H., Perplies, H., Wedemeier, M., Sebastian, I., Boogaerts, W., Hviid, S.F., Dierker, C., Osterloh, B., Boker, W., Koch, M., Michaelis, H., Belyaev, D., Dannenberg, A., Tschimmel, M., Russo, P., Roatsch, T., & Matz, K.D. 2007. Venus Monitoring Camera for Venus Express. *Planet. Space Sci.*, **55**(12), 1701–1711.

McElroy, C.T., Prather, M., & Rodriguez, J.M. 1982. Escape of Hydrogen from Venus. *Science*, **215**, 1614–1615.

Mills, F.P., & Allen, M. 2007. A review of selected issues concerning the chemistry in Venus' middle atmosphere. *Planetary and Space Science*, **55**(12), 1729–1740.

Mills, F.P., Esposito, L.W., & Yung, Y.L. 2007. Atmospheric composition, chemistry and clouds. *Geophysical Monograph Series*, **176**, 73–100.

Mueller-Wodarg, I., & Tingle, S. 2009. Vertical structure above the clouds: Towards a unified model. *In: XLIII Rencontres de Moriond, Venus Express Scientific Workshop.*

NAIF. 2009. *The SPICE Toolkit.* http://naif.jpl.nasa.gov/naif/toolkit.html.

Nakamura, M., Imamura, T., Ueno, M., Iwagami, N., Satoh, T., Watanabe, S., Taguchi, M., Takahashi, Y., Suzuki, M., Abe, T., Hashimoto, G.L., Sakanoi, T., Okano, S., Kasaba, Y., Yoshida, J., Yamada, M., Ishii, N., Yamada, T., Uemizu, K., Fukuhara, T., & Oyama, K.-I. 2007. Planet-C: Venus Climate Orbiter mission of Japan. *Planet. Space Sci.*, **55**(12), 1831–1842.

Neckel, H., & Labs, D. 1994. Solar Limb Darkening 1986-1990. *Solar Physics*, **153**, 91–114.

Neefs, E., Mahieux, A., & Clairquin, R. 2006. *Experimenter to (Science) Archive Interface Control Document.* Tech. rept. IASB/BIRA.

Nevejans, D., Neefs, E., Van Ransbeeck, E., Berkenbosch, S., Clairquin, R., De Vos, L., Moelans, W., Glorieux, S., Baeke, A., Korablev, O., Vinogradov, I., Kalinnikov, Y., Bach, B., Dubois, J.-P., & Villard, E. 2006. Compact high-resolution space-borne echelle grating spectrometer with AOTF based on order sorting for the infrared domain from 2.2 to 4.3 micrometer. *Applied Optics*, **45**(21), 5191–5206.

Palmer, C. 2002. *Diffraction grating handbook.* Erwin loewen edn. New York: Thermo RGL.

Petty, G. W. 2008. *A first course in atmospheric thermodynamics.* Vol. 1. Madison, Wisconsin: Sundog.

Pollack, J.B., Dalton, J.B., Grinspoon, D.H., Wattson, R.B., Freedman, R., Crisp, D., Allen, D.A., Bézard, B., de Bergh, C., Giver, L.P., Ma, Q., & Tipping, R. 1993. Near-Infrared Light from Venus' Nightside: A Spectroscopic Analysis. *Icarus*, **103**(1), 1–42.

Pyo, Tae-Soo. 2003. *Blaze Function and the Groove Shadowing Effect.*

Robert, S., Borkov, Y., Vander Auwera, J., Drummond, R., Mahieux, A., Wilquet, V., Vandaele, A. C., Perevalov, V., Tashkun, S., & Bertaux, J.-L. 2011. Assignment and Rotational Analysis of New Absorption Bands of the Carbon Dioxide Isotopologues in Venus Spectra. *J. Quant. Spectrosc. Radiat. Transfer*, **(in preparation)**.

Rodgers, C.D. 2000. *Inverse methods for atmospheric sounding: Theory and practice.* World Scientific. University of Oxford.

Rodgers, D. 1990. Characterization and Error Analysis of Profiles Retrieved From Remote Sounding Measurements. *J. Geophys. Res.*, **95**(D5), 5587–5595.

Roldan, C., López Valverde, M.A., & López Puertas, M. 2000. Non-LTE infrared emissions of CO_2 in the atmosphere of Venus. *Icarus*, **147**, 11–25.

Rossow, W. B., Del Genio, A., Limaye, S.S., Travis, L.D., & Stone, P. 1980. Cloud morphology and motions from Pioneer Venus images. *J. Geophys. Res.*, **85**, 8107–8128.

Rothman, L.S., & Young, L.D.G. 1981. Infrared energy levels and intensities of carbon dioxide. *Journal of Quantitative Spectroscopy and Radiative Transfer*, **25**(6), 505–524.

Rothman, L.S., Gordon, I.E., Barbe, A., Benner, D., Bernath, P., Birk, M., Boudon, V., Brown, L.R., Campargue, A., Champion, J.-P., Chance, K., Coudert, L.H., Dana, V., Devi, V., Fally, S., Flaud, J.-M., Gamache, R., Goldman, A., Jacquemart, D., Kleiner, I., Lacome, N., Lafferty, W., Mandin, J.-Y., Massie, S., Mikhailenko, S., Miller, C., Moazzen-Ahmadi, N., Naumenko, O., Nikitin, A., Orphal, J., Perevalov, V., Perrin, A., Predoi-Cross, A., Rinsland, C.P., Rotger, M., Simeckova, M., Smith, M.A.H., Sung, K., Tashkun, S., Tennyson, J., Toth, R.A., Vandaele, A. C., & Vander Auwera, J. 2009. The HITRAN 2008 molecular spectroscopic database. *J. Quant. Spectrosc. Radiat. Transfer*, **110**(9-10), 533–572.

Schubert, G. 1983. *General circulation and the dynamical state of the Venus atmosphere.* Vol. 1. Tucson: University of Arizona Press. Pages 681–765.

Seiff, A., Schofield, J.T., Kliore, A., Taylor, F.W., Limaye, S.S., Revercomb, H.E., Sromovsky, L.A., Kerzhanovich, V.V., Moroz, V.I., & Marov, M.Ya. 1985. Models of the structure of the atmosphere of Venus from the surface to 100 kilometers altitude. *Adv. Space Res.*, **5**(11), 3–58.

Song, I., & Gweon, D. 2008. A spectral detector using the dispersion of an acousto-optic tunable filter for confocal spectral imaging microscopy. *Measurement Science and Technology*, **19**.

Sonnabend, G., Sornig, M., Krotz, P., Stupar, D., & Schieder, R. 2008. Ultra high spectral resolution observations of planetary atmospheres using the Cologne tuneable heterodyne infrared spectrometer. *J. Quant. Spectrosc. Radiat. Transfer*, **109**(6), 1016–1029.

Sonnabend, G., Kroetz, P., Sornig, M., & Stupar, D. 2010. Direct observations of Venus upper mesospheric temperatures from ground based spectroscopy of CO_2. *Geophys. Res. Lett.*, **37**, doi:10.1029/2010GL043335.

Sornig, M., Livengood, T., Sonnabend, G., Kroetz, P., Stupar, D., Kostiuk, T., & Scheider, R. 2008. Venus upper atmosphere winds from ground-based heterodyne spectroscopy of CO_2 at 10 microns wavelength. *Planet. Space Sci.*, **56**, 1399–1406.

Svedhem, H., Titov, D., McCoy, D., Lebreton, J.-P., Barabash, S., Bertaux, J.-L., Drossart, P., Formisano, V., Häusler, B., Korablev, O., Markiewicz, W.J., Nevejans, D., Pätzold, M., Piccioni, G., Zhang, T.L., Taylor, F.W., Lellouch, E., Koschny, D., Witasse, O., Eggel, H., Warhaut, M., Accomazzo, A., Rodriguez-Canabal, J., Fabrega, J., Shirmann, T., Clochet, A., & Coradini, M. 2007. Venus Express: The first European mission to Venus. *Planet. Space Sci.*, **55**(12), 1636–1652.

Tashkun, S.A., Perevalov, V.I., Teffo, J.L., Bykov, A.D., & Lavrentieva, N.N. 2003. CDSD-1000, the high-temperature carbon dioxide spectroscopic databank. *Journal of Quantitative Spectroscopy and Radiative Transfer*, **82**, 165–196.

Taylor, F.W., Crisp, D., & Bézard, B. 1997. *Near-infrared sounding of the lower atmosphere of Venus.* The University os Arizona Press, Tucson. Pages 325–351.

Taylor, R. C., & al., et. 2000. *Glossary of Meteorology.*

Titov, D.V., & al., et. 2006. Venus Express science planning. *Planetary and Space Science*, **54**(13-14), 1279–1297.

Uchida, N. 1971. Optical Properties of Single-Crystal Paratellurite (TeO_2). *Phys. Rev.B*, **4**(10), 3736–3745.

Vandaele, A. C., De Mazière, M., Drummond, R., Mahieux, A., Neefs, E., Wilquet, V., Belyaev, D., Fedorova, A., Korablev, O., Montmessin, F., & Bertaux, J.-L. 2008. Composition of the Venus mesosphere measured by SOIR on board Venus Express. *J. Geophys. Res.*, doi:10.1029/2008JE003140.

von Zahn, U., Fricke, K.H., Hunten, D.M., Krankowsky, D., Mauersberger, K., & Nier, A.O. 1980. The Upper Atmosphere of Venus during Morning Conditions. *Journal of Geophysical Research*, **85**(A13), 7829–7840.

Wilquet, V., Mahieux, A., Vandaele, A.C., Perevalov, V.I., Tashkun, S.A., Fedorova, A., Korablev, O., Montmessin, F., Dahoo, R., & Bertaux, J.-L. 2008. Line parameters for the 01111-00001 band of 12C16O18O from SOIR measurements of the Venus atmosphere. *Journal of Quantitative Spectroscopy and Radiative Transfer*, **109**, 895–905.

Wilquet, V., Fedorova, A., Montmessin, F., Drummond, R., Mahieux, A., Vandaele, A. C., Villard, E., Korablev, O., & Bertaux, J.-L. 2009. Preliminary characterization of the upper haze by SPICAV/SOIR solar occultation in UV to mid-IR onboard Venus Express. *J. Geophys. Res.*, **114**(E00B42), doi:10.1029/2008JE003186.

Wilquet, V., Vandaele, A. C., Mahieux, A., Robert, S., Montmessin, F., & Bertaux, J.-L. 2011. Aerosol characterization and climatoly observed by the SOIR instrument on board Venus Express. *Icarus*, **(Submitted)**.

Xu, Jieping, & Stroud, Robert. 1992. *Acousto-Optic devices*. New-York: John Wiley & Sons, Inc.

Yano, T., & Watanabe, A. 1976. Acoustooptic TeO_2 tunable filter using far-off-axis anisotropic Bragg diffraction. *Applied Optics*, **15**(9), 2250–2258.

Zasova, L., Moroz, V.I., Linkin, V.M., Khatountsev, I.A., & Maiorov, B.S. 2006. Structure of the Venusian Atmosphere from Surface up to 100 km. *Cosmic Research*, **44**(4), 364–383.

Zasova, L.V., Ignatiev, N., Khatuntsev, I., & Linkin, V. 2007. Structure of the Venus atmosphere. *Planet. Space Sci.*, **55**(12), 1712–1728.

Zhang, H., Shi, G., Nakajima, T., & Suzuki, T. 2006. The effects of the choice of the k-interval number on radiative calculations. *J. Quant. Spectrosc. Radiat. Transfer*, **98**(1), 31–43.

Appendix

Appendix A

List of publications

1. J.L. Bertaux, A.C. Vandaele, O. Korablev, E. Villard, A. Fedorova, D. Fussen, E. Quémerais, D. Beliaev, **A. Mahieux**, F. Montmessin, C. Müller, E. Neefs, D. Nevejans, V. Wilquet, J.P. Dubois, A. Hauchecorne, A. Stepanov, I. Vinogradov, A. Rodin and the SPICAV team, *Venus: a warm layer in the cryosphere and new measurements of HF, HCl, H_2O and HDO*, Nature **450** (29 November), 646-649, doi:10.1038/nature05974, 2007
2. V. Wilquet, **A. Mahieux**, A.C. Vandaele, V. Perevalov, S. Tashkun, F. Montmessin, J.-L. Bertaux, *Line parameters for the 01111-00001 band of $^{12}C^{16}O^{18}O$ from SOIR measurements of the Venus atmosphere*, Journal of Quantitative Spectroscopy and Radiative Transfer, **109**:895-905, 2008
3. **A. Mahieux**, V. Wilquet, A.C. Vandaele, E. Neefs, S. Berkenbosch, R. Clairquin, D. Fussen, N. Mateshvili, D. Nevejans, B. Ristic, A. Fedorova, O. Korablev, E. Villard, F. Montmessin, J.L. Bertaux, *In flight performances of the SOIR instrument on board Venus Express*, Applied Optics, Vol. **47**, No. 13, 2008
4. A.C. Vandaele, M. De Mazière, R. Drummond, **A. Mahieux**, E. Neefs, V. Wilquet, O. Korablev, A. Fedorova, D. Belyaev, F. Montmessin, J.-L. Bertaux, *Composition of the Venus mesosphere measured by Solar Occultation at Infrared on board Venus Express*, Journal Geophysical Research, **113**, E00B23, doi:10.1029/2008JE003140, 2008
5. A. Fedorova, O. Korablev, A.C. Vandaele, J-L. Bertaux, D. Belyaev, **A. Mahieux**, E. Neefs, V. Wilquet, R. Drummond, F. Montmessin, E. Villard, *HDO and H_2O vertical distributions and isotopic ratio in the Venus mesosphere by Solar Occultation at Infrared spectrometer on board Venus Express*, Journal of Geophysical Research, **113**, E00B22, doi:10.1029/2008JE003146, 2008
6. D. Belyaev, O. Korablev, A. Fedorova, J.L. Bertaux, A.C. Vandaele, R. Drummond, **A. Mahieux**, V. Wilquet, R. Drummond, *First observations of SO_2 above Venus' clouds by means of Solar Occultation in the Infrared*, Journal of Geophysical Research, **113**, E00B25, doi:10.1029/ 2008JE003143, 2008
7. V. Wilquet, **A. Mahieux**, A.C. Vandaele, F. Montmessin, O. Korablev, A. Fedorova, J.-L. Bertaux, *Characterization of the upper venusian haze from UV to mid-IR by SPICAV/SOIR on VEX*, Journal of Geophysical Research, **114**, 2009
8. **A. Mahieux**, V. Wilquet, R. Drummond, D. Belyaev, A. Federova, A.C. Vandaele, *A new method for determining the transfer function of an Acousto optical tunable filter*, Optics Express, Vol. **17**, No 3, 2009
9. R. Drummond, A.C. Vandaele, F. Daerden, L. Neary, D. Fussen, E. Neefs, **A. Mahieux**, V. Wilquet, E. Marcq, F. Montmessin, J.L. Bertaux, *Studying methane and other trace species in the Mars atmosphere using a SOIR instrument*, PSS, Vol **59**, 292-298, 2011
10. **A. Mahieux**, A.C. Vandaele, E. Neefs, S. Robert, V. Wilquet, R. Drummond, A. Federova and J.L. Bertaux, *Densities and temperatures in the Venus mesosphere and lower thermo-*

sphere retrieved from SOIR on board Venus Express; Retrieval technique, Journal of Geophysical Research, Vol. **115**, E12014, doi:10.1029/2010JE003589, 2010

11. Peter Krötz, Guido Sonnabend, Frank Schmülling, Theodor Kostiuk, Jeff Goldsteind, Manuela Sornig, Dusan Stupar, Timothy Livengood, Tilak Hewagama, Kelly Fast, Arnaud Mahieux, *Observations of Venus Upper Atmosphere Temperatures from Ground Based High-Resolution Spectroscopy of CO_2*, Icarus, (submitted), 2011
12. **A. Mahieux**, A.C. Vandaele, S. Robert, V. Wilquet, R. Drummond, and J.L. Bertaux, *Carbon dioxide isotopic ratios in the Venus atmosphere from SOIR results on board Venus Express*, Icarus, (submitted), 2011
13. D. Belyaev, F. Montmessin, J.-L. Bertaux, **A. Mahieux**, A. Fedorova, O. Korablev, E. Marcq, Y.Yung, X. Zhang, *Vertical profiling of SO_2 and SO above Venus' clouds by SPICAV/SOIR solar occultations*, Icarus, (submitted), 2011

Appendix B

Abbreviations list

- ACS: Absorption cross section
- AOTF: Acousto optical tunable filter
- ASPERA: Analyzer of Space Plasma and Energetic Atoms (VEX)
- AU: Astronomical unit
- BIRA-IASB: Belgische Instituut voor Ruimte Aëronomie - Institut d'Aéronomie Spatiale de Belgique
- DOF: Degree of freedom
- ESA: European Space Agency
- FOV: Field of view
- FSR: Free spectral range
- FWHM: Full width at half maximum
- ILP: Instrument line profile
- IR: Infrared
- JAXA: Japan Aerospace Exploration Agency
- LST: Local solar time
- LTE: Local thermodynamical equilibrium
- MEX: Mars Express
- OD: Optical depth
- OEM: Optimal estimation method
- OS: Occultation season
- PENE: Penumbra ending time
- PENS: Penumbra starting time
- PFS: Planetary Fourier Spectrometer (VEX)
- PPNU: Pixel-to-pixel non uniformity
- RMS: Residual mean square
- S2N: Signal to noise ratio
- sinc: sinus cardinal
- SO: Solar occultation
- SOIR: Solar Occultation in the InfraRed (VEX)
- SPICAM: Spectroscopy for Investigation of Characteristics of the Atmosphere of Mars (MEX)
- SPICAV: Spectroscopy for Investigation of Characteristics of the Atmosphere of Venus (VEX)
- SSI: Spectral sampling interval
- UV: Ultraviolet
- VeRa: Venus Radio Science Experiment (VEX)
- VEX: Venus Express
- VIRA: Venus international reference atmosphere (VEX)
- VIRTIS: Visible and Infrared Thermal Imaging Spectrometer (VEX)
- VMC: Venus Monitoring Camera (VEX)
- vmr: Volume mixing ratio

Appendix C

Main variables list

- a: In the OEM, constant term of the polynomial background [1]
- α: On the echelle grating, incident angle [deg]
- α_B: Angle between the incident ray and the fact normal in the place perpendicular to the grooves; it contains the grating normal [deg]
- b: In the OEM, linear term of the polynomial background [cm]
- BF: Blaze function [1]
- β: On the echelle grating, refracted angle [deg]
- c: In the OEM, quadratic term of the polynomial background [cm^2]
- d: In the OEM, Doppler shift due to the satellite velocity [cm^{-1}]
- e: In the OEM, constant term of the wavenumber to pixel relation [cm^{-1}]
- f: In the OEM, linear term of the wavenumber to pixel relation [1]
- f_{AOTF}: AOTF frequency [kHz]
- γ: On the echelle grating, angle between the incident ray and the plane perpendicular to the grooves; it contains the grating normal [deg]
- d_{AOTF}: In the OEM, displacement term of the AOTF maximum [cm^{-1}]
- $g(z)$: In the OEM, gravitational acceleration profile [m/s^2]
- λ: Wavelength [μm]
- n: Diffraction order [1]
- $n(z)$ or n: In the OEM, density profile [$molec/cm^3$]
- n_{AOTF}: In the OEM, adaptation points of the AOTF function [1]
- N: On the echelle grating, reciprocal of the groove spacing [μm^{-1}]
- $\tilde{\nu}$: Wavenumber [cm^{-1}]
- p: Pixel number [1]
- σ: On the echelle grating, groove spacing [μm]
- t: In the OEM, time [s]
- $T(z)$ or T: In the OEM, temperature profile [K]
- Tr: In the OEM, transmittance [1]
- θ_B: On the echelle grating, blaze angle [deg]
- τ: In the OEM, optical depth [s]
- z: In the OEM, altitude [km]

Appendix D

Venus exploration summary

The following tables summarize the missions that were sent to Venus since the 1960s.

Spacecraft	Year	Country	Type	Principal discoveries
Venera 1	1962	USSR	Fly-by	Contact lost.
Mariner 1	1962	USA	Fly-by	Crashed during launch.
Mariner 2	1962	USA	Probe	Planet temperature. No magnetic field detected.
Venera 2	1965	USSR	Fly-by	Contact lost.
Venera 3	1965	USSR	Fly-by	Crashed. Entered the atmosphere.
Venera 4	1967	USSR	Probe	Crushed by pressure before reaching ground. First atmospheric chemical analysis.
Mariner 5	1967	USA	Fly-by	Density and temperature profiles.
Venera 5	1969	USSR	Probe	Crushed by pressure before reaching surface. Atmospheric composition analysis.
Venera 6	1969	USSR	Probe	Crushed by pressure before reaching surface. Atmospheric composition analysis.
Mariner 10	1969	USA	Fly-by	First imaging system. Atmospheric circulation and cloud-top temp.
Venera 7	1970	USSR	Lander	First successful soft landing. Surface temperature and pressure.
Venera 8	1972	USSR	Lander	Wind and soil measurement.
Venera 9	1975	USSR	Orbiter Lander	First spacecraft in orbit around Venus. Images of the landing site.

Table D.1: Missions to Venus.

Spacecraft	Year	Country	Type	Principal discoveries
Venera 10	1975	USSR	Orbiter Lander	First spacecraft in orbit around Venus. Images of the landing site.
Pioneer Venus	1978	USA	Orbiter 4 probes	Surface probing and mapping. Atmosphere composition study.
Venera 11	1978	USSR	Fly-by Lander	Evidence of lightening and thunder.
Venera 12	1978	USSR	Fly-by Lander	Same as Venera 11
Venera 13	1981	USSR	Fly-by Lander	Color images of the surface. Conducted soil analysis.
Venera 14	1981	USSR	Fly-by Lander	Same as Venera 14.
Venera 15	1983	USSR	Orbiter	Radar mapping of the surface. Study of mesosphere and cloud tops.
Venera 16	1983	USSR	Orbiter	Same as Venera 15.
Vega 1	1984	USSR	Fly-by Lander Balloon	Spectrometry. Winds records. Precise temperature profiles down to surface.
Vega 2	1984	USSR	Fly-by Lander Balloon	Spectrometry. Winds records. Precise temperature profiles down to surface.
Magellan	1989	USA	Orbiter	Almost-global radar mapping of the surface.
Galileo	1990	USA	Fly-by	Spectral imaging of night-side IR emissions. Lightning detection.
Cassini-Huygens	1998 1999	USA ESA	Fly-by	Spectral imaging of night-side IR emissions.
Venus Express	2005	EU	Orbiter	Surface, clouds, atmosphere study.
Akatsuki	2010	Japan	Orbiter	Atmosphere and surface study.

Table D.1 (Continued)

Appendix E

The Venus Express payload

ASPERA

The Aspera-4 is a copy of the Aspera-3 instrument flying on Mars Express [Barabash *et al.* (2007)]. It is made of 5 sensors, and measures the solar wind plasma. The measurement goals are various: (1) Investigate the interaction between the solar wind and the Venus atmosphere; (2) Characterize quantitatively the impact of plasma processes on the atmosphere; (3) Obtain the global plasma and neutral gas distribution; (4) Identify the chemical composition and quantitatively characterize the flux of the outflowing atmospheric gases; (5) Investigate the plasma domains of the near-Venus environment; (6) Provide undisturbed solar wind parameters.

MAG

MAG is a magnetometer with two flux gate sensors to measure magnitude and direction of the magnetic field around Venus [Zhang *et al.* (2006)]. Since Venus has no internal magnetic field, large portions of its exosphere resides in the shocked flow of the solar plasma. The solar wind directly interacts with the top of the ionosphere and forms a complex system of plasma clouds, tail rays, filaments, and ionospheric holes on the night side, through which a substantial amount of material leaves the planet. MAG studies these features, through the fact that the orbit of Venus Express crosses the plasma clouds.

PFS

The Planetary Fourier Spectrometer is an infrared spectrometer optimized to study the atmosphere [Formisano *et al.* (2006)]. The two channels of the instrument together cover spectral range from 0.9 to 45 μm with a boundary at about 5 μm. The spectral resolution of the instrument is about 1.3 cm^{-1} over the full range. Unfortunately, the instrument never worked, as the shutter mechanism never opened, and the instrument never could see the planet's atmosphere.

SPICAV/SOIR

It is made of three channels: SPICAV-IR, SPICAV-UV and SOIR. The two French channels, SPICAV-IR and SPICAV-UV are infrared and ultraviolet spectrometers [Bertaux *et al.* (2007)].

SPICAV-UV is is a highly sensitive instrument in the range of 110-310 nm with resolution of 1.5 nm based on an intensified CCD detector. SPICAV-IR covers the range from 0.7 to 1.7 μm with a resolving power of 1500. SPICAV operates both in nadir viewing and in stellar occultation modes. When working in stellar occultation mode, the UV channel sounds vertical distribution of sulfur-bearing gases (SO_2 and SO) above the clouds, and also CO_2, temperature and the aerosol content.

SPICAV also operates in nadir mode. On the night side, these observations covers several spectral windows and allows the instrument to monitor the abundance of atmospheric water in the lower atmosphere, the total cloud opacity, and the surface temperature. The night-side NO

and O_2 airglow emissions are mapped by SPICAV to trace the thermospheric circulation [Bougher *et al.* (1997a)]. On the day side, observations of the Lyman-alpha hydrogen and oxygen emissions allows studies of escape of these species.

VERA

The Venus Radio Science Experiment uses radio signals of the telecommunication subsystem at X- and S-bands (3.5 and 13 cm wavelengths, respectively) to probe the neutral atmosphere and the ionosphere, the surface properties, the gravity field, and the interplanetary medium [Häusler *et al.* (2006)]. The main goal of the experiment is to investigate the vertical structure of the atmosphere and ionosphere of Venus by radio occultation. The same measurements sounds the abundance of H_2SO_4 vapor below the clouds (40-50 km).

VIRTIS

The VIRTIS instrument consists of two major parts: a mapping spectrometer (VIRTIS-M) that covers the range from 0.25 to 5 μm with moderate spectral resolution ($\lambda/\Delta\lambda \approx 200$), and a high spectral resolution spectrometer (VIRTIS-H) for the spectral range from 2 to 5 μm ($\lambda/\Delta\lambda \approx 1200$) [Drossart *et al.* (2007)].

VIRTIS monitors the abundance of trace gases (H_2O, CO, SO_2, COS) in the lower atmosphere, the total cloud opacity, and their variations. The variability of the lower atmosphere composition gives an indirect insight into the problems of deep atmospheric dynamics, surface-atmosphere interaction, and volcanic activity. On the day side, VIRTIS sounds gas and aerosol composition at the cloud tops.

The second goal is the investigation of the atmospheric dynamics. VIRTIS measures the wind speeds by tracking cloud features in the UV and IR ranges that correspond to 70 and 50 km altitudes, respectively. They are complemented by observations of the O_2 airglow at 1.27 μm, which is considered a tracer of the lower thermosphere circulation (100-120 km) to yield a 3-D time variable picture of Venus atmospheric dynamics. The third objective is to study the temperature and aerosol distribution in the mesosphere between 60 and 90km by measuring thermal IR emission in the 4-5 μm range.

The limb observations allows VIRTIS to investigate the vertical structure of haze layers above the cloud top with vertical resolution between few hundred meters and 2 km. In addition, VIRTIS maps the Venus surface in the 1 μm window on the night side. It is able to detect hot spots related to possible volcanic activity. Spatial resolution of these observations is limited by scattering in the clouds and is probably limited to about 50 km. Further night-side observations are used to search for lightning.

VMC

The VMC is a wide-angle camera for observation of the atmosphere and the surface through four narrow-band filters [Markiewicz *et al.* (2007)]. The camera is made up of four different channels: UV, visible and two IR channels. VMC tracks the atmospheric features visible at the different wavelength and study the dynamics of the atmosphere.

Appendix F

Orders definition

This table summarizes all the diffractions order 101 to 194, giving their boundaries in wavenumbers for pixel 1 and 320, and the AOTF frequency of the order center.

The values were calculated using the Equations 3.22 and 3.21 for the pixel-to-wavenumber relation, taking fullscan 264.1 (10/01/2007), and Equation 3.26 for the wavenumber to AOTF-frequency, with the miniscans 142 to 502 (from 10/09/2006 to 04/09/2007).

Order	$\nu_{\min}$	$\nu_{\max}$	ν_{mean}	f_{AOTF}
101	2257.16	2276.55	2266.86	12847.55
102	2279.51	2299.09	2289.30	12995.02
103	2301.86	2321.63	2311.75	13142.42
104	2324.21	2344.17	2334.19	13289.76
105	2346.55	2366.71	2356.63	13437.03
106	2368.90	2389.25	2379.08	13584.24
107	2391.25	2411.79	2401.52	13731.38
108	2413.60	2434.33	2423.97	13878.46
109	2435.95	2456.87	2446.41	14025.48
110	2458.29	2479.41	2468.85	14172.43
111	2480.64	2501.95	2491.30	14319.32
112	2502.99	2524.49	2513.74	14466.14
113	2525.34	2547.03	2536.19	14612.90
114	2547.69	2569.57	2558.63	14759.59
115	2570.04	2592.11	2581.08	14906.23
116	2592.38	2614.65	2603.52	15052.79
117	2614.73	2637.19	2625.96	15199.29
118	2637.08	2659.73	2648.41	15345.73
119	2659.43	2682.27	2670.85	15492.11
120	2681.78	2704.81	2693.30	15638.42

Table F.1: Table of the boundaries of all diffraction orders, with boundaries $\nu_{\min}$, $\nu_{\max}$ ν_{mean} in wavenumber cm^{-1} and central AOTF frequency f_{AOTF} in kHz.

Order	$\nu_{\min}$	$\nu_{\max}$	ν_{mean}	f_{AOTF}
121	2704.12	2727.35	2715.74	15784.66
122	2726.47	2749.89	2738.18	15930.84
123	2748.82	2772.43	2760.63	16076.96
124	2771.17	2794.97	2783.07	16223.01
125	2793.52	2817.51	2805.52	16369.00
126	2815.86	2840.05	2827.96	16514.93
127	2838.21	2862.59	2850.40	16660.79
128	2860.56	2885.13	2872.85	16806.58
129	2882.91	2907.67	2895.29	16952.32
130	2905.26	2930.21	2917.74	17097.98
131	2927.61	2952.75	2940.18	17243.59
132	2949.95	2975.29	2962.62	17389.13
133	2972.30	2997.83	2985.07	17534.60
134	2994.65	3020.37	3007.51	17680.01
135	3017.00	3042.91	3029.96	17825.36
136	3039.35	3065.45	3052.40	17970.64
137	3061.69	3087.99	3074.84	18115.86
138	3084.04	3110.54	3097.29	18261.02
139	3106.39	3133.08	3119.74	18406.11
140	3128.74	3155.62	3142.18	18551.13
141	3151.09	3178.16	3164.63	18696.09
142	3173.43	3200.70	3187.07	18840.99
143	3195.78	3223.24	3209.51	18985.83
144	3218.13	3245.78	3231.96	19130.60
145	3240.48	3268.32	3254.40	19275.30
146	3262.83	3290.86	3276.85	19419.94
147	3285.18	3313.40	3299.29	19564.52
148	3307.52	3335.94	3321.73	19709.03
149	3329.87	3358.48	3344.18	19853.48
150	3352.22	3381.02	3366.62	19997.86
151	3374.57	3403.56	3389.07	20142.18
152	3396.92	3426.10	3411.51	20286.44
153	3419.26	3448.64	3433.95	20430.63
154	3441.61	3471.18	3456.40	20574.76
155	3463.96	3493.72	3478.84	20718.82
156	3486.31	3516.26	3501.29	20862.82
157	3508.66	3538.80	3523.73	21006.75

Table F.1 (Continued)

Order	$\nu_{\min}$	$\nu_{\max}$	ν_{mean}	f_{AOTF}
158	3531.00	3561.34	3546.17	21150.62
159	3553.35	3583.88	3568.62	21294.43
160	3575.70	3606.42	3591.06	21438.17
161	3598.05	3628.96	3613.51	21581.85
162	3620.40	3651.50	3635.95	21725.46
163	3642.75	3674.04	3658.40	21869.01
164	3665.09	3696.58	3680.84	22012.50
165	3687.44	3719.12	3703.28	22155.92
166	3709.79	3741.66	3725.73	22299.28
167	3732.14	3764.20	3748.17	22442.57
168	3754.49	3786.74	3770.62	22585.80
169	3776.83	3809.28	3793.06	22728.96
170	3799.18	3831.82	3815.50	22872.06
171	3821.53	3854.36	3837.95	23015.10
172	3843.88	3876.90	3860.39	23158.07
173	3866.23	3899.44	3882.84	23300.98
174	3888.58	3921.98	3905.28	23443.82
175	3910.92	3944.52	3927.72	23586.60
176	3933.27	3967.06	3950.17	23729.32
177	3955.62	3989.60	3972.61	23871.97
178	3977.97	4012.14	3995.06	24014.55
179	4000.32	4034.68	4017.50	24157.07
180	4022.66	4057.22	4039.94	24299.53
181	4045.01	4079.76	4062.39	24441.93
182	4067.36	4102.30	4084.83	24584.26
183	4089.71	4124.84	4107.28	24726.52
184	4112.06	4147.38	4129.72	24868.72
185	4134.40	4169.92	4152.16	25010.86
186	4156.75	4192.46	4174.61	25152.93
187	4179.10	4215.00	4197.05	25294.94
188	4201.45	4237.54	4219.50	25436.89
189	4223.80	4260.08	4241.94	25578.77
190	4246.15	4282.62	4264.39	25720.58
191	4268.49	4305.16	4286.83	25862.34
192	4290.84	4327.70	4309.27	26004.02
193	4313.19	4350.24	4331.72	26145.65
194	4335.54	4372.78	4354.16	26287.21

Table F.1 (Continued)

Appendix G

Detector thermal background, dark current and non-linearity corrections

The characteristics described in this section were studied and modeled by Eddy Neefs, and were published in Mahieux *et al.* (2008).

Before the start of the measurement, the detector is cooled down to a temperature of 88 K. This precooling lasts for 600 s.

One of the multiple advantages of using an AOTF as bandpass filter for order selection is that it can easily be used as an electronic background chopper. Each measurement (given integration time and number of accumulations) is immediately followed by an identical measurement with the AOTF switched off. Background measurements are subtracted on board from the measurements themselves; this is what reduces the time for one measurement to 250 ms, as half of the time is used to measure the background.

So, thermal background and detector dark current are directly subtracted from the measurements. In fact, one spectrum is the subtraction of two recordings performed one after the other; the first recording is taken with the AOTF on and corresponds to the number of signal photons S plus the number of background photons $B\cdot$. The second recording with AOTF off corresponds to the background only (B) and contains a contribution of the detector dark current and the thermal emission of the optics between the AOTF and the detector. Signals S and $S+B$ are obtained on-board after digitization of the analog output of the detector, and usually only the digital difference $(S+B)-B$ is transmitted to ground.

The AOTF state is supposed to remain constant between the measurements of $(S+B)$ and B. The AOTF temperature is assumed to remain constant as the AOTF is only on for 20 ms or 30 ms, the integration time, during the 250 ms that takes the whole measurement. The crystal characteristics remain the same during the measurement of $S+B$ and B, and the surface, perpendicular to the light path, does not change, either. So, background signal would depend only on temperature which is constant, and constantly measured on-board.

For the low signal intensities (below 25% of the full well capacity) the detector has a nonlinear response [Hsieh *et al.* (1997)]. It is important to correct for this behavior to not distort the ratios between weak and stronger absorption lines. Both absorption spectra (AOTF on) and background spectra (AOTF off) should be subject to this correction. However, since onboard background subtraction ($(S+B)-B$) is applied, spectra containing only the signal contribution S are available on ground. Therefore, an approximate method for nonlinearity correction has to be used (see Figure G.1). During observation sessions of the dark sky a so-called linearity plot is constituted, giving the thermal background plus the detector dark signal (B) as a function of integration time. The linearity plot in Figure G.1 (21/02/2006) confirms the nonlinear behavior for low collected pixel charge. The pixel charge is converted by the detector read-out process into analog-to-digital converter (ADC) units. In Figure G.1 the ADC units are scaled to correspond to one accumulation

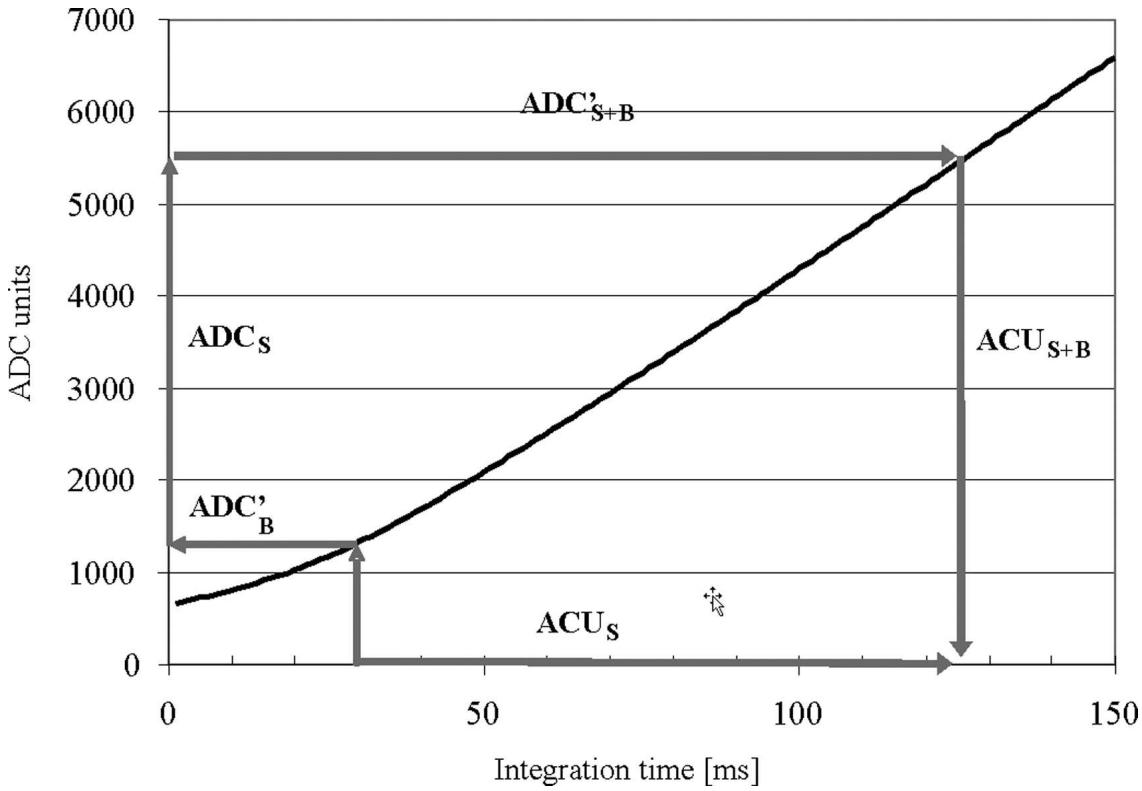

Figure G.1: Method for detector nonlinearity correction. ADC_S: ADC is the value available on ground, ADC'_{S+B} and ADC'_B are approximation of codes for signal plus background and background, and ACU_{S+B}, ACU_B, and ACU_S are the total, signal, and background pixel charge in arbitrary units.

and one pixel. With measurement 1 ($S + B$) and measurement 2 (B) ADC values ADC_{S+B} and ADC_B correspond. Only the subtraction of these ADC values $ADC_S = ADC_{S+B} + ADC_B$ is available on ground.

It is assumed that the linearity plot provides a good approximation (ADC'_B) for ADC_B at the given integration time of a spectrum and for the instrument temperature at the time of the measurement. Then the total signal $S + B$ before subtraction can be estimated by adding ADC'_B to the transmitted ADC value ADC_S: $ADC_{S+B} \approx ADC'_{S+B} = ADC_S + ADC'_B$.

Since the linearity plot does not give the relation between the physical number of electrons or charge on a pixel and the recorded ADC value (no calibration are performed), the notion of arbitrary charge units (ACU) is introduced; the integration time (in ms) at which a code ADC'_B is registered is taken as the (arbitrary) charge accumulated on the pixel. The relation between ADC and ACU can be approximated by a polynomial of degree 10 for ADC values below 6000, and by a linear function for ADC values above 6000. Now the number of photons $S + B$ and B can be expressed as ACU_{S+B} and ACU_B (ACU_B is nothing other than the integration time in milliseconds), and the number of photons that can be attributed to the signal S (pure signal, no background), corrected for nonlinear detector effects, is $ACU_S = ACU_{S+B}$ - ACU_B (see Figure G.1). The detector residual error was measured when no light was passing through the optics. The standard deviation is about 0.2 ADC units.

Appendix H

Molecular absorption cross section calculation

For the single absorption lines of different gaseous species i, it comes [Bandwell & McCash (1994) and references therein]:

$$ACS(\nu, z) = \sum_{i=1}^{n_{molecules}} n_i \cdot ACS\left(n_i, T, p\right) \tag{H.1}$$

$$= \sum_{i=1}^{n_{molecules}} n_i \sum_{k=1}^{n_{transitions}} S_{ik}(T) \cdot \phi(\nu, \nu_{ik}, T, p, p_i) \tag{H.2}$$

where T and p are the temperature and pressure at an altitude z, n_i and p_i the the density and the partial pressure of species i at altitude z. It represents the absorption due to single absorption lines. The sum on k represents the sum on all transitions ν_{ik} participating in the absorption of light.

The absorption coefficient α_{ik} ($\mathrm{cm}^2 \cdot$ molecule^{-1}) for a particular line k of species i is given as:

$$\alpha_{ik}(\nu, T, p, p_i) = S_{ik}(T) \cdot \phi(\nu, \nu_{ik}, T, p, p_i) \tag{H.3}$$

where $\phi(\nu, \nu_{ik}, T, p, p_i)$ is the normalized line shape

$$\int_{line} \phi(\nu')d\nu' = 1 \tag{H.4}$$

The intensity $S_{ik}(T)$ exhibits a temperature dependence which can be described as:

$$S_{ik}(T) = S_{ik}(t_0) \cdot \frac{Q_i(t_0)}{Q_i(T)} \cdot \exp\left[c_2 \cdot E_k \cdot \left(\frac{1}{t_0} - \frac{1}{T}\right)\right] \cdot \frac{1 - \exp\left[\frac{c_2 \cdot \nu_{0,k}}{T}\right]}{1 - \exp\left[\frac{c_2 \cdot \nu_{0,k}}{t_0}\right]} \tag{H.5}$$

where c_2 is the second Planck constant $\frac{h \cdot c}{k_B}$ (1.4387 cm $\cdot$ K), with h the Planck constant, k_B the Boltzmann constant, and c the speed of light. $\nu_{0,k}$ is the central wavenumber of the k^{th} transition, E_k is the energy of the lower state (cm^{-1}), and $S_{ik}(t_0)$ is the intensity at the reference temperature t_0 ($\mathrm{cm}^{-1} \cdot$ molecule$^{-1} \cdot$ cm^2). $Q(T)$ and $Q(t_0)$ are the total partition functions under local thermodynamic equilibrium conditions, at temperature T and t_0, respectively. These functions describe the temperature dependence of the line intensity of the transition. They are obtained from tabulated values for all species under temperature conditions varying between 70 K and 3000 K [Rothman *et al.* (2009)].

The Voigt profile is used to model the line shape. Natural broadening of the lines, which occurs as a consequence of the uncertainty in photon energy, is small. Collision broadening is caused by

secondary interaction with other gas molecules and atoms. Absorption lines under collisional regime are described by a Lorentzian function. Doppler broadening describes the statistical distribution of frequency shifts due to thermal motion. This effect is characterized by a Gaussian function and is most significant under low pressure conditions when the collision broadening effect is small.

The Doppler profile ϕ_D of a line centered on $\nu_{0,k}$ wavenumber

$$\phi_D(\nu) = \frac{\sqrt{\ln 2}}{\pi} \cdot \frac{1}{\gamma_D} \cdot \exp\left[-\ln 2 \cdot \left(\frac{\nu - \nu_{0,k}}{\gamma_D} \right)^2 \right] \tag{H.6}$$

is characterized by its half width γ_D which depends on the molecular mass MM of the absorbing species, as well as on the temperature

$$\gamma_D = \sqrt{\frac{2 \cdot \ln 2 \cdot k_B \cdot T}{MM \cdot c^2}} \tag{H.7}$$

The half width γ_L of the Lorentzian profile ϕ_L

$$\phi_L(\nu) = \frac{1}{\pi} \cdot \frac{\gamma_L}{(\nu - \nu_{0,k})^2 + \gamma_L^2} \tag{H.8}$$

is composed of a self broadening contribution and of a foreign broadening contribution, which are pressure and temperature dependent:

$$\gamma_L = p_i \cdot \gamma_L^{self} + (P - p_i) \cdot \gamma_L^{foreign} \tag{H.9}$$

$$\gamma_L^{self} = \gamma_L^{self}(t_0) \cdot \left(\tfrac{t_0}{T}\right)^{n_{self}} \tag{H.10}$$

$$\gamma_L^{foreign} = \gamma_L^{foreign}(t_0) \cdot \left(\tfrac{t_0}{T}\right)^{n_{foreign}} \tag{H.11}$$

where p_i is the partial pressure of species i, p_0 and t_0 are the reference pressure and temperature and n_{self} and $n_{foreign}$ are the temperature coefficients of respectively the self and the foreign broadenings. The values of γ_L^{self} and $\gamma_L^{foreign}$ ($cm^{-1}atm^{-1}$) are tabulated values in the databases.

Pressure induced shifts are also taken into account in the determination of the line absorption. The central wavenumber is displaced by δ:

$$\delta = p_i \cdot \delta_{self} + (P - p_i) \cdot \delta_{foreign} \tag{H.12}$$

$$\delta_{self} = \delta_{self}(t_0) \cdot \left(\tfrac{t_0}{T}\right)^{n^s_{self}} \tag{H.13}$$

$$\delta_{foreign} = \delta_{foreign}(t_0) \cdot \left(\tfrac{t_0}{T}\right)^{n^s_{foreign}} \tag{H.14}$$

if self (δ_{self}) and foreign ($\delta_{foreign}$) shifts are considered. n^s_{self} and $n^s_{foreign}$ are the temperature coefficients of respectively the self and the foreign shifts.

When both broadening effects must be considered, the absorption line is best reproduced by a Voigt profile ϕ_V, which is the convolution of the Doppler and Lorentzian profiles:

$$\phi_V(\nu) = \sqrt{\frac{\ln 2}{\pi}} \cdot \frac{1}{\gamma_D} \cdot K(x, y) \tag{H.15}$$

where

$$K(x, y) = \frac{y}{\pi} \cdot \int_{-\infty}^{\infty} \frac{\exp\left(-T^2\right)}{y^2 + (x - T)^2} \cdot dt = \Re\left[W(x, y)\right] \tag{H.16}$$

in which

$$x = \sqrt{\ln 2} \cdot \tfrac{\nu - \nu_{0,k}}{\gamma_D} \tag{H.17}$$

$$y = \sqrt{\ln 2} \cdot \tfrac{\gamma_L}{\gamma_D} \tag{H.18}$$

and $W(x, y)$ is the complex error function

$$W(x, y) = \frac{\imath}{\pi} \int_{-\infty}^{\infty} \frac{\exp\left(-T^2\right)}{x + \imath \cdot y - T} \cdot dt \tag{H.19}$$

Appendix I

Spectral line catalogue

Spectroscopic parameters, such as line position, intensity, and broadening coefficients, as well as absorption cross sections are taken, for practical reasons, from existing spectroscopic databases. ASIMUT can directly import data from the two widely used HITRAN 2008 [Rothman *et al.* (2009)] and GEISA [Jacquinet-Husson *et al.* (2005)] databases, but also from the CDSD [Tashkun *et al.* (2003)] database whose format is similar to that of HITRAN.

Molecules included in the HITRAN and GEISA databases cover a wide range of atmospheric species. The isotopologue ID has been chosen as the one defined in HITRAN, directly in relation to their relative abundance in Earth atmosphere. For some species, the GEISA database reports more isotopologues than HITRAN. This is the case for the $^{18}O^{13}C^{18}O$, $^{16}O^{13}C^{34}S$, $^{17}O^{12}C^{32}S$, and $^{12}C^{13}CH_6$ species.

Absorption cross sections can be read from the HITRAN and GEISA compilations, in which different data columns can be associated to different temperature and pressure conditions.

Appendix J

Non-local thermodynamical equilibrium

Non-Local Thermodynamical Emissions (non-LTE) emissions of CO_2 on the dayside upper atmosphere of Venus provide a way of investigating the structure and dynamics of Venus lower thermosphere [Roldan *et al.* (2000); Gilli *et al.* (2009)]. Emissions due to excitation of CO_2 molecules on the the dayside by solar radiations are observed on the nightside of the planet, in the low atmosphere above 90 km. The excited molecules are transported from the dayside to the nightside of Venus by the subsolar to antisolar circulation. These molecules return to their ground-state in a non-collisional manner by releasing photons in a series of emission bands around 4.3 μm. The non-LTE situations of pure radiative excitations, like here CO_2, are relatively insensitive to the actual temperature, while their density dependence is more significant. The strongest emissions are fluorescence transitions. The strongest measured emission is found at 4.3 μm, and weaker ones are at 4.7 μm and 2.7 μm [López Valverde *et al.* (2007)]. The VIRTIS instrument on Venus Express measured two emission peaks in the 110 - 140 km range, one weaker at 125 - 135 km for the 4.277 μm band and one at 115 - 120 km at the 4.315 μm band. The features were mainly measured at 0900 and 1500 local time [Garcia *et al.* (2009)].

The emitting non-LTE region were determined by Deming *et al.* (1983): the peak of the emissions occurs around 109 km with a half width of $\pm$ 10 km on the night side.

The non-LTE infrared emissions are probably an explanation to understand the cold lower thermosphere observed on Venus, and the small amplitudes of its variations with solar cycle [Bougher (1995); Bougher *et al.* (1997b)]: they probably have a thermal cooling effect, and are a key in the energy balance between 80 and 150 km.

The Venus thermosphere is much different from that of the Earth or Mars. The average lapse rate in Venus thermosphere is around 1.1 - 1.8 K/km, while on Earth is observed 2 - 5 K/km and on Mars 1 - 4K/km. The small thermosphere temperature dependence with solar maximum (about 20% or 50 K on Venus, while on Earth about 100% or 800 K, and on Mars about 75% or 150K) is due to the CO_2 cooling effect. The very low nightside temperatures, with an incredible negative lapse rates of -1.2 K/km are due to the very low rotation rate of Venus (the time between two sunrises is 177 Earth days). It is actually the amount of O which makes CO_2 cool the atmosphere: the atomic oxygen is particularly effective in exciting CO_2 vibrational states which lead to the 15 μm emissions and hence cooling, so the O/CO_2 ratio determines the effectiveness of CO_2 cooling.

Appendix K

List of orbits

In this Appendix, the list of all the successful measurements performed since the beginning of the mission are listed.

For the occultations, the informations presented are:

1. The phase or Medium Term Planning (MTP). The whole mission is divided in MTP by ESOC, and a MTP lasts for approximately one month.
2. The orbit number. One orbit lasts for approximately 24 hours.
3. The case. This number is used to discriminate between two measurements that were taken during one orbit.
4. The date. The satellite is at perigee approximately at midnight UTC.
5. The type of measurement. It can be an ingress or an egress.
6. The distance between VEX and the tangent point at the limbs, in km. The value is calculated for a tangent altitude of 120 km.
7. The height resolution, or the height of one bin projected at the tangent point, in km. The value is calculated for a tangent altitude of 120 km.
8. The longitude of the tangent point, in degrees. The value is calculated for a tangent altitude of 120 km.
9. The latitude of the tangent point, in degrees. The value is calculated for a tangent altitude of 120 km.
10. The speed of the spacecraft projected on the line of sight, in km/s. The value is calculated for a tangent altitude of 120 km.
11. The local solar time at the tangent point, in hours. The value is calculated for a tangent altitude of 120 km.
12. The four orders that were measured during the occultation.
13. The AOTF frequencies that were programed for the four diffraction orders, in Hz.
14. The chosen binning case.

Phase	Orbit	Case	Date	Type	Dist. to limb	Height res.	Longitude	Latitude	Speed	LST	Order 1	Order 2	Order 3	Order 4	Frequancy 1	Frequency 2	Frequency 3	Frequency 4	Binning
0	21	1	12/05/2006	IN	1362	1	286	86	9	4	121	121	121	122	15733	15792	15850	15909	2x16
1	35	1	26/05/2006	IN	1654	1	306	77	8	5	166	167	167	168	22267	22384	22502	22619	2x16
1	36	1	27/05/2006	IN	1695	1	308	76	7	5	108	109	109	110	13831	13960	14089	14218	2x16
1	39	1	30/05/2006	IN	1881	2	315	71	7	5	121	121	121	122	15733	15792	15850	15909	2x16
4	108	1	07/08/2006	IN	11584	8	338	5	-4	18	105	106	107	108	13497	13642	13787	13933	2x16
4	110	1	09/08/2006	IN	13202	8	344	-9	-4	18	120	121	122	123	15677	15823	15968	16114	2x16
4	111	1	10/08/2006	E	4281	3	352	73	-8	18	120	121	122	123	15677	15823	15968	16114	2x16
4	113	1	12/08/2006	IN	15057	9	353	-28	-3	18	133	134	135	136	17568	17713	17858	18003	2x16
4	114	1	13/08/2006	E	3957	3	3	78	-8	18	169	171	172	173	22802	22947	23092	23238	2x16
4	116	1	15/08/2006	IN	16415	10	2	-44	-3	18	189	190	191	192	25564	25709	25855	26000	2x16
4	118	1	17/08/2006	E	3731	2	22	83	-9	17	189	190	191	192	25564	25709	25855	26000	2x16
4	121	1	20/08/2006	E	3650	2	43	86	-9	16	133	134	135	136	17568	17713	17858	18003	2x16
4	124	1	23/08/2006	E	3621	2	90	88	-9	14	130	131	132	133	17131	17277	17422	17567	2x16
5	130	1	29/08/2006	E	2984	2	196	86	-9	8	180	181	182	183	24256	24401	24546	24692	2x16
5	132	1	31/08/2006	E	3043	2	210	84	-9	8	133	134	135	136	17568	17713	17858	18003	2x16
5	133	1	01/09/2006	E	3080	2	216	84	-9	7	120	121	122	123	15677	15823	15968	16114	2x16
5	134	1	02/09/2006	IN	16156	10	242	-47	-3	6	189	190	191	192	25564	25709	25855	26000	2x16
5	135	1	03/09/2006	IN	15771	10	245	-42	-3	6	169	171	172	173	22802	22947	23092	23238	2x16
5	136	1	04/09/2006	E	3229	2	231	81	-9	7	106	121	147	171	13642	15823	19603	22947	2x16
5	137	1	05/09/2006	E	3295	2	236	80	-8	7	146	147	148	149	19458	19603	19748	19894	2x16
5	141	1	09/09/2006	IN	12539	8	262	-8	-4	6	146	147	148	149	19458	19603	19748	19894	2x16
5	143	1	11/09/2006	E	4042	3	261	70	-7	6	130	131	132	133	17131	17277	17422	17567	2x16
5	144	1	12/09/2006	IN	10148	7	270	13	-4	6	126	127	128	129	16550	16695	16841	16986	2x16
5	145	1	13/09/2006	IN	9116	7	273	22	-5	6	120	121	122	123	15677	15823	15968	16114	2x16
5	145	2	13/09/2006	E	4681	4	269	63	-7	6	120	121	122	123	15677	15823	15968	16114	2x16

Table K.1: Table of the SOIR successful measured orbits. The table gives the MTP phase (medium term planning number) assigned by ESOC, the orbit and case number, the date, the ingress or egress case, the distance between Venus Express and the tangent point in km, the vertical resolution at the tangent point in km, the longitude and latitude in degrees, the local solar time, the four measured orders and the four AOTF frequencies and finally the binning case.

Phase	Orbit	Case	Date	Type	Dist. to limb	Height res.	Longitude	Latitude	Speed	LST	Order 1	Order 2	Order 3	Order 4	Frequancy 1	Frequency 2	Frequency 3	Frequency 4	Binning
7	211	1	18/11/2006	IN	1949	2	296	73	7	18	127	128	129	130	16695	16841	16986	17131	2x16
8	217	1	24/11/2006	E	9717	6	317	-14	3	18	120	121	122	123	15677	15823	15968	16114	2x16
8	219	1	26/11/2006	IN	1828	1	316	80	8	18	120	121	122	123	15677	15823	15968	16114	2x16
8	221	1	28/11/2006	E	11249	7	329	-31	3	18	170	171	172	173	22802	22947	23092	23238	2x16
8	223	1	30/11/2006	IN	1829	1	324	82	9	19	170	171	172	173	22802	22947	23092	23238	2x16
8	225	1	02/12/2006	IN	1836	1	327	83	9	19	105	106	107	108	13497	13642	13787	13933	2x16
8	227	1	04/12/2006	IN	1847	1	329	84	9	19	133	134	135	136	17568	17713	17858	18003	2x16
8	229	1	06/12/2006	IN	1861	1	330	85	9	20	189	190	191	192	25564	25709	25855	26000	2x16
8	232	1	09/12/2006	IN	1886	1	325	87	9	20	127	128	129	130	16695	16841	16986	17131	2x16
8	235	1	12/12/2006	IN	1915	1	307	88	9	22	110	111	112	113	14223	14368	14514	14659	2x16
9	242	1	19/12/2006	E	13884	8	207	-71	2	6	121	172	130	107	15823	23092	17131	13787	2x16
9	244	1	21/12/2006	IN	2030	1	250	85	9	4	121	172	111	112	15823	23092	14369	14514	2x16
9	247	1	24/12/2006	IN	1382	1	259	85	9	4	121	172	149	192	15823	23092	19894	26000	2x16
9	249	1	26/12/2006	E	12492	8	233	-46	3	6	121	172	111	183	15823	23092	14369	24692	2x16
9	251	1	28/12/2006	IN	1450	1	263	83	9	5	121	172	112	181	15823	23092	14514	24401	2x16
9	255	1	01/01/2007	IN	1538	1	269	80	8	5	121	172	148	191	15823	23092	19748	25855	2x16
9	256	1	02/01/2007	E	10168	7	256	-17	3	6	121	172	112	133	15823	23092	14514	17568	2x16
9	259	1	05/01/2007	IN	1669	1	277	77	8	5	121	172	133	134	15823	23092	17568	17713	2x16
9	261	1	07/01/2007	E	7699	5	272	8	4	6	121	172	132	133	15823	23092	17422	17568	2x16
9	262	1	08/01/2007	IN	1848	2	284	73	7	5	121	172	111	133	15823	23092	14369	17568	2x16
12	332	1	19/03/2007	IN	11331	8	310	3	-4	18	121	171	149	133	15809	23031	19869	17554	2x12
12	334	1	21/03/2007	IN	12795	8	316	-11	-4	18	121	171	149	190	15809	23031	19869	25742	2x12
12	335	1	22/03/2007	IN	13423	8	319	-17	-4	18	147	149	112	166	19580	19869	14496	22314	2x12
12	341	1	28/03/2007	E	3270	2	349	83	-9	17	149	190	112	130	19869	25742	14496	17119	2x12
12	343	1	30/03/2007	E	3205	2	1	85	-9	17	121	171	190	190	15809	23031	25742	25742	2x12
12	345	1	01/04/2007	E	3163	2	15	86	-9	16	121	171	149	133	15809	23031	19869	17554	2x12
12	347	1	03/04/2007	E	3139	2	39	87	-9	15	121	171	149	133	15809	23031	19869	17554	2x12
12	349	1	05/04/2007	E	3131	2	81	88	-9	13	121	171	149	190	15809	23031	19869	25742	2x12
13	356	1	12/04/2007	E	3218	2	182	84	-9	8	149	190	112	130	19869	25742	14496	17119	2x12
13	357	1	13/04/2007	E	3246	2	187	84	-9	7	133	149	180	130	17554	19869	24317	17119	2x12

Table K.1 (Continued)

Phase	Orbit	Case	Date	Type	Dist. to limb	Height res.	Longitude	Latitude	Speed	LST	Order 1	Order 2	Order 3	Order 4	Frequancy 1	Frequency 2	Frequency 3	Frequency 4	Binning
13	358	1	14/04/2007	E	3280	2	193	83	-9	7	121	171	149	133	15809	23031	19869	17554	2x12
13	359	1	15/04/2007	IN	15641	9	216	-45	-3	6	121	171	149	190	15809	23031	19869	25742	2x12
13	361	1	17/04/2007	E	3415	2	207	80	-8	7	147	149	112	166	19580	19869	14496	22314	2x12
13	362	1	18/04/2007	IN	14373	9	224	-29	-3	6	121	171	149	133	15809	23031	19869	17554	2x12
13	363	1	19/04/2007	E	3546	2	215	77	-8	7	121	171	149	190	15809	23031	19869	25742	2x12
13	365	1	21/04/2007	IN	12732	8	233	-13	-3	6	121	171	149	133	15809	23031	19869	17554	2x12
13	366	1	22/04/2007	E	3850	3	228	73	-8	7	149	190	112	130	19869	25742	14496	17119	2x12
15	433	2	28/06/2007	E	5122	12	262	33	5	18	121	171	124	130	15809	23031	16246	17119	2x12
15	434	1	29/06/2007	IN	1761	1	264	74	7	18	121	171	111	125	15809	23031	14350	16392	2x12
15	434	2	29/06/2007	E	5735	4	265	27	5	18	121	171	111	125	15809	23031	14350	16392	2x12
15	435	1	30/06/2007	IN	1711	1	267	75	7	18	121	171	112	190	15809	23031	14496	25742	2x12
15	435	2	30/06/2007	E	6359	4	269	21	4	18	121	171	112	190	15809	23031	14496	25742	2x12
16	436	1	01/07/2007	IN	1674	1	269	76	7	18	121	171	149	137	15809	23031	19869	18134	2x12
16	436	2	01/07/2007	E	6954	5	272	15	4	18	121	171	149	137	15809	23031	19869	18134	2x12
16	437	1	02/07/2007	IN	1646	1	272	77	8	18	125	171	111	180	16392	23031	14350	24317	2x12
16	438	1	03/07/2007	IN	1627	1	274	78	8	18	121	171	149	132	15809	23031	19869	17409	2x12
16	440	1	05/07/2007	IN	1600	1	279	79	8	18	121	171	118	151	15809	23031	15372	20157	2x12
16	441	1	06/07/2007	IN	1593	1	281	80	8	18	125	171	112	168	16392	23031	14496	22601	2x12
16	442	1	07/07/2007	IN	1586	1	284	80	8	18	121	171	149	184	15809	23031	19869	24888	2x12
16	443	1	08/07/2007	IN	1581	1	286	81	8	18	121	171	111	188	15809	23031	14350	25457	2x12
16	444	1	09/07/2007	E	10823	7	297	-23	3	18	125	171	112	133	16392	23031	14496	17554	2x12
16	445	1	10/07/2007	IN	1579	1	290	82	9	19	121	171	149	130	15809	23031	19869	17119	2x12
16	446	1	11/07/2007	E	11570	7	303	-32	3	18	121	171	149	108	15809	23031	19869	13911	2x12
16	447	1	12/07/2007	IN	1579	1	294	83	9	19	121	171	111	136	15809	23031	14350	17989	2x12
16	449	1	14/07/2007	IN	1584	1	297	84	9	19	125	171	112	132	16392	23031	14496	17409	2x12
16	450	1	15/07/2007	E	12803	8	316	-47	3	18	121	171	149	183	15809	23031	19869	24745	2x12
16	452	1	17/07/2007	E	13291	8	323	-55	3	18	121	171	111	190	15809	23031	14350	25742	2x12
16	456	1	21/07/2007	IN	1621	1	296	87	10	20	121	171	112	145	15809	23031	14496	19291	2x12
16	458	1	23/07/2007	IN	1637	1	289	87	10	21	125	171	149	108	16392	23031	19869	13911	2x12
16	460	1	25/07/2007	IN	1654	1	274	88	10	23	121	171	111	137	15809	23031	14350	18134	2x12

Table K.1 (Continued)

Phase	Orbit	Case	Date	Type	Dist. to limb	Height res.	Longitude	Latitude	Speed	LST	Order 1	Order 2	Order 3	Order 4	Frequancy 1	Frequency 2	Frequency 3	Frequency 4	Binning
16	462	1	27/07/2007	IN	1673	1	256	88	10	0	121	171	149	180	15809	23031	19869	24317	2x12
17	465	1	30/07/2007	IN	1706	1	235	87	10	2	121	171	149	190	15797	23046	19877	25757	2x12
17	466	1	31/07/2007	IN	1718	1	231	87	9	3	125	171	112	191	16383	23046	14474	25899	2x12
17	467	1	01/08/2007	IN	1731	1	228	86	9	3	149	179	174	145	19877	24191	23476	19297	2x12
17	471	1	05/08/2007	IN	1789	1	226	84	9	4	121	172	123	180	15797	23190	16090	24334	2x12
17	473	1	07/08/2007	IN	1825	1	227	83	9	5	184	188	193	194	24904	25473	26183	26325	2x12
17	477	1	11/08/2007	IN	1920	1	234	80	9	5	125	172	118	136	16383	23190	15356	17989	2x12
17	479	1	13/08/2007	IN	1987	1	237	79	8	5	125	172	149	132	16383	23190	19877	17406	2x12
17	480	1	14/08/2007	IN	2028	1	239	78	8	5	131	132	133	134	17260	17406	17552	17698	2x12
17	481	1	15/08/2007	IN	2074	1	241	77	8	5	142	143	144	145	18862	19007	19152	19297	2x12
17	482	1	16/08/2007	IN	2129	1	243	75	8	5	121	171	111	137	15797	23046	14327	18135	2x12
17	484	1	18/08/2007	IN	2274	2	248	73	7	5	125	172	149	180	16383	23190	19877	24334	2x12
17	485	1	19/08/2007	IN	2376	2	250	71	7	5	112	149	119	174	14474	19877	15503	23476	2x12
17	485	2	19/08/2007	E	7954	5	242	10	4	6	125	172	112	188	16383	23190	14474	25473	2x12
17	486	1	20/08/2007	IN	2511	2	252	69	7	6	121	171	149	190	15797	23046	19877	25757	2x12
17	486	2	20/08/2007	E	7280	5	246	17	4	6	125	172	112	191	16383	23190	14474	25899	2x12
17	487	1	21/08/2007	IN	2696	2	254	66	7	6	121	171	149	190	15797	23046	19877	25757	2x12
17	487	2	21/08/2007	E	6523	16	249	24	5	6	121	171	149	190	15797	23046	19877	25757	2x12
17	488	1	22/08/2007	IN	2991	4	256	62	6	6	125	172	112	191	16383	23190	14474	25899	2x12
17	488	2	22/08/2007	E	5613	7	253	33	5	6	125	172	112	191	16383	23190	14474	25899	2x12
21	583	1	25/11/2007	E	2297	1	159	85	-9	8	111	132	133	149	14327	17406	17552	19877	2x12
21	586	1	28/11/2007	E	2383	2	175	83	-9	7	112	132	133	149	14474	17406	17552	19877	2x12
21	591	1	03/12/2007	IN	11741	7	209	-10	-4	6	105	111	147	149	13441	14327	19587	19877	2x12
21	593	1	05/12/2007	IN	10468	7	215	2	-4	6	112	147	149	162	14474	19587	19877	21754	2x12
21	595	1	07/12/2007	IN	8975	6	221	15	-4	6	105	112	119	149	13441	14474	15503	19877	2x12
21	597	1	09/12/2007	IN	7060	5	226	32	-5	6	111	119	149	161	14327	15503	19877	21610	2x12
24	667	1	17/02/2008	IN	1785	1	258	80	8	18	105	112	149	166	13441	14474	19877	22329	2x12
24	669	1	19/02/2008	IN	1758	1	262	81	9	19	105	112	149	166	13441	14474	19877	22329	2x12
24	671	1	21/02/2008	IN	1741	1	266	82	9	19	105	112	149	166	13441	14474	19877	22329	2x12
24	674	1	24/02/2008	IN	1728	1	271	84	9	19	105	112	149	166	13441	14474	19877	22329	2x12

Table K.1 (Continued)

Phase	Orbit	Case	Date	Type	Dist. to limb	Height res.	Longitude	Latitude	Speed	LST	Order 1	Order 2	Order 3	Order 4	Frequancy 1	Frequency 2	Frequency 3	Frequency 4	Binning
24	675	1	25/02/2008	IN	1726	1	272	84	9	19	105	112	149	166	13441	14474	19877	22329	2x12
24	677	1	27/02/2008	IN	1726	1	274	85	9	19	105	112	149	166	13441	14474	19877	22329	2x12
24	679	1	29/02/2008	IN	1730	1	273	86	9	20	105	112	149	166	13441	14474	19877	22329	2x12
24	681	1	02/03/2008	IN	1737	1	270	87	10	20	105	112	149	166	13441	14474	19877	22329	2x12
24	684	1	05/03/2008	IN	1753	1	254	88	10	22	105	112	149	166	13441	14474	19877	22329	2x12
24	685	1	06/03/2008	IN	1760	1	245	88	10	23	105	112	149	166	13441	14474	19877	22329	2x12
24	686	1	07/03/2008	IN	1767	1	235	88	10	24	105	112	149	166	13441	14474	19877	22329	2x12
24	687	1	08/03/2008	IN	1776	1	225	88	10	1	105	112	149	166	13441	14474	19877	22329	2x12
25	688	1	09/03/2008	IN	1785	1	216	88	10	1	149	166	105	112	19885	22306	13445	14471	2x12
25	689	1	10/03/2008	IN	1794	1	209	87	10	2	149	166	180	175	19885	22306	24313	23597	2x12
25	690	1	11/03/2008	IN	1805	1	204	87	9	3	149	166	180	181	19885	22306	24313	24456	2x12
25	691	1	12/03/2008	IN	1817	1	201	86	9	3	149	166	180	182	19885	22306	24313	24599	2x12
25	693	1	14/03/2008	IN	1844	1	197	86	9	4	149	166	130	134	19885	22306	17099	17681	2x12
25	695	1	16/03/2008	IN	1877	1	197	84	9	4	149	166	130	135	19885	22306	17099	17826	2x12
25	697	1	18/03/2008	IN	1915	1	198	83	9	4	149	166	130	127	19885	22306	17099	16663	2x12
25	699	1	20/03/2008	IN	1963	1	201	82	9	5	149	166	178	185	19885	22306	24027	25027	2x12
25	703	1	24/03/2008	IN	2100	1	208	78	8	5	149	166	105	112	19885	22306	13445	14471	2x12
25	705	1	26/03/2008	IN	2203	2	212	76	8	5	149	166	190	188	19885	22306	25740	25455	2x12
25	706	1	27/03/2008	IN	2269	2	214	75	8	5	149	166	190	191	19885	22306	25740	25882	2x12
25	709	1	30/03/2008	IN	2572	2	220	70	7	5	149	166	105	112	19885	22306	13445	14471	2x12
25	710	1	31/03/2008	IN	2744	2	222	68	7	6	149	166	117	118	19885	22306	15203	15349	2x12
25	710	2	31/03/2008	E	7439	5	217	18	4	6	149	166	121	171	19885	22306	15787	23024	2x12
25	711	2	01/04/2008	E	6593	15	220	26	5	6	149	166	121	171	19885	22306	15787	23024	2x12
29	801	1	30/06/2008	E	2564	2	82	88	-9	10	149	130	190	114	19855	17099	25740	14764	2x12
29	803	1	02/07/2008	E	2575	2	105	87	-9	8	149	130	190	115	19855	17099	25740	14911	2x12
29	805	1	04/07/2008	E	2595	2	120	85	-9	8	149	130	190	138	19855	17099	25740	18262	2x12
29	807	1	06/07/2008	E	2625	2	132	84	-9	7	149	130	190	139	19855	17099	25740	18407	2x12
29	809	1	08/07/2008	E	2668	2	143	83	-9	7	149	130	190	150	19855	17099	25740	20000	2x12
29	811	1	10/07/2008	IN	13788	8	169	-35	-3	6	149	130	190	152	19855	17099	25740	20289	2x12
29	812	1	11/07/2008	E	2763	2	156	80	-8	7	149	130	190	177	19855	17099	25740	23883	2x12

Table K.1 (Continued)

Phase	Orbit	Case	Date	Type	Dist. to limb	Height res.	Longitude	Latitude	Speed	LST	Order 1	Order 2	Order 3	Order 4	Frequancy 1	Frequency 2	Frequency 3	Frequency 4	Binning
29	813	1	12/07/2008	IN	12918	8	175	-25	-3	6	149	130	190	186	19855	17099	25740	25170	2x12
29	815	1	14/07/2008	E	2915	2	169	77	-8	7	149	130	190	187	19855	17099	25740	25312	2x12
32	884	2	21/09/2008	E	5932	15	213	29	5	18	121	130	149	171	15787	17099	19855	23024	2x12
32	885	1	22/09/2008	E	6588	5	216	23	5	18	133	180	149	190	17536	24313	19855	25740	2x12
32	887	1	24/09/2008	E	7896	5	222	11	4	18	130	180	149	190	17099	24313	19855	25740	2x12
32	889	1	26/09/2008	E	9072	6	229	1	4	18	121	130	149	171	15787	17099	19855	23024	2x12
32	893	1	30/09/2008	E	11090	7	241	-19	3	18	185	187	149	180	25027	25312	19855	24313	2x12
32	895	1	02/10/2008	E	11945	7	248	-28	3	18	112	119	149	155	14471	15495	19855	20722	2x12
33	926	1	02/11/2008	E	12147	7	161	-26	3	6	185	187	149	190	25027	25312	19855	25740	2x12
33	930	1	06/11/2008	IN	1657	1	189	79	8	5	121	171	149	180	15787	23024	19855	24313	2x12
33	932	1	08/11/2008	E	9017	6	181	5	4	6	112	119	149	155	14471	15495	19855	20722	2x12
33	936	2	12/11/2008	E	5787	11	195	34	5	6	121	130	149	171	15787	17099	19855	23024	2x12
36	1012	2	27/01/2009	IN	13894	8	245	-42	-3	18	121	149	171	190	15787	19855	23024	25740	2x12
36	1013	1	28/01/2009	E	1595	1	269	86	-9	17	114	126	139	194	14764	16517	18407	26310	2x12
36	1014	2	29/01/2009	IN	14473	9	251	-51	-3	18	121	149	171	130	15787	19855	23024	17099	2x12
36	1015	2	30/01/2009	IN	14716	9	254	-55	-3	18	121	149	171	130	15787	19855	23024	17099	2x12
36	1016	2	31/01/2009	IN	14929	9	256	-60	-3	18	121	149	171	190	15787	19855	23024	25740	2x12
36	1018	1	02/02/2009	IN	15260	9	261	-68	-3	18	121	149	171	190	15787	19855	23024	25740	2x12
36	1019	2	03/02/2009	IN	15382	9	262	-72	-3	18	121	149	171	130	15787	19855	23024	17099	2x12
36	1020	2	04/02/2009	IN	15475	9	263	-76	-3	19	121	149	171	130	15787	19855	23024	17099	2x12
36	1021	2	05/02/2009	IN	15540	9	262	-81	-3	19	121	149	171	190	15787	19855	23024	25740	2x12
36	1022	2	06/02/2009	IN	15575	9	255	-85	-3	20	121	149	171	130	15787	19855	23024	17099	2x12
36	1023	2	07/02/2009	IN	15581	9	212	-88	-3	23	121	149	171	190	15787	19855	23024	25740	2x12
37	1024	1	08/02/2009	IN	15558	9	138	-86	-3	4	121	149	171	130	15787	19855	23024	17099	2x12
37	1025	1	09/02/2009	IN	15507	9	124	-82	-3	5	121	149	171	130	15787	19855	23024	17099	2x12
37	1026	1	10/02/2009	IN	15428	9	121	-78	-3	5	121	149	171	190	15787	19855	23024	25740	2x12
37	1027	1	11/02/2009	IN	15320	9	122	-74	-3	5	121	149	171	190	15787	19855	23024	25740	2x12
37	1028	1	12/02/2009	IN	15185	9	123	-70	-3	6	121	149	171	130	15787	19855	23024	17099	2x12
37	1029	1	13/02/2009	IN	15021	9	125	-66	-3	6	121	149	171	190	15787	19855	23024	25740	2x12
37	1030	1	14/02/2009	IN	14829	9	127	-61	-3	6	121	149	171	190	15787	19855	23024	25740	2x12

Table K.1 (Continued)

Phase	Orbit	Case	Date	Type	Dist. to limb	Height res.	Longitude	Latitude	Speed	LST	Order 1	Order 2	Order 3	Order 4	Frequency 1	Frequency 2	Frequency 3	Frequency 4	Binning
37	1031	1	15/02/2009	IN	14609	9	130	-57	-3	6	121	149	171	130	15787	19855	23024	17099	2x12
37	1032	1	16/02/2009	IN	14362	8	132	-53	-3	6	121	149	171	190	15787	19855	23024	25740	2x12
37	1033	1	17/02/2009	IN	14086	8	135	-48	-3	6	121	149	171	130	15787	19855	23024	17099	2x12
37	1034	1	18/02/2009	E	1522	1	104	86	-9	8	122	123	124	125	15933	16079	16225	16371	2x12
37	1035	1	19/02/2009	IN	13452	8	140	-40	-3	6	121	149	171	190	15787	19855	23024	25740	2x12
37	1036	1	20/02/2009	E	1543	1	114	85	-9	8	114	126	139	194	14764	16517	18407	26310	2x12
37	1037	1	21/02/2009	IN	12706	8	146	-30	-3	6	121	149	171	130	15787	19855	23024	17099	2x12
37	1038	1	22/02/2009	E	1571	1	124	84	-9	8	123	124	125	126	16079	16225	16371	16517	2x12
37	1039	1	23/02/2009	IN	11847	7	152	-21	-3	6	121	149	171	130	15787	19855	23024	17099	2x12
37	1040	1	24/02/2009	E	1610	1	133	83	-8	7	145	146	147	148	19277	19421	19566	19711	2x12
37	1041	1	25/02/2009	IN	10874	7	157	-11	-3	6	121	149	171	130	15787	19855	23024	17099	2x12
37	1042	1	26/02/2009	E	1664	1	142	82	-8	7	115	116	117	118	14911	15057	15203	15349	2x12
37	1043	1	27/02/2009	IN	9778	6	163	0	-4	6	121	149	171	190	15787	19855	23024	25740	2x12
37	1044	1	28/02/2009	E	1745	1	151	80	-8	7	114	126	139	194	14764	16517	18407	26310	2x12
37	1047	1	03/03/2009	IN	7147	5	174	24	-4	6	121	149	171	130	15787	19855	23024	17099	2x12
37	1048	1	04/03/2009	IN	6356	5	177	31	-5	6	121	149	171	190	15787	19855	23024	25740	2x12
37	1049	1	05/03/2009	IN	5452	7	180	40	-5	6	121	149	171	190	15787	19855	23024	25740	2x12
37	1049	2	05/03/2009	E	2270	4	174	73	-7	7	121	149	171	190	15787	19855	23024	25740	2x12
40	1110	2	05/05/2009	E	6364	15	189	29	5	18	130	149	180	190	17099	19855	24313	25740	2x12
40	1111	2	06/05/2009	E	7175	20	192	22	5	18	112	121	171	149	14471	15787	23024	19855	2x12
40	1112	1	07/05/2009	E	7843	5	195	16	5	18	130	149	180	190	17099	19855	24313	25740	2x12
40	1114	1	09/05/2009	E	9160	6	202	4	4	18	130	149	180	190	17099	19855	24313	25740	2x12
40	1115	1	10/05/2009	IN	1758	1	200	79	8	18	112	121	171	149	14471	15787	23024	19855	2x12
40	1116	1	11/05/2009	E	10326	6	208	-7	4	18	130	149	180	190	17099	19855	24313	25740	2x12
40	1117	1	12/05/2009	IN	1681	1	204	81	9	18	146	147	148	149	19421	19566	19711	19855	2x12
40	1118	1	13/05/2009	E	11363	7	214	-17	4	18	130	149	180	190	17099	19855	24313	25740	2x12
40	1119	1	14/05/2009	IN	1630	1	208	82	9	19	175	177	178	179	23597	23883	24027	24170	2x12
40	1120	1	15/05/2009	E	12283	7	221	-26	3	18	112	121	171	149	14471	15787	23024	19855	2x12
40	1121	1	16/05/2009	IN	1595	1	212	83	9	19	106	176	161	162	13592	23740	21587	21731	2x12
40	1124	1	19/05/2009	E	13788	8	234	-44	3	18	121	149	166	171	15787	19855	22306	23024	2x12

Table K.1 (Continued)

Phase	Orbit	Case	Date	Type	Dist. to limb	Height res.	Longitude	Latitude	Speed	LST	Order 1	Order 2	Order 3	Order 4	Frequancy 1	Frequency 2	Frequency 3	Frequency 4	Binning
40	1125	1	20/05/2009	IN	1547	1	216	85	9	19	156	157	158	159	20866	21010	21154	21299	2x12
40	1126	1	21/05/2009	E	14377	9	240	-52	3	18	130	149	166	190	17099	19855	22306	25740	2x12
40	1128	1	23/05/2009	E	14857	9	248	-61	3	18	149	161	162	166	19855	21587	21731	22306	2x12
40	1130	1	25/05/2009	E	15228	9	255	-69	3	18	130	149	166	190	17099	19855	22306	25740	2x12
40	1132	1	27/05/2009	E	15490	9	264	-77	3	18	130	149	166	190	17099	19855	22306	25740	2x12
40	1133	1	28/05/2009	IN	1510	1	198	88	10	22	116	141	153	154	15057	18697	20433	20578	2x12
41	1137	1	01/06/2009	IN	1518	1	166	88	10	1	160	163	164	165	21443	21874	22018	22162	2x12
41	1139	1	03/06/2009	E	15538	9	91	-75	3	7	121	149	166	171	15787	19855	22306	23024	2x12
41	1141	1	05/06/2009	E	15299	9	100	-67	3	6	130	149	166	190	17099	19855	22306	25740	2x12
41	1152	1	16/06/2009	IN	1809	1	154	80	9	5	167	168	169	173	22449	22593	22737	23310	2x12
41	1154	1	18/06/2009	E	10763	7	144	-8	4	6	149	161	162	166	19855	21587	21731	22306	2x12
41	1158	1	22/06/2009	E	8029	5	158	17	4	6	112	121	171	149	14471	15787	23024	19855	2x12
41	1160	1	24/06/2009	IN	2963	5	168	65	7	6	180	130	149	190	24313	17099	19855	25740	2x12
41	1160	2	24/06/2009	E	6182	8	165	34	5	6	180	130	149	190	24313	17099	19855	25740	2x12
44	1223	1	26/08/2009	IN	6031	5	177	34	-5	18	149	130	190	114	19855	17099	25740	14764	2x12
44	1224	1	27/08/2009	IN	6936	5	180	25	-5	18	149	130	190	110	19855	17099	25740	14178	2x12
44	1230	1	02/09/2009	IN	10804	7	198	-11	-4	18	149	130	190	145	19855	17099	25740	19277	2x12
44	1238	1	10/09/2009	IN	13847	8	221	-49	-3	18	149	130	190	145	19855	17099	25740	19277	2x12
44	1247	1	19/09/2009	IN	15055	9	222	-86	-3	20	149	130	190	145	19855	17099	25740	19277	2x12
45	1248	1	20/09/2009	IN	15053	9	161	-88	-3	0	149	101	102	103	19855	12857	13004	13151	2x12
45	1250	1	22/09/2009	IN	14970	9	96	-81	-3	5	149	103	104	105	19855	13151	13298	13445	2x12
45	1252	1	24/09/2009	IN	14781	9	95	-74	-3	5	149	164	165	166	19855	22018	22162	22306	2x12
45	1254	1	26/09/2009	IN	14488	9	98	-65	-3	6	149	166	167	168	19855	22306	22449	22593	2x12
45	1256	1	28/09/2009	IN	14091	8	103	-57	-3	6	149	121	171	166	19855	15787	23024	22306	2x12
45	1260	1	02/10/2009	IN	12990	8	114	-40	-3	6	149	130	180	190	19855	17099	24313	25740	2x12
45	1262	1	04/10/2009	IN	12286	7	119	-31	-3	6	149	130	180	190	19855	17099	24313	25740	2x12
45	1264	1	06/10/2009	IN	11482	7	125	-22	-3	6	149	140	141	176	19855	18552	18697	23740	2x12
45	1266	1	08/10/2009	IN	10575	6	131	-13	-3	6	149	130	134	135	19855	17099	17681	17826	2x12
45	1268	1	10/10/2009	IN	9565	6	137	-3	-4	6	149	149	148	150	19855	19866	19711	20000	2x12
48	1335	1	16/12/2009	IN	3118	5	163	65	7	18	148	149	150	190	19711	19855	20000	25740	2x12

Table K.1 (Continued)

Phase	Orbit	Case	Date	Type	Dist. to limb	Height res.	Longitude	Latitude	Speed	LST	Order 1	Order 2	Order 3	Order 4	Frequancy 1	Frequency 2	Frequency 3	Frequency 4	Binning
48	1336	1	17/12/2009	IN	2802	2	165	69	7	18	148	189	190	191	19711	25597	25740	25882	2x12
48	1336	2	17/12/2009	E	7340	19	167	24	5	18	148	189	190	191	19711	25597	25740	25882	2x12
48	1337	1	18/12/2009	IN	2669	2	168	71	8	18	148	189	190	191	19711	25597	25740	25882	2x12
48	1337	2	18/12/2009	E	8018	5	170	18	5	18	148	128	130	134	19711	16808	17099	17681	2x12
48	1339	1	20/12/2009	IN	2405	2	173	75	8	18	148	189	190	191	19711	25597	25740	25882	2x12
48	1340	1	21/12/2009	IN	2316	2	175	76	8	18	148	149	150	190	19711	19855	20000	25740	2x12
48	1341	1	22/12/2009	E	10742	7	182	-6	4	18	148	128	130	134	19711	16808	17099	17681	2x12
48	1342	1	23/12/2009	IN	2186	2	180	78	8	18	148	149	150	190	19711	19855	20000	25740	2x12
48	1343	1	24/12/2009	IN	2136	1	182	79	9	18	148	189	190	191	19711	25597	25740	25882	2x12
48	1344	1	25/12/2009	E	12349	7	192	-22	3	18	148	149	150	190	19711	19855	20000	25740	2x12
48	1345	1	26/12/2009	E	12818	8	195	-27	3	18	148	189	190	191	19711	25597	25740	25882	2x12
48	1346	1	27/12/2009	E	13255	8	198	-31	3	18	148	149	150	190	19711	19855	20000	25740	2x12
48	1347	1	28/12/2009	IN	2000	1	189	82	9	19	148	149	150	190	19711	19855	20000	25740	2x12
49	1374	1	24/01/2010	IN	2101	1	120	80	9	5	119	120	121	122	15493	15639	15785	15931	2x12
49	1375	1	25/01/2010	E	12709	8	106	-22	3	6	107	149	142	109	13735	19850	18838	14029	2x12
49	1376	1	26/01/2010	IN	2219	2	123	78	8	5	109	128	138	152	14029	16805	18258	20283	2x12
49	1380	1	30/01/2010	IN	2661	2	131	72	8	5	149	148	143	141	19850	19706	18983	18693	2x12
49	1381	1	31/01/2010	IN	2861	2	133	70	7	5	115	116	117	149	14908	15054	15200	19850	2x12
49	1381	2	31/01/2010	E	8877	6	126	13	4	6	104	165	160	149	13295	22153	21435	19850	2x12
49	1382	1	01/02/2010	IN	3146	2	135	67	7	6	149	150	142	179	19850	19994	18838	24155	2x12
49	1382	2	01/02/2010	E	7966	21	129	21	5	6	113	129	140	151	14615	16951	18548	20139	2x12
49	1383	1	02/02/2010	IN	3614	3	136	62	7	6	127	131	144	153	16660	17242	19127	20427	2x12
49	1383	2	02/02/2010	E	6841	13	133	31	5	6	127	131	144	153	16660	17242	19127	20427	2x12
52	1446	1	06/04/2010	IN	5361	4	145	37	-5	18	149	185	189	191	19850	25010	25579	25863	2x12
52	1446	2	06/04/2010	E	2020	4	145	76	1	18	149	185	189	191	19850	25010	25579	25863	2x12
52	1447	1	07/04/2010	IN	6208	4	148	29	-5	18	122	121	125	175	15931	15785	16368	23584	2x12
52	1447	2	07/04/2010	E	1476	4	149	78	-7	18	122	121	125	175	15931	15785	16368	23584	2x12
52	1448	1	08/04/2010	IN	7030	21	151	21	-5	18	150	184	188	189	19994	24868	25437	25579	2x12
52	1448	2	08/04/2010	E	1370	1	153	80	-8	18	141	125	175	180	18693	16368	23584	24298	2x12
52	1450	1	10/04/2010	IN	8298	5	157	9	-4	18	148	184	185	191	19706	24868	25010	25863	2x12

Table K.1 (Continued)

Phase	Orbit	Case	Date	Type	Dist. to limb	Height res.	Longitude	Latitude	Speed	LST	Order 1	Order 2	Order 3	Order 4	Frequancy 1	Frequency 2	Frequency 3	Frequency 4	Binning
52	1457	1	17/04/2010	IN	11759	7	178	-26	-3	18	150	185	189	191	19994	25010	25579	25863	2x12
52	1459	1	19/04/2010	E	1758	1	195	84	-9	17	148	141	117	112	19706	18693	15200	14469	2x12
52	1460	1	20/04/2010	IN	12909	8	187	-39	-3	18	148	141	116	112	19706	18693	15054	14469	2x12
52	1461	1	21/04/2010	E	1712	1	205	85	-9	17	165	160	148	117	22153	21435	19706	15200	2x12
52	1462	1	22/04/2010	IN	13474	8	192	-48	-3	18	166	156	148	148	22296	20859	19706	19693	2x12
52	1464	1	24/04/2010	E	1659	1	224	86	-9	16	165	160	150	111	22153	21435	19994	14322	2x12
52	1465	1	25/04/2010	IN	14117	8	200	-60	-3	18	166	160	149	111	22296	21435	19850	14322	2x12
52	1466	1	26/04/2010	IN	14278	8	203	-64	-3	18	149	117	111	122	19850	15200	14322	15931	2x12
52	1467	1	27/04/2010	E	1617	1	248	87	-10	15	166	156	150	149	22296	20859	19994	19850	2x12
52	1468	1	28/04/2010	E	1605	1	259	88	-10	15	149	141	112	122	19850	18693	14469	15931	2x12
52	1468	1	28/04/2010	E	1605	1	259	88	-10	15	149	141	112	122	19850	18693	14469	15931	2x12
52	1469	1	29/04/2010	IN	14607	9	207	-76	-3	19	166	156	148	112	22296	20859	19706	14469	2x12
53	1480	1	10/05/2010	E	1506	1	31	87	-9	9	165	156	150	141	22153	20859	19994	18693	2x12
53	1482	1	12/05/2010	E	1497	1	42	86	-9	8	150	116	141	112	19994	15054	18693	14469	2x12
53	1484	1	14/05/2010	IN	12890	8	85	-43	-3	6	149	184	189	190	19850	24868	25579	25721	2x12
53	1486	1	16/05/2010	E	1491	1	62	85	-9	8	150	185	189	191	19994	25010	25579	25863	2x12
53	1487	1	17/05/2010	E	1491	1	67	84	-9	8	148	184	185	189	19706	24868	25010	25579	2x12
53	1490	1	20/05/2010	E	1500	1	80	83	-8	7	150	185	188	190	19994	25010	25437	25721	2x12
53	1493	1	23/05/2010	E	1526	1	93	82	-8	7	148	184	190	191	19706	24868	25721	25863	2x12
53	1494	1	24/05/2010	IN	8730	5	114	3	-4	6	122	125	130	175	15931	16368	17096	23584	2x12
53	1498	1	28/05/2010	IN	6345	18	125	26	-4	6	141	125	175	180	18693	16368	23584	24298	2x12
53	1498	2	28/05/2010	E	1657	1	114	78	-7	7	122	125	130	175	15931	16368	17096	23584	2x12
53	1499	1	29/05/2010	IN	5749	15	128	31	-5	6	122	125	175	180	15931	16368	23584	24298	2x12
53	1499	2	29/05/2010	E	1683	2	117	77	-7	7	122	125	175	180	15931	16368	23584	24298	2x12
56	1565	1	03/08/2010	IN	10389	7	333	-11.79	-4	6	179	148	155	165	24155	19706	20715	22153	2x12
56	1567	1	05/08/2010	E	11774	8	159	-11.35	-4	18	141	149	156	166	18693	19850	20859	22296	2x12
56	1581	1	19/08/2010	IN	14405	23	14	-77.71	-3	7	179	148	155	165	24155	19706	20715	22153	2x12
57	1586	1	24/08/2010	E	16700	32	24	-82	-3	7	120	141	175	189	15639	18693	23584	25579	2x12
57	1588	1	26/08/2010	E	16562	32	37	-73	-3	6	120	125	172	174	15639	16368	23155	23441	2x12
57	1593	1	31/08/2010	IN	13536	17	242	-57	-3	18	185	187	189	191	25010	25294	25579	25863	2x12

Table K.1 (Continued)

Phase	Orbit	Case	Date	Type	Dist. to limb	Height res.	Longitude	Latitude	Speed	LST	Order 1	Order 2	Order 3	Order 4	Frequancy 1	Frequency 2	Frequency 3	Frequency 4	Binning
57	1594	1	01/09/2010	IN	13320	16	245	-53	-3	18	184	186	188	190	24868	25152	25437	25721	2x12
57	1595	1	02/09/2010	E	14958	27	63	-42	-3	6	184	186	188	190	24868	25152	25437	25721	2x12
57	1596	1	03/09/2010	IN	12820	14	250	-45	-3	18	185	187	189	191	25010	25294	25579	25863	2x12
57	1598	1	05/09/2010	IN	12213	11	256	-37	9	18	184	186	188	190	24868	25152	25437	25721	2x12
57	1599	1	06/09/2010	E	13207	22	77	-22	-4	6	121	126	173	175	15785	16514	23298	23584	2x12
57	1600	1	07/09/2010	E	12667	20	80	-16	-4	6	121	125	172	174	15785	16368	23155	23441	2x12
57	1601	1	08/09/2010	E	12079	18	83	-11	-4	6	120	126	173	174	15639	16514	23298	23441	2x12
57	1602	1	09/09/2010	IN	10811	8	267	-21	-3	18	121	125	172	175	15785	16368	23155	23584	2x12
57	1604	1	11/09/2010	IN	9982	10	273	-12	-4	18	120	126	173	175	15639	16514	23298	23584	2x12
57	1606	1	13/09/2010	IN	9067	11	279	-3	-4	18	120	141	175	189	15639	18693	23584	25579	2x12
57	1606	2	13/09/2010	E	8046	6	100	25	-4	6	120	141	175	189	15639	18693	23584	25579	2x12

Table K.1 (Continued)

Appendix L

List of the species absorbing in each order

The following Tables summarize the isotopologues of each species that are observed and retrieved from the SOIR measurements. The species that is given is the one presenting the strongest line intensities multiplied by its volume mixing ratio in each order. The first Table gives the species from which vertical profiles are obtained, while the last one concerns the detection limits. The isotopologues are given in the Hitran format [Rothman *et al.* (2009)]. Note that even some species absorb in the three first and two last orders, the signal to noise ratio is too low to obtain reliable vertical profiles.

Order	CO_2	H_2O	CO	HCl	HF	SO_2
101						
102						
103						
104	626					
105	626					
106	626					
107	626					
108	626					
109	626					
110	628					
111	628					
112	628					626
113	628					
114						
115	628					
116	628					
117	628					
118		162				
119		162				
120		162				
121		162				
122		162				
123		162				
124		162				
125		162				
126		162		15, 17		
127				15, 17		

Table L.1: List of the isotopologues of each species absorbing in each order and allowing the retrieval of vertical density profiles.

Order	CO_2	H_2O	CO	HCl	HF	SO_2
128				15, 17		
129				15, 17		
130				15, 17		
131				15, 17		
132				15, 17		
133				15, 17		
134				15, 17		
135		161		15, 17		
136		161		15, 17		
137		161				
138		161				
139		161				
140	626					
141	626					
142	626					
143	626					
144	626					
145	636					
146	636					
147	626					
148	626					
149	626					
150	626					
151	626					
152	636					
153	636					
154	636					
155	636					
156	636					
157	636					
158	636					
159	626					
160	626					
161	626					
162	626					
163	636					
164	626					
165	626					
166	626					
167	626					
168		161				
169		161				
170		161				
171		161				
172		161				
173		161				
174		161				
175		161				
176		161				
177	628				19	
178	628				19	
179	626				19	
180					19	
181					19	
182					19	
183		161			19	

Table L.1 (Continued)

Order	CO_2	H_2O	CO	HCl	HF	SO_2
184		161			19	
185		161			19	
186		161	36		19	
187			26			
188			26			
189			26			
190			26			
191			26			
192			26			
193						
194						

Table L.1 (Continued)

Order	OCS	H_2CO	CH_4	HI	HBr	OH
101						
102						
103						
104						
105						
106						
107						
108						
109						
110						
111						
112					19	
113					19	
114					19	
115					19	
116					19	
117					19	
118						
119						
120						
121						
122						
123		126				
124		126				
125		126				
126		126				
127		126				
128		126				
129						
130	622					
131						
132						
133						
134			211			
135			211			
136			211			
137			211			
138						

Table L.2: List of the isotopologues of each species absorbing in each order and allowing the retrieval of detection limit profiles.

Order	OCS	H_2CO	CH_4	HI	HBr	OH
139						
140						
141						
142						
143						
144						
145						
146						
147						
148						
149						
150						
151						
152						
153						
154						
155						61
156						61
157						61
158						61
159						
160						
161						
162						
163						
164						
165						
166						
167						
168						
169						
170						
171						
172						
173						
174						
175						
176						
177						
178						
179						
180						
181						
182						
183	622					
184						
185						
186						
187						
188						
189						
190				17		
191				17		
192				17		
193						
194						

Table L.2 (Continued)